université de BORDEAUX

THÈSE PRÉSENTÉE
POUR OBTENIR LE GRADE DE

DOCTEURE DE L'UNIVERSITÉ DE BORDEAUX

ÉCOLE DOCTORALE DES SCIENCES DE LA VIE ET DE LA SANTÉ
SPÉCIALITÉ : BIOLOGIE CELLULAIRE ET PHYSIOPATHOLOGIE

Par Violeta Milanović

Etude de la mécanotransduction cellulaire au sein de cellules vivantes à l'aide de techniques de microscopie de polarisation sur molécule unique.

Studying cellular mechanotransduction in living cells using single molecule fluorescence polarization microscopy

Sous la direction de : Olivier ROSSIER

Soutenue le 01 Octobre 2025

Membres du jury :

M. WEHRLE-HALLER, Bernhard	Professor, UNIGE	Rapporteur
M. HYTÖNEN, Vesa	Professor, TAU	Rapporteur
Mme. ALBIGES-RIZO, Corinne	Directrice de recherche (CNRS), IAB	Examinatrice
M. NASSOY, Pierre	Directeur de recherche (CNRS), LP2N	Présidente
Mme. BRASSELET Sophie	Directrice de recherche (CNRS), IF	Membre invitée
M. ROSSIER Olivier	Chargé de recherche (INSERM), IINS	Directeur de thèse

Ову дисертацију посвећујем малој Виолети.

Њој која се није осећала као да има место у свету.

Њој која ће много тога пребродити.

Сада стваращ своје место.

Ja sam žena, ali smem.

Draga Dimitrijević Dejanović

Acknowledgements

Firstly, I would like to thank my jury members for accepting to evaluate my work. Thank you to Bernhard Wehrle-Haller and Vesa Hytönen for taking the time to review this thesis. I extend my gratitude towards Corinne Albiges-Rizo and Pierre Nassoy for agreeing to be a part of my jury for the defense.

Special thanks to Sophie Brasselet, without whom this project would not exist. Thank you for your continuous support, endless knowledge and kindness. I feel truly privileged to have had you as such a big part of my thesis and my research.

A person who deserves equal praise is certainly Charitra Sree Senthil Kumar. Thank you for being the most wonderful fellow PhD student on this project. Thank you for finding the time to stay next to the setup and supervise my acquisitions while I prepare samples for the next day. Thank you for meeting me many times on Zoom or chatting on WhatsApp to solve coding issues that continue to be born from perfectly working codes, thank you for all the intelligence and effort you have put in to better this project and help us get closer to our goal. Thank you for your kindness and friendship.

Huge thank you to Manos Mavrakis and also Shizue Omi-Massieau for the development of the protein constructs. Thank you for your fast responsiveness, your knowledge and kindness.

Big thanks to Ben Goult for the development of the talin protein constructs as well. Thanks also for borrowing Yasumi to us for a couple of months, she was a wonderful addition to our team!

Thank you, Florian Levet, for your help in our 3D analysis streamline creation.

Thanks to our collaborator Luke Lavis for always generously sending us Janelia Fluors.

Thank you to my supervisor Olivier Rossier, without whom I would not have been on this project, and would not have had the opportunity to be writing this right now. Thank you for all of your support Olivier. Thank you for always finding positivity in any situation, and making efforts to improve yourself. Thank you for teaching me from the start how to stay organized. As someone who loves organization, I would be very frustrated if I searched for data from my first year to write this manuscript, and couldn't find something I need. Luckily, all was waiting for me neatly named in Olivier fashion. Thank you for all your great advice during writing this thesis. I hope you

are happy with the work we created together and that it will result in a nice paper. I will come back to the lab with champagne to mark the office ceiling. Milanović et al. 202#. Can't wait.
I want to say thank you to all the people in my team who made this experience much more than a PhD thesis. To the people who supported me every day of my thesis, and, despite the challenge that my PhD has been, have made me sad that it is ending.
Firstly, thank you to my big MEF brother Adrien. From day 1, I have had questions, until the last day of your contract, and you have, with the same kindness, answered all of them. Please stay so kind and wonderful. And do not let the world take advantage of that. Xuesi (also known as Suzy, Xuezi, Zuzu, Xuesss, Zuzizu, etc.), thank you for all your sweetness and support and for being a wonderful PhD sister. Thank you for being sassy so that my "mean" jokes are not standing alone. You are so intelligent, hard-working and wonderful to work with, and I hope that wherever you end up, all of that will be appreciated and praised. (To be read in queen's English) Dearest esteemed Morgane, would you be so kind to accept my eternal gratitude for thy support? (Now back to simplified English) I truly admire the person you are and am really thankful for all your support, advice, and contributions to my thesis. Thank you for being a wonderful friend and role model. You are a true gem and this team is lucky to have you as a permanent researcher. Bea bellissima, I am so happy you joined our team so early on in my thesis and that I had all this time to enjoy your friendship. Thank you for your support and understanding. I wish nothing less for you than to be happy and fulfilled. You have so much to offer as a person, and so much knowledge and creativity as a researcher. You are a wonderful human to have as a friend and as a colleague, and I hope your life will lead you wherever that is appreciated. Lorenzo, stronza di Italia, ma dai. Don't laugh, ah. It is not funny. Hehe. Thank you for choosing to join our team. You are a wonderful addition to my fourth year, and truly a person who has made this experience even more unique and wonderful. Thanks to our organization queen, chief of the GG police Melanie. Thank you for all the effort you put to make this a good place to work at, and for all the scientific work you do to make our research possible. Thank you for always being cheerful and helpful. Thank you Dounia for all your efforts too. You are indeed such a sweet being and I am so happy to know you. You bring so much brightness into every day I come to work. Also, stop being so pretty. Eloina, my sweet daughter, you are such a kind, wonderful, selfless human being, a

wonderful friend and colleague, and an amazing mother. My only hope for you is that your life will treat you as nice as you treat everyone around you. You deserve that and so much more. Thanks also to the boss man Nassim. You are literally already ready to be a boss. So competent, intelligent, hardworking, friendly, compassionate and getting along with everyone. You are such a nice and peaceful presence in the office. Thanks for all your support, especially during the past couple of months – hyping me about the amount of stuff I wrote and then listening to me showing you my progress. I can't wait to see your defense. I am certain it will be one of the most impressive works done during a PhD at IINS. Amine, thanks for coming back to this team. You are such a cool person, and this group is lucky to have someone as hardworking as you. Seriously, you should rest sometimes. Thanks for all your support, scientific advice and humor. Please never change. Yonathan, thanks for choosing to join and stay in our team. It is so wonderful knowing someone as wonderful and smart as you is going to be Morgane's first PhD student. I wish you joined even earlier so that I can enjoy your company for longer. Thanks for all your support, friendliness, for listening to me complain and complementing on my muscles.

Thanks also to Theo, Tianchi, and our alumni Maureen and Filipe.

Thanks to our team leader Greg, without whom my thesis wouldn't have been the same.

Thanks to other IINS people. My friend Tomas, funny, smart, wonderful human being. You are truly one of my favorite people at IINS. I will miss our fist bumps, funny conversations and rant sessions. I hope that life will take you somewhere where you will be happy. Hopefully somewhere sunny, with a direct, cheap flight. Hugs! Lots of love for Anushka and Ihssane.

A sad malo na jeziku najstarijeg naroda.

Mojim prijateljima, hvala vam. Hvala za sve ove godine koje ste uz mene.

Mojoj Milici, mojoj cimi, mojoj bebi. Hvala ti što si me pozvala na koncert tog marta 2017. godine, jer je to izrodilo jedno od mojih najdražih prijateljstava. Jer mi je dalo nekoga koga, bez ikakvog preuveličavanja, smatram sestrom. Životni put nas je trenutno geografski razdvojio, ali ti se ne osećam nimalo manje blisko. Hvala ti za divne tri godine u Studenjaku. Za svu ljubav i podršku, sav smeh, guranje pred ispite, đuskanje u KSTu, olakšavanje muka Hemijskog Fakulteta. Hvala ti što čuvaš naše prijateljstvo i bliskost. Želim da ga zauvek negujemo <3

Hvala i Mladenu, Milicinom bratu, jer mi je javio da je produžen rok za stipendiju Francuskog instituta za Master studije, jer bez iste ne bih uspela da dođem u Bordo, a verovatno ni nađem i budem primljena na ovaj doktorat.

Mom Mihailu, predivnoj osobi bez koje ne mogu da zamislim svoj život. Hvala ovom nežnom, predivnom biću, mom predivnom prijatelju. Hvala ti za svu ljubav i za to što nikada, apsolutno nikada, tvoja podrška za mene ne jenjava. Imaš posebno mesto u mom srcu i stolicu u mom krugu prijatelja za ceo život.

Icko, veliki zagrljaj za tebe. Ti si imala zaista posebno mesto u mojoj tezi. Od HFa do našeg zajedničkoj deljenja iskustva IINSa. Jako sam srećna što te imam u životu i radujem se (i nadam) da vidim kako će život nastaviti da nas spaja. Nedostaje mi moja soul sister već <3 Jako sam ponosna na tebe i sve što postižeš i samo se nadam da će svet nastaviti da te nagrađuje za sve divno što si.

Emi - mojoj nerođenoj starijoj sestri i majci mog omiljenog deteta, Koleta. Još divnije od čišćenja prve godine HFa u junu, bilo je to što sam dolazila na Venac i dobila tebe kao prijatelja. Hvala ti za svu podršku i iskrenost i za to što ostaješ uz mene sve ove godine. Hvala ti što si uvek moj nesebični navijač.

Thank you my pisces sister Kojić for fighting for our žalopojka romantika mentality. Jako sam srećna što te imam u životu i nestrpljivo čekam naše blejice. Hvala ti što si jedno divno biće, uvek spremna da se bori za ono u šta veruje, i za ljude koje voli. https://youtu.be/FTQbiNvZqaY?si=8SuHcMUf0GAPIqG9

Mojoj Anđeli, osobi bez koje, bez ikakve sumnje, ne bih bila osoba koja jesam danas. Hvala ti za sve. Za svu ljubav, za svaki veliki i mali poguraj, za neiscrpnu podršku u mojim najtežim i najsrećnijim trenucima. Ti si jedna od najdivnijih ljudi koje sam ikad upoznala. Osećam se incredibly lucky što te imam u svom životu. Ponoviću, hvala ti za sve. Jer, to nije samo rečenica koju tek tako kažem, već nešto što zaslužuje da se nađe na ovako bitnom mestu.

Hvala mojim beogradskim roditeljima, Snežani i Milosavu Kiurski, za svu ljubav, podršku i neizbrojivu količinu obroka koje sam pojela dok sam učila sa Mihailom kod vas u stanu.

Veliki zagrljaj i hvala za Jecukr!

Veliko hvala i ženama iz mog komšiluka, uz koje sam odrasla. Hvala Sanji, Miki, Sandri i Zorki za svu vašu ljubav, humor, podršku i podstrek vašoj maloj drugarici Violeti. Hvala vam što ste me naučile da porodica mogu biti i oni koji nisu krvno srodstvo. Hvala vam za vaš udeo u formiranju osobe koja jesam danas.

Thank you to my Master thesis supervisor, Jean Chrisophe Baret, for inspiring me to do a PhD. Thanks also to my tutor, Michel Thiebaut de Schotten. Thank you both for all your kind words and support.

Thank you to all my Fresnel friends. Even though I was not an official part of the institute, you made me feel as welcome as anyone else. Thank you for letting me be a part of the gang. Special thanks and lots of love for Elio and Federico.

Lots of love for Elhame, Sarah and Zouzou <3 Merci ktir <3

Merci du fond du cœur à Pierre et Josiane Crespos. Vous nous avez ouvert votre porte et votre cœur à un moment où cela comptait plus que tout. Merci pour tout ce que vous avez fait pour nous. Je suis tellement heureuse d'avoir eu la chance de vous connaître. J'espère que vous savez à quel point je vous suis reconnaissante.

Hvala mojoj porodici. Mama, tata, Acika, hvala vam što od mog rođenja negujete sve što jesam. Mama, tata, hvala vam, pre svega, što ste dobri ljudi. Ovaj doktorat, ili bilo šta veće ili manje za mene ne znači ništa ukoliko nisam pre svega dobar čovek. A ne bi bilo tako da za uzor nemam divne i poštene ljude koji svoj život žive tako da budu srećni, ali ne na račun tuđe muke. Hvala vam za sve. Za početak što ste me doveli na ovaj svet. Što ste mi od malena dozvolili da budem svoja i gurali me ka tome da razvijam sebe, a ne neku vašu ideju mene. Hvala vam za časove plesa, densa, folklora, hora, za rukomet, odbojku, za časove klavira, pevanja, za to što ste mi verovali da odem u Ameriku sa 17 godina, za to što od kad znam za sebe, osećam se saslušano i poštovano. Hvala vam što ste me uvek podržali, a i dalje to radite, u tome da nađem sebe i svoju svrhu, ili

više njih. Bez svega toga, ja ne bih bila osoba koja jesam danas. Ne bih znala da se na isti način borim za sebe, svoja verovanja i mišljenja. Verujem da je najvažniji zadatak roditelja da nauče dete kako da pronađe svoj put i da njime ide časno - u skladu sa sobom i svetom oko sebe. Vi ste mi dali i više od toga. Dali ste mi snagu da u svakom trenutku prepoznam ko sam, da se držim svojih vrednosti i biram pravi put, čak i kad nije najlakši. Volim vas najviše.

Moj Acke, hvala ti što si divan veliki bato. Od malena, kada me neko oslovljavao kao – Acikina sestra, ja sam bila ponosna, a još sam ponosnija danas. Na mog velikog batu koji se konstantno trudi da sebe poboljša na svakom frontu. Hvala ti što si jedno divno biće, što se trudiš da si uvek prema svima čovek. Oprostiću ti što si omiljeni celoj rodbini. Razumem ih ♡. Ostani zauvek tako predivan i omiljeni svima. Voli te seka puno!

Tanjice mila, tebe ne smemo zaboraviti! Presrećna sam što te Acika ima uz sebe. Ti si jedno predivno, milo, pametno biće i privilegija nam je što si i deo života ostatka porodice. I tebe volim puno!

Želim da se zahvalim i svojoj učiteljici, Zorki Antonijević. Kao što su me i roditelji gurali da se uvek borim za sebe, tako ih je i ona podsticala da to rade. Hvala učiteljice za to što mi niste kratili krila, već me gurali da unapredim sebe, da znam šta je moje mišljenje i kako da se za njega borim. Zauvek ćete ostati za mene jedan od najbitnijih pedagoga i neko ko je definitivno uticao u velikoj meri na to ko sam i gde sam ja danas.

Veliko hvala i ljubav za moju mnogobrojnu rodbinu, koju neću izlistavati ovde, jer će morati nekoliko dodatnih stabala drveća da poseku za štampu. Posebno ću izdvojiti tetka Jelu, tetka Vesnu i moju Mumu.

Amer, hayete, there are no words to truly express how thankful I am to you, and for you. Your unwavering, genuine, and selfless support has carried me not only through this thesis, but through so much more. You constantly remind me of my worth, of my competence, my intelligence, and my abilities, especially in moments when I forget them myself. I often struggle with feeling like I’m not enough, but you make me feel that who I am is not only enough, but

something to be proud of. You make me believe that those who work with me are lucky to have me. And I know that I am endlessly lucky to have you—by my side, through everything. My biggest supporter, my most loving cheerleader. My companion through it all, my anchor, my safe place. Thank you for everything. Kel lahza bt arrebne aktar menak.. ma ba2a fiye ontur la nbalesh 3omrna sawa ♡

Abstract

Mechanotransduction, the process by which mechanical forces are converted into biochemical signals, is fundamental to cellular adhesion, migration, and the spatial organization and integrity of tissues. Integrin adhesion sites (IAS) serve as the mechanical interface between the extracellular matrix and the cytoskeleton, and host a complex network of force-sensitive proteins such as talin. Key protein in integrin adhesive structure, talin establishes the physical linkage that transmits cell mechanical forces to its surroundings. Far from being a rigid structural element, talin is a large multimodular protein carrying multiple domains with binding sites which are exposed when talin is stretched by force. This complex mechanical response led to propose the interesting hypothesis of a talin code in which both the shape of talin scaffolds and the set of partners bound to talin could serve as a readout for the mechanical information encoded by cells. While the force-induced conformational changes of talin have been extensively studied in vitro, how talin conformation is changing within the native architecture of living cells still remain poorly resolved, particularly in terms of spatial orientation.

This thesis focuses primarily on talin molecular orientation in focal adhesions (FAs) using single-molecule fluorescence polarization microscopy. To probe distinct mechanical segments along talin, we engineered a panel of talin constructs fused to mEos3.2 at specific domains - neck, R3, R12, and the C-terminus. Using an optimized live-cell imaging pipeline, we successfully extracted mEos3.2 in-plane (ρ), out-of-plane (η), and wobbling (δ) angles used as proxies for talin domain orientation. The orientation distributions of talin domains were consistent with their known mechanical context: domains closer to integrins, such as the neck and R3, exhibited strong directional alignment along the focal adhesion axis, while R12 and C-terminal tags showed more isotropic behavior. These results in living cells recapitulated those we obtained in fixed samples, confirming the robustness and reproducibility of the approach under basal contractile conditions.

This thesis demonstrates that molecular orientation serves as a powerful and previously underused live-cell readout of mechanical state. Beyond talin, the molecular tools, methods and insights developed here provide a framework to study how proteins such as integrins, vinculin, or actin reorganize under force in their native environment. With continued technological development, orientation-resolved single-molecule microscopy holds strong potential to decode the mechanical logic of adhesion and signaling in both physiological and pathological contexts.

Keywords: mechanotransduction, cell adhesion, single protein tracking, fluorescence polarization

Resumé

La mécanotransduction, processus par lequel les forces mécaniques sont converties en signaux biochimiques, est fondamentale pour l'adhésion cellulaire, la migration, ainsi que l'organisation spatiale et l'intégrité des tissus. Les sites d'adhésion dépendants des intégrines (IAS) constituent l'interface mécanique entre la matrice extracellulaire et le cytosquelette, et accueillent un réseau complexe de protéines sensibles à la force, telles que la taline. La taline, une protéine clé dans les structures adhésives, établit le lien physique qui transmet les forces mécaniques des cellules à leur environnement. Elle est une protéine multimodulaire dont les domaines de liaison sont exposés lorsqu'elle est étirée par la force. L'idée d'un "code de la taline" a été proposée, suggérant que sa forme et ses partenaires de liaison pourraient refléter les informations mécaniques encodées par les cellules. Bien que les changements conformationnels de la taline induits par la force aient été largement étudiés in vitro, la forme de la taline au sein de l'architecture native des cellules vivantes reste inconnue, en particulier en ce qui concerne leur orientation spatiale.

Cette thèse se concentre principalement sur la taline, et explore son orientation moléculaire dans les adhésions focales (AF) à l'aide de la microscopie de polarisation en fluorescence à molécule unique. Afin d'étudier l'orientation de différents segments de la taline, nous avons conçu une série de constructions de la taline en insérant la protéine fluorescente mEos3.2 à des domaines spécifiques — le cou, les domaines R3, R12 et l'extrémité C-terminale. Grâce à notre pipeline optimisé d'imagerie en cellule vivante, nous avons extrait avec succès les angles dans le plan focal (ρ), hors du plan (η), et les fluctuations angulaires (δ) de la mEos3.2 servant de reporteur de l'orientation des différents domaines le long de la taline. Les distributions d'orientation de ces domaines sont cohérentes avec leur contexte mécanique: les domaines proches du site d'interaction avec les intégrines, tels que le cou et R3, présentent un alignement directionnel marqué le long de l'axe des adhésions focales, tandis que R12 et la partie C-terminale montrent un comportement orientationnel plus isotrope. Ces résultats obtenus en cellule vivante reproduisent ceux observés sur échantillons fixés, confirmant la robustesse et la reproductibilité de l'approche dans des conditions contractiles basales.

Cette thèse démontre que l'orientation moléculaire constitue un indicateur puissant, encore peu exploité, de l'état mécanique en cellule vivante. Au-delà de la taline, les méthodes, les outils moléculaires et les connaissances développées ici fournissent un cadre pour étudier comment des protéines telles que les intégrines, la vinculine ou l'actine se réorganisent sous contrainte dans leur environnement natif. La microscopie de molécule unique résolue en orientation offre

un fort potentiel pour décoder la logique mécanique de l'adhésion et de la signalisation, dans des contextes tant physiologiques que pathologiques.

Mots clés : mécano-transduction, adhésion cellulaire, suivi de protéines individuelles, polarisation de fluorescence

Table of contents

Acknowledgements 7
Abstract 15
Resumé 16
Table of contents 18
List of figures 23
Abbreviations 30
INTRODUCTION 33
1. Mechanotransduction and mechanosensing: General concepts 35
2. Structures involved in force generation, transmission and sensing 37
2. 1. The extracellular matrix 37
2. 2. Cytoskeleton 38
2. 2. 1. Actin filaments 39
2. 2. 2. Microtubules 40
2. 2. 3. Intermediate filaments 41
2. 3. Integrin Adhesion Sites (IAS) – the connection of the cell to the ECM 43
2. 3. 1. Nascent Adhesions 44
2. 3. 2. Focal complexes 45
2. 3. 3. Focal adhesions 45
3. Focal adhesions – a closer look at the molecular complexity 47
3. 1. Main players establishing the ECM-cytoskeleton physical linkages 47
3. 1. 1. Integrins 47
General Overview 47
Integrin activation 47
3. 1. 2. Talin – a mechanosensitive and mechanosignaling hub 49
Generalities 49
Talin mechanosensing 50

3. 2. FAs – a complex molecular composition 54
3. 3. FAs – 3D architecture 55
4. Hypothesis: talin mechanotransduction “code” sensing and encoding mechanical stimuli – Overview and Thesis Objectives 57
Super-Resolution Approaches for Investigating Focal Adhesions 61
1. Fluorescence microscopy 63
2. How to excite your sample 64
3. Limit of diffraction and super-resolution fluorescence microscopy 66
4. Single-molecule localization microscopy (SMLM) principle 69
5. Implementing SMLM in 2D 70
5. 1. PALM and sptPALM 70
5. 2. STORM 74
5. 3. DNA-PAINT 75
6. Uncovering the third dimension with SMLM 76
6. 1. Interferometric Photoactivation and Localization Microscope (iPALM) 76
6. 2. Supercritical angle fluorescence microscopy (SAF) 77
6. 3. Astigmatism coupled with super resolution 80
6. 4. Minimal fluorescence photon fluxes (MINFLUX) 80
7. Accessing protein orientation via super resolution 81
7. 1. Principles of polarization microscopy 82
7. 2. Ensemble polarization microscopy 83
7. 3. Single-molecule orientation and localization microscopy (SMOLM) 85
7. 4. Our choice of method 87
METHODS 89
1. Cell lines: maintenance and manipulation 91
1. 1. Transfection protocols 91
1. 1. 1. Amaxa nucleofection kit 91
1. 1. 2. NEON transfection kit 91
1. 2. Coverslip preparation 92
1. 3. Cell seeding 92

1. 4. Cell fixation 93
1. 5. Nanobody labeling 93
1. 6. Pharmacological drugs treatment 93
1. 6. 1. Calyculin A 93
1. 6. 2. RHOK inhibitor Y-27632 94
1. 6. 3. Para-amino-blebbistatin 95
2. SMLM modalities: microscope set-ups and acquisitions, image processing and data analysis 95
2. 1. Using sptPALM for studying 2D protein dynamics 95
2. 1. 1. sptPALM microscope and acquisitions 95
2. 1. 2. sptPALM image processing and data analysis 96
2. 2. Using SAF for measuring 3D protein localization 100
2. 2. 1. SAF microscope and acquisitions 100
2. 2. 2. SAF image processing and data analysis 100
2. 3. Using Polarization microscopy for retrieving protein domain orientation 102
2. 3. 1. 4polar3D microscope and acquisitions 102
2. 3. 2. 4polar3D image processing 105
2. 3. 3. Measuring orientations within FAs 107
2. 3. 4. Defining a polarization ratio 107
RESULTS 109
1. 3D localization and tracking of focal adhesion proteins: From fixed to live-cell imaging .. 111
1. 1. SAF-STORM shows layered Z-organization of focal adhesion proteins in MEF cells .. 111
1. 2. A new labeling protocol provides bright single-molecule signal for live-cell 3D imaging 115
1. 3. Successful implementation of 3D tracking in living cells using astigmatism and optimized labeling 120
2. Development and validation of protein constructs designed for polarization experiments 122

2. 1. Rationale when designing protein constructs for polarization experiments 122
2. 2. Designing protein constructs fused with Eos and constrained Eos 123
2. 2. 1. Designing Talin constructs for defining orientation of distinct talin domains ... 123
2. 2. 2. Towards more rigidly bound mEos 125
2. 2. 3. Designing Actins constructs for SMLOM 126
2. 2. 4. Designing integrins for defining conformational changes during activation 127
2. 3. Validation of protein constructs using cellular localization and protein dynamic analysis 129
2. 3. 1. Talin constructs show consistent behavior across multiple tagging sites 130
2. 3. 2. Truncated mEos3.2 impairs talin imaging performance 135
2. 3. 3. Truncated mEos3.2-actin constructs support functional dynamics and improved rigidity 136
2. 3. 4. Only full-length extracellularly labeled integrin supports robust single-molecule imaging 139
3. 4Polar3D reveals changes in orientation in FA proteins 142
3. 1. Integrin polarization experiments reveal Mn^{2+}-induced changes in out-of-plane orientation 143
3. 2. In-plane orientation (ρ) reveals axial gradients along the talin molecule in basal conditions 145
3. 3. Out-of-plane orientation (η) shows no site-specific difference in talins, but fixation affects distribution 151
3. 4. Drug-induced contractility changes as a tool to probe talin dynamics 153
3. 4. 1. Focal adhesion responses confirm pharmacological drug effects on contractility 153
3. 4. 2. Single particle tracking under the effect of drugs shows moderate to intense effects on talin dynamics 157
3. 4. 2. 1. Increased contractility through CalyculinA mildly restricts talin mobility only at talin-neck 158

3. 4. 2. 2. Reduced contractility via RhoK inhibition slightly enhances talin diffusion across FAs 163
3. 4. 2. 3. Talin becomes highly diffusive under the effect of para-amino-blebbistatin 168
3. 5. Next step: observing talin orientation under the effect of pharmacological drugs and in Vinculin KO cells 174
3. 5. 1. Photoselection issue 174
3. 5. 2. CalyculinA increases preferential orientation in talin tagged at the C-terminus 177
3. 5. 3. Rescuing vinculin seems to rescue talin-neck orientation too 178
Discussion and perspectives 181
Bibliography 187
Appendix 1 201
Development of a reliable C-terminus tagged mouse β3 integrin 201
Appendix 2 212

List of figures

Figure 1. Different morphologies of collagen fibers in the ECM. 38
Figure 2. Cytoskeleton of eukaryotic cells. 43
Figure 3. IAS diversity 46
Figure 4. Integrin conformational changes induce by ligand binding 48
Figure 5. Domain organization and structure of talin 50
Figure 6. Unfolding force-extension curves of FL-talin rod 51
Figure 7. Scale models of talin in different conformations 52
Figure 8. Schematic model of focal adhesion molecular architecture. 56
Figure 9. Fluorescence fundamentals 64
Figure 10. The physical basis of epifluorescence and TIRF illumination 65
Figure 11. Confocal vs light sheet microscopy 66
Figure 12. Spatial scale in life sciences and microscopy 67
Figure 13. How to choose the right super resolution technique 68
Figure 14. Single-molecule localization microscopy (SMLM) principle 70
Figure 15. Photoactivation of PA-mCherry showcasing the principle of PALM 71
Figure 16. Principle of PALM 72
Figure 17. Structure and spectra of mEos photoconvertible protein 74
Figure 18. SAF principle 78
Figure 19. Correlation between SAF ratio and dye depth 79
Figure 20. Schematic representation of a molecular angular distribution f(Ω), showing the mean orientation and angular spread (wobble) 83
Figure 21. Representative examples of ensemble polarization microscopy results 84
Figure 22. Example of single-molecule orientation and localization microscopy (SMOLM) results 86
Figure 23. CalyculinA structure 94
Figure 24. Y-27632 structure 94
Figure 25. Para-amino-blebbistatin structure 95

Figure 26. Appearance of the MSD curves obtained as a function of the movement behavior after adjustment by regression. 99
Figure 27. Dynamic behavior of integrin molecules described by sptPALM 100
Figure 28. Localization of vinculin, color coded in Z (nm), obtained with SAF microscopy and processed with NEO 101
Figure 29. Analysis streamline for SAF experiments 102
Figure 30. Four polarization-resolved images of the sample at the focal plane obtained on a 4polar3D microscope 103
Figure 31. Schematic representation of the setup for 4polar3D 104
Figure 32. Example of four PSFs obtained from a single molecule along the four polarized channels 105
Figure 33. 4Polar3D output images 107
Figure 34. SAF-STORM reveals distinct axial layers of focal-adhesion proteins in fixed MEFs. . 112
Figure 35. Box-plot quantification confirms near-membrane integrin and a progressive Z-rise through vinculin→zyxin→ α-actinin. 113
Figure 36. Z distributions obtained by iPALM, expressed in nm 114
Figure 37. High background from “in situ” labeling of Halo/SNAP-tagged talin with Janelia Fluor dyes 116
Figure 38. Comparison of labeling strategies for single-molecule imaging of talin inside focal adhesions 118
Figure 39. Optimized pre-incubation labeling normalizes talin dynamics; “in situ” labeling skews diffusion or blocks tracking 119
Figure 40. Example of 3D single-molecule tracking of talin in living cells using astigmatism-based sptPALM with optimized Halo/SNAP labeling 121
Figure 41. Schematic representation of mEos3.2 insertion sites in the talin molecule for polarization microscopy experiments 124
Figure 42. Truncation analysis of mEos3.2 revealing fluorescence retention after N- and C-terminal deletions 125
Figure 43. Actin fibers orientation obtained with 4-polar STORM 126

Figure 44. Actin constructs developed for polarization microscopy 127
Figure 45. Schematic representation of mEos insertion sites on integrin and its significance for conformational change reporting 128
Figure 46. Schematic representation of β3-integrin constructs with rigidified mEos3.2 variants for polarization microscopy. 129
Figure 47. Single-particle tracking PALM (sptPALM) acquisition of talin constructs with mEos3.2 at distinct tagging positions show good SNR and sparse detections 131
Figure 48. Super-resolution reconstructions and diffusion mode classification of talin constructs in MEFs 132
Figure 49. Diffusion coefficient distributions of talin constructs inside and outside focal adhesions shows very similar behavior 133
Figure 50. Percentage of diffusion modes for talin constructs inside and outside focal adhesions reveals no significant difference among constructs too 134
Figure 51. Talin constructs tagged at different positions show similar D_{diff} inside and outside focal adhesions 134
Figure 52. Truncated mEos3.2 bound to talin requires higher excitation and is unsuitable for polarization microscopy 135
Figure 53. Truncated mEos3.2-actin constructs incorporate robustly into stress fibers 137
Figure 54. Actin constructs with truncated mEos3.2 show reduced diffusivity compared to mEos2-actin 137
Figure 55. Truncated actin constructs preserve physiological retrograde flow speeds 138
Figure 56. Full-length mEos3.2 at K97 supports brighter and denser integrin imaging than truncated variants 140
Figure 57. K97 tagged and C-terminally tagged integrin show comparable immobility inside focal adhesions 141
Figure 58. K97 integrin shows a slightly larger shift toward immobile population upon Mn^{2+} activation than C-terminally tagged integrin 142
Figure 59. Acquisition window during 4Polar3D single-molecule polarization microscopy experiments 143

Figure 60. Mn^{2+} activation selectively increases the out-of-plane tilt (η) of the extracellularly labeled β3 integrin, while the cytoplasmic C-terminus tagged integrin remains unchanged.. . 145
Figure 61. Visual data obtained via single molecule polarization microscopy – example of talin-neck-mEos3.2. 147
Figure 62. In fixed cells, talin's in-plane orientation (ρ) is strongly aligned at the neck and progressively more isotropic toward the C-terminus 148
Figure 63. A polarization-ratio metric confirms stronger directional alignment at the talin neck in fixed cells 149
Figure 64. Live-cell ρ distributions reproduce the axial gradient observed in fixed cells, with alignment strongest at the neck. 150
Figure 65.In live cells, polarization ratios remain highest at the neck and are elevated (and more variable) for R3 compared to fixed conditions 151
Figure 66. Out-of-plane orientation (η) shows no site-specific differences across talin constructs, but fixation increases η 152
Figure 67. Wobbling (δ) remains within an orientation-retrieval-compatible range; fixation decreases δ 153
Figure 68. CalyculinA induces FA growth over 60 minutes, validating increased contractility.. 154
Figure 69. RhoK inhibition by Y-27632 reduces FA size and promotes protrusive spreading . 155
Figure 70. Para-amino-blebbistatin rapidly decreases FA size without inducing new protrusions. 155
Figure 71. Quantitative analysis of focal adhesion dynamics under pharmacological treatments in live MEFs. 157
Figure 72. CalyculinA produces no overt trajectory-level change for most talin constructs; talin-neck shows a modest reduction of visually diffusive tracks 159
Figure 73. Inside FAs, only talin-neck shows a slight shift of log(D) toward lower values after CalyculinA 160
Figure 74. Inside FAs, fractional populations change minimally after CalyculinA; only R12 shows a noticeable drop in diffusive fraction (~9%) 160

Figure 75. Inside FAs, the diffusion coefficient of the freely diffusive population (D_{diff}) is not significantly altered by CalyculinA 161
Figure 76. Outside FAs, talin-neck log(D) shifts slightly toward lower values after CalyculinA, while other constructs remain largely unchanged 162
Figure 77. Outside FAs, only R12 exhibits a noticeable reduction in the diffusive fraction (~6.5%) after CalyculinA; other constructs change by ≤~2% 162
Figure 78. Outside FAs, D_{diff} remains statistically unchanged across all talin constructs after CalyculinA 163
Figure 79. RhoK inhibition (using Y-27632) modestly increases visually diffusive talin trajectories within FAs across constructs 164
Figure 80. Inside FAs, Y-27632 slightly shifts log(D) distributions toward higher values, consistent with mildly faster talin mobility 165
Figure 81. Inside FAs, Y-27632 modestly reduces the immobile fraction and increases the diffusive fraction across constructs 165
Figure 82. Inside FAs, the diffusion coefficient of freely diffusive talin (D_{diff}) is not significantly altered by Y-27632. 166
Figure 83. Outside FAs, Y-27632 shifts talin log(D) distributions toward faster diffusion. 167
Figure 84. Outside FAs, Y-27632 increases the diffusive and confined fractions and decreases the immobile fraction across all talin tagging positions 167
Figure 85. Outside FAs, the diffusion coefficient of freely diffusing talin (Ddiff) increases with Y-27632 across constructs, contrasting with the lack of change inside FAs 168
Figure 86. Para-amino-blebbistatin treatment produces abundant diffusive talin trajectories. 169
Figure 87. Inside focal adhesions, para-amino-blebbistatin treatment markedly shifts the distribution of diffusion coefficients toward higher values across all talin constructs 170
Figure 88. Para-amino-blebbistatin strongly reduces the immobile and confined fractions of talin inside FAs, with a corresponding increase in the diffusive population 171
Figure 89. Freely diffusive talin molecules inside FAs display markedly higher diffusion coefficients after para-amino-blebbistatin treatment 171

Figure 90. Outside FAs, para-amino-blebbistatin induces a pronounced shift in log(D) distributions toward faster dynamics for all constructs 172
Figure 91. Para-amino-blebbistatin drastically decreases the immobile fraction of talin outside FAs, accompanied by increases in both confined and diffusive populations. 173
Figure 92. Outside FAs, the freely diffusive population of talin exhibits large increases in D_{diff} after para-amino-blebbistatin treatment 173
Figure 93. Raw in-plane orientation (ρ) in live MEFs reveals excitation photoselection prior to correction. 175
Figure 94. Photoselection correction using an outside-FA reference population. 176
Figure 95. In-plane orientation (ρ) of talin in live MEFs after photoselection correction partially recovers orientation gradient along the talin molecule seen in the first set of experiments .. 176
Figure 96. Calyculin A enhances preferential alignment for C-terminally tagged talin after photoselection correction 177
Figure 97. Vinculin depletion and rescue modulate talin neck alignment after photoselection correction 179
Figure 98. Mouse β3 integrin (INT2) is more diffusive than human 6His-tagged β3 integrin, both at baseline and after Mn^{2+} activation 202
Figure 99. INT2 (mouse) displays a higher proportion of diffusive trajectories compared to human 6His-β3 integrin, independent of Mn^{2+} activation. 202
Figure 100. The diffusion coefficient of diffusive integrins (D_{diff}) is higher in INT2 compared to 6His-tagged β3 integrin 203
Figure 101. Schematic overview of β3 integrin constructs used to test the influence of His-tag and linker length 203
Figure 102. Super-resolution reconstructions and trajectory classification of β3 integrin constructs under basal and Mn^{2+}-activated conditions. 204
Figure 103. Both N-terminal His-tag and linker length influence human β3 integrin diffusivity, with Mn^{2+} activation reducing construct-dependent differences 205
Figure 104. Species origin modulates β3 integrin diffusivity for 12-aa linker constructs, with mouse integrin remaining more mobile and less activation-responsive than human 206

Figure 105. Linker length overrides species-specific differences, yielding nearly identical dynamics for human and mouse β3 integrins with 14-aa linkers 206
Figure 106. Inside FAs, Mn^{2+} activation decreases diffusion most strongly in mouse constructs INT2 and INT6 207
Figure 107. Outside FAs, both human and mouse 14-aa linker constructs show strong decreases in diffusion upon Mn^{2+} activation, alongside human 12-aa linker 208
Figure 108. D_{diff} analysis confirms construct- and activation-dependent differences in integrin mobility 210

Abbreviations

2D – two dimensional
3D – three dimensional
6His – 6 histidine tag
AA – amino acid
ABP – actin binding proteins
AF – Alexa fluor
AKAP – mechanically-gated A-kinase anchoring protein
AS – adhesion sites
ATP – adenosine triphosphate
BC – bent-closed
BFP – back focal plane
BFP – blue fluorescent protein
CFP – cyan fluorescent protein
Cterm – C terminus tagged
DNA – deoxyribonucleic acid
DMEM – Dulbecco's modified eagle's medium
dsDNA – double-stranded deoxyribonucleic acid
EC – extended-closed
ECM – extracellular matrix
EDTA – ethylenediaminetetraacetic acid
EMCCD – electron multiplying charge-coupled device
EO – extended-open
F-actin – filamentous actin
FA – focal adhesion
FAK – focal adhesion kinase
FBS – fetal bovine serum
FITC – fluorescein isothiocyanate
FL – full-length
FX – focal complex
G-actin – globular actin
GFP – green fluorescent protein
GTP – guanosine triphosphate
IAS – integrin adhesion sites
IF – intermediate filaments
IgG – immunoglobulin G
iPALM – interferometric photoactivated localization microscopy
iSCAT – interferometric scattering microscopy
JF – Janelia Fluor
K – lysine

KO – knock out
LSFM – light-sheet fluorescence microscopy
MAP – microtubule-associated protein
MEF – mouse embryonic fibroblast
MINFLUX – minimal fluorescence photon fluxes
MSD – mean square displacement
NA – nascent adhesion
NA – numerical aperture
PALM – photoactivated localization microscopy
PAINT – point accumulation in nanoscale topography
PBS – phosphate buffered saline
PFA – paraformaldehyde
PFS – perfect focus system
PH domain – pleckstrin homology domain
PIP2 – phosphatidylinositol (4,5) bisphosphate
POLCAM – polarization camera-based orientation microscopy
PSF – point spread function
PTB – phosphotyrosine binding
qPAINT – quantitative point accumulation in nanoscale topography
RIAM – rap1-GTP-interacting adaptor molecule
RhoA – Ras homolog family member A
ROCK – rho-associated protein kinase
ROI – region of interest
SAF – supercritical angle fluorescence
SEM – scanning electron microscopy
SIM – structured illumination microscopy
SMLM – single-molecule localization microscopy
SMOLM – single-molecule orientation and localization microscopy
SNR – signal-to-noise ratio
sptPALM – single particle tracking photoactivated localization microscopy
STED – stimulated emission depletion
STORM – stochastic optical reconstruction microscopy
THATCH – talin helical actin targeting CH domain
TIRF – total internal reflection fluorescence
TLN – talin
U2OS – human osteosarcoma cell line
UAF – under-critical angle fluorescence
ULF – unit length filament
VBS – vinculin binding site
WT – wild type
YFP – yellow fluorescent protein

INTRODUCTION

1. Mechanotransduction and mechanosensing: General concepts

Cell migration represents one of the crucial physiological processes. It is involved in embryonic development, tissue regeneration, immune response, as well as the start and progression of diseases such as lung cancer (Chen et al., 2024) or head and neck squamous cell carcinoma (HNSCC) (Cao et al., 2020). Cells migrate due to their ability to remodel their microenvironment by adhering and generating forces on neighboring cells and the extracellular matrix (ECM) through macromolecular assemblies called integrin-dependent adhesion sites (IAS) (Geiger et al., 2009). The conversion of mechanical forces into biochemical signals is in part ensured by integrins and associated proteins, and the so-called integrin mechanotransduction, the process by which mechanical cues are converted into biochemical signals, is essential during the cell migration and therefore physiological processes it is involved in (Hoffman et al., 2011).

A foundational study by Lo et al., 2000 demonstrated that cells can actively sense and respond to substrate rigidity, a phenomenon they termed durotaxis. Using fibroblasts migrating on substrates with controlled stiffness gradients, they showed that cells preferentially move toward stiffer regions, exert stronger traction forces, and alter their morphology in response to mechanical feedback from the extracellular matrix. This directional migration, driven by mechanical rather than chemical cues, exemplifies how integrin-based adhesion sites function as mechanosensitive platforms. These findings highlight the essential role of force sensing in guiding cellular behavior and laid the groundwork for understanding how physical properties of the environment influence migration, adhesion, and tissue organization.

At the molecular level, *in vitro* and *in cellulo* approaches showed that force regulates the tension of proteins present in cell adhesion sites (Yao et al., 2016; Ringer et al., 2017). Yet, how force changes the conformation of proteins directly in IAS is still unknown, due to the lack of techniques able to quantify the conformational states and mechanical responses of individual proteins in living cells.

To fully understand how mechanical forces are transduced at IAS, it is essential to move beyond compositional analyses and examine the spatial and orientational organization of individual

proteins within these structures. IAS are not only biochemically complex but also mechanically anisotropic, with many of their core components, such as talin and integrin, undergoing force-induced conformational changes and adopting defined orientations relative to the plasma membrane and the actin cytoskeleton (Yao et al., 2016; Ringer et al., 2017; Dedden et al., 2019). These orientations are closely linked to protein function, interaction dynamics, and mechanical engagement (Guo et al., 2024; Brasselet and Alonso, 2024). Furthermore, IAS are organized into discrete vertical layers spanning only tens of nanometers in the z-dimension, and this 3D stratification is functionally significant, reflecting mechanical connectivity and signaling hierarchy across the adhesion interface (Kanchanawong et al., 2010; Liu et al., 2015; Oria et al., 2017). Traditional imaging techniques lack the resolution to access this level of detail. Therefore, approaches that combine single-molecule sensitivity with both orientational and 3D spatial resolution are crucial to dissect how molecular conformation and positioning contribute to mechanotransduction (Zhanghao et al., 2019; Rimoli et al., 2022). In this context, orientation-resolved and 3D localization microscopy provide a powerful framework to directly visualize how individual proteins behave under force in the native environment of living cells (Rimoli et al., 2022; Brasselet and Alonso, 2024).

The words mechanotransduction, mechanosensing, mechanosensitive, and related terms are often used interchangeably. However, this can create confusion when discussing the subtle, but important distinctions between these processes and their underlying mechanisms. Therefore, it is useful to define these terms clearly at the outset, to facilitate precise discussion throughout this thesis (Box 1).

Box 1: The *mechano* guide

- **Mechanotransduction:** The general mechanism through which cells perceive a mechanical stimulus, translate it into a biochemical signal, and trigger an intracellular reaction. I.e. the conversion of intracellular or external mechanical forces into biochemical signals
- **Mechanosensing:** The act of sensing a mechanical stimulus by the cell.
- **Mechanosensitive:** A subcellular structure or protein complex which is sensitive to mechanical stimuli by undergoing force-dependent conformational changes such as

deformation or reorganization. This can trigger also the recruitment of binding partners (Guo et al., 2024)

- **Mechanosignaling:** An intracellular signaling event which is triggered by a mechanical force such as shear stress or cyclic strain. This can involve phosphorylation of a target protein (Sawada et al., 2006), influx of a secondary messenger (e.g. Ca^{2+}) (Zhao et al., 2018) or translocation of a transcription factor (Dupont et al., 2011).
- **Mechanotransmission:** How forces are transmitted across the cell and different subcellular structures.
- **Mechanoreciprocity:** Bi-directional relationship in cell-tissue interactions. Cells can respond to ECM properties and also remodel it.
- **Mechanoresponse:** The final response of a cell after the detection of a mechanical stimuli and activation of specific mechanosignaling pathways.

2. Structures involved in force generation, transmission and sensing

2. 1. The extracellular matrix

The extracellular matrix (ECM) is a complex, dynamic structure, fundamental to the form and function of soft connective tissues (Humphrey et al., 2014). Beyond from having a structural role, the ECM performs many additional functions, as it is a major component of the microenvironment of a cell. These functions involve stimulation of cell proliferation, adhesion and migration, cell differentiation, as well as cell death (Lu et al., 2011). Secreted and remodeled by cells, this non-cellular, three-dimensional macromolecular network is composed of collagens, proteoglycans, glycosaminoglycans, elastin, fibronectin, laminins, and other glycoproteins. These components interact with each other and with cell adhesion receptors, creating a complex network in which cells are embedded within tissues and organs. Through these receptors, signals from the ECM are transmitted into cells, influencing essential functions mentioned previously. The ECM undergoes continuous remodeling, driven by various matrix-degrading enzymes in

conjunction with cellular mechanically-driven reorganization during normal and pathological conditions. Deregulation of its composition and structure is associated with development and progression of several pathologic conditions (Theocharis et al., 2016) including cancer progression and metastatic development (Despotović et al., 2020). In colorectal cancer, collagen fibers within the ECM display increased alignment and reduced structural isotropy compared to healthy tissue, reflecting a marked reorganization of the matrix (Figure 1). Such changes in ECM architecture have been implicated in modulating cellular behavior during tumor progression.

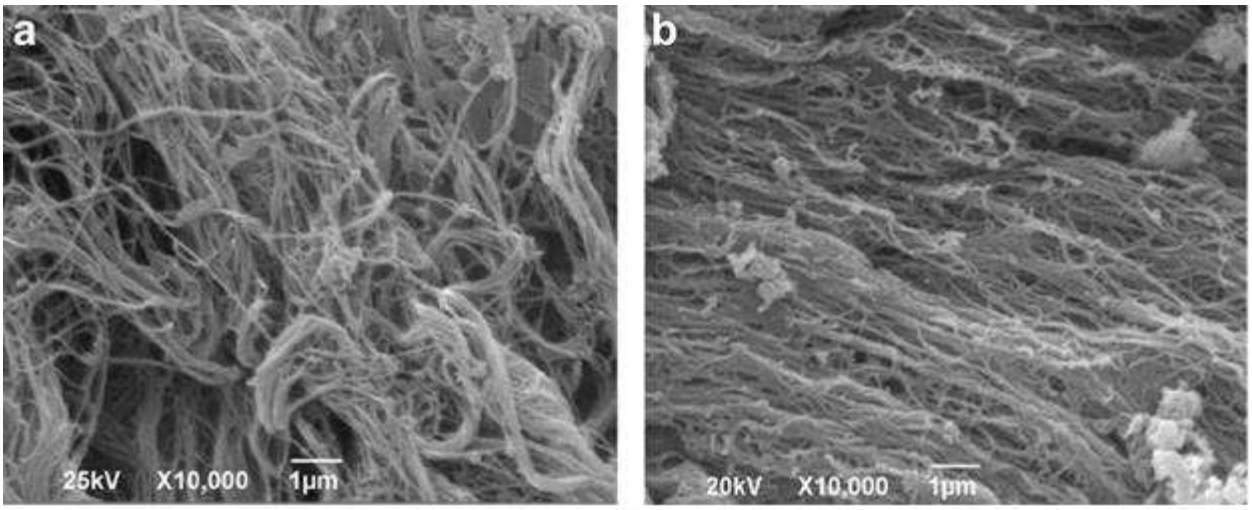

Figure 1. ***Different morphologies of collagen fibers in the ECM.*** *Scanning electron microscopy (SEM) images of collagen fibers in the lamina propria of colon mucosa in healthy patients (**a**) and in cancer patients, 10 cm away from the malignant tumor (**b**) In healthy patients. (**a**) Thin collagen fibers form a relatively dense network, while in cancer patients (**b**) the fibers are thicker are more aligned. Scale bar: 1µm. Magnification x10 000 Figure adapted from (Despotović et al., 2020).*

2. 2. Cytoskeleton

The machinery that empowers cells to mechanically remodel their microenvironment is primarily established by the cell cytoskeleton. The term cytoskeleton represents an interconnected network of filamentous polymers, regulatory and molecular motor proteins. Despite the connotations of the word skeleton, this structure is not at all static and provides much more to the cell than keeping its shape. In general, we can divide its functions into three broad ones: it spatially organizes the contents of the cell; it connects the cell both physically and biochemically to the external environment; it generates, senses and transmits coordinated forces that enable the cell to change shape and move (Fletcher and Mullins, 2010; Sala et al., 2024). Three major filamentous elements comprise the cytoskeleton of mammalian cells: actin filaments,

microtubules and intermediate filaments, along with associated proteins (Hohmann and Dehghani, 2019).

A key mechanical property that differentiates these three cytoskeletal systems, and underlies their distinct roles in cellular mechanoresponses, is their persistence length (Lp), the length scale over which a filament resists bending due to thermal fluctuations. Microtubules are the stiffest (Lp ≈ 1 mm), acting as rigid structural beams; actin filaments are semi-flexible (Lp ≈ 10 µm), suited for force generation and rapid remodeling; while intermediate filaments are highly flexible (Lp ≈ 0.3–1 µm), enabling them to withstand large deformations without breaking (Gittes et al., 1993; Brangwynne et al., 2006). These mechanical differences help explain why microtubules serve as compression-resistant struts, actin supports dynamic force transmission and shape change, and intermediate filaments provide mechanical resilience during stress.

2. 2. 1. Actin filaments

Actin is the most abundant protein in the majority of eukaryotic cells. Its structure is highly conserved and it is involved in more protein-protein interactions than any other known protein (Dominguez and Holmes, 2011). In their fundamental structure, actin filaments (Filamentous actin/F-actin) are linear, double-stranded polymers with a diameter of 5-9 nm (Holmes et al., 1990), formed by globular actin (G-actin) monomers. Each monomer is aligned in the same direction, resulting in F-actin having a plus (barbed) end and a minus (pointed) end (Pollard, 1986). Actin filaments elongate towards the cell's leading edge by adding G-actin monomers to their barbed end. Depolymerization occurs at the other side, i.e. at the pointed end, performing a thread milling dynamics whereby the actin grows in the direction of the movement and retracts at the rear (Brill-Karniely et al., 2009; Dominguez and Holmes, 2011). This structure of actin filaments is essential for regulation of many cellular functions, such as cell motility, muscle contraction, phagocytosis and synaptic transmission (Blanchoin et al., 2014; Chazeau and Giannone, 2016; Pollard and John A. Cooper, 2009)

An impressive feature of actin filaments is the variety of structures they can form in a cell: lamellipodium, stress fibers, filipodia, dendritic spines or blebs, with each one for them having a specific organization and function. This stems from the intrinsic properties of actin, but also from the numerous proteins that can interact with actin filaments. These proteins are known as actin

binding proteins (ABPs) (Blanchoin et al., 2014). For example, F-actin can form a branched actin network, known as the lamellipodium, through nucleation by the Arp2/3 complex (Svitkina and Borisy, 1999). Some other ABPs are regulators such as profilin, which promotes polymerization (Carlsson et al., 1977), capping proteins like adducin (Kuhlman et al., 1996), and severing proteins such as cofilin, which destabilizes F-actin (Galkin et al., 2011).

Another very important trait of F-actin is that it associates with myosin molecular motors to form contractile structures. Thanks to energy generated by ATP hydrolysis, myosin can generate mechanical force to move or pull along this molecular rail. More precisely, myosin heads use the principle of lever arms to allow the actin filaments to move towards each other (Uyeda et al., 1996). The formation of actin-myosin complexes is fundamental to muscle contraction and serves as the primary driver of cellular forces during mechanotransduction. In the structures we will examine later, it is myosin II that plays this role of protein motor. Predominantly expressed in non-muscle cells, myosin II is crucial for adhesion and migration processes (Vicente-Manzanares et al., 2009).

One actin structure of particular importance in force transmission, which incorporates myosin II, is the contractile stress fiber. Located at the rear of certain adhesive structures (Hotulainen and Lappalainen, 2006), contractile stress fibers consist of networks of actin filaments arranged antiparallelly, connected by cross-linking proteins such as α-actinin, filamin, and myosin II (Blanchoin et al., 2014). In addition, mechanosensitive proteins such as zyxin are recruited to sites of stress fiber strain, where they participate in fiber repair and reinforcement (Yoshigi et al., 2005). To be more specific, the way that stress fibers allow force transmission is by connecting the cell cytoskeleton to the extracellular matrix via focal adhesion sites (Blanchoin et al., 2014). The formation and activity of these fibers are RhoA activation dependent and promote myosin-dependent contraction (Oakes et al., 2017; Dominguez and Holmes, 2011). Therefore, inhibiting RhoA activation impairs the formation of stress fibers and reduces cell contractility.

2. 2. 2. Microtubules

Another structurally and functionally important component of the eukaryotic cell cytoskeleton is microtubules. They are essential for cell mechanics, cell division, intracellular transport and cell motility (Vleugel et al., 2016). Microtubules are long, stiff polymers composed of α- and β-tubulin

heterodimers (Brouhard and Rice, 2018), forming a hollow structure around 25 nm in diameter. They are highly dynamic structures, and in fact, the key to their functional versatility is their ability to assemble and disassemble over many cycles (Ohi and Zanic, 2016). Microtubule elongation occurs through the addition of GTP-bound tubulin heterodimers, creating a GTP-cap at the + end. Loss of this GTP-cap triggers a depolymerization event known as microtubule catastrophe. The dynamic balance between microtubule growth and shrinkage is tightly regulated by microtubule-associated proteins (MAPs), including molecular motors like kinesins and dyneins, as well as polymerases (Brouhard and Rice, 2018).

Beyond these canonical roles, microtubules directly interface with integrin adhesion sites (IAS). Dynamic microtubule plus-ends repeatedly target focal adhesions, facilitating their turnover and local signaling. Cortical complexes containing KANK family proteins bind the talin rod domain; KANK1/2 thereby recruit microtubule-stabilizing factors to the adhesion periphery and fine-tune FA stability and cell migration (Seetharaman and Etienne-Manneville, 2019; Bouchet et al., 2016).

2. 2. 3. Intermediate filaments

Intermediate filaments (IFs) represent a group of fibrous proteins that have different biological functions important to human health (Eldirany et al., 2021). IF-forming proteins constitute a large class of proteins encoded by at least 70 genes, assembling into filaments with a diameter of approximately 10 nm (Herrmann and Aebi, 2016). They are grouped in five classes according to their structure and sequence homology: acidic keratins (type I), basic keratins (type II), homopolymers of vimentin, desmin, peripherin, or glial fibrillary acidic protein (type III), neurofilaments (type IV) and lamins, i.e. nuclear filaments (type V), and their expression will depend on the tissue type (Hohmann and Dehghani, 2019).

The monomers of IFs are filaments approximately 45 nm in length, characterized by a highly organized assembly process. In this way, a structure of eight tetramers (i.e. 32 monomers) called ULF (unit length filament), measuring about 60 nm in length, is formed. These ULFs align sequentially to create immature intermediate filaments, roughly 16 nm in diameter and several microns long. Eventually, these filaments undergo radial compaction, resulting in mature IFs with a diameter of 10 nm (Herrmann and Aebi, 2016).

IFs have many tissue-specific roles including mechanical support of cells and regulation of their intracellular organization, stress response, cell growth, proliferation, migration and death (Eldirany et al., 2021). Here are two notable examples of proteins involved in cell adhesion and motility: vimentin, which is associated to the formation and maturation of focal adhesions (Tsuruta and Jones, 2003), whose depletion increases stress fiber formation and myosin activity (Gregor et al., 2014); synemin, which interacts with different components of focal adhesions, such as talin and vinculin (Sun et al., 2008).

Intermediate filaments also link directly to IAS. The cytolinker plectin binds the β4-integrin subunit, connecting keratin IFs to hemidesmosomes and reinforcing epithelial adhesion to the basement membrane (Rezniczek et al., 1998). Vimentin IFs align with and stabilize focal adhesions, restraining traction forces and guiding persistent cell migration (Battaglia et al., 2018). Schematic summary of these three main cytoskeleton elements in eukaryotic cells is shown in Figure *2*.

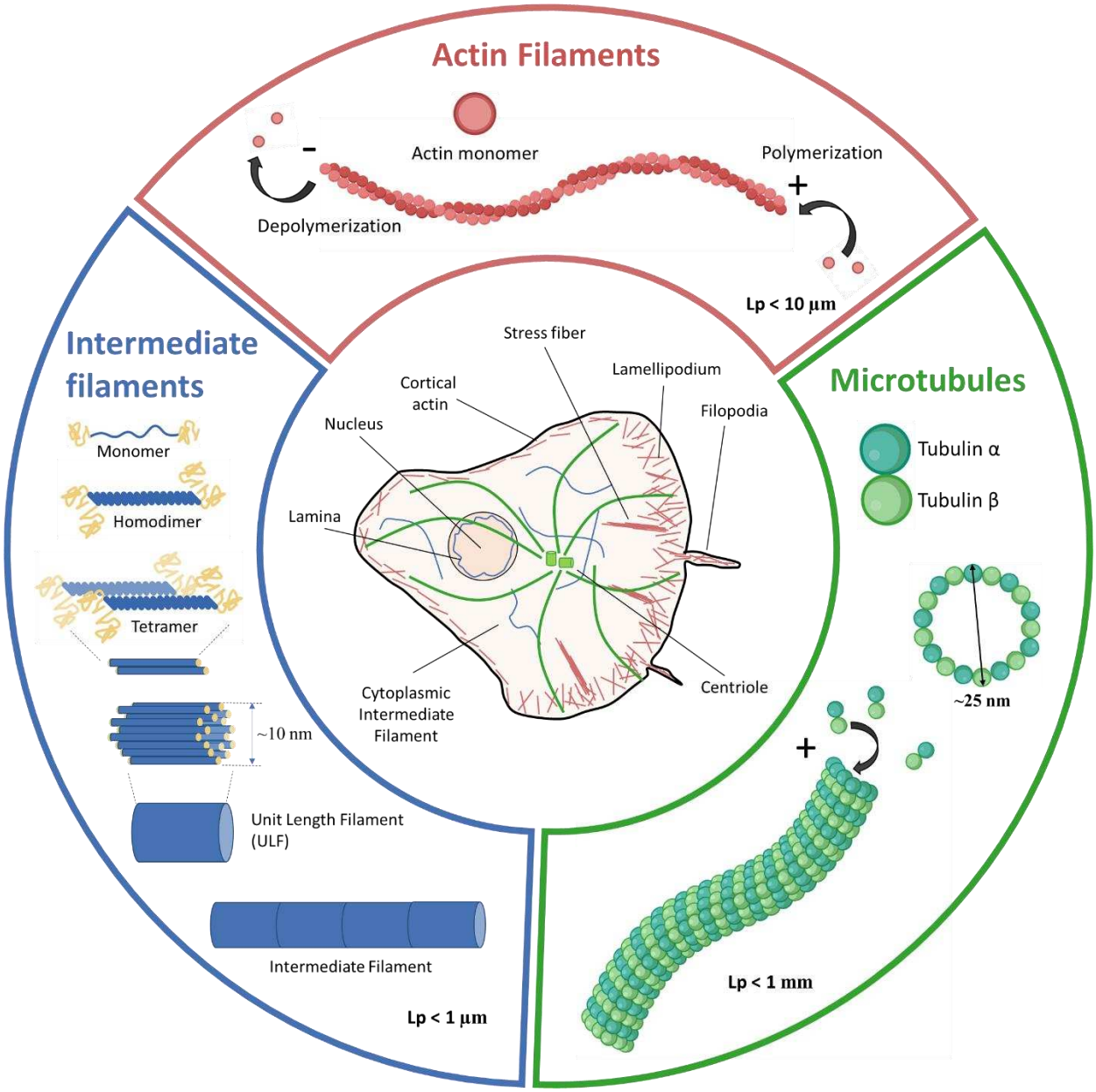

Figure 2. ***Cytoskeleton of eukaryotic cells*** *Schematic of the three main cytoskeleton elements of eukaryotic cells: actin filaments, intermediate filaments and microtubules (Lp: persistence length).*

2. 3. Integrin Adhesion Sites (IAS) – the connection of the cell to the ECM

The mechanical forces that the cytoskeleton generates are exerted across the microenvironment of the cell, and vice versa – forces arising from the neighboring cells and the ECM are sensed by the cytoskeleton, and then converted into biochemical signals (Han and de Rooij, 2016). These mechanical connections and signal transduction are supported by cell-cell and cell-ECM adhesion sites (Orré et al., 2019). Among these, integrin-based adhesions (IAS) represent the primary

structures responsible for anchoring the cell to the ECM and transmitting mechanical signals across the membrane. At the heart of many of these adhesion sites lies a family of transmembrane receptors known as integrins. These heterodimeric proteins connect the extracellular matrix to the intracellular actin cytoskeleton via a network of adaptor and signaling molecules. Integrins are well-suited for this role due to their ability to sense the highly dynamic and complex mechanical and biochemical properties of the ECM. This sensing capacity stems from their ability to undergo tightly regulated allosteric conformational changes, switching between inactive and active states depending on ligand binding and intracellular cues. These conformational changes enable bidirectional signaling - from the inside of the cell outward (inside-out) and from the ECM inward (outside-in) - as well as integrin clustering, a process that initiates the formation of adhesion complexes (Wehrle-Haller, 2012).

Integrins cluster and assemble many ancillary proteins in specialized adhesion structures (Figure 3). These structures differ in their morphology, subcellular localization, lifespan as well as protein composition (Sun et al., 2014). Through their clustering and interaction with adaptor proteins such as talin and kindlin, integrins organize into distinct adhesion subtypes including nascent adhesions, focal complexes, and mature focal adhesions.

We will have a quick overview of different morphologies of IAS. However, the main focus of my thesis was the architecture of mature Focal Adhesions (FAs) introduced in the following.

2. 3. 1. Nascent Adhesions

IAS initiate as nascent adhesions (NAs) - small, dot-like structures located in the lamellipodium, a cytoskeletal protrusion at the leading edge of migrating cells. They have a very short lifetime (on the order of ~1 minute) (Choi et al., 2008) and serve as early signaling and mechanosensing platforms, acting as precursors to mature focal adhesions. Integrins, upon activation, cluster to form NAs, which then recruit various adaptor and signaling proteins to stabilize and potentially mature into larger adhesion complexes. Protein recruitment occurs in a defined temporal hierarchy: talin and kindlin are among the first to bind activated integrins, followed by the sequential recruitment of proteins such as paxillin and vinculin, whose association depends on force generation and adhesion state. This ordered assembly ensures the mechanical and signaling competence of adhesions from their earliest stages (Bachir et al., 2014).

NAs are characterized by rapid turnover, and their formation is largely independent of myosin II activity. Their small size and dynamic nature make them challenging to study, requiring super-resolution microscopy techniques such as interferometric scattering (iSCAT) microscopy (Park et al., 2020). Despite their critical role in early adhesion and matrix sampling, the precise mechanisms regulating their formation, dynamics, and maturation are still not fully understood, motivating ongoing research in the field (Henning Stumpf et al., 2020).

2. 3. 2. Focal complexes

The maturation from nascent adhesions (NAs) to mature focal adhesions (FAs) is a gradual and continuous process. During this progression, cells form intermediate structures known as focal complexes (FXs), which serve as transitional adhesion sites (Zamir et al., 2008). FXs are slightly larger than NAs - typically around 0.5–1 µm in diameter, compared to NA sizes of <0.3 µm - and are located 3–5 µm behind the leading edge, at the lamellipodium–lamellum interface (Bachir et al., 2017). While NAs and FXs share a broadly similar molecular composition (Nobes and Hall, 1995), the formation of FXs is dependent on myosin II activity, marking a shift toward force-sensitive maturation (Choi et al., 2008; Schiller et al., 2011).

2. 3. 3. Focal adhesions

Focal adhesions (FAs) are large, stable IAS that function as critical hubs for the mechanical and biochemical coupling between cells and the extracellular matrix (ECM). Compared to NAs and FXs, FAs are significantly more stable, with lifespans ranging from 20 minutes to over an hour, and they can reach sizes of up to several micrometers in length (Legerstee et al., 2019). They arise through the maturation of a subset of NAs and FXs, which progressively grow and stabilize through force-dependent protein recruitment and reinforcement. FAs are sites of signaling activity and mechanical force transmission, enabling cells to exert traction forces on the ECM and respond dynamically to mechanical stimuli. These forces are transmitted through the integrin-actin linkage within FAs and can deform the surrounding matrix, modulating cellular behavior and mechanotransduction pathways (Balaban et al., 2001; Gardel et al., 2010).

Their formation and maintenance are governed by a complex interplay of regulatory processes, including protein phosphorylation, calcium signaling, and localized proteolysis, which coordinate with cytoskeletal tension generated by myosin II and matrix stiffness (Orré et al., 2019). FA

maturation involves a coordinated series of interactions between integrins, scaffolding proteins like talin and vinculin, and membrane phosphoinositides (e.g., $PI(4,5)P_2$), which act as spatial modulators of adhesion protein recruitment (Wehrle-Haller, 2012). The continuous assembly and disassembly of focal adhesions - a process closely linked to intracellular contractile forces and extracellular mechanical properties - ensure that adhesion dynamics are appropriately regulated in response to the cell's mechanical environment (Albiges-Rizo et al., 2009).

Summary of the morphology, diversity and localization of integrin adhesion sites is shown in Figure 3.

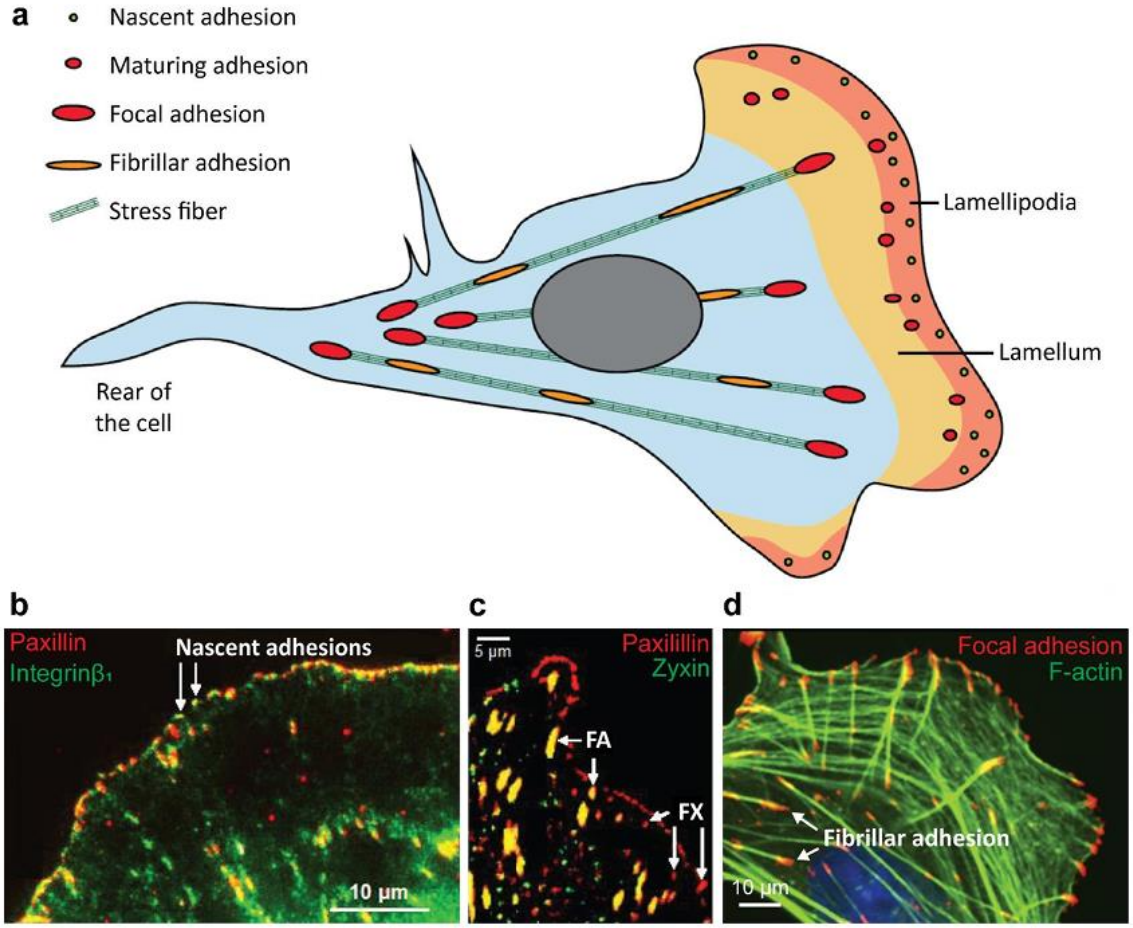

Figure 3. ***IAS diversity*** *(**a**) IAS diversity in migrating cells, (**b**) Endogenous paxillin (red) and expressed β1 integrin (green) imaged using TIRF in CHO cells. Colocalization of paxillin and integrin β1 corresponds to nascent adhesion (arrows). Adapted from (Choi et al., 2008). (**c**) Endothelial cells co-transfected with paxillin (red) and zyxin (green). Solely red structures correspond to maturing adhesions (FX). Colocalized paxillin and zyxin show focal adhesion (FA). Adapted from (Zaidel-Bar et al., 2003). (**d**) Human osteosarcoma cells labelled with antiphosphotyrosine as a marker of FA (red), phalloidin for F-actin, and therefore stress fibers (green), and DAPI for the nucleus (blue). More central structures can correspond to fibrillar adhesion. Adapted from (Burridge and Wittchen, 2013).*

3. Focal adhesions – a closer look at the molecular complexity

3. 1. Main players establishing the ECM-cytoskeleton physical linkages

3. 1. 1. Integrins

General Overview

Integrins are transmembrane heterodimeric receptors composed of one α and one β subunit, which together provide a physical and functional bridge between the extracellular matrix (ECM) and the cytoskeleton (Bachmann et al., 2019). In mammals, 24 distinct integrin heterodimers arise from different combinations of 18 α and 8 β subunits, allowing cell- and tissue-specific ECM recognition (Barczyk et al., 2010). These include receptors for fibronectin (e.g., α5β1), laminins (e.g., α6β4), collagens (e.g., α1β1), and vitronectin (e.g., αvβ3). Identified in the 1980s (Tamkun et al., 1986), integrins play a central role in sensing the chemical and mechanical properties of the extracellular environment and relaying these cues into intracellular signaling responses (Ruoslahti and Giancotti, 1989). This dual functionality - mechanical anchoring and biochemical signaling - positions integrins as essential mechanotransducers.

Integrin activation

Each integrin is composed of one α and one β subunit, associating non-covalently to form a functional receptor with a total molecular weight around 150 kDa (Nermut et al., 1988). Structurally, integrins exhibit remarkable conformational plasticity. They transition among at least three distinct states: a bent-closed (BC) conformation with low ligand affinity, an extended-closed (EC) intermediate state, and an extended-open (EO) conformation with high affinity for ligands (Takagi and Springer, 2002; Nishida et al., 2006) (Figure 4). These transitions are influenced by both extracellular ligand binding and intracellular interactions with adaptor proteins like talin and kindlin (Calderwood et al., 2003).

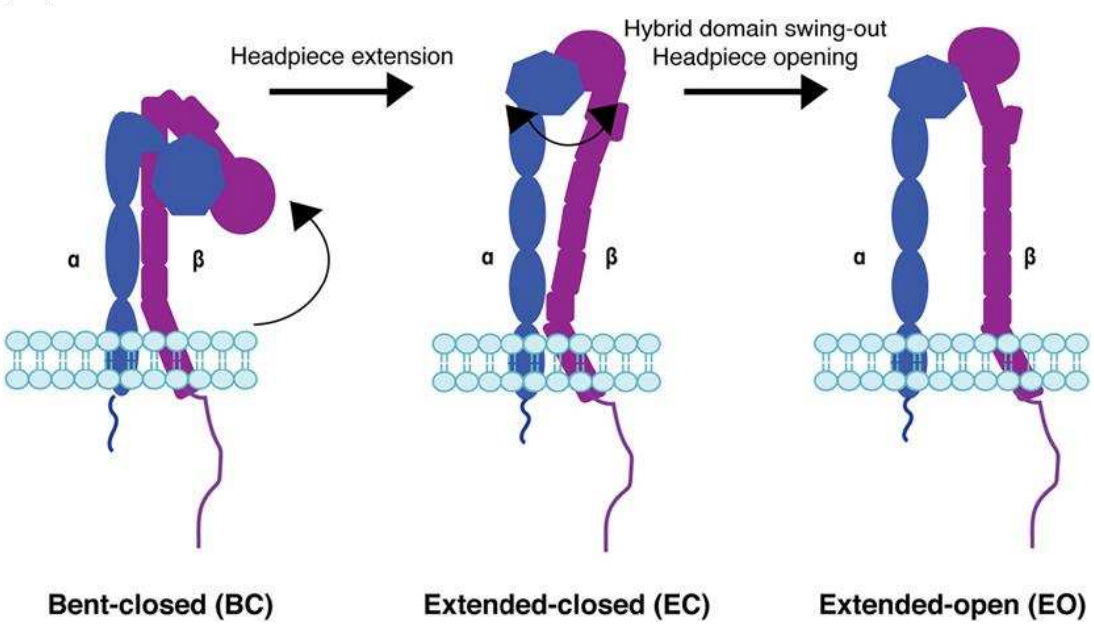

Figure 4. ***Integrin conformational changes induced by ligand binding****. Affinity for the ligand increase from bent closed to extended closed and then extended open confirmations (Kadry and Calderwood, 2020)*

Inside-out signaling is initiated when cytosolic adaptors bind conserved motifs (such as NPxY and NxxY) in the β-subunit tail, inducing separation of the α and β cytoplasmic domains and promoting the extended conformation (Ulmer et al., 2003; Smith et al., 2006). Conversely, outside-in signaling begins with ligand engagement, which stabilizes the EO state and triggers recruitment of downstream signaling proteins such as FAK and Src.

The binding strength of integrin receptors are modulated not only by ligand availability but also by mechanical conditions, divalent cations like Mn^{2+}, and the cytoskeletal context. Notably, integrin activation is mechanically regulated: tensile force applied through the cytoskeleton stabilizes the high-affinity conformation and facilitates integrin clustering, leading to the formation of adhesion complexes (Wehrle-Haller, 2012). These mechanical inputs influence receptor lifetime and organization on the membrane, making integrins both sensors and effectors of mechanical signals. Importantly, bonds between integrin β1 and fibronectin (FN) were shown to behave as catch bonds. That is, their lifetime increases under the application of mechanical force. This was demonstrated using atomic force microscopy (AFM)-based single-molecule force spectroscopy (Kong et al., 2009), supporting the idea that integrins act as force-sensitive adhesion receptors.

Ultimately, integrins do not function in isolation but are embedded within complex macromolecular assemblies such as integrin adhesion sites (IAS), where they coordinate with other mechanosensitive proteins such as talin and vinculin to support adhesion, signaling, and force transduction (Rossier et al., 2012; Orré et al., 2021). Moreover, integrin activation can be induced experimentally using divalent cations such as manganese (Mn^{2+}), which stabilize the high-affinity conformation by altering the metal ion-dependent adhesion site (MIDAS) in the β subunit (Dransfield et al., 1992; Anderson et al., 2022). Thus, integrins are not merely passive anchors, but active participants in the dynamic mechanical dialogue between cells and their environment.

3. 1. 2. Talin – a mechanosensitive and mechanosignaling hub

Generalities

As a key partner and activator of integrins, the other essential protein establishing the physical linkage between the ECM and the actin cytoskeleton is talin. Talin is a multidomain cytosolic protein, with a molecular weight of approximately 270kDa. Vertebrates possess two paralogs: talin-1 (TLN1) and talin-2 (TLN2), which share 76% of their protein sequence (Gough and Goult, 2018). They differ in their expression patterns and mechanical properties. TLN1 is ubiquitously expressed and plays a fundamental role in development; indeed, its deletion is embryonically lethal, indicating its essential function in early life processes. In contrast, TLN2 is tissue-specific and not embryonically lethal, suggesting a more specialized and possibly redundant role in certain contexts. Functionally, while both paralogs can support integrin activation and cell spreading, TLN2 displays higher mechanical tension and immobilization in focal adhesions, and mediates force transmission differently than TLN1, largely due to differences in their rod domains (Austen et al., 2015). Throughout my work, the focus was given on the ubiquitous talin-1, which will hereafter be referred to simply as "talin."

At the structural level, TLN1 and TLN2 share the similarity of being a large, flexible, rod-shaped protein. Both talins possess a long flexible rod domain, consisting of 13 sequential α-helical bundles (R1-R13). Talin N-terminal FERM domain called “talin-head” is made of 4 globular segments called F_0 to F_4. Talin-head and -rod domains are connected to each other via an unstructured linker, often referred to as “neck”. Talin-neck includes a cleavage site for several

proteases, such as calpain-2 (Goult et al., 2021; Calderwood et al., 2013). An overview of talin's domain organization and structure is presented in Figure 5.

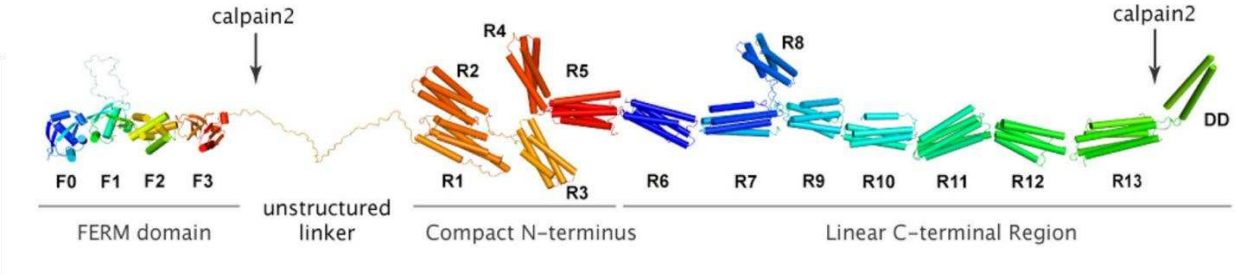

Figure 5. ***Domain organization and structure of talin*** *(Calderwood et al., 2013).*

Talin N-terminal FERM domain activates integrins, while its C-terminal rod domain links them to the actin cytoskeleton. (Yao et al., 2016; Goult et al., 2009; Giannone et al., 2003). The FERM domain binds directly to the cytoplasmic domains of the integrin β-subunits, which leads to increased affinity of integrin for ECM ligands. The rod domain's α-helical bundles (R1-R13) are arranged like beads on a string and connect to F-actin either directly, through actin-binding sites, or indirectly through vinculin (Goult et al., 2021).

Recent in vivo work has emphasized the critical importance of direct talin–actin binding, particularly via the ABS3 site on R13. Deng et al., 2025 introduced a point mutation (KVK/DDD) in ABS3 that disrupts actin binding and found that this was sufficient to prevent focal adhesion maturation, reduce traction force generation, and result in mid-gestation embryonic lethality in mice. These findings highlight that ABS3-mediated linkage to actin is not merely redundant with other connections but is essential for proper mechanotransduction during development.

Talin mechanosensing

Talin's mechanical properties are very important, particularly under forces generated during cell migration and adhesion maturation. Talin's mechanosensing capacity arises from force-induced unfolding, as predicted in Hytönen and Vogel, 2008 using steered molecular dynamics (SMD) to simulate how tensile forces expose vinculin binding sites buried within the talin rod. This mechanism was later confirmed experimentally by Rio et al., 2009 and Yao et al., 2016 who demonstrated force-dependent unfolding of its 13 rod domains (R1–R13) using magnetic tweezer

assays. Each domain unfolds at characteristic forces (5–25 pN) and refolds below 3 pN, acting as reversible mechanical switches (Yao et al., 2016) (Figure 6).

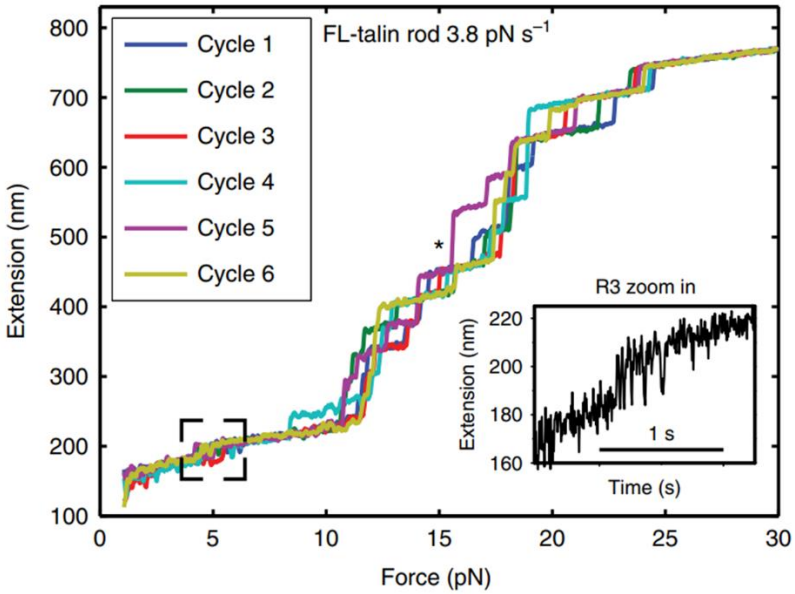

Figure 6. ***Unfolding force-extension curves of FL-talin rod****. Loading rate of 3.8 pN s^{-1}. The different curves represent repeated force cycles obtained from a single protein tether (zoom: the R3 unfolding step occurs at 5 pN; scale bar, 1 s). (Yao et al., 2016)*

Talin extension can vary between 50 and 350 nm in living cells, as observed during actin-driven stretching cycles and retrograde flow (Margadant et al., 2011), while maintaining linkage forces below 10 pN. In contrast, in vitro single-molecule force spectroscopy experiments have shown that talin can theoretically stretch up to more than 600 nm when fully unfolded under force (Figure 7) (Barnett and Goult, 2022).

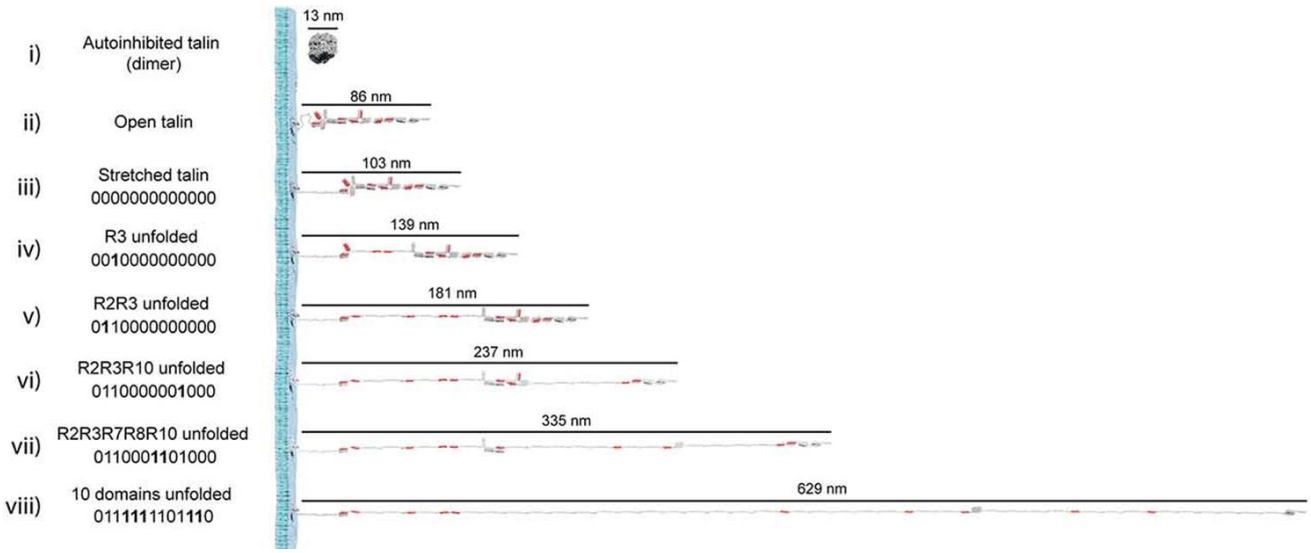

Figure 7. ***Scale models of talin in different conformations****. The binary string represented by each state is shown, with 0000000000000 showing the fully folded state and 1111111111111 the fully open state. In each subsequent binary string, the changing switch is indicated in bold. Lengths are shown in nanometers. (Barnett and Goult, 2022)*

Unfolding of the rod exposes vinculin-binding sites (VBSs), particularly in weak domains like R3 (~5 pN) (Rio et al., 2009). Vinculin binding locks unfolded domains, thereby stabilizing adhesions (Yao et al., 2016; Ciobanasu et al., 2014). However stronger forces (>25 pN) can trigger vinculin dissociation (Gao et al., 2019). Interestingly, vinculin binding itself induces coil-to-helix contractions within talin needed for stable association (Tapia-Rojo et al., 2020).

It is important note that these unfolding events do not occur under the same force for each domain (Yao et al., 2016). This discrete unfolding allows fine-tuned interactions that arise from mechanical stimuli.

High-resolution force microscopy using genetically encoded FRET tension sensors inserted at different positions within the talin molecule has demonstrated that talin experiences a clear force gradient across its length in living cells. Using multiplexed sensors, one near the N-terminal rod region and another near the C-terminal region between ABS2 and ABS3, Ringer et al., 2017 observed higher forces (>7 pN) at the N-terminal part of the rod and lower forces at the C-terminal region in focal adhesions, revealing a piconewton-scale gradient. This gradient is actomyosin- and vinculin-dependent, indicating that intramolecular tension is not uniformly distributed but decreases from the N- towards the C-terminus (Ringer et al., 2017). Single-sensor FRET experiments had previously detected ~5–10 pN tensions across talin during cell spreading (e.g. Austen et al., 2015), but only the multiplexed, dual-sensor approach revealed the

intramolecular distribution of force, with higher forces (>7 pN) toward the N-terminal rod region and lower forces at the C-terminal region between ABS2 and ABS3. This nuanced insight supports the idea that talin is not uniformly loaded: instead, it functions as a molecular "force buffer", with distinct mechanical states along its rod that modulate partner recruitment.

To have a better overview of talin's molecular interactions and how they vary depending on its mechanical state, Table 1 compiles known binding partners across different domains of talin, distinguishing between folded and force-unfolded conformations. These interactions underpin talin's role as a mechanosensitive hub, modulating its ability to recruit or release specific proteins during adhesion dynamics.

Talin Domain	**Conformational State**	**Binding Partner(s)**	**Interaction Type / Function**	**Reference(s)**
F0	Folded	Rap1	Recruitment to plasma membrane	(Goult et al., 2010; Plak et al., 2016; Zhu et al., 2017)
F2–F3	Folded	Integrin β tail	Integrin activation (FERM binding)	(Calderwood et al., 2002; Ulmer et al., 2003)
F2–F3	Folded	PIP2	Enhances integrin binding	(Martel et al., 2001; Anthis et al., 2009)
F3	Folded	FAK	Localization to nascent adhesions	(Lawson et al., 2012)
F3	Autoinhibited (folded)	—	Interaction blocked by R9 (auto-inhibition)	(Goksoy et al., 2008; Dedden et al., 2019)
R3	Folded	RIAM	Membrane recruitment / integrin activation	(Chang et al., 2014; Yang et al., 2014)
R3	Unfolded	Vinculin (VBS)	Vinculin recruitment, force reinforcement	(Yao et al., 2016; Rio et al., 2009)
R4–R8	Folded	F-actin (ABS2)	Actin linkage, regulated by force	(Hemmings et al., 1996)
R7	Folded	KANK1	Microtubule anchoring & cross-talk	(Li et al., 2023)
R8	Folded	RIAM	Adhesion assembly / competition with DLC1	(Chang et al., 2014; Yao et al., 2016)
R8	Folded	DLC1	Inhibits Rho signaling, supports early adhesion	(Dahal et al., 2022)
R8	Unfolded	Vinculin	Reinforcement of FAs	(Gingras et al., 2005)
R9-R10	Unfolded	PKA (RIIα)	Mechanically gated AKAP interaction	(Kang et al., 2024)

R11	Folded	Integrin (alt. site)	Secondary β tail binding site	(Rodius et al., 2008)
R13	Folded	F-actin (ABS3)	Rearward actin anchorage	(Goldmann and Isenberg, 1991)
Rod (various)	Unfolded (force-exposed)	Vinculin (11 sites total)	Stabilization and force transmission	(Gingras et al., 2005; Franz et al., 2023)

Table 1. Summary of key domain-specific talin interactions in folded and unfolded states. The table includes validated interactions with integrins, cytoskeletal elements, and regulatory proteins based on biochemical, structural, and force-dependent studies. Distinct conformational states enable talin to act as a mechanosensitive scaffold within integrin adhesion sites.

These extensive molecular interactions, which are highly dependent on talin's mechanical state, underpin its critical role in integrin activation and in driving mechano-responsive formation of nascent adhesion structures.

Altogether, the force-dependent unfolding of talin domains and the selective recruitment of interaction partners suggest that talin operates as more than a mechanical scaffold. It may serve as a central node in a mechanotransduction code, where distinct conformations and binding states along the molecule reflect different mechanical contexts (Goult et al., 2021). In this view, the spatial organization of talin, including its orientation, conformation, and partner distribution, could provide a structural logic for how mechanical signals are interpreted at adhesion sites. Understanding how talin adopts specific nanoscale shapes or orientations in response to mechanical inputs may therefore be key to decoding how cells convert physical forces into biochemical outcomes. This motivates the need for quantitative approaches that can resolve the 3D localization and orientation of talin domains in living cells, which forms the basis for the research presented in this thesis.

3. 2. FAs – a complex molecular composition

Proteomic analyses have revealed the remarkable complexity of the FA proteome. Thousands of proteins have been identified at IAS, but meta-analyses across multiple datasets have converged on a "consensus adhesome" of approximately 60 core proteins that are consistently enriched in FAs (Horton et al., 2015). These proteins form functional modules, such as the talin–vinculin complex, the FAK–paxillin signaling axis, and the α-actinin–zyxin–VASP module, each contributing

to distinct aspects of adhesion dynamics and signaling. Notably, the composition of FAs is sensitive to mechanical tension: inhibition of myosin-II, which reduces intracellular contractility, leads to the selective depletion of force-sensitive components such as zyxin, paxillin, and α-actinin (Horton et al., 2015; Schiller et al., 2013; Kuo et al., 2011; Schiller et al., 2011). However, structural and signaling roles of FA components may be partially independent; for example, inhibition of FAK and Src kinases reduces protein phosphorylation and cell migration without altering FA morphology (Horton et al., 2016; Giannone et al., 2003). This underscores the functional compartmentalization within FAs, where force transmission, mechanosensing, and signaling can be independently regulated yet spatially coordinated to support cellular adhesion, migration, and mechanotransduction.

3. 3. FAs – 3D architecture

Beyond their compositional complexity, FAs are also distinguished by a highly ordered three-dimensional (3D) architecture. This nanoscale stratification is essential for their function as mechanotransducive and force-transmitting complexes. Super-resolution microscopy studies, particularly those employing three-dimensional imaging techniques such as interferometric photoactivated localization microscopy (iPALM) with spatial resolution on the order of ~10–20 nm, have revealed that FAs are vertically organized into distinct molecular layers along the z-axis - defined as the axis perpendicular to the plasma membrane (Figure 8) (Kanchanawong et al., 2010; Liu et al., 2015; Paszek et al., 2012). These studies revealed the existence of a physical gap of up to 50 nm between integrin cytoplasmic tails and actin filaments, highlighting the role of tilted linkers such as talin that extend across the following nanolayers. The most membrane-proximal layer, known as the integrin signaling layer, contains the cytoplasmic tails of integrins along with associated signaling molecules such as FAK and paxillin. Positioned above this is the force transduction layer, where structural adaptors like talin and vinculin bridge integrins to the actin cytoskeleton. Finally, the actin-regulatory layer lies further into the cytoplasm and includes proteins such as α-actinin, zyxin, and VASP, which are involved in actin filament organization and regulation.

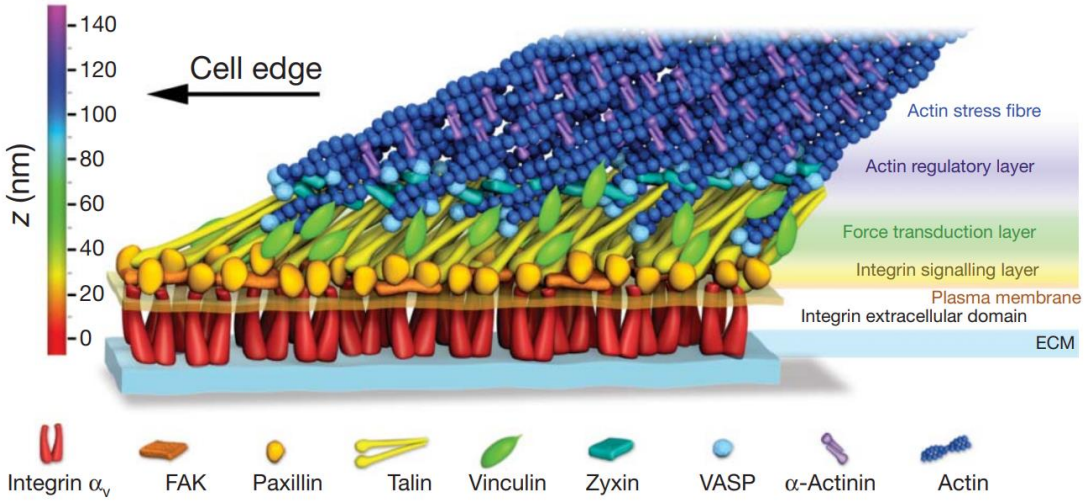

Figure 8. ***Schematic model of focal adhesion molecular architecture****. This distribution was obtained experimentally in fixed samples using iPALM. Note: the schematic model does not depict protein stoichiometry (Kanchanawong et al., 2010).*

The precise vertical positioning of these proteins is functionally significant: for instance, vinculin exhibits a shift in axial localization during FA maturation, reflecting changes in its activation state and binding partners (Case et al., 2015). This nanostructural organization imposes spatial constraints on molecular interactions within FAs and may act as a regulatory mechanism by segregating or facilitating specific protein–protein interactions based on their axial positioning. Thus, the 3D architecture of FAs not only reflects the molecular composition of these complexes but also encodes information essential for their mechanosensitive function. In that sense, talin appears to be a key player in FAs nanolayered architecture as it spans across multiple layers and adopts a tilted conformation under mechanical tension, linking membrane-bound integrins to actin filaments located tens of nanometers away from the membrane (Kanchanawong et al., 2010; Liu et al., 2015). However, this tilt has been inferred indirectly by comparing the localization clouds of N- and C-terminally tagged constructs of talin and α-actinin in super-resolution datasets. While informative, this approach lacks the resolution to capture real-time talin conformational dynamics, thus calling for more direct, live-cell measurements of molecular orientation.

4. Hypothesis: talin mechanotransduction “code” sensing and encoding mechanical stimuli – Overview and Thesis Objectives

Mechanotransduction, the conversion of mechanical cues into biochemical signals, is a foundational process in cell biology, underpinning behaviors such as migration, differentiation, and immune responses (Hoffman et al., 2011; Rocha et al., 2022). At the core of this process are integrin-based adhesion sites, which serve as physical and signaling bridges between the ECM and the actin cytoskeleton (Geiger et al., 2009; Orré et al., 2019). Integrins themselves are force-sensitive: they transition from bent, low-affinity forms to extended, high-affinity conformations in response to mechanical or biochemical inputs (Takagi and Springer, 2002; Shimaoka et al., 2002; Li and Springer, 2018).

Talin, a key adaptor, links integrins to F-actin and undergoes step-by-step unfolding in response to tension, exposing cryptic binding sites for vinculin and other regulators (Yao et al., 2016; Rio et al., 2009). These interactions reinforce the integrin–actin linkage and enable force transduction across the adhesion site (Atherton et al., 2016; Elosegui-Artola et al., 2016). At the cellular level, mechanotransduction is influenced by actomyosin contractility and ECM stiffness, forming a reciprocal feedback loop: cells apply force, sense mechanical resistance, and adjust their adhesion dynamics accordingly (Kumar et al., 2006; Wolfenson et al., 2013).

Furthermore, super-resolution microscopy has revealed that IAS are organized into nanoscale vertical layers, separating integrin signaling, force transmission, and actin regulatory functions (Kanchanawong et al., 2010; Liu et al., 2015). Talin spans across these layers, adopting tilted conformations under force to link membrane-bound integrins with distant actin structures (Oria et al., 2017).

Although force-dependent behaviors of individual proteins have been characterized in vitro or through isolated single-molecule experiments, we still lack a complete understanding of how protein conformation and orientation are regulated by force inside intact, living cells (Yao et al., 2016; Dedden et al., 2019). The spatial arrangement of molecules such as talin within IAS - and how it correlates with mechanical load - remains elusive. Do talin molecules in living cells behave

similarly to their in vitro counterparts? Are they extended, tilted, or retracted under different force regimes?

Understanding mechanotransduction at the molecular level holds significant biomedical relevance. Defects in mechanotransduction are implicated in cancer metastasis, fibrosis, cardiovascular disease, and immune dysfunctions (Butcher et al., 2009; Di et al., 2023). Protein orientation is particularly crucial, as it governs how mechanical inputs are converted into structural changes and signaling responses. For talin and integrin, orientation dictates not just force propagation and mechanical engagement, but also accessibility of binding sites and phosphorylation motifs.

Moreover, the vertical stratification of adhesion components implies that spatial organization, including orientation, is not random but functionally encoded to regulate mechanical and biochemical responses (Liu et al., 2015; Oria et al., 2017).

Despite powerful techniques like force spectroscopy, iPALM, and traction force microscopy, existing methods rarely resolve orientation and conformation simultaneously in live cells. Most experiments rely on fixed samples, bulk biochemical readouts, or infer protein mechanics indirectly (Kanchanawong et al., 2010; Zhanghao et al., 2019). In short, there remains a critical gap in techniques that can assess both spatial positioning and orientational dynamics of single proteins under physiological forces.

What is the objective of this research?

The central objective of this thesis is to understand how mechanical forces are sensed and transduced at the molecular level within integrin adhesion sites (IAS), with particular emphasis on the *orientation* and *conformational states* of key mechanosensitive proteins in living cells. These proteins act as molecular switches: they stretch, rotate, and reorganize in response to tension, regulating adhesion strength, downstream signaling, and cytoskeletal linkage. While many studies have focused on protein composition or force-dependent binding, the spatial orientation of these molecules remains poorly explored, despite its critical role in force transmission and signaling activation.

Proteins such as talin and integrin are not mechanically isotropic. Instead, their structural and functional roles depend on their directional alignment within adhesion complexes. These

directional alignments influence whether force is effectively transmitted and whether binding sites are exposed to partners such as vinculin or kindlin. While direct measurements of angular orientation remain limited, studies have shown that force-induced conformational changes, such as domain unfolding and differential loading along talin's length, are highly structured and spatially coordinated (Yao et al., 2016; Ringer et al., 2017). This supports the notion that orientation may serve as a proxy for mechanical engagement, and highlights the need for approaches that can resolve nanoscale angular information in living cells.

However, despite extensive in vitro studies demonstrating the sensitivity of protein orientation to mechanical force, direct observation of these behaviors within *living cells* has remained elusive. Most imaging approaches either rely on fixed samples, lack angular resolution, or fail to resolve single-molecule dynamics in cellular environments.

This thesis directly addresses this gap using single-molecule fluorescence polarization microscopy (Rimoli et al., 2022; Brasselet and Alonso, 2024) in living cells. By designing and validating novel constructs of talin and integrin, and applying fluorescence polarization microscopy, this work provides the first dynamic measurements of protein orientation in IAS in living cells with molecular precision.

Where conventional imaging offers only spatial localization, this approach adds an angular dimension in 3D - revealing how individual proteins align, rotate, and unfold under mechanical tension. For example, it enables direct testing of longstanding models of talin extension and integrin activation within the stratified architecture of IAS, in real time and under physiological force loads. Moreover, the integration of orientation data with 3D spatial localization allows a more complete understanding of how protein geometry encodes mechanical information in cells. By doing so, this work not only enhances our mechanistic understanding of mechanotransduction but also opens new avenues for interrogating force-sensitive signaling with previously inaccessible detail.

Super-Resolution Approaches for Investigating Focal Adhesions

1. Fluorescence microscopy

Fluorescence microscopy is a technique that is often used to study localization and dynamics of macromolecules (Lakowicz, 2006). It requires the labeling of macromolecules with a fluorescent compound called “fluorophore”. Fluorescence consists in the emission of light by a fluorophore that happens within nanoseconds after its excitation induced by the absorption of light. The excitation light is typically of a shorter wavelength than the emitted light. In fact, this difference, known as the Stokes shift, is the critical property that makes fluorescence so powerful. By filtering out the excitation light, it is possible to only observe objects that are emitting fluorescent light.

To understand the details of the fluorescence process, a useful approach based on energy consideration was developed by Alexander Jablonski in 1930s (Lichtman and Conchello, 2005). His representation, famously known as the Jablonski diagram, provides a scheme of energy levels of electronic and vibrational states of a molecule and outlines possible routes between the excited states (Lakowicz, 2006). The spectral characteristics associated with the absorption and emission of energy by a molecule can be related to the amplitude of the energy step needed to move a molecule from one energy state to another. Figure 9 displays a Jablonski diagram describing the absorption and emission spectra of FITC, a commonly used fluorophore. Each arrow aligns the spectra with the energy of the absorbed (arrows pointing up) or emitted (arrows pointing down) photons. The color code is correlated with the color of the photons emitted. This diagram clearly illustrates the Stokes shift mentioned above between absorbed and emitted photons.

Temporally, fluorescence emission occurs on the nanosecond timescale, which is significantly faster than the conformational changes of most proteins - ranging from microseconds to seconds depending on the structural rearrangement involved. This temporal separation enables fluorescence-based methods to act as instantaneous reporters of protein conformational state, making them particularly well-suited for real-time studies of mechanosensitive molecular dynamics (Lakowicz, 2006).

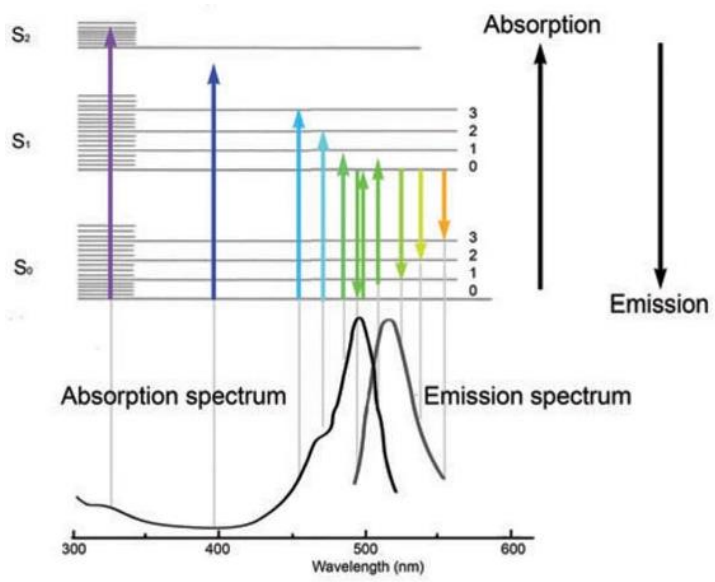

Figure 9. ***Fluorescence fundamentals****. Absorption and emission spectra of FITC, a common fluorophore, and the Jablonski diagram showing the energy of the absorbed (arrows pointing up) or emitted (arrows pointing down) photons for specific wavelengths. (Lichtman and Conchello, 2005)*

2. How to excite your sample

There are various ways to excite fluorescent molecules labeling subcellular structures of interest. Total Internal Reflection Fluorescence Microscopy (TIRF) is a powerful imaging technique ideally suited for studying biological events occurring near the ventral cell membrane. This approach, developed in the 1980s and pioneered by Daniel Axelrod (Axelrod, 1981), relies on the principle of total internal reflection to achieve selective excitation of fluorophores near the cell-substrate interface. When a light beam encounters the interface between two media of different refractive indices, such as glass and an aqueous biological sample, part of the light is reflected, while another portion is refracted. If the beam strikes the interface at a perpendicular angle, the entire sample is illuminated, resulting in conventional epifluorescence (Figure 10a). In contrast, when the angle of incidence exceeds a critical value, the beam undergoes total internal reflection (Figure 10b). Although the light does not enter the second medium, it generates an evanescent wave that extends approximately 100–300 nm beyond the interface, with an intensity that decays exponentially with distance. This evanescent field selectively excites fluorophores located in the immediate vicinity of the plasma membrane, while those further away remain unexcited. Consequently, TIRF microscopy provides high-contrast imaging of cellular structures situated at

or near the cell surface, such as membrane receptors, endocytic or exocytic vesicles, and adhesion sites (Axelrod, 1981).

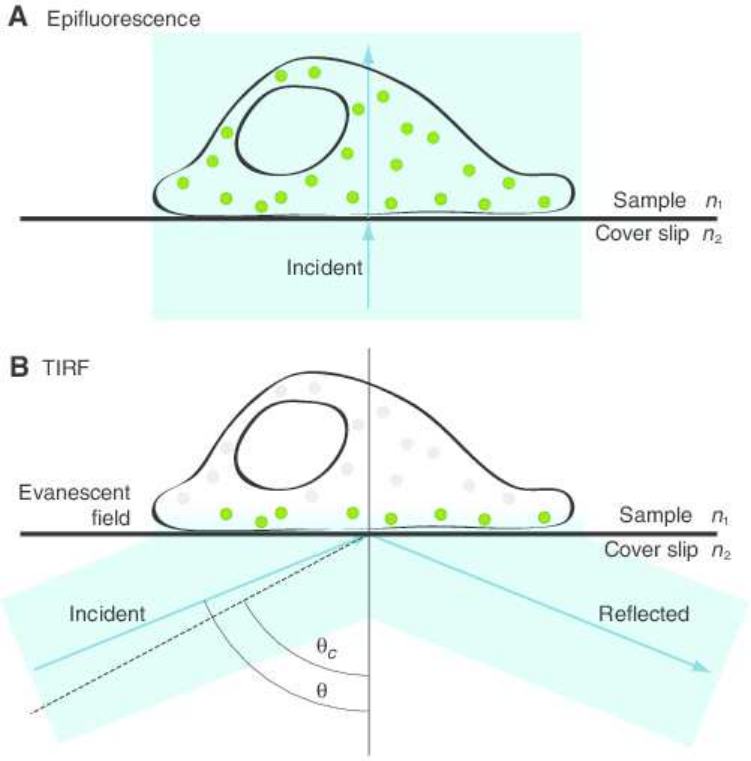

Figure 10. ***The physical basis of epifluorescence and TIRF illumination****. Schematic illustration of the coverslip–sample interface. (**a**) Epifluorescence. The excitation beam travels directly through the interface of the coverslip and the sample. All fluorophores in the entire sample are excited. (**b**) TIRF. The excitation beam enters from the left of the scheme, at incidence angle, which is greater than the critical angle, indicated by the dashed line. Angles are measured from the normal. The excitation beam is reflected off the coverslip-sample interface, generating an evanescent field on the opposite side of the interface, in the sample. Only fluorophores in the evanescent field are excited when imaging in TIRF, as indicated by the green color. The refractive index of the sample (n1) must be less than the index of refraction of the cover slip (n2) to achieve TIR (Mattheyses et al., 2010).*

While TIRF is ideal for visualizing near-membrane events in two dimensions, its axial resolution is limited and not suited for imaging deeper structures within cells or in 3D. For this reason, complementary techniques such as confocal and light-sheet fluorescence microscopy are used to image molecular processes throughout the cell volume with greater spatial context.

Confocal microscopy (Figure 11a) operates by scanning a focused laser beam point-by-point across the sample, combined with a pinhole that eliminates out-of-focus light. This provides excellent optical sectioning capability, typically achieving axial resolutions of ~500–800 nm and lateral resolutions of ~200–250 nm. It is particularly suitable for reconstructing 3D volumes and

studying the spatial distribution of proteins in thicker samples, albeit at the cost of slower acquisition and higher photobleaching compared to TIRF.

Light-sheet fluorescence microscopy (LSFM) (Figure 11b), by contrast, uses a thin sheet of light to illuminate only the focal plane of interest, thereby drastically reducing photobleaching and improving temporal resolution. LSFM enables rapid 3D imaging with subcellular resolution, and some configurations can achieve axial sectioning below 500 nm (Shechtman et al., 2014). This makes it highly suitable for dynamic imaging of large samples or fragile systems. Recent advancements in lattice light-sheet and tilted light-sheet approaches have pushed this resolution further while maintaining gentle illumination conditions (Shechtman et al., 2017; Broeken et al., 2014). Moreover, new designs allow 3D single-molecule localization microscopy (SMLM) with improved axial precision by combining light-sheet illumination with engineered point spread functions (Gustavsson et al., 2018b).

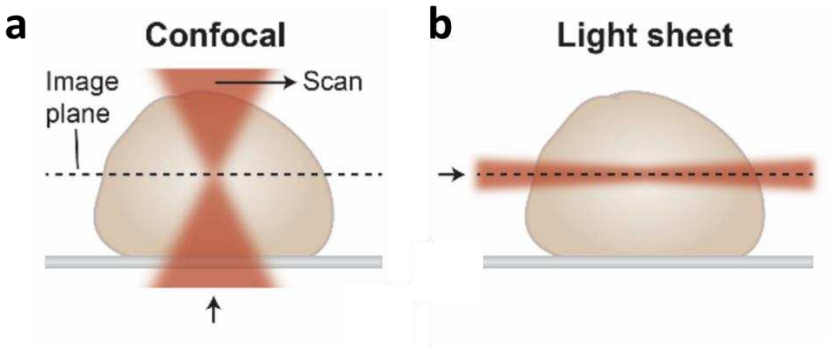

Figure 11. ***Confocal vs light sheet microscopy.*** *(**a**) Confocal illumination enables contrast improvement by blocking out of focus light, but requires scanning in order to build up an image, (**b**) Light sheet only illuminates the sample plane that is imaged, allowing for reduced background, photobleaching and photodamage. Adapted from (Gustavsson et al., 2018a)*

As FAs, our structures of interest, are within a couple of hundreds of nanometers above the cell membrane, TIRF is perfectly suited for our studies.

3. Limit of diffraction and super-resolution fluorescence microscopy

As a consequence of the optical phenomenon of light diffraction, standard optical microscopy's resolution is limited to roughly half the wavelength of light around 200nm. Because of this, the

point spread function (PSF), is not a point, but an airy pattern, with a central peak approximately 200-250 nm in X and Y axis, and the resolution even lower in Z - around 500 nm. Therefore, diffraction leads to blurring of structures below this spatial scale (Figure 12). Moreover, the objects located too close to each other (i.e. below the diffraction limit), cannot be distinguished even when the fluorescent reporter itself is small (e.g. GFP: d=5 nm). This is where super-resolution microscopy comes into play. These methods are able to overcome the diffraction limit and enable insights into biological structures such as nuclear structures, chromatin complexes, adhesion site proteins or cytoskeletal filaments closer to molecular scales (Lelek et al., 2021; Turkowyd et al., 2016; Rossier et al., 2012).

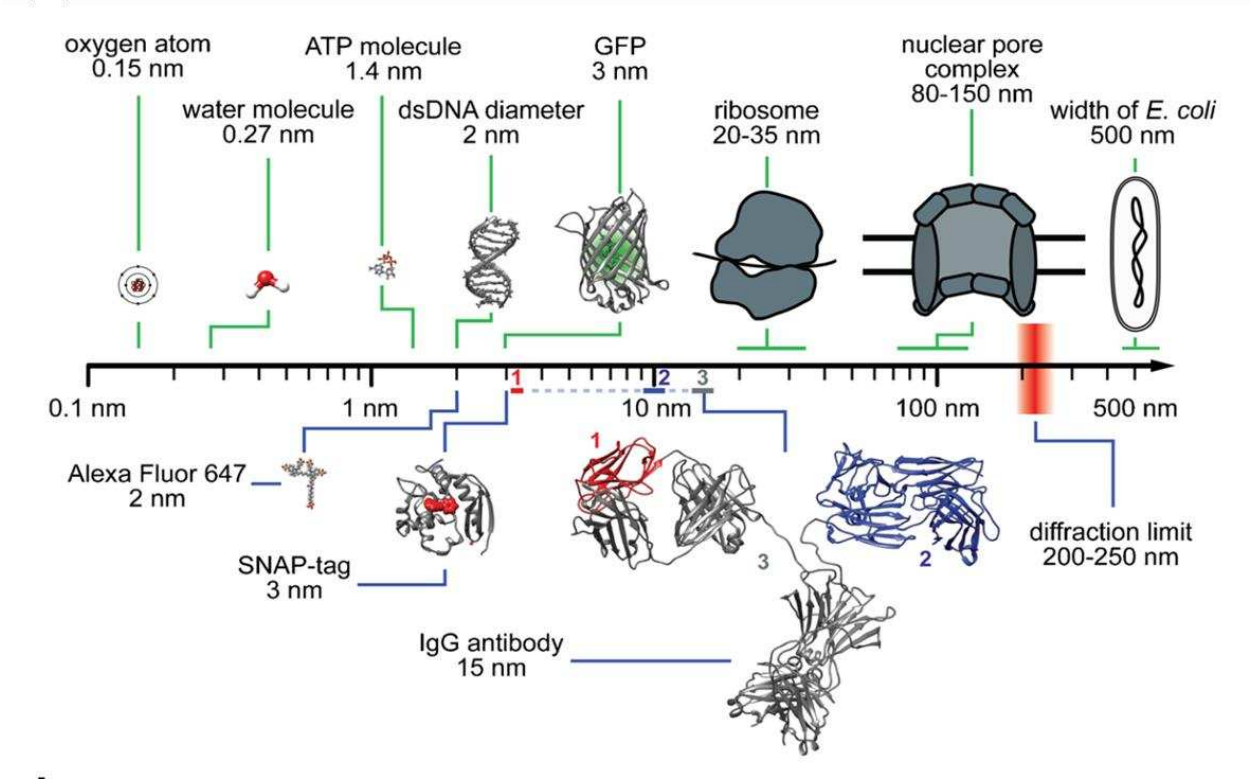

Figure 12. ***Spatial scale in life sciences and microscopy****. Due to the diffraction limit, traditional optical microscopy is limited to objects smaller than 200-250 nm. (Turkowyd et al., 2016)*

Today, there is a plethora of different super-resolution techniques available and your choice will depend on the nature of your samples, as well as the needs of your experiment. In Valli et al., 2021, they provide a convenient simplified guide for choosing the right technique (Figure 13).

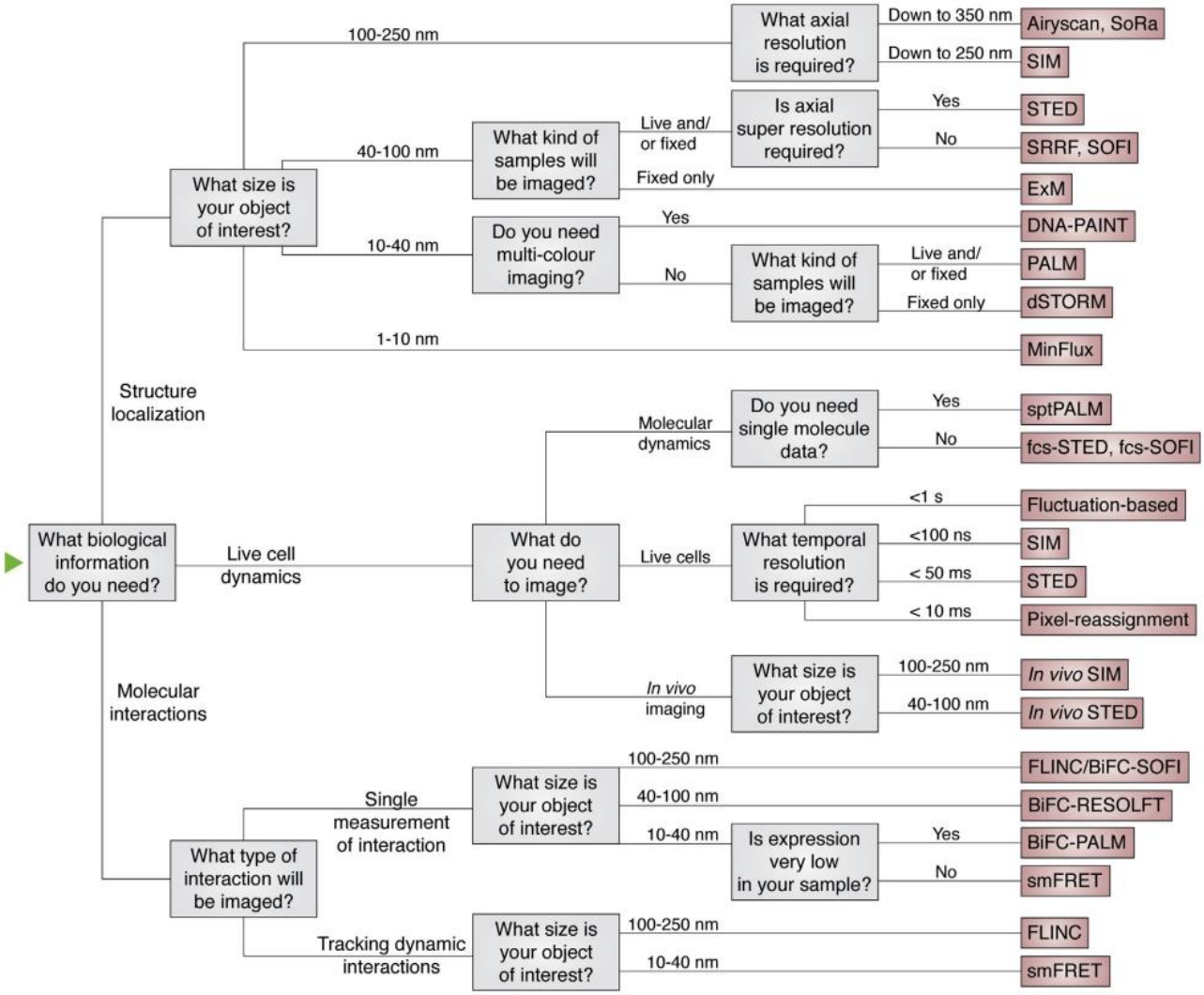

Figure 13. ***How to choose the right super-resolution technique*** *(Valli et al., 2021).*

Super-resolution microscopy methods can be divided into three main categories: stimulated emission depletion (STED), structured illumination microscopy (SIM) and single-molecule localization microscopy (SMLM). Unlike STED or SIM, which rely on patterned illumination and nonlinear optics, SMLM achieves sub-diffraction resolution by stochastically activating a sparse subset of fluorophores at a time and reconstructing the image from many sequential frames, each capturing a distinct set of emitters. As I have been implementing SMLM techniques in my project, I will describe the ones used, as well as some additional ones to obtain a fuller understanding of our choice of methods.

4. Single-molecule localization microscopy (SMLM) principle

Single-Molecule Localization Microscopy (SMLM) encompasses a family of super-resolution fluorescence imaging techniques that enable spatial resolutions beyond the classical diffraction limit, typically achieving localization precisions in the range of 20–50 nm or better. In the case of MINFLUX, the stochastic on-off switching of individual fluorophores is combined with a targeted excitation beam containing an intensity minimum, such as a doughnut shape, in order to localize the emitter with resolutions going down to a couple of nm (Balzarotti et al., 2017).

The core principle of SMLM is that the position of an individual fluorescent molecule can be determined with nanometric precision, provided that its PSF is spatially isolated from those of neighboring emitters. This is made possible because sub-pixel displacements in the emitter's position result in quantifiable changes in the intensity distribution across detector pixels, which can be modeled and fitted, typically with a Gaussian function, to extract precise molecular coordinates (Figure 14a).

To ensure such spatial isolation, SMLM techniques rely on temporal separation of fluorescence emissions. This is most commonly achieved through photoswitching, whereby fluorophores stochastically transition between a fluorescent (ON) and one or more non-fluorescent (OFF) states. By modulating the chemical environment and/or excitation conditions, only a sparse, random subset of fluorophores is activated in any given acquisition frame (Figure 14b). Over the course of thousands of imaging cycles, the entire population of fluorophores is sampled in isolation, and their localizations are cumulatively used to reconstruct a high-resolution image. The localization precision is not limited by the diffraction limit itself, but rather by the signal-to-noise ratio (SNR), the number of detected photons, and the accuracy of the PSF fitting model. Consequently, SMLM allows the spatial mapping of biological structures at the nanoscale.

SMLM techniques are compatible with both fixed and live-cell imaging, although live-cell applications require careful consideration of photophysical and phototoxic constraints. Critical experimental factors influencing the performance of SMLM include the choice of fluorophores, labeling strategies that preserve the biological context, sample preparation protocols, imaging

hardware (such as camera sensitivity and stability), and computational methods for precise molecule localization and image reconstruction.

By enabling the visualization of biological structures and molecular organization at nanometer resolution, SMLM has become a powerful tool for studying complex cellular processes at the molecular level. While most super-resolution techniques enable high-precision localization, certain modalities also incorporate temporal resolution, allowing dynamic tracking of molecular behavior (Lelek et al., 2021; Valli et al., 2021; Liu et al., 2022; Turkowyd et al., 2016; Rossier et al., 2012).

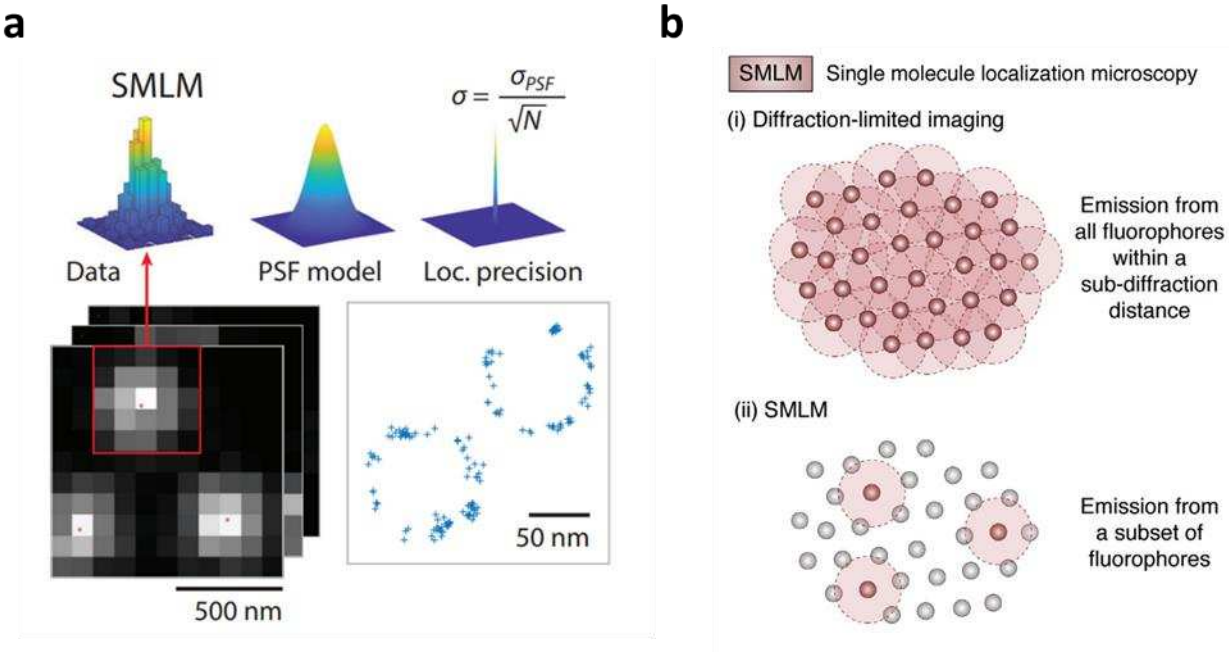

Figure 14. ***Single-molecule localization microscopy (SMLM) principle****. (**a**) Isolated emitters are identified and cropped in small subregions (red box) and fitted with a point spread function (PSF) model; the localization (Loc.) precision σ depends on the number of detected photons N. The positions of emitters are output as coordinates (blue crosses). (Liu et al., 2022), (**b**) Principle of SMLM (Valli et al., 2021).*

5. Implementing SMLM in 2D

5. 1. PALM and sptPALM

PALM (photoactivated localization microscopy) represents an SMLM technique based on the use of fluorescent proteins that can selectively be activated and deactivated with light. These proteins are either referred to as photoactivatable – if they transition, following irradiation, from

a non-fluorescent state to the "ON" state (example: Figure 15); photoconvertible – if they change their emission spectrum from one maximum to another; or photoswitchable – if they are able to switch from the "ON" when exposed to one wavelength to the "OFF" state when exposed to another wavelength.

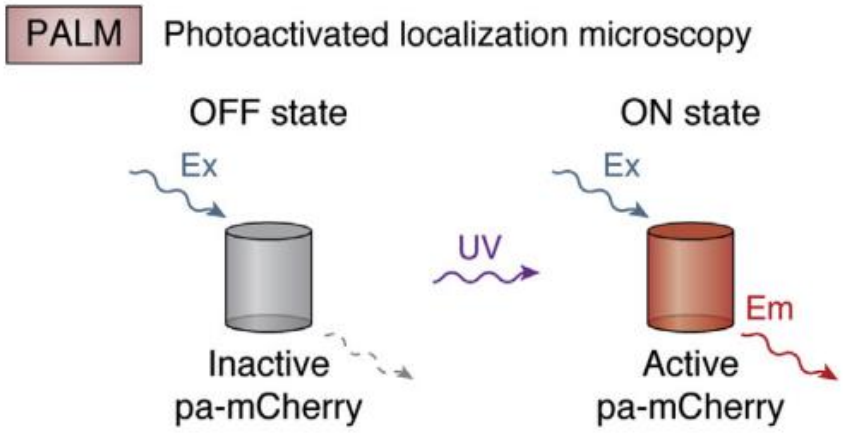

Figure 15. ***Photoactivation of PA-mCherry showcasing the principle of PALM****. PALM uses photoactivatable fluorophores that need to be activated by 405 nm light before being excited. (Valli et al., 2021)*

The principle of PALM (Figure 16) is based on taking advantage of these properties to sequentially activate and localize fluorescent molecules, before they bleach. After repeating iteratively these "activation-photobleaching" cycles, it is possible to determine, at the nanoscale, positions of a large number of molecules and therefore reconstruct an image with higher resolution than the one available solely through conventional microscopy (Betzig et al., 2006).

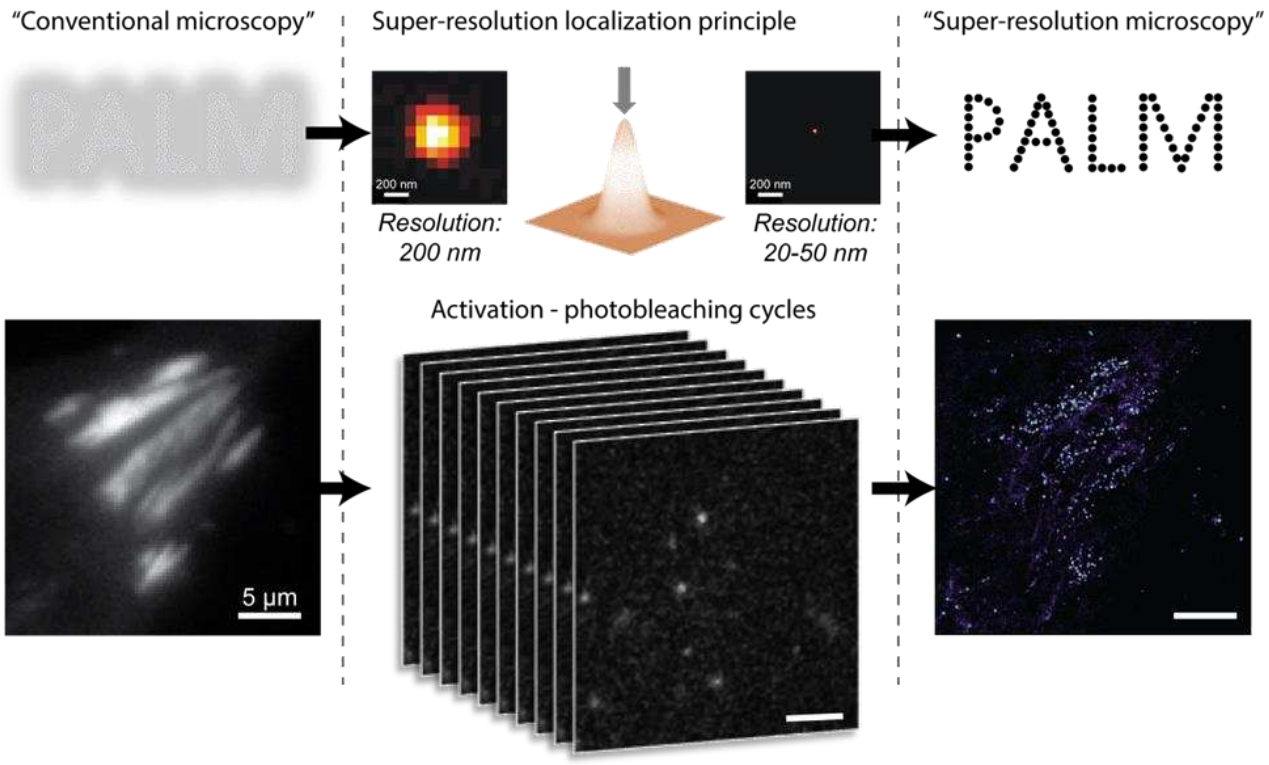

Figure 16. ***Principle of PALM****. Left – Conventional microscopy has a resolution of around 200 nm and cannot distinguish certain structures. Top: logo PALM, Bottom: FA observed in conventional microscopy. Middle – Top: single molecule detection principle. The resolution of a single molecule detected is reduced to 20-50 nm by calculation. Bottom: Repeated activation-photobleaching cycles enable reconstruction of a super-resolved image. Right – Super-resolution microscopy detects finer structures. Top: PALM logo; bottom: FA observed in super resolution. Scale bar of 200 µm for single molecule detection images, 5 µm for FA images.*

One major advantage of PALM is that it enables the precise mapping of protein distributions with a resolution down to 20–50 nm in the lateral plane, without requiring antibody labeling. This makes it ideal for use in live-cell imaging with genetically encoded tags. Moreover, by combining PALM with time-resolved acquisition, dynamic molecular behaviors can be studied using sptPALM. In our team, using sptPALM, the correlation between integrin activation and their immobilization was demonstrated (Rossier et al., 2012) as well as the recruitment of talin directly from the cytosol into focal adhesions, unlike kindlin, which diffuses along the plasma membrane before being recruited to the adhesion site (Orré et al., 2021). The computational techniques used for sptPALM will be described later in this work.

Despite its strengths, PALM does have limitations. The technique is relatively slow compared to other SMLM methods like STORM, due to the low brightness and longer maturation times of photoactivatable fluorescent proteins. sptPALM requires long emission times for accurate

tracking, which can reduce the number of usable molecules. Additionally, traditional PALM is inherently 2D, providing limited or no information in the Z-axis.

Overall, PALM and sptPALM provide a powerful, genetically encoded solution for probing both molecular localization and dynamics at nanometer resolution in living cells, with the trade-off of lower photon counts and axial resolution.

mEos – our fluorophore of choice

In this project, I primarily employ the photoconvertible protein Eos in its monomeric variant (mEos), fused to our proteins of interest. Upon illumination with a 405 nm laser, the chromophore, originally having displayed green fluorescence in its native form, is cleaved and subsequently emits red fluorescence when excited with a 561 nm laser (Figure 17). This fluorescent protein undergoes photobleaching after a few seconds of excitation-emission cycles, which is sufficient for conducting sptPALM experiments. The gene encoding this fluorescent protein was originally identified in the stony coral *Lobophyllia hemprichii* (Wiedenmann et al., 2004). There are several derived variants of this molecule, including Eos2 (McKinney et al., 2009) or mEos3.2 (Zhang et al., 2012). While their functional mechanisms are comparable, the latter represents an optimized version that does not multimerize and has improved conversion efficiency, which is why we chose it when developing our constructs that will be described later on.

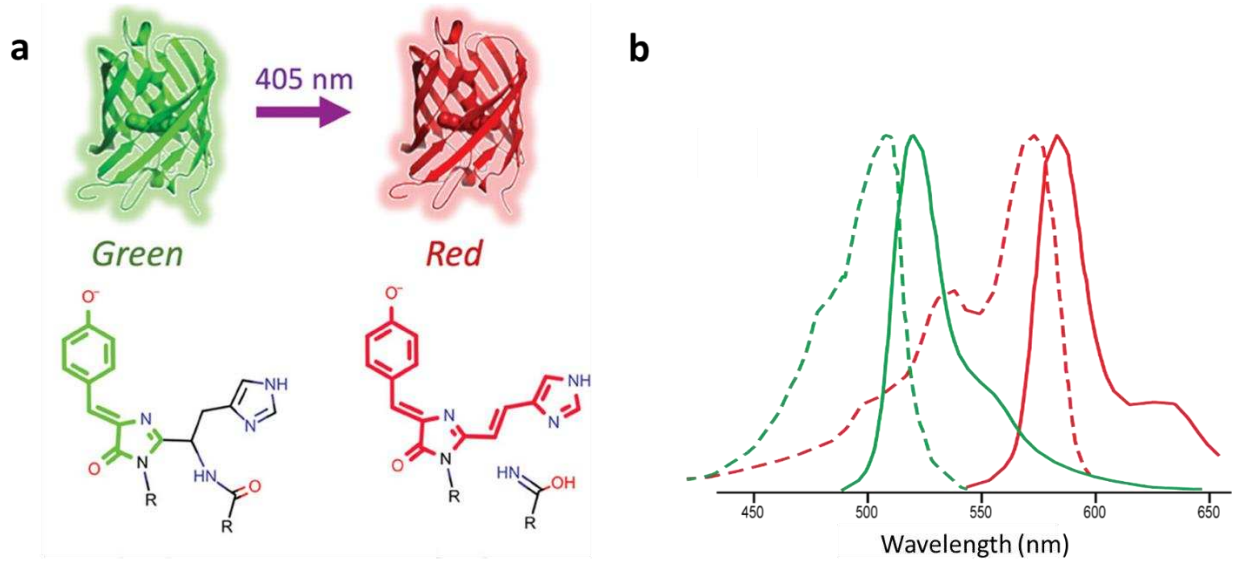

Figure 17. ***Structure and spectra of mEos photoconvertible protein.*** *(**a**) Photoconversion mechanism. Figure adapted from Maity et al., 2024. (**b**) Comparison of spectra of the native (green) and the photoconverted (red) protein (dotted lines: absorption, continuous lines: emission).*

5. 2. STORM

STORM (Stochastic Optical Reconstruction Microscopy) differs from other super-resolution techniques like PALM primarily in its use of synthetic, photoswitchable organic dyes rather than photoactivatable fluorescent proteins, allowing for higher photon yield and superior localization precision. Organic dyes used in STORM (e.g., Cy5, Alexa Fluor 647) are driven into a long-lived dark state by intense excitation and reducing environments, from which they stochastically return to a fluorescent state, enabling single-molecule detection.

A critical factor in STORM's performance is the imaging buffer, which typically contains reducing agents and oxygen scavengers (such as β-mercaptoethanol, cysteamine, or glucose oxidase/catalase systems) that enhance the reversible photoswitching behavior of the dyes and minimize photobleaching. This allows repeated switching cycles and high-accuracy localization across thousands of frames, ultimately enabling molecular-scale resolution (Rust et al., 2006). However, not all fluorophores are compatible with STORM. Dye performance depends heavily on buffer composition, redox environment, and laser intensity. Optimization of imaging conditions is essential to avoid premature bleaching or insufficient blinking. Furthermore, because STORM requires specialized buffers, live-cell imaging is more challenging (Dempsey et al., 2011).

In Owen et al., 2017, using STORM, they investigated how kindlin-3, but not talin-1, is required for the formation and clustering of high-affinity β2-integrins at the nanoscale level during inside-out signaling in leukocytes.

Advantages of STORM include extremely high localization precision (often better than 20 nm), due to the high photon output of synthetic dyes. It also allows dense labeling using antibodies or small molecules, enabling visualization of fine structural details in fixed samples. Drawbacks include limited compatibility with live-cell imaging, the reliance on chemically controlled conditions, and the requirement for careful tuning of both dye and buffer systems. Additionally, multicolor STORM imaging can be complex, as each dye may require distinct switching and buffer

parameters. Overall, STORM offers unmatched spatial resolution in fixed samples and is ideal for nanoscale structural mapping when labeling and buffer conditions are carefully optimized.

5. 3. DNA-PAINT

DNA-PAINT (DNA-based Points Accumulation for Imaging in Nanoscale Topography) is a localization-based super-resolution microscopy technique that utilizes the transient hybridization of dye-labeled 'imager' strands to complementary 'docking' strands covalently linked to the target of interest (Schlichthaerle et al., 2021). Unlike PALM or STORM, which rely on the intrinsic photoswitching behavior of fluorophores, DNA-PAINT decouples the blinking mechanism from dye photophysics. Instead, stochastic fluorescence arises from the dynamic binding and unbinding of short DNA strands, making signal generation programmable and highly reproducible.

In DNA-PAINT, imager strands diffusing freely in solution are moving too fast to be detected. It is only when transiently hybridized to docking strands that emitted fluorescence lead to efficient fluorophore position detection. Because these imager strands are continually replenished from the buffer, photobleaching is effectively bypassed. This allows for repeated detection events at the same site and enables accumulation of high photon counts, resulting in extremely precise localization - often reaching spatial resolutions better than 5 nm.

One of the major strengths of DNA-PAINT lies in its multiplexing capacity. Through the use of orthogonal DNA sequences, multiple targets can be imaged sequentially in a process known as Exchange-PAINT, without any need for spectral separation. This permits virtually unlimited multiplexed imaging using only a single fluorophore and optical channel. Moreover, DNA-PAINT enables quantitative molecular counting through a kinetic analysis approach called qPAINT, which interprets binding frequency as a readout of molecule number.

DNA-PAINT too can be used for the study of adhesion sites. In Schlichthaerle et al., 2021, they use DNA PAINT to study mechanical engagement of single integrin receptors and downstream influence on actin binding. Fischer et al., 2021 used DNA-PAINT to map the spatial organization of talin-1, kindlin-2, and integrins in spreading cells, revealing their distinct nanoscale arrangements during adhesion maturation.

Despite these advantages, DNA-PAINT also presents limitations. Because it requires the continuous diffusion of imager strands in solution and relatively long binding times, imaging is inherently slower than in PALM or STORM. Additionally, DNA-PAINT is currently restricted to fixed-cell imaging due to challenges in delivering and maintaining functional DNA strands in live cells. Background fluorescence from unbound imager strands can also reduce contrast, necessitating imaging modes such as TIRF or oblique illumination to confine excitation to the focal plane. Finally, the use of antibody–DNA conjugates introduces a physical offset between the fluorophore and the target molecule, known as a linkage error, although this can be minimized using nanobodies or direct labeling strategies.

While PALM, STORM, and DNA-PAINT have significantly advanced our understanding of protein localization and organization in two dimensions, the molecular architecture and function of focal adhesions are intrinsically three-dimensional. Key components such as integrins, talin, and vinculin are stratified vertically within adhesion sites and dynamically rearrange under force and signaling cues. As such, accessing only the lateral (XY) plane provides an incomplete picture. To capture the full complexity of adhesion site dynamics, including protein layering, vertical force transmission, and spatiotemporal remodeling, techniques capable of resolving molecular localization and motion in three dimensions are essential.

6. Uncovering the third dimension with SMLM

6. 1. Interferometric Photoactivation and Localization Microscope (iPALM)

iPALM (interferometric Photoactivated Localization Microscopy) extends the capabilities of traditional PALM by adding precise axial localization using interferometry. In iPALM, photoactivatable fluorophores are localized not only in the lateral (XY) plane but also with exceptional precision along the axial (Z) axis - down to 10-20 nm - by exploiting the interference pattern created by splitting the emission light into two paths and recombining them (Shtengel et al., 2014). This technique uses a two-objective geometry, between which the sample is placed. Emitted fluorescence will be collected by both objectives and recombined to allow interference signals that encode the axial position of the fluorophores with nanometric accuracy.

One of the most important advantages of iPALM is its ability to reconstruct 3D architectures of molecular assemblies with near-isotropic resolution, which has proven particularly valuable for studying stratified structures like focal adhesions, nuclear pores, or microvilli. Moreover, iPALM is compatible with the genetically encoded photoactivatable proteins used in PALM, making it suitable for live-cell or fixed-cell studies, depending on experimental conditions.

However, the complexity of the iPALM setup, which requires interferometric alignment, precise calibration, and a specialized sample chamber, limits its accessibility and throughput. The method also typically involves lower acquisition speed and is more susceptible to sample-induced aberrations compared to other approaches, making its application in living samples very difficult. In Kanchanawong et al., 2010 they used iPALM to describe the axial organization of FA proteins in fixed cells. They have revealed that FAs are organized into nanoscale vertical layers, bringing us closer to understanding function and dynamics of this macromolecular structure in 3D. Of course, to fully understand these concepts, it is necessary to study them in living cells.

6. 2. Supercritical angle fluorescence microscopy (SAF)

A fluorophore can be modeled like a dipolar emitter radiating in the far field. However, this dipole also has a non-propagative near-field component that depends on the surrounding refractive index n_m. In the presence of an interface with a medium with a refractive index lower than that of the glass interface ($n_g > n_m$), the transmitted light follows the Snell-Descartes law of refraction (Figure 18a). The refracted light is emitted within a cone that is defined by the critical angle $\theta_c=\arcsin(n_m/n_g)$. This part of the refracted light is called under-critical angle fluorescence (UAF). However, if the distance between the interface and the fluorophore is smaller than the wavelength of the fluorescence (λ_{em}), an additional emission is observed. This emission is called SAF (super-critical angle fluorescence). This type of emission can be detected for fluorophores in a cellular medium, which are located close to the coverslip (within ~100-200 nm). The SAF emission can contain as much as 50% of the emitted light when the fluorophore is directly in contact with the glass interface (Figure 18b).

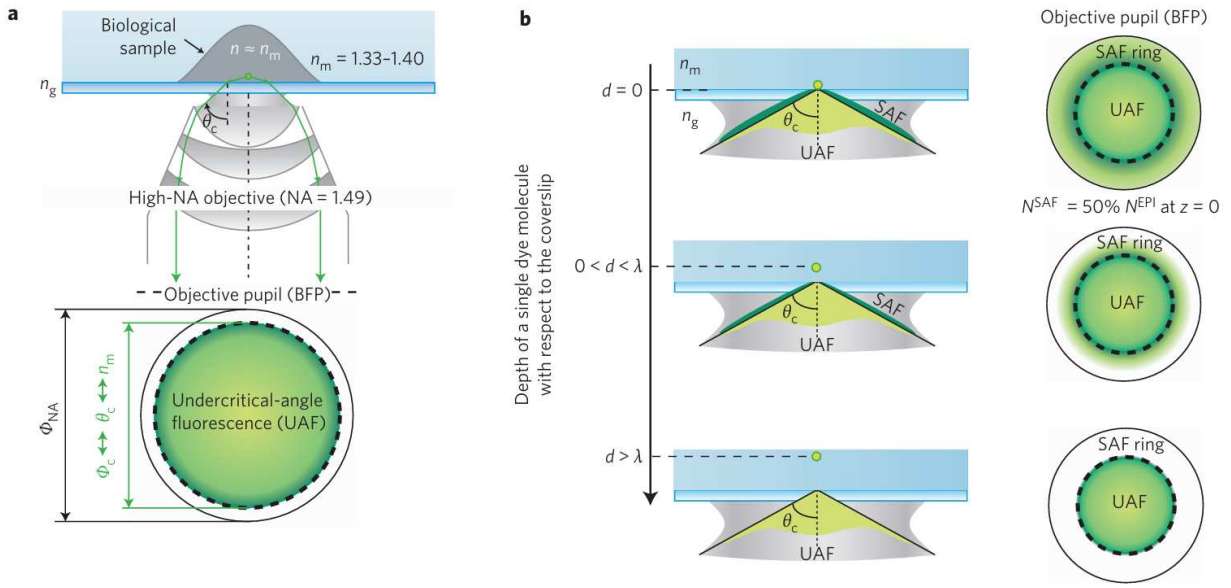

Figure 18. ***SAF principle.*** *(**a**) The far-field emission component (UAF) has an angular distribution which is determined by the law of refraction and limited by the critical angle ϑc. This angular distribution of light can be retrieved on the back focal plane within a plane disk of diameter Φc, which is related to ϑc. (**b**), A position of the near-field component (SAF) of a dye located in the near-field region (between 0 and λem) is collected by the objective beyond ϑc. The number of SAF photons, NSAF, can be as high as 50% of NEPI when the dye is in close proximity to the coverslip and decreases exponentially as the dye depth d increases (Bourg et al., 2015).*

By comparing the ratio between SAF and UAF, it is possible to determine the absolute depth of the fluorophore (Z position in nm). This ratio is called the SAF ratio and decreases with the distance of the fluorophore to the interface (Figure 19). As the result of the depth being measured from the glass coverslip, this value is absolute and therefore the experiments do not require the use of fiducial markers as a reference point in Z (Bourg et al., 2015).

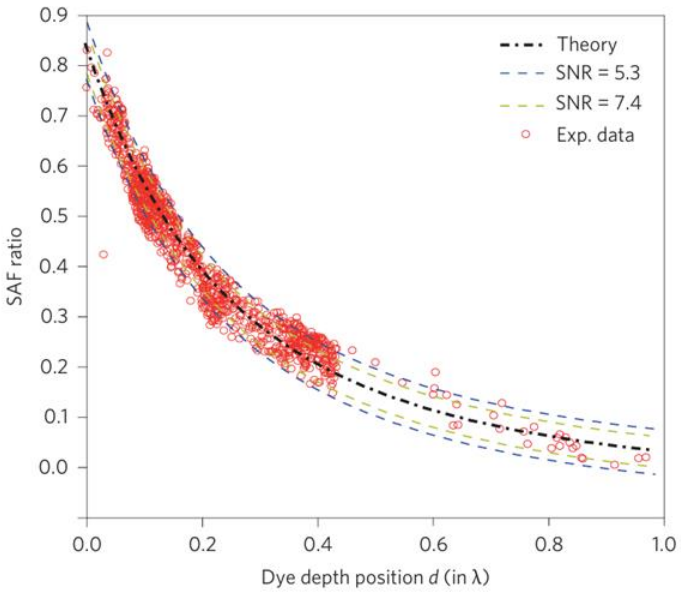

Figure 19. ***Correlation between SAF ratio and dye depth****. Theoretical decay of the SAF ratio (black line) as a function of dye depth d for n_m=1.33 and n_g=1.515. A total of 5,000 iterations of a Monte Carlo simulation of this theory were performed for two different SNRs: 5.30 (blue error line) and 7.43 (green error line) (Bourg et al., 2015).*

SAF microscopy offers a key advantage in its ability to selectively detect fluorophores located in the vicinity of the coverslip interface. This makes it particularly suitable for studying membrane-associated structures such as focal adhesions, vesicle docking, or receptor clustering.

In our team, SAF microscopy was applied to study the axial distribution and immobilization behavior of kindlin in focal adhesions. In this context, Orré et al. (2021) showed that kindlin become immobilized within FAs with prior lateral diffusion along the plasma membrane contrary to talin molecules that are recruited directly from the cytosol. This conclusion was made by the use of SAF imaging as well as single-molecule tracking. This finding highlighted a previously underappreciated recruitment pathway and demonstrated the power of SAF in resolving protein behavior within the critical ~100 nm region near the coverslip interface where FAs form. In fact, SAF can be coupled with single-molecule localization techniques to gain both spatial and dynamic insight into protein behavior, which is why I chose it as a first technique towards 3D tracking in living cells.

However, SAF does have limitations. Its axial selectivity decreases with increasing fluorophore distance from the interface, and SAF detection requires specialized optics to collect high-angle emission. Additionally, compared to interferometric or multi-plane approaches, SAF lacks z-

positioning above ~150 nm, making it less suitable for imaging deeper cellular regions. It is also sensitive to refractive index mismatches and is often difficult to reproduce as the calibration is very sensitive. More on this topic will be presented in the results section.

6. 3. Astigmatism coupled with super resolution

Astigmatism is a widely adopted optical strategy to extend single-molecule localization microscopy (SMLM) into three dimensions by encoding the axial (z) position of fluorescent emitters into the shape of the point spread function (PSF). The method, first demonstrated by Huang et al., 2008, involves the insertion of a cylindrical lens into the emission path, which introduces astigmatism to the optical system. As a result, the PSF becomes elliptical-elongated along the x or y axis depending on whether the molecule is positioned above or below the focal plane. By fitting these asymmetric PSFs with calibrated models, the 3D coordinates of each fluorophore can be retrieved with nanometric precision (Huang et al., 2008)

This approach is relatively straightforward to implement on conventional widefield or TIRF-based SMLM. In typical configurations, astigmatism yields a lateral resolution of ~20 nm and axial localization precision in the range of 40–50 nm (Oudjedi et al., 2016) and an axial depth of ~800 nm (Izeddin et al., 2012a). However, limitations include a trade-off in signal-to-noise ratio due to PSF elongation, particularly when imaging dim emitters. Precise calibration using fiducials is also essential to maintain accuracy over the entire axial range, as compared to SAF where the axial value is absolute. Additionally, axial localization precision tends to be lower than lateral precision and can degrade with optical aberrations or sample depth.

Nevertheless, this approach is compatible with live-cell imaging, and provides robust performance for high-throughput 3D localization. It supports rapid acquisition speeds and is compatible with a wide range of fluorophores. This is why, in the recent years, our team has started to implement astigmatism coupled with sptPALM in order to track FA proteins in living cells in 3D.

6. 4. Minimal fluorescence photon fluxes (MINFLUX)

MINFLUX (Minimal Fluorescence Photon Fluxes) represents a recent advancement in single-molecule localization with nanometer precision, although it differs fundamentally from

traditional SMLM techniques like PALM or STORM. Instead of localizing single emitters by fitting diffraction-limited PSFs, MINFLUX relies on a donut-shaped excitation beam with a central intensity minimum that is scanned near the fluorophore. By triangulating the molecule's position based on where the least fluorescence is emitted, it achieves localization precisions of 1-3 nm using significantly fewer photons than camera-based methods (Schmidt et al., 2021). This results in superior spatial and temporal resolution, enabling tracking of individual molecules with temporal resolution below 100 µs.

Despite its remarkable resolution, MINFLUX presents several limitations. It is very low throughput as one can only detect one molecule after the other. Its implementation requires complex hardware with nanometer-precision beam steering and real-time feedback, making it technically demanding and less accessible than conventional SMLM. The method is optimized for a small field of view and is most effective when the rough positions of fluorophores are already known, which restricts its use in densely labeled samples or large-scale structural mapping. Moreover, due to its high price, it is not available to many researchers. Nevertheless, MINFLUX excels in applications requiring ultra-high precision and fast temporal sampling, making it particularly promising for studying dynamic protein behaviors at the nanoscale.

MINFLUX offers an exciting opportunity to probe the nanometer-scale movements and conformational changes of force-sensitive proteins like talin or integrin in living cells. Its ability to resolve both fast dynamics and subtle structural transitions opens the door for future exploration of mechanotransduction processes at unprecedented spatiotemporal resolution, which is why our team has recently started a collaboration on this topic. We performed some preliminary experiments with the company Abberior, and another part of the team has been working on tracking in live cells in collaboration with Muller team (ETH Zurich).

7. Accessing protein orientation via super resolution

Determining the orientational organization at the molecular level is crucial for understanding many biological processes, including talin mechanotransduction code. Accessing single-domain orientation provides a powerful way to infer talin's conformation, since force-induced unfolding

leads to angular rearrangements that control partner binding and signaling outcomes (Brasselet and Alonso, 2024).

Over the past couple of decades, there have been many efforts to improve and perfect polarization microscopy methods. These methods, ranging from ensemble to single-molecule 3D orientation and localization, provide a way to obtain information on how matter is structured and organized (Kress et al., 2011; Rimoli et al., 2022; Curcio et al., 2020; Brasselet and Alonso, 2024; Bruggeman et al., 2024). First, let's start with understanding the principles of polarization microscopy.

7. 1. Principles of polarization microscopy

Polarization microscopy is an optical imaging method that exploits the anisotropic interaction between polarized light and molecular transition dipoles. In fluorescence the probability of a fluorophore being excited depends on the orientation of its transition dipole relative to the electric field vector of the light. Similarly, when a fluorophore emits light, the orientation of its transition dipole will determine the electric field vector orientation of the emitted light. This fundamental property allows polarization microscopy to reveal molecular orientation and rotational dynamics, two features closely related to structure, mechanical state, and functional organization within biological systems (Brosseau and Dogariu, 2006).

By analyzing how fluorescence intensity varies with the orientation of polarized light, polarization microscopy can probe the orientation distribution of molecules, whether they are fixed, aligned, or rotating freely. This includes not only measuring the average orientation of dipoles but also their wobble, or degree of angular freedom, which can reflect how strongly a molecule is mechanically constrained in its environment. The ability to accurately determine molecular orientation critically depends on the use of rigidly bound fluorescent reporters. Flexible linkers or loosely attached fluorophores can undergo rapid rotational motion, leading to signal averaging that obscures true dipole orientation, which is why it is crucial to develop protein constructs with rigidly bound fluorescent reporters (Brasselet and Alonso, 2024; Martins et al., 2025). Schematic representation of the angular distribution f(Ω)**,** including mean dipole direction and wobble, is shown in Figure 20.

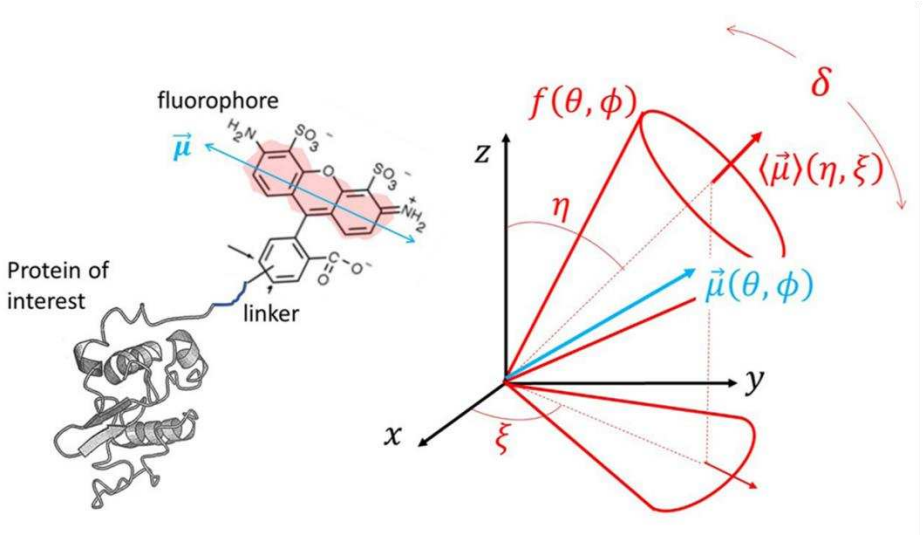

Figure 20. ***Schematic representation of a molecular angular distribution f(Ω), showing the mean orientation and angular spread (wobble).*** *Adapted from (Brasselet and Alonso, 2024).*

Depending on the spatial and temporal resolution, polarization microscopy can operate in either ensemble or single-molecule regimes, with each providing complementary information. While ensemble approaches assess collective orientation over many molecules in a diffraction-limited volume, single-molecule polarization techniques enable precise measurements of individual dipole orientations. Together, these approaches contribute to a detailed understanding of molecular organization and mechanics within cells and tissues (Brasselet and Alonso, 2024).

7. 2. Ensemble polarization microscopy

Ensemble polarization microscopy probes the average orientation and ordering of many molecular dipoles within each local imaging volume of the sample. This modality does not resolve single molecules, but it is highly effective for identifying spatial variations in orientational organization across larger biological structures. Typically, polarized excitation light is rotated or modulated, and the changes in fluorescence intensity are used to calculate angular distributions and order parameters at each image location (Florine-Casteel, 1990; Kinosita et al., 1977; Stallinga, 2015).

A commonly used method is linear dichroism imaging, where molecules that are aligned with the excitation polarization absorb more efficiently than those oriented perpendicularly. The resulting contrast reflects the azimuthal orientation of the dipoles in the sample plane. This is especially

useful in studies of cytoskeletal architecture, lipid membrane domains, and aligned extracellular matrix proteins, where local anisotropy indicates structural or mechanical polarity (Réfrégier et al., 2011; Ferrand et al., 2014).

Representative examples of ensemble polarization imaging, including actin, membranes, and microtubule orientation maps, are shown in Figure 21. These highlight the ability of ensemble techniques to provide spatially resolved, color-coded images of molecular order and orientation.

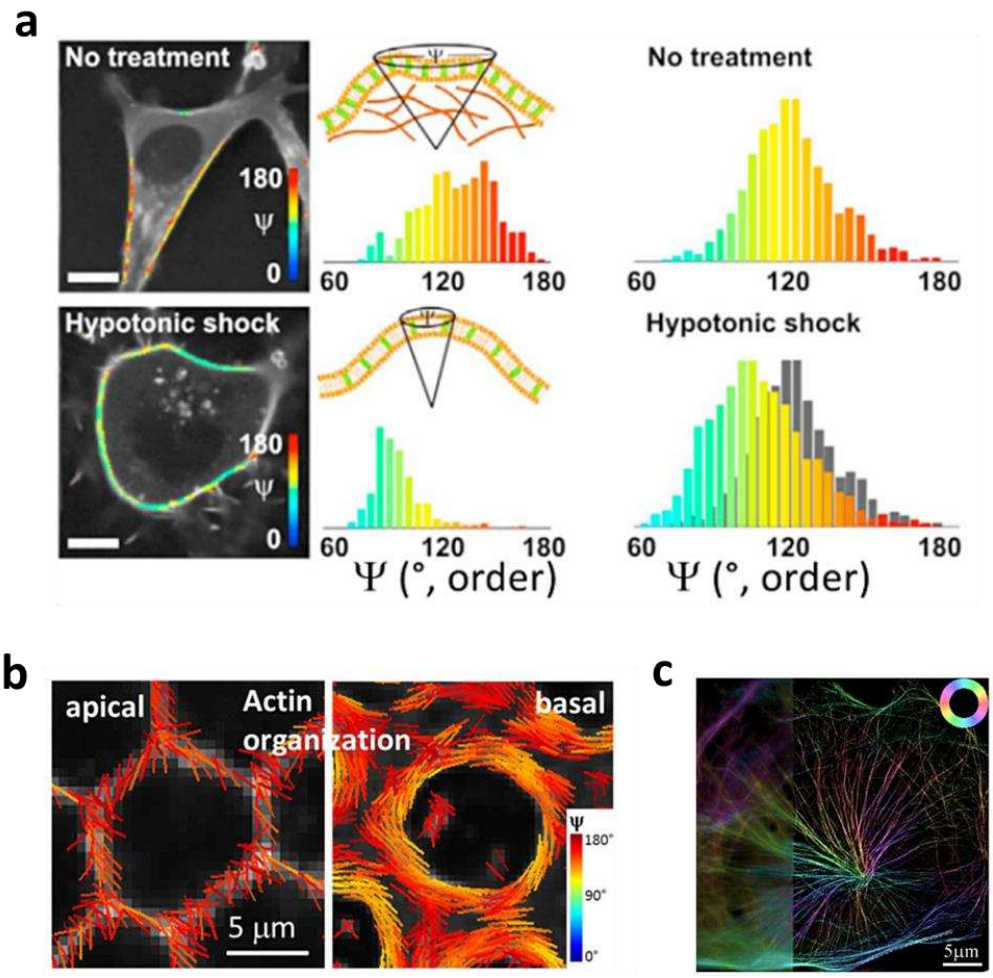

Figure 21. ***Representative examples of ensemble polarization microscopy results****. (**a**) Fluorescence intensity and molecular order map of lipid membranes. (**b**) Orientation mapping of actin filaments in fixed Drosophila embryos. (**c**) Orientation mapping of microtubules in live cells using polarized widefield and pSIM. Adapted from (Kress et al., 2013)-(a), (Mavrakis et al., 2014)-(b), (Zhanghao et al., 2019)-(c).*

Ensemble measurements have been applied to visualize molecular order in filamentous systems such as collagen fibers, actin bundles, and spindle structures, providing functional insights into tissue mechanics and intracellular force distribution. The resulting images are often encoded with

orientation (hue) and order (intensity) to provide intuitive maps of molecular alignment over entire fields of view (Mavrakis et al., 2014; Juanes et al., 2019). Importantly, ensemble techniques are compatible with live-cell and tissue imaging (Martins et al., 2025) and can be extended using polarized structured illumination microscopy (pSIM) to achieve higher spatial resolution (Zhanghao et al., 2019).

Ensemble measurements of integrin orientation have revealed that mechanical activation is not only force-dependent, but also highly sensitive to molecular alignment. Using polarized TIRF microscopy, Nordenfelt et al., 2017 demonstrated that integrin β-subunits adopt distinct angular distributions in the membrane depending on their activation state, with active conformations exhibiting increased tilt relative to the membrane plane. Complementing this, Swaminathan and Gloerich, 2021 proposed that integrins act as directional mechanosensors, preferentially responding to forces aligned with their molecular axis. Together, these findings support the idea that orientation-specific engagement of integrins is a fundamental mechanism by which cells interpret mechanical cues at adhesion sites.

7. 3. Single-molecule orientation and localization microscopy (SMOLM)

Single-molecule orientation and localization microscopy (SMOLM) is a recent advancement that overcomes the spatial averaging of ensemble techniques by analyzing individual fluorescent emitters. SMOLM achieves this by extracting both 3D spatial localization and orientation information from the image of each molecule's emission, typically encoded in the shape of its orientation-dependent point spread function (PSF), or by splitting the signal into four polarized detection channels. This enables not only nanometer-scale resolution in space, but also angular resolution of dipole alignment with degree-level precision (Brosseau and Dogariu, 2006; Rimoli et al., 2022; Stallinga, 2015; Kumar et al., 2025). It has so far been used primarily to describe actin filament orientation. A typical SMOLM result, showing the orientation and wobble of many individual emitters bound to actin, is illustrated in Figure 22.

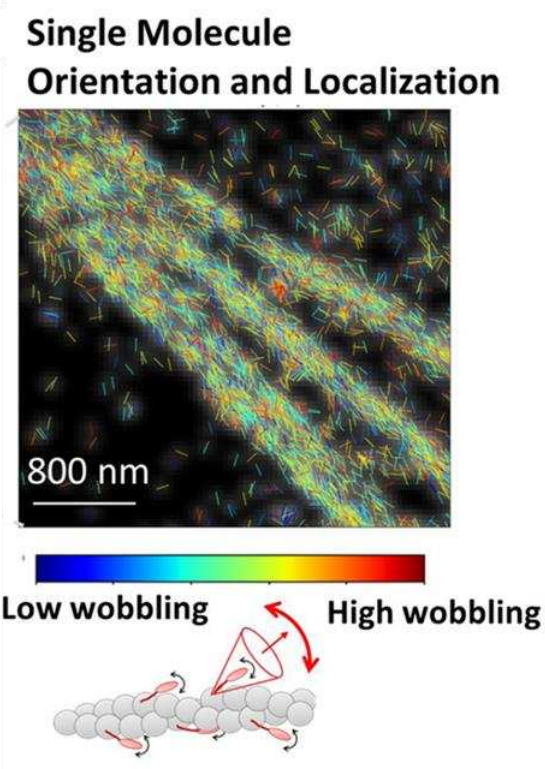

Figure 22. ***Example of single-molecule orientation and localization microscopy (SMOLM) results.*** *Each stick represents an individual molecule, with direction indicating orientation and color encoding wobble. Adapted from (Rimoli et al., 2022).*

In SMOLM, orientation is typically described using the second moment matrix of the dipole orientation distribution. To simplify the interpretation, this matrix is decomposed into a compact set of five Stokes-Gell-Mann parameters, which capture both the mean orientation and the extent of rotational freedom (wobble) (Alonso, 2023; Curcio et al., 2020; Brasselet and Alonso, 2024). These parameters are derived directly from the observed PSFs using basis decomposition methods that remain valid even when molecules are wobbling anisotropically or emitting under non-ideal conditions (Toprak and Selvin, 2007; Brasselet and Alonso, 2024).

A crucial strength of SMOLM lies in its capacity to resolve nanoscale heterogeneity in molecular orientation that would be obscured in ensemble measurements. For example, within a focal adhesion or along a single actin filament, different molecules may adopt different orientations depending on their mechanical loading, binding state, or conformational change. SMOLM enables the detection of these variations, providing insight into how local mechanical conditions affect molecular alignment and structural organization (Juanes et al., 2019; Brasselet and Alonso, 2024).

This level of orientational sensitivity is especially relevant to mechanobiology, where mechanical forces at the molecular scale regulate protein conformation, binding interactions, and cellular signaling. For instance, mechanosensitive proteins such as talin and integrin undergo force-induced conformational changes that involve extension and stretching of structural domains. SMOLM is uniquely suited to detect these changes in live-cell environments, offering a direct readout of mechanical function at the molecular level. It has not, however, yet been applied to integrin or talin in living cells. As SMOLM can be implemented using wide-field detection schemes and tailored PSF engineering, it is compatible with real-time dynamic measurements, including protein turnover, force response, and structural remodeling in adhesion complexes or cytoskeletal assemblies (Brosseau and Dogariu, 2006; Rimoli et al., 2022; Stallinga, 2015; Kumar et al., 2025).

In summary, SMOLM brings a new dimension to fluorescence microscopy by resolving molecular orientation with single-molecule resolution. This capability is transformative for mechanobiology, where structural anisotropy and force-induced alignment are critical to understanding how cells sense and respond to mechanical cues. Its implementation in this thesis aims to expand its application to live-cell force-sensing contexts, where direct measurements of orientation dynamics have not yet been fully explored.

7. 4. Our choice of method

Given the highly organized, force-bearing nature of FAs, studying their molecular orientation at nanometer resolution is crucial to understand how mechanical forces regulate protein structure and function at the single-molecule level. Traditional ensemble polarization techniques provide valuable information on average orientation across large regions but fail to resolve nanoscale heterogeneity, particularly within densely packed structures like FAs, where proteins can experience different mechanical states depending on their position and binding partners. Single-molecule orientation and localization microscopy (SMOLM) uniquely addresses this limitation by resolving the orientation and wobble of individual fluorophores, revealing subtle variations in molecular alignment that would otherwise be obscured. This is especially relevant for proteins such as talin and integrin, which undergo conformational changes and domain stretching under mechanical stress. By using SMOLM, it becomes possible to correlate local orientation with

molecular function, allowing direct readout of conformational states, force-induced alignment, or protein anchoring within adhesions. Furthermore, since focal adhesions integrate multiple signaling and mechanical inputs, being able to monitor orientation at the single-molecule level in live cells offers a powerful tool to dissect how spatially confined molecular mechanics influence adhesion assembly, maturation, and turnover. For these reasons, the implementation of SMOLM in this thesis provides a novel avenue to explore protein orientation dynamics in FAs with unprecedented spatial and angular resolution, extending current capabilities in live-cell mechanobiology and opening new insights into force-regulated molecular behavior.

METHODS

1. Cell lines: maintenance and manipulation

During my thesis, I conducted the vast majority of my experiments using wild type immortalized Mouse Embryonic Fibroblasts (MEFs) provided by M.P. Sheetz from Columbia University, USA. For the purpose of studying the determinants of protein orientation in FAs, we also used MEF Vinculin knock-out (KO) cells. As vinculin is required for cell polarization and migration (Thievessen et al., 2015), using these cells allowed us to study the orientation of talin in absence of vinculin. Both cell lines were cultured in Dulbecco's Modified Eagle's Medium (DMEM) supplemented with 10% non-decomplemented fetal bovine serum (FBS), 1% GlutaMAX supplement, 100 U/mL penicillin-streptomycin, and 15mM HEPES. The cells were grown in 25 cm^2 or 75 cm^2 flasks, depending on the needs, and passaged twice a week to prevent confluence. At each passage, cells were rinsed three times with PBS, detached using a 0.05% trypsin-EDTA solution for 1 to 3 minutes at 37°C (0.5 - 1 mL per flask). Trypsin activity was stopped by adding 5 mL of culture medium. After centrifugation for 5 minutes at 300g, the supernatant was removed, and the cells were resuspended in fresh culture medium, seeded into flasks, and placed in an incubator (37°C, 5% CO_2).

1. 1. Transfection protocols

1. 1. 1. Amaxa nucleofection kit

To transfect MEFs, we most commonly use the Amaxa nucleofection kit (Lonza, MEF kit) following the manufacturer's instructions. Typically, cells are transfected with a plasmid to label the FAs: YFP-Paxillin (1.5 µg DNA for 1 to 2 million cells). Cells are co-transfected with the protein of interest coupled to a fluorescent reporter (typically mEos in my experiments) for single molecule visualization in PALM/sptPALM (4.5 µg DNA for 1 to 2 million cells). We use the MEF T-020 program for electroporation (Lonza protocol). After electroporation, cells are resuspended in a preheated fresh culture medium in a 6-well plate and placed in an incubator (37°C, 5% CO_2).

1. 1. 2. NEON transfection kit

Specifically, for single-molecule fluorescence polarization microscopy experiments, I used the NEON transfection system and their transfection kit. This system requires less cells (100 000

cells/transfection), has a high transfection efficiency (~80%) and high cell viability (~75%). The same plasmids were used, in this case 0.5 µg of the YFP-Paxillin DNA and 2 µg of the DNA for the protein_of_interest-mEos. NEON electroporation protocol for MEFs was used, with the following parameters: tip size - 10µL; pulse voltage (v) = 1350; pulse width (ms) = 30. After electroporation, cells are resuspended in a preheated culture medium in a 12-well plate and placed in an incubator (37°C, 5% CO2).

1. 2. Coverslip preparation

To ensure the cleanliness of the glass coverslips, that is, the absence of fluorescent material and prevent non-specific adsorption, they are cleaned beforehand. They are placed in various sequential baths: nitric acid (65%, overnight), ultrapure water (6 baths of 30 minutes each), and absolute ethanol. Coverslips are then sterilized at 240°C for 8 hours. The day before the acquisitions, coverslips (18 mm in diameter, 170 µm in thickness) are coated with a solution of human fibronectin (Roche) diluted to 10 µg/mL in PBS, and incubated for 1.5 hours at 37°C. They are then rinsed three times with PBS and stored at 37°C until their use.

1. 3. Cell seeding

Cells are seeded on glass coverslips on the day of the acquisitions, typically 24 to 72 hours after transfection. They are rinsed three times with PBS, detached by adding 150 µL (for 12-well plates) or 300 µL (for 6-well plates) of 0.05% trypsin-EDTA solution for 1 to 3 minutes at 37°C. The trypsin activity is then neutralized by adding culture medium (1 or 2 mL). The cells are counted using a Malassez cell, centrifuged for 5 minutes at 300g, and the cell pellet is resuspended in culture media or Ringer solution, depending on the experiment. Ringer solution is a salt-rich medium that mimics extracellular concentrations and provides an optimal environment for imaging. It contains: 150 mM NaCl, 5 mM CaCl2, 1 mM MgCl2, 10 mM HEPES, and 2g/L glucose (11.1 mM). The pH is controlled and maintained at 7.4. For all of my experiments, 50 000 are seeded on fibronectin-coated glass coverslips. After 3 hours of spreading in Ringer, or 1.5 hours in culture medium, the cells can be observed under the microscope. In case the cells were spread in culture medium, the coverslip is washed 1 time with Ringer and then placed in it for imaging. Culture medium cannot be used during imaging due to its strong autofluorescence.

1. 4. Cell fixation

For experiments with fixed cells, I performed chemical fixation using 4% PFA. 3-5h after seeding the cells on the fibronectin-coated coverslips, they were incubated with fixative for 20 minutes at 37 °C in 4% PFA in 1X PBS. After that the cells were washed 3 times with 1X PBS and stored in PBS 1X until further use.

1. 5. Nanobody labeling

To study 3D localization of proteins in FAs using SAF, we performed a co-transfection of RFP-Paxillin (used to label FAs) with protein constructs coupled with a GFP (β3Integrin-K80-GFP-β3 Integrin, GFP-Vinculin, α-actinin-GFP, GFP-CAAX, GFP-Actin and Zyxin-GFP). After fixation, the samples were labeled with a nanobody against GFP labeled either with Alexa Fluor 647 (AF 647), a fluorophore compatible for STORM (provided by Matthieu Sainlos, IINS Bordeaux). The protocol goes as following:

After seeding the cells and fixing them in 4% PFA, the coverslips were incubated in 50 mM NH_4Cl for 15 minutes, and washed 3 times with 1X PBS. Then incubated in Triton X100 0.2% in 1X PBS for 20 minutes, and washed with 1X PBS once again 3 times. Finally, the coverslips were incubated in PBS-BSA 3% for 20 minutes to prevent unspecific binding, after which 3 washings were performed with PBS-BSA 0.2%.

Using cooled centrifuge, the nanobody-AF647 aliquots were centrifuged at maximum speed for 5-10 minutes, to concentrate any impurities in the pellet. The labeling solution was made in PBS-BSA 0.2% at a 100nM working concentration. Coverslips were flipped upside down onto 150 µL of labeling solution on a parafilm sheet and kept at 4 °C overnight. The next day the cells were washed 3 times PBS-BSA 0.2% and 1X PBS respectively.

1. 6. Pharmacological drugs treatment

1. 6. 1. Calyculin A

Isolated from the marine sponge *Discodermia calyx*, Calyculin A (Figure 23) represents a potent inhibitor of protein phosphatases 1 and 2A. Reversible protein threonine/serine phosphorylation regulates numerous cellular functions including cell proliferation, carcinogenesis, apoptosis as

well as muscle contraction (Wakimoto et al., 2002). Inhibiting protein phosphatases 1 and 2A, increases myosin light chain phosphorylation, thereby enhancing actomyosin contractility and inducing a high-tension state in cells. In my experiments, we used Calyculin A to study protein behavior in conditions of increased contractility. Cells were incubated for 30 minutes in 10-20 nM Calyculin A, before cell imaging.

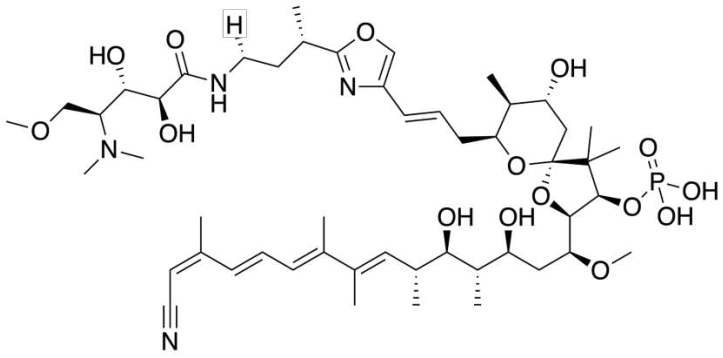

Figure 23. ***CalyculinA structure***

1. 6. 2. RHOK inhibitor Y-27632

Y-27632 (Figure 24) represents a biochemical tool used in the study of the rho-associated protein kinase (ROCK) signaling pathways. Y-27632 selectively inhibits ROCK1, although it does inhibit other protein kinases such as PKCs at higher concentration (Uehata et al., 1997). ROCK1 plays a role in cell motility, metastasis, and angiogenesis (Rath and Olson, 2012). Inhibition of ROCK reduces cell contractility by blocking ROCK-mediated phosphorylation of myosin light chain, thereby impairing actomyosin tension and stress fiber formation. In my experiments, we used a 25 µM solution of Y-27632 to study molecular behavior at lowered contractility. The solution was added 15 minutes before the acquisition and the acquisition was carried out in the same solution to maintain low contractility conditions.

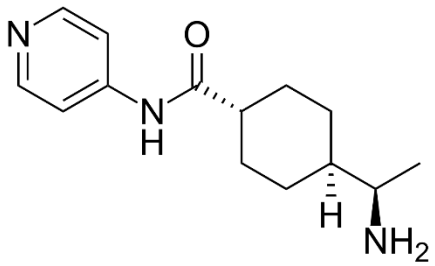

Figure 24. ***Y-27632 structure***

1. 6. 3. Para-amino-blebbistatin

Blebbistatin is a selective inhibitor of non-muscle myosin II ATPase activity, which reduces actomyosin contractility by blocking myosin-driven force generation and stabilizing cells in a low-tension state (Kovács et al., 2004). The initial version of blebbistatin was found not compatible with fluorescence microscopy in living cells due to cytotoxicity of photochemical side-products induced by fluorescence illumination. This is why some derivatives – including para-amino-blebbistatin (Figure 25) were developed. Compared to blebbistatin, para-amino-blebbistatin has better water solubility and photostability, it does not fluoresce and induce a photo-cytotoxic effect on cells (Várkuti et al., 2016). This is why we decided to use para-amino-blebbistatin as a tool to reduce cell contractility. The solution of was added 15 minutes before the acquisition and the acquisition was carried out in the same solution to maintain low contractility conditions. Working concentration was 50 µM.

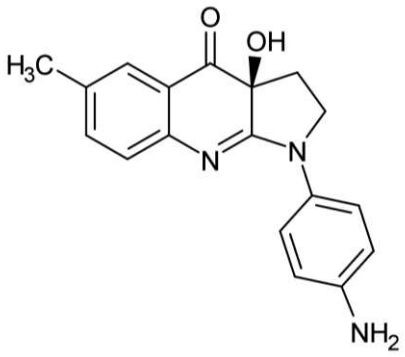

Figure 25. ***Para-amino-blebbistatin structure***

2. SMLM modalities: microscope set-ups and acquisitions, image processing and data analysis

2. 1. Using sptPALM for studying 2D protein dynamics

2. 1. 1. sptPALM microscope and acquisitions

Before the start of the experiment, using a power meter, laser intensities are checked. For the 561 nm laser beam, 5mW is used at the objective output, to allow individual fluorophores to emit

on several consecutive planes and avoid too rapid photobleaching. 1.5 to 3 hours after seeding the cells, the glass coverslip is placed in a Ludin chamber (Life Imaging Services). The chamber is then mounted on a motorized inverted microscope (Nikon Ti) equipped with a 100X oil immersion objective with an NA of 1.49 and a Perfect Focus System (PFS), placed in a chamber whose temperature is set at 37°C. As we imaged protein behavior inside FA that are located at the cell membrane, acquisitions are always done in TIRF, with an area of interest approximately 25 µm by 25 µm.

A typical sptPALM acquisition consisted – in repeating the following sequence 5 times (unless the cell underwent retraction or strong loss of single molecule signals due to photobleaching):

- Recording 20 consecutive images of the YFP signal (50 Hz) to determine the position of FAs and follow their potential displacement over time.
- Recording of 4,000 consecutive images of the photoconverted fluorophore mEos3.2 (50 Hz). To observe the mEos molecules, the 405 nm (Omicron) and 561 nm (Cobolt Jive) lasers are simultaneously used to illuminate the samples. In this way, the 561nm laser excites the fluorescence of proteins photoconverted with 405nm laser. The power of each laser is adjusted to maintain a low density of fluorophores in emission, well separated spatially.

Repeating the cycle more times is possible, however not necessary and potentially harmful. With a total of 20 000 frames and good signal density, we are able to determine the protein localization and reconstruct protein trajectories, without major phototoxicity due to laser illumination on the cells.

Single molecule fluorescence is detected using an EMCCD (charge coupled device, Evolve Photometrics) sensor mounted downstream of a dichroic filter and an emission filter (D101-R561 and F39-617 respectively, Chroma). YFP is visualized using a GFP filter cube (excitation: ET470/40X, dichroic: T495LPXR, emission: ET525/50 Chroma).

2. 1. 2. sptPALM image processing and data analysis

a - Single molecule localization

A commonly used method for super-resolution localization analysis is based on a Gaussian fitting. This consists in fitting the signal from individual fluorophore diffraction spots to a two-dimensional Gaussian curve, involving significant computational times. In our team, we use a

method developed by Jean-Baptiste Sibarita (IINS) (Izeddin et al., 2012b), whose localization accuracy is similar (1 to 4 nm range in their study), with the computational times reduced by a factor of 10. Their approach relies on noise suppression and particle detection by wavelet segmentation of the images. To determine the precise location of each fluorophore, the particle centroid is defined with its central x and y positions. After finding the precise location of each detection, they are all plotted on the same image, forming a super-resolution reconstructed image.

The pointing accuracy of the setup in our lab was measured by the experimental error of repeated localizations of purified mEos proteins which were immobilized on a substrate. Based on this data, the resolution of our system is estimated at between 20 and 50 nm.

b - Single molecule tracking

To be able to obtain trajectories of a molecule's movement, we must be able to track its position in time. When a fluorescent molecule emits fluorescence for a given period of time enabling its detection in consecutive frames, it is possible to reconstruct its trajectory by linking its successive positions. Many factors will limit the duration of tracking as fluorescent molecule can bluish, enter a black state, or diffuse out of focus (Racine et al., 2007). Furthermore, to avoid the incorrect reconnection of trajectories between different molecules, one must define a distance between two localized points from two successive images, beyond which the two detections have to be considered as coming from two different molecules. In the case of our team's setup, we use a 3-pixel limit in low resolution, meaning that the maximum displacement of a molecule between two images (typically 20 ms) is 480 nm. This is why, during the acquisitions, we carefully adapt laser powers in order to have an optimal density of photoconverted molecules to maximize the number of trajectories while avoiding photoactivation of molecules that are too close to each other.

To sort out the different types of molecular motion that proteins adopt, we use the calculation for each reconstructed trajectory of the Mean Square Displacement (MSD) (Chazeau et al., 2014; Rossier et al., 2012; Orré et al., 2021). The MSD represents the evolution of the surface explored by an object as a function of a time interval ($n \cdot \Delta t$). For each trajectory, the MSD is calculated as follows:

$$MSD(t = n \cdot \Delta t) = \frac{\sum_{i=1}^{N-n}(x_{i+n}-x_i)^2+(y_{i+n}-y_i)^2}{N-n}$$ *Equation 1*

Where N is the total number of images of the trajectory, and x and y spatial coordinates of the particle at the time t. To reduce the level of noise in the MSD curves obtained, we restricted our MSD analysis to trajectories longer than 13 points, i.e. 260 ms.

MSDs can be plotted as a function of time, providing information about different modes of motion (Figure 26). For freely diffusing molecules, the MSD increases linearly with time. For confined molecules, the MSD has a linear increase over the first few points, then the slope of the curve decreases over the long term. Lastly, for immobile molecules, the MSD is constant and close to zero. For each trajectory, this regression defining the diffusion behavior is calculated according to the following relationship:

$$MSD(t) = \frac{4r_{conf}^2}{3}(1 - e^{-\frac{t}{\tau}})$$ *Equation 2*

With r_{conf} being the measured confinement radius and τ the time constant $\tau = (r^2_{conf}/3D_{conf})$.

Only the first 80% of MSD points are included for this fitting, as the last points come from the average of fewer data points and are therefore less accurate.

We can then define D, the instantaneous diffusion coefficient as the slope of the linear regression calculated over the first 4 MSD values ($n \cdot \Delta t$ with n ranging from 1 to 4). According to this, we consider trajectories with a $D < 0.011\ \mu m^2 \cdot s^{-1}$ immobile, as they correspond to molecules exploring an area smaller than that defined by the spatial resolution (approx. 0.05 µm²) during the time used to fit the initial slope of the curve (4 points = 80 ms). To distinguish trajectories with free diffusion from those with confined diffusion, we use the constant τ calculated for each trajectory. Thus, trajectories representing free diffusion and confined diffusion events are defined as trajectories for which the time constant τ is respectively less than and greater than half the time interval used to calculate the MSD (i.e. 260 ms/2 = 130 ms).

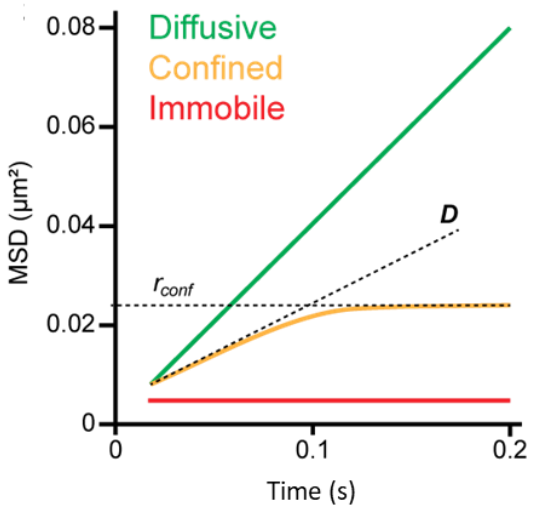

Figure 26. ***Appearance of the MSD curves obtained as a function of the movement behavior after adjustment by regression****.*

To better understand molecular behavior within regions of interest (ROIs), here FAs, we create a binary mask which allows discrimination between detections inside and outside of the ROI. We use a Matlab script developed by C. Leduc and L. Cognet (Laboratoire Photonique, Numérique et Nanosciences, Talence, France). As the same trajectory can contain detections both inside and outside of the ROI, we slice it in such a way as to be clearly classified. This approach was used in our lab (Rossier et al., 2012) to show that integrins diffuse freely outside of FAs and are mostly immobile inside FAs (Figure 27a, c-e) due to their activation by a tripartite fibronectin-integrin-talin interaction. CAAX motif was used as a diffusive control in this case (Figure 27b, c-e). As summarized in this figure, this type of analysis allows us to quantitatively plot the distribution of diffusion coefficients obtained for all the tracked molecules in a given ROI (Figure 27c.) After sorting all tracks into the type of molecular motion they displayed, we can represent tracks with a color-code to represent their dynamic behavior. These composite images overlaying color-coded trajectories on low resolution images of FAs can serve as a valuable visual representation as they highlight predominant molecular dynamic behaviors in subcellular regions (in this case – diffusion outside, and immobilization inside FAs). More quantitatively, we can also calculate the fractions of proteins as a function of their dynamical behavior (Figure 27d), as well as represent the D of diffusive molecules (Figure 27e), to better understand how does the speed of molecules defined as diffusive differ.

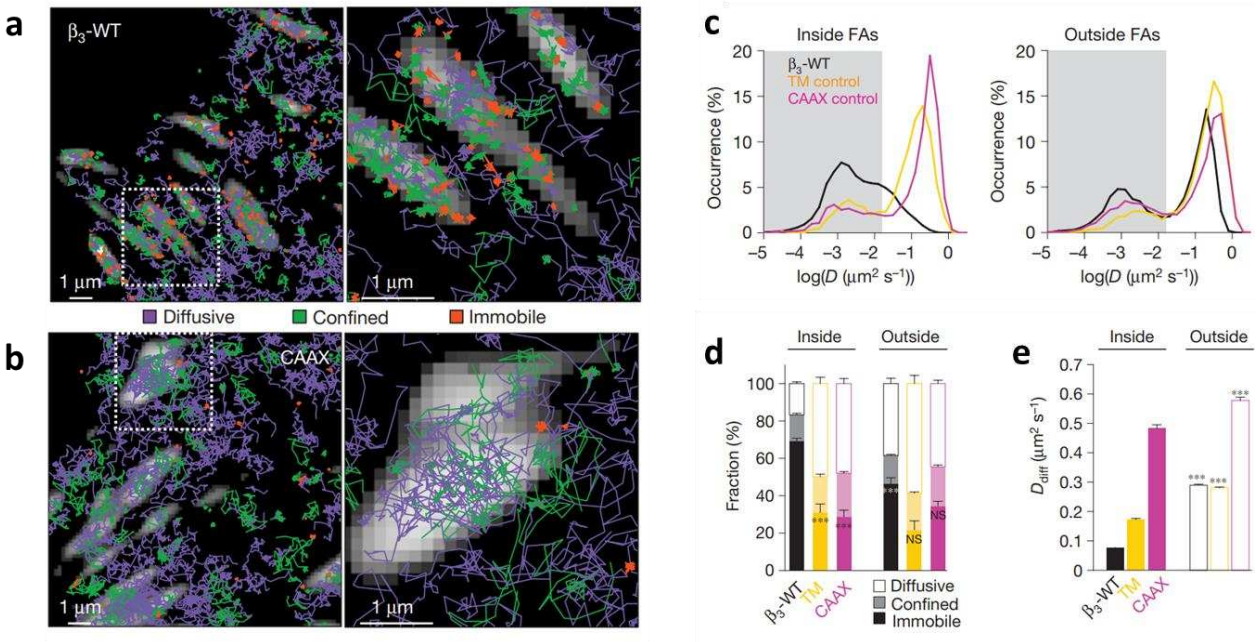

Figure 27. ***Dynamic behavior of integrin molecules described by sptPALM****. (**a**) Representation of integrin β3 integrin trajectories obtained by sptPALM superimposed on the location of FA (greyscale), color-coded by diffusion mode (diffusive, confined, immobile). (**b**) The same type of representation for the diffusive control CAAX (**c**) Logarithmic representation of the distribution of instantaneous diffusion coefficients D for both cases inside (left) and outside (right) FAs. (**d**) Fraction of diffusive, confined and immobile populations inside and outside FAs (mean ± s.e.m. for cells). (**e**) D for free-diffusive events (mean ± s.e.m. for trajectories). Adapted from (Rossier et al., 2012).*

2. 2. Using SAF for measuring 3D protein localization

2. 2. 1. SAF microscope and acquisitions

The setup used for SAF microscopy experiments is the same one used for sptPALM experiments, with the right-side port of the microscope dedicated for SAF detection. The detection path is composed of a SAFe module (Abbelight) and two OrcaFlash4 v3 (Hamamatsu) cameras. All the acquisitions were performed using the NEO software (Abbelight). To achieve single molecule regime in STORM acquisitions, a dedicated buffer (Smart kit, Abbelight) was used. The exposure time was set at 50 ms, optimal timing with the buffer to capture all emitted photons in a single frame.

2. 2. 2. SAF image processing and data analysis

a - Data processing

Processing of the data acquired with SAF microscopy was performed in NEO, an analysis software provided by Abbelight. The processing is based on Gaussian fitting, as for most SMLM techniques. Background signal was removed using a local background subtraction algorithm that estimates and subtracts diffuse fluorescence around each detected molecule prior to Gaussian fitting. After removing the background signal, for each molecule detected, the number of photons collected in the epifluorescence path and in the under-critical angle fluorescence (UAF) path are measured in order to calculate the SAF ratio and therefore extract the corresponding axial position of the molecule. Lateral drifts are corrected from the localized data through a cross correlation-based algorithm. DONALD benefits from the unique property of being free of any axial drift, as the supercritical emission allows one to extract the absolute axial position of the fluorophore regarding the coverslip/sample interface. After processing, we obtain an image of the cell with localizations color-coded in Z (nm) (example given in Figure 28), and are able to save the detections CSV files for further analysis.

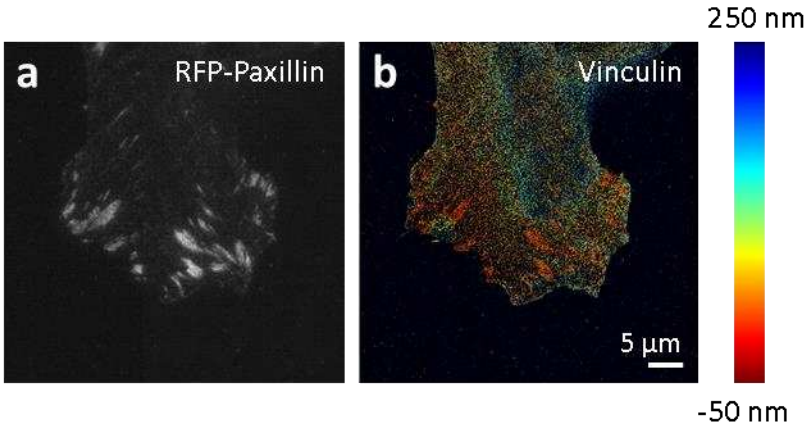

Figure 28. ***Localization of vinculin, color coded in Z (nm), obtained with SAF microscopy and processed with NEO.***

b - Measuring Z position in FAs

Processing of the data acquired with SAF microscopy was performed with NEO software. The latter software mostly provided visualizations tools. In order to obtain quantitative distribution of the z-position of proteins detected inside versus outside FAs, we needed to develop a collaboration with Florian Levet (IINS) that has develop a powerful software platform for point cloud data visualization and quantification called POCA (Levet and Sibarita, 2023). Using an ImageJ plugin created by Florian Levet (IINS), we created binary masks using RFP-Paxillin images

as a FAs reference. These masks were then exported and used in the PoCA software. By applying the mask on the CSV files obtained with the NEO app, we were able to export the Z localization of all molecules found within FAs, plot them and compare the distributions of different proteins under scrutiny.

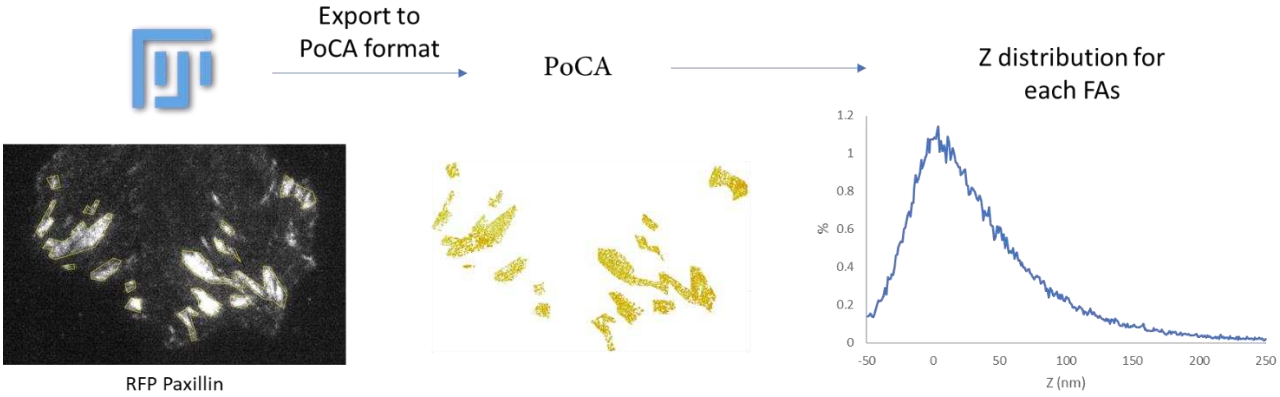

Figure 29. ***Analysis streamline for SAF experiments.*** *SAF-based SMLM data were processed using NEO software to obtain 3D localizations of individual molecules. Binary masks of FAs were generated from RFP-paxillin images using an ImageJ plugin and imported into the PoCA platform (Levet and Sibarita, 2023). These masks were applied to the NEO-generated CSV files to extract and quantify the Z-positions of molecules located specifically within FAs, enabling comparison of axial distributions across different proteins.*

2. 3. Using Polarization microscopy for retrieving protein domain orientation

2. 3. 1. 4polar3D microscope and acquisitions

1-2 hours after seeding the cells in culture medium, the glass coverslip is washed with Ringer then placed in a Ludin chamber. The chamber is then mounted on the 4polar3D microscope available at the Institut Fresnel (S. Brasselet, Marseille) (Kumar et al., 2025).

The 4polar3D microscope used in this work is a total internal reflection fluorescence (TIRF) imaging system, built upon a commercial inverted microscope base (Eclipse Ti2-E, Nikon), with a custom TIRF excitation module and polarization-resolved detection paths. Fluorescence excitation is achieved using a 561 nm continuous-wave laser (Coherent), which is expanded tenfold (GBE10-A, Thorlabs) and subsequently focused at the back focal plane of a high numerical aperture objective (CFI SR HP Apo TIRF 100XC Oil, Nikon) using an achromatic lens (AC254-400-A-ML, Thorlabs). Both the beam expander and focusing lens are mounted on a translation stage, allowing the system to switch between epifluorescence and TIRF illumination.

To compensate for polarization distortions introduced by reflective surfaces, particularly the dichroic mirror (Di01-R405/488/561/635-25x36, Semrock), a pair of achromatic wave plates (AQWP05M-600 and AHWP05M-600, Thorlabs) is inserted upstream of the beam expander. This minimizes photoselection artifacts by preserving the uniformity of the excitation polarization.

The detection side, mounted on the right-side port of the microscope, uses a non-polarizing beam splitter to divide the emitted fluorescence into two paths. Each path contains a 1× relay system composed of achromatic lenses (AC254-150-A-ML and AC508-150-A-ML, Thorlabs), with an adjustable iris placed at the conjugate back focal plane to control the effective numerical aperture. In one of the detection arms, a half-wave plate (AHWP05M-600, Thorlabs) is used to rotate the polarization by 45° relative to the other arm.

Immediately downstream, Wollaston prisms (Quartz Wollaston Polarizer 68-820, Edmund Optics) generate two orthogonal polarization channels per path, resulting in four total polarization-resolved images of the sample at the focal plane (Figure 30).

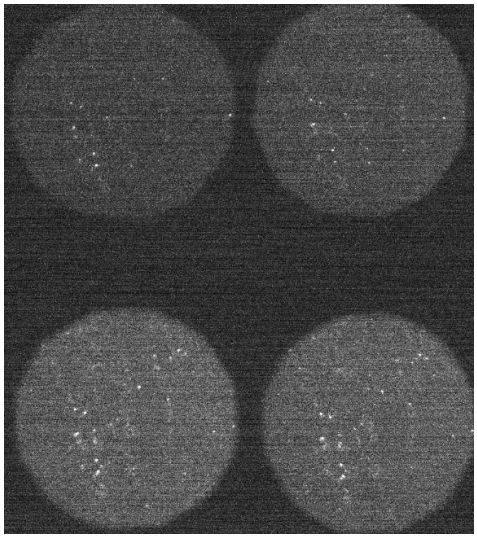

Figure 30. ***Four polarization-resolved images of the sample at the focal plane obtained on a 4polar3D microscope****. Emitted fluorescence is split into two paths by a non-polarizing beam splitter. A half-wave plate in one path rotates the polarization by 45°, and Wollaston prisms in both arms generate two orthogonal polarization channels per path, resulting in four polarization-resolved images at the focal plane. This configuration enables the extraction of single-molecule orientation information.*

These are recombined onto a single sCMOS camera (ORCA-Fusion C14440-20UP, Hamamatsu), operated in ultra-quiet mode with exposure times between 100 and 185 ms. A flip-mounted Bertrand lens is used to image the back focal plane for calibration of the numerical apertures. To

maintain stability during acquisition, the microscope is equipped with a piezoelectric XYZ stage (U-780.DNS, Physik Instrumente) and Nikon's Perfect Focus System (PFS).

A schematic representation of the 4polar3D setup is depicted in Figure 31.

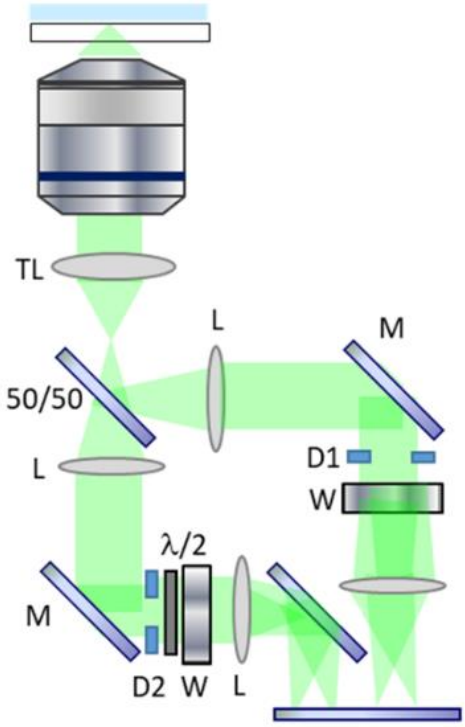

Figure 31. ***Schematic representation of the setup for 4polar3D****. Excitation light (561 nm) is expanded, polarization-corrected using wave plates (λ/2), and focused at the back focal plane of a high-NA TIRF objective (TL) to enable TIRF illumination. Emitted fluorescence is split by a 50/50 non-polarizing beam splitter into two detection arms (D1, D2), each relayed by lenses (L) and directed by mirrors (M). One path includes a half-wave plate to rotate polarization by 45°. Wollaston prisms (W) in both arms separate orthogonal polarization components, yielding four polarization-resolved images projected onto a single sCMOS camera. Abbreviations: TL – objective lens; L – lens; M – mirror; W – Wollaston prism; λ/2 – half-wave plate; D1/D2 – detection paths.*

Acquisitions were done at room temperature due to absence of an environmental chamber around the 4polar3D microscope. For each new cell, a fresh coverslip was taken from the incubator. For both fixed and living cell cases, the aim was acquiring 20 000 frames, at ~ 5.4Hz (185 ms exposure time). The acquisition would be stopped early in case the cell retracted, bleached or ruptured. YFP-Paxillin streams (20 images, 5.4Hz) were taken at the beginning and the end as a reference of the FAs position.

2. 3. 2. 4polar3D image processing

Figure 32 shows how signal looks like during our acquisitions. The arrows depict the polarization direction projection of the four channels (0°, 90°, 45° and 135°).

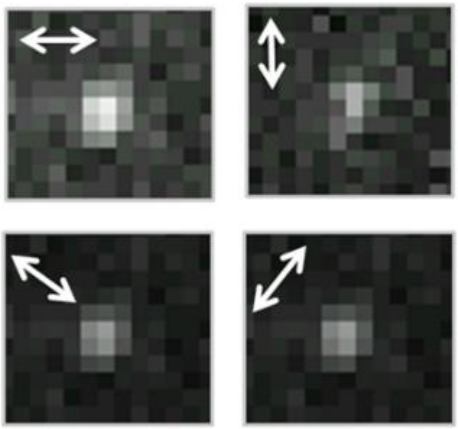

Figure 32. ***Example of four PSFs obtained from a single molecule along the four polarized channels*** *(the arrow represents the polarization direction projection) (0°, 90°, 45° and 135°).*

To analyze the acquired data, we used custom MATLAB scripts. The four polarization-resolved image channels were first aligned using an affine transformation, based on reference images of fluorescent nanobeads. Typically, a field of view containing around 10 fluorescent beads was used to estimate the spatial transformation needed to register the different polarization projections and correct for any geometric distortions. One of the polarization channels served as the reference for this registration procedure, and affine transformations were then applied to the other three channels using functions from the MATLAB Image Processing Toolbox.

The 4polar3D method requires detection of individual molecules across all four polarization projections. Affine registration was directly applied to the single-molecule data during the pairing process, following the approach described in Rimoli et al., 2022, to refine the association of each molecule's polarization-resolved projections. For both nanobeads and single molecules, detection was carried out using the same strategy as in the previously established 4polar method (Rimoli et al., 2022). This method is based on calculating the likelihood of detecting a single-molecule signal above the noise, using a maximum likelihood estimation of the PSF peak within a typical 11×11 pixel window. Although single-molecule PSFs in polarized imaging are known to deviate from symmetric Gaussian profiles, especially in the case of fixed dipoles, this

approximation is sufficient for the detection step, as verified through Monte Carlo simulations by Sophie Brasselet's collaborators.

The pairing of each molecule across the four polarization channels was performed using a vector-based translation estimation between the registered images. This translation vector was determined using high-precision localizations of the detected molecules themselves. A statistical estimation procedure was implemented, using the first 1000 frames of the SMLM acquisition stack, as described in Cruz et al., 2016. All possible pairwise vectors connecting detected molecules across channels were calculated, and the squared norms of differences between all such vectors were computed to build a statistical distribution. Candidate pairs whose vector differences fell below 4.2 times the standard deviation of this distribution were retained. This significance threshold assumes a Gaussian distribution of differences and ensures a 95% confidence level for consistent directionality between matched PSFs.

Molecules were initially paired between the (0°–90°) and (45°–135°) image pairs by selecting the nearest neighbors within a tolerance defined by the localization precision, and using the estimated inter-image vector distance from the reference channel. Final matching of the full four-image sets was performed by linking the two intermediate pairs (from 0° and 45° projections) based on the same vector estimation strategy.

To assess the theoretical limits of localization and orientation precision, the Fisher information matrix and associated Cramér–Rao bound were computed for each detected molecule. These values provided an estimate of the minimum expected uncertainty for each PSF parameter, including the localization precision, across all four polarization projections (Sergé et al., 2008).

Once molecules are detected along the four channels, their parameters (2D localization, background level, PSF radius) are determined. Their intensities are estimated by PSF integration, using a PSF fit based on a Gaussian shape function (Gauss-Newton regression and minimization of a least squares analysis), a symmetric Gaussian function, or a box integration approach. From the four intensities obtained along the four polarized channels, the parameters in-plane orientation (ρ), off-plane orientation (η) and wobbling angle (δ) are estimated for each molecule. The final 4polar3D depicts the parameters as sticks images, using one stick per molecule

detected, whose orientation relative to the horizontal axis is ρ, and whose color is either encoding ρ, η, δ (Figure 33).

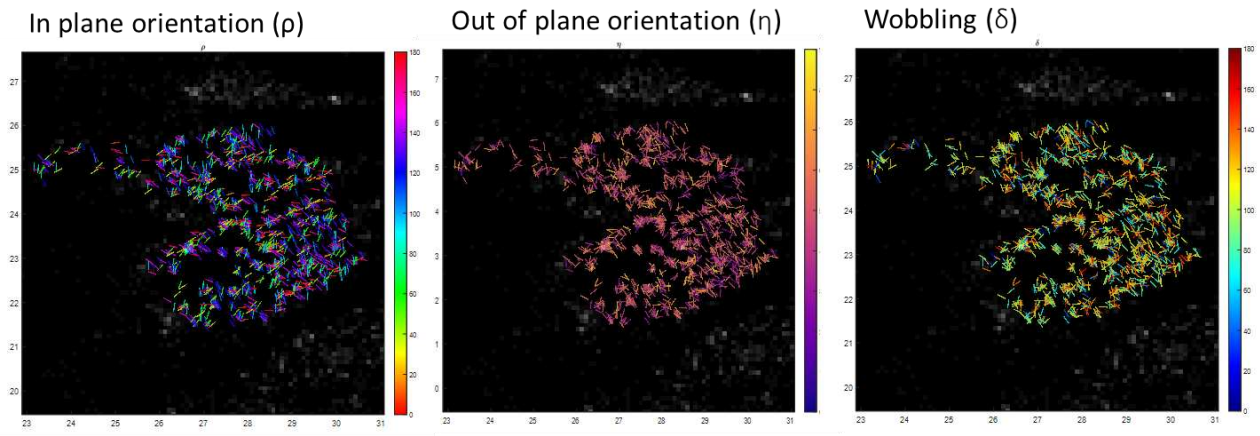

Figure 33. ***4Polar3D output images.*** *Stick figures whose orientation relative to the horizontal axis represents the in-plane orientation (ρ), and which are color-coded to indicate ρ, off-plane orientation (η), and wobbling angle (δ), respectively.*

2. 3. 3. Measuring orientations within FAs

To be able to compare the in-plane orientation (ρ) of molecules detected in different FAs from different cells, we chose to normalize it by rotating it along the mean orientation of the FA. Using ImageJ, we draw for each FA, a line depicting the FA mean orientation and measured the absolute angle. The final 'ρ rotated' was obtained by subtracting the angle of the FA from the raw values ρ measured for each molecule detected. This rotation was necessary only for the in-plane orientation angle ρ, as the off-plane and wobbling angles are not affected by the adhesion orientation.

2. 3. 4. Defining a polarization ratio

In order to interpret and compare how different domains along a protein are differentially oriented, we defined a *polarization ratio* for our reporters of interest that measures orientation anisotropy found in FAs. This ratio was determined from orientation polar distribution by the ratio between the intensity of signal (i.e., number of detections) at the angle where ρ rotated is maximally populated and the signal at the perpendicular angle. When the molecular orientation does not display a preferred orientation, the polarization ratio is close to 1, whereas a distribution with a favored orientation "orientational anisotropy" will give rise to a polarization ratio higher than 1.

RESULTS

1. 3D localization and tracking of focal adhesion proteins: From fixed to live-cell imaging

1. 1. SAF-STORM shows layered Z-organization of focal adhesion proteins in MEF cells

In order to evaluate the 3D capability of a SAF microscope that the lab had acquired, we decided to test whether we could recapitulate the findings from Kanchanawong et al., 2010 that revealed, using an iPALM microscope, that proteins in FAs were organized in superimposed nanolayers with specific set of adhesion proteins associated with distinct FA functions. Contrary to iPALM that used PALM strategy using photoactivation of a genetically encoded mEos reporter, I performed STORM experiments using the SAF modality in order to obtain the Z distribution of proteins inside FAs. To do so, MEFs were co-transfected with a protein of interest labeled with GFP and RFP-paxillin as a FA reporter. Transfected cells were spread for 3-5 hours on fibronectin-coated coverslips in regular cell culture medium with fetal bovine serum to promote FA formation. After fixation, proteins of interest were labeled using a nanobody against GFP coupled with a STORM-compatible organic fluorophore (AF647). Imaging was performed using the Abbelight company STORM solution to induce fluorophore blinking. The following constructs were successfully imaged using SAF modality to retrieve x, y and z-positions: GFP-β3 Integrin (labeled extracellularly at K80), GFP-CAAX (as a membrane label), GFP-Vinculin, GFP-Zyxin, GFP-α-actinin and GFP-actin (3 cells for each protein of interest). Examples of cells imaged are given in Figure 34, with color coding the detected molecule Z-position going from red (-50 nm), to dark blue (250 nm).

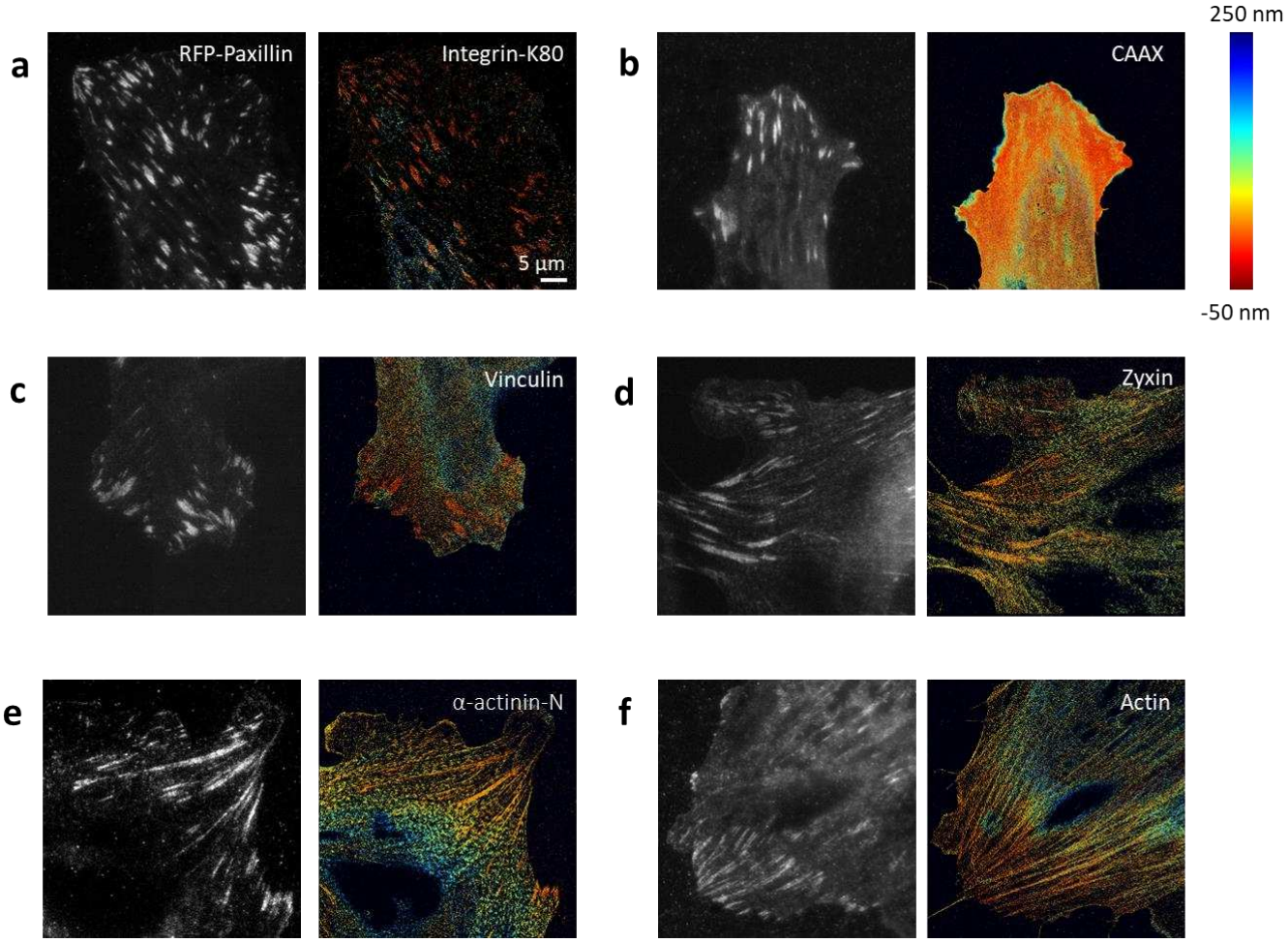

*Figure 34. 3**D SAF-STORM reconstructions of focal adhesion proteins in fixed MEFs**. MEFs were co-transfected with the indicated GFP-tagged protein of interest and RFP–paxillin as a FA marker, plated on fibronectin-coated coverslips for 3–5 h, and fixed. Proteins of interest were immunolabeled with AF647-coupled anti-GFP nanobody. Super-resolution imaging was performed using the SAF-STORM modality (Abbelight), with axial positions determined from SAF/undercritical emission ratios. The resulting Z-positions represent absolute distances from the coverslip–medium interface, with red corresponding to –50 nm and dark blue to 250 nm. In each panel: left, diffraction-limited RFP–paxillin image showing FA morphology; right, corresponding SAF-STORM reconstruction image of the protein of interest whose Z-position is color-coded. (**a**) β3-integrin labeled extracellularly at K80; (**b**) CAAX (membrane anchor); (**c**) vinculin; (**d**) zyxin; (**e**) α-actinin (N-terminal tag); (**f**) actin. Scale bars, 5 µm.*

Using the NEO software, designed and provided by Abbelight to retrieve for each molecule detected its axial position determined from SAF/undercritical emission ratio, I processed data and obtained CSV files containing 3D localizations of proteins of interest. Using the software PoCA (Levet and Sibarita, 2023) combined to a specific plugin designed by our collaborator F. Levet, I defined from RFP-paxillin images, regions of interest (ROIs) around FAs to include only detections inside FAs. I plotted all detections found inside FAs (Figure 35), choosing box plots as they concisely represent the median, interquartile range, and outliers of the Z distributions, enabling

direct comparison of axial spread between proteins, as well as comparing with the distribution obtained by Kanchanawong et al., 2010 using iPALM.

Integrin constructs with GFP label inserted in integrin extracellular domain, display a lowest z-distribution (Z_{mean} ≈ 5 nm) than the one found for CAAX molecules (Z_{mean} ≈ 25 nm), which are anchored to the inner leaflet of the plasma membrane. We see a trend of increasing axial positions, going from integrin, vinculin, zyxin and α-actinin (Z_{mean} ≈ 5, 35, 44 and 52 nm respectively).

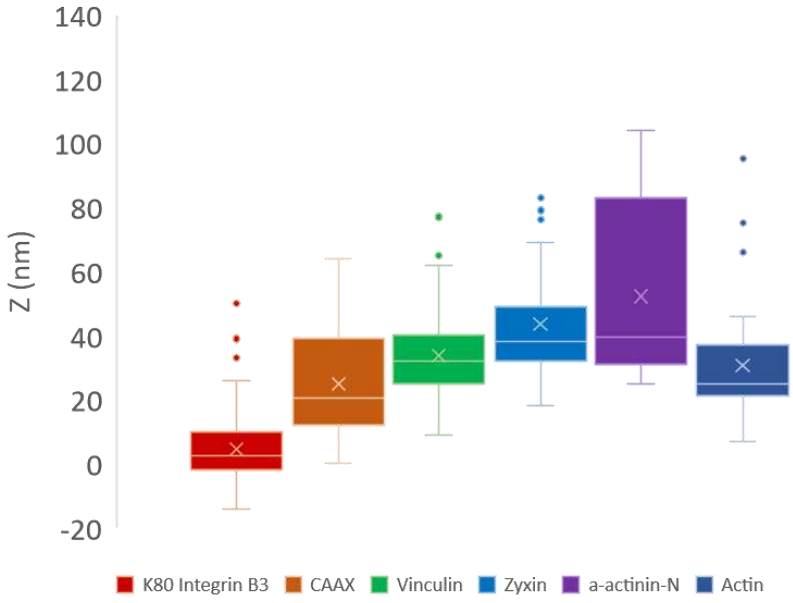

Figure 35. ***Box-plot quantification confirms near-membrane integrin and a progressive Z-rise through vinculin → zyxin → α-actinin.*** *MEFs were prepared and imaged as in Figure 34. 3D localizations inside FAs were selected using PoCA (Levet and Sibarita, 2023) with a custom ROI-selection plugin in ImageJ. Box plots show the median (line), mean (X), interquartile range (box), and whiskers (range within 1.5 × IQR); outliers are plotted individually. Median Z-positions: β3-integrinK80 ≈ 5 nm (n = 80 FAs), CAAX ≈ 25 nm (n = 34), vinculin ≈ 35 nm (n = 91), zyxin ≈ 44 nm (n = 63), α-actinin-N ≈ 52 nm (n = 40), actin ≈ 30 nm (n = 39). Three cells were analyzed for each protein.*

This trend is in line with findings from Kanchanawong et al., 2010 (Figure 36). The Z values (in nm) differ because SAF measures absolute axial positions relative to the coverslip-medium interface, whereas iPALM yields relative axial positions referenced to a calibration plane. Moreover, consistent with the iPALM results, α-actinin in my dataset exhibited a broader axial distribution, with the interquartile range (25–75%) spanning ~52 nm, compared to 12-18 nm for other proteins under scrutiny (Figure 35). The only discrepancy between our observations and

those reported by Kanchanawong et al., 2010 concerns the Z localization of actin. In iPALM measurements, the Z_{centre} of actin was closest to that of α-actinin-C, whereas in our data actin is positioned at $Z_{mean} \approx 30$ nm, placing it closest to the Z_{mean} of zyxin. This difference may arise from their use of U2OS cells, in contrast to the MEF cells used in our study.

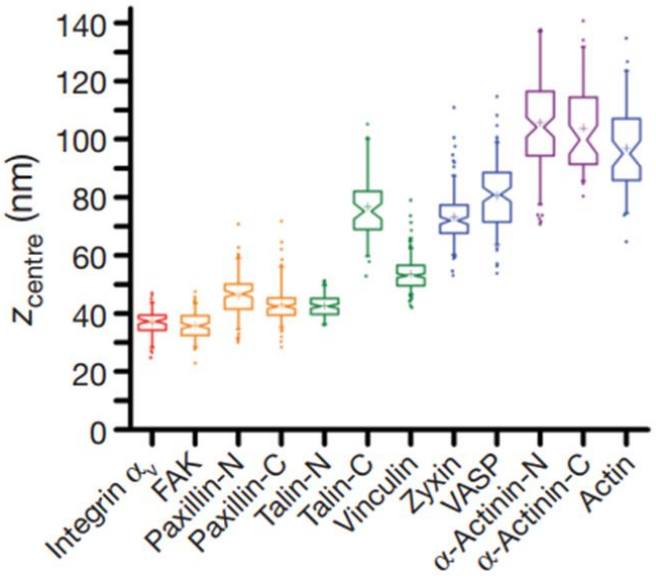

Figure 36. ***Z distributions obtained by iPALM, expressed in nm.*** *Peak position (z_{centre}) of proteins in focal adhesions. Notched boxes, 1st and 3rd quartiles, median and confidence interval; whiskers, 5th and 95th percentiles; +, means, outliers also shown. Adapted from (Kanchanawong et al., 2010).*

These SAF-STORM experiments using fixed samples confirmed a stratified Z-distribution of focal adhesion components, consistent with the vertical architecture described by Kanchanawong et al., 2010. As the ultimate goal was to achieve 3D tracking in living cells, we then combined the PALM strategy using mEos photo-activatable fluorescent proteins with the SAF modality in fixed samples, to assess whether we could reproduce the nanolayered organization observed with the STORM modality. Using a PALM SMLM approach with mEos3.2, we found that genetically encoded fluorescent proteins produced a lower signal-to-noise ratio than organic dyes, which reduced the reliability of SAF ratio measurements. This lower SNR increased the uncertainty in quantifying the relative intensities of the SAF and undercritical emission components, leading to noisier estimations of molecular Z-positions. As a result, the axial localization precision was insufficient to resolve the nanolayered organization of focal adhesions, in contrast to the results obtained with the brighter organic fluorophores.

1. 2. A new labeling protocol provides bright single-molecule signal for live-cell 3D imaging

Because of the sub-optimal photophysical properties of encoded fluorescent proteins (mEos) mentioned above, we decided to move onto other protein labeling approaches which can lead us to uncovering the 3D localization and tracking of proteins in living cells. To do so, we focused on testing different live protein-labeling strategies with bright organic dyes. As potential candidates, we decided to investigate protein labeling with Halo or SNAP tags. Halo-Tag and SNAP-tag are self-labeling protein tags that enable specific and covalent attachment of synthetic probes to proteins of interest in living cells. Halo Tag, derived from a modified haloalkane dehalogenase, reacts with chloroalkane ligands, while SNAP-tag, based on human O^6-alkylguanine-DNA alkyl transferase, reacts with O6-benzylguanine derivatives. These tags have diverse applications, including protein localization and tracking in living cells when chloroalkane ligands or O6-benzylguanine derivatives are functionalized with organic fluorophores (Hoelzel and Zhang, 2020; Cook et al., 2023; Cole, 2013).

In order to test these self-labeling protein strategies in the context of cell adhesion, I used various focal adhesion protein constructs already available in our team carrying either Halo or SNAP tags, including: Talin-Halo, Talin-SNAP, Talin-Halo-SNAP, Halo-CAAX, SNAP-CAAX, SNAP-Kindlin2, Halo-Kindlin2 and Lifeact-Halo. Thanks to our collaborator Luke Lavis (Janelia Research Campus, Virginia, USA), we had access to a wide set of bright and photostable organic fluorophores called JaneliaFluors (JF) to test. These JaneliaFluors were functionalized with either Halo or SNAP-reactive ligands. Moreover they were modified into photoactivatable versions for PALM strategy (PA-JF549-SNAP, PA-JF647-SNAP, PA-JF549-Halo, PA-JF647-Halo) or into self-blinking dyes (JF549b-Halo, JF646b-Halo and JFX650b-Halo) suitable for live STORM imaging as it does not require specific STORM solution often detrimental for live-cell conditions.

The initial protocol for labeling Halo or SNAP tags with JaneliaFluors consisted of incubating already spread living cells with the cell permeable Halo- or SNAP reactive fluorophores (Concentration 100 nM in Ringer solution) right before the experiment during 30-60 minutes followed by three 30 min washing and rinsing steps (Grimm et al., 2017). Halo or SNAP-tagged proteins were co-transfected with YFP-paxillin to detect focal adhesions. With this “in situ”

strategy of labeling, we observe a lot of fluorescent background due to unbound ligands floating inside cells and unspecific labeling onto the coverslips' surface as well as in cell internal organelles (Figure 37). In the case of talin tagged with Halo or SNAP for instance, we could observe in some instances increased fluorescent labeling inside focal adhesions but that was partially masked due to the strong fluorescent background. To avoid unspecific labeling which will prevent precise localization and tracking of specific proteins, I tested alternative labeling protocols which could provide more specific labeling to provide higher contrast.

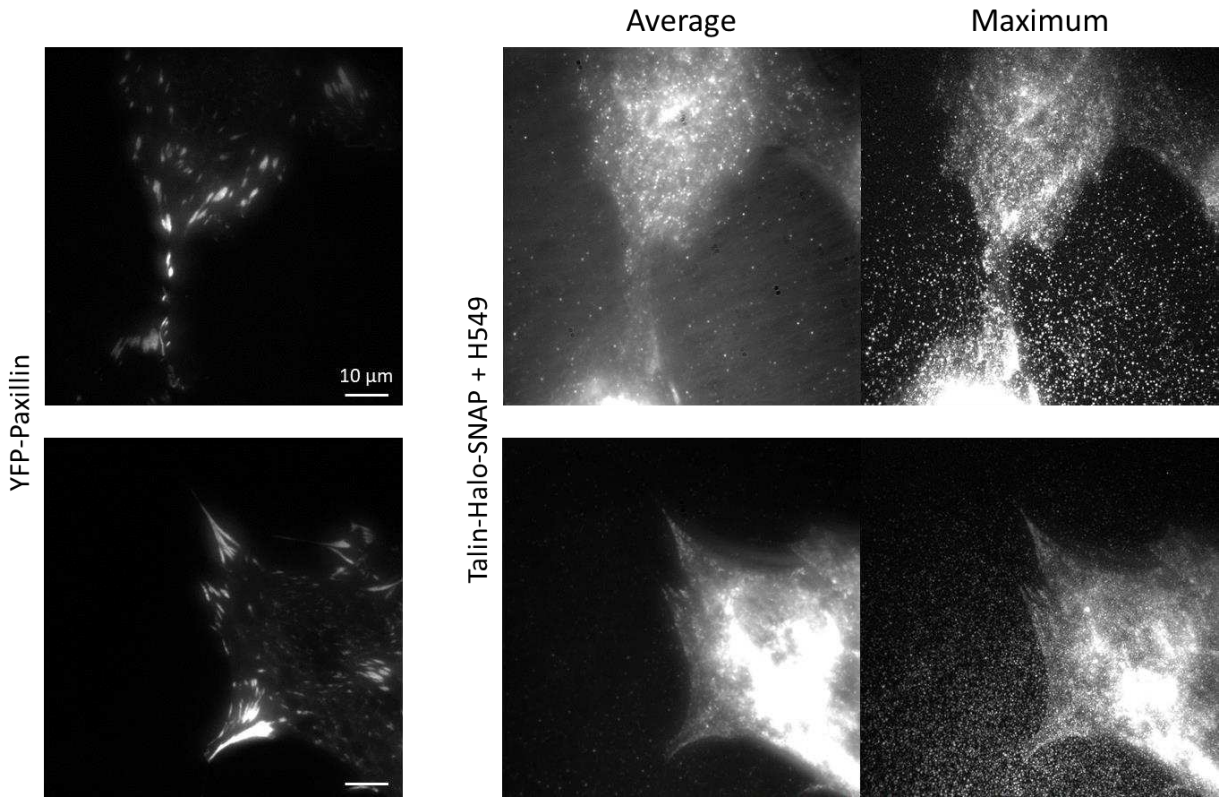

Figure 37. ***High background from "in situ" labeling of Halo/SNAP-tagged talin with Janelia Fluor dyes.*** *MEFs co-expressing YFP–paxillin (FA marker, left panel) and Talin-Halo-SNAP (right panel) were labeled with Janelia Fluor H549 for 30 min immediately before imaging ("in situ" protocol). Images show average and maximum-intensity projections from an 80 s sptPALM acquisition (20 ms exposure time) performed in TIRF. This short-incubation approach results in strong background from unbound fluorophores and non-specific labeling, preventing single-molecule resolution. Scale bar: 10 µm.*

Instead of labeling proteins with JF dyes just prior to imaging, I decided to incubate the fluorophores with transfected cells still in culture, the day before the experiment, allowing for optimal cell penetration and reaction of JF dyes with proteins of interest. Then the next day, we proceed as normally with cell seeding onto our fibronectin-coated coverslips. My hypothesis for

developing this protocol was that the cell preparation protocol (rinsing + enzymatic trypsin-based detachment + resuspension) constitutes an extended washing step allowing to rinse the labeling solution, but more importantly permitting unreacted dyes to diffuse out from cells' cytosol and hopefully get rid of all unreacted dyes. Different timing and duration of labeling were tested: labeling solution was applied either immediately after transfection or on the following day for an overnight or a 2-4h duration. After doing so, I concluded that the best signal to noise ratio is achieved if the following protocol is followed:

48h before the imaging experiment, cells were transfected. 24h later, labeling solution (100 nM) in pre-warmed (37 ˚C) culture medium was added to cells in culture. Cells were incubated at 37 ˚C with 5% CO_2 for 2-4h. Labeling could be extended overnight in the same conditions (37 ˚C, 5% CO_2) if it is a construct that shows lower labeling degree. After the incubation step, labeling medium was replaced with fresh pre-warmed regular culture medium until the next day. Then on the day of imaging experiment we prepare cells following the regular cell preparation protocol with cell washing, trypsin-induced detachment and cell plating onto FN-coated coverslips.

Compared to the “in situ” labeling (Figure 37), this new strategy clearly improved the issue of unspecific labeling at the coverslips’ surface as we could not anymore detect fluorescent dyes adsorbed on the glass surface. Similar improvement was also found for unspecific labeling of internal cell organelles suggesting our strategy allows unreacted dyes initially trapped in recycling organelles to be released with time. Thanks to these improvements, it became possible to perform live single molecule detection enabling both localization (Figure 38) and tracking (Figure 39) of proteins.

To assess our labeling protocol specificity in single molecule imaging and tracking, we first compared super-resolved reconstructed images of talin in focal adhesions obtained by single molecule PALM imaging of talin-Halo-SNAP or talin-Halo labeled with JF dyes following either the “in situ” or the optimized protocol (Figure 38). As a reference we used talin fused to a genetically encoded fluorescent protein (Talin-Cterm-mEos3.2) previously used in our lab to define the dynamic organization of talin in focal adhesions (Rossier et al., 2012; Orré et al., 2021).

When Talin-Halo-SNAP was labeled with JF H549 under the optimized protocol, we observed a strong enrichment of localizations in FA regions, with clear single-molecule signal and well-

defined trajectories suitable for sptPALM analysis (Figure 38b). By contrast, the in-situ protocol generated higher background, with a noticeable population of fast-diffusing signals outside of FAs, consistent with unbound or non-specifically bound dye molecules.

A similar comparison with the Talin-Halo construct (Figure 38c, d) confirmed that the optimized 2 h incubation protocol produced images with higher FA contrast and reduced cytoplasmic noise compared to the in situ labeling, enabling more robust detection of bound talin molecules. In particular, the optimized protocol consistently yielded sharper FA outlines and fewer spurious tracks in the background regions, indicating improved labeling specificity.

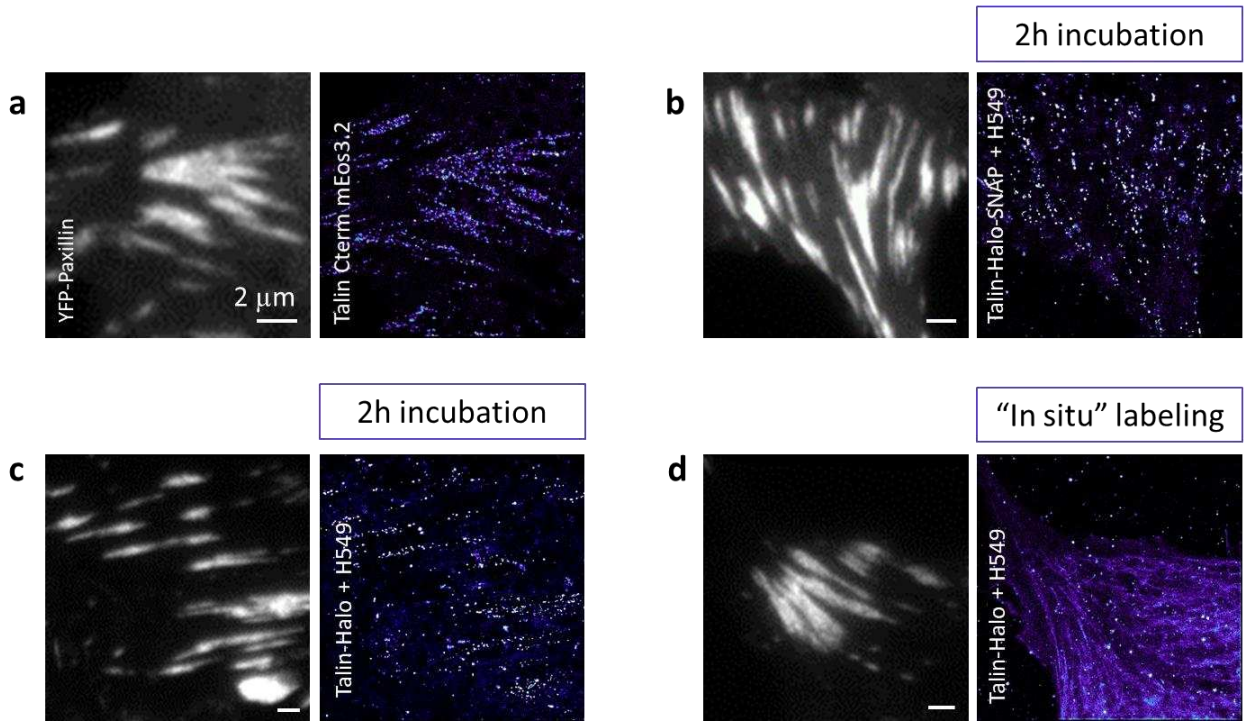

Figure 38. ***Comparison of labeling strategies for single-molecule imaging of talin inside focal adhesions.*** *MEFs co-expressing YFP–paxillin (FA marker; left panels) and the indicated talin constructs (right panels), were labeled with Janelia Fluor H549 via Halo or Halo–SNAP tags. Super-resolution reconstructions were obtained from 400 s sptPALM acquisitions in TIRF. (**a**) Control Talin-Cterm–mEos3.2; (**b**) Talin-Halo-SNAP labeled with JF-H549 using the optimized protocol (2 h incubation, 24 h before imaging); (**c**) Talin-Halo labeled with JF-H549 using the optimized protocol; (**d**) Talin-Halo labeled "in situ" (30 min before imaging). Optimized pre-incubation labeling yields lower background and clear single-molecule localizations compared to "in situ" labeling. Scale bar: 2 µm.*

To validate whether our optimized labeling protocol effectively eliminates unreacted JF dyes from the cytosol, we compared the dynamic behavior of talin constructs against the well-established Talin-Cterm-mEos3.2 control. As expected, the reference mEos3.2 construct displayed dynamics dominated by immobilized molecules within focal adhesions, consistent with

previous reports of talin anchoring at these sites. In contrast, under the “in situ” labeling protocol, Talin-Halo-SNAP generated such a high density of fluorescent signals that tracking was not feasible, due to extensive trajectory overlap and reconnection between distinct entities. For Talin-Halo labeled in situ, tracking was technically possible, but the vast majority of trajectories were highly diffusive (Figure 39). This behavior indicates poor removal of unbound JF dyes, which appear as fast-diffusing entities in the cytoplasm and obscure the genuine dynamics of talin.

When applying the optimized 2 h incubation protocol, the behavior of both Halo-tagged constructs changed markedly. For Talin-Halo, the diffusion profile inverted: immobile trajectories became the predominant population, with reduced presence of the fast-diffusing pool, approaching the dynamic signature of the mEos3.2 control. For Talin-Halo-SNAP, although a small residual diffusive population persisted, the optimized protocol yielded clear, trackable single-molecule signals and a diffusion distribution much closer to the control. The improvement with Talin-Halo-SNAP was particularly noteworthy because the in-situ protocol had previously rendered this construct unusable for tracking.

Altogether, these results demonstrate that the optimized labeling protocol effectively reduces the background of unreacted dyes, diminishes the artifactual diffusive pool, and restores a dynamic behavior more consistent with the well-validated mEos3.2-tagged talin control.

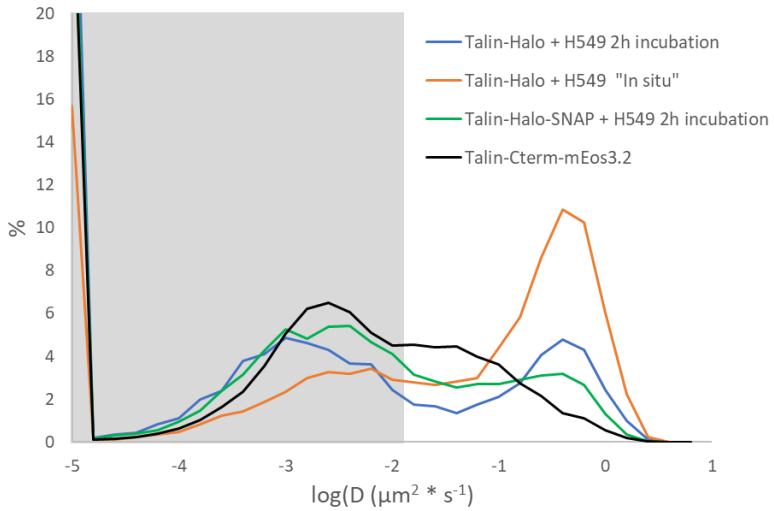

Figure 39. ***Optimized pre-incubation labeling normalizes talin dynamics; “in situ” labeling significantly increases diffusion.*** *Diffusion coefficient distributions (log scale) of talin constructs labeled “in situ” (30 min before imaging) or with the optimized protocol (2 h incubation, 24 h before imaging), compared to control Talin-Cterm-mEos3.2. Grey area indicates immobile trajectories (D < 0.008 µm² s⁻¹). Number of cells: Talin-Halo + H549 (2 h), n = 7; Talin-Halo +*

H549 ("in situ"), n = 3; Talin-Halo-SNAP + H549 (2 h), n = 7; Talin-Cterm–mEos3.2, n = 6. Optimized labeling reduces excessive diffusion and restores dynamics closer to the mEos3.2 control.

The new labeling protocol, based on pre-incubation 24 hours before imaging, enabled low-background, high-contrast single-molecule detection of Halo/SNAP-tagged constructs and restored dynamic behavior comparable to established controls. Importantly, by harnessing the superior properties of JF dyes - namely their enhanced brightness, photostability, and longer fluorescence lifetimes compared to fluorescent proteins, this protocol provides a more robust and durable labeling strategy. As a result, it is particularly well-suited for demanding live-cell 3D single-molecule imaging applications

1. 3. Successful implementation of 3D tracking in living cells using astigmatism and optimized labeling

The optimized labeling protocol described above became the starting point towards 3D tracking of talin in living cells in our lab. For proof-of-principle experiments, I selected the Talin-Halo-SNAP construct labeled with JF-H549 in MEFs. As shown in Figure 38Figure 38 and Figure 39, this dual-tag construct combined with the optimized pre-incubation strategy provided high-contrast single-molecule signal and reliable tracking performance, in contrast to the suboptimal behavior observed with Talin-Halo or with "in situ" labeling. Teaming up with Tianchi Chen, a post-doc in the lab, we implemented astigmatism-based sptPALM, a technique that allows 3D tracking through PSF deformation by a cylindrical lens (Izeddin et al., 2012). This modality provides the axial position of detected molecules with ~50 nm accuracy.

Leveraging the brightness and stability of JF dyes, we were able to establish two complementary acquisition regimes that reveal distinct aspects of talin dynamics. Under fast tracking conditions (20 mW at 50 Hz (20 ms exposure)), we captured rapid molecular behaviors and transient immobilization events. By contrast, under slow tracking conditions (2 mW at 2 Hz (500 ms exposure)), we obtained exceptionally long trajectories, which revealed immobilization phases followed by slow retrograde flows of talin, consistent with previously reported dynamics. Together, these results highlight the versatility of our labeling and imaging strategy, which can resolve both fast immobilization events and extended slow molecular motions within living cells (Figure 40Figure 40).

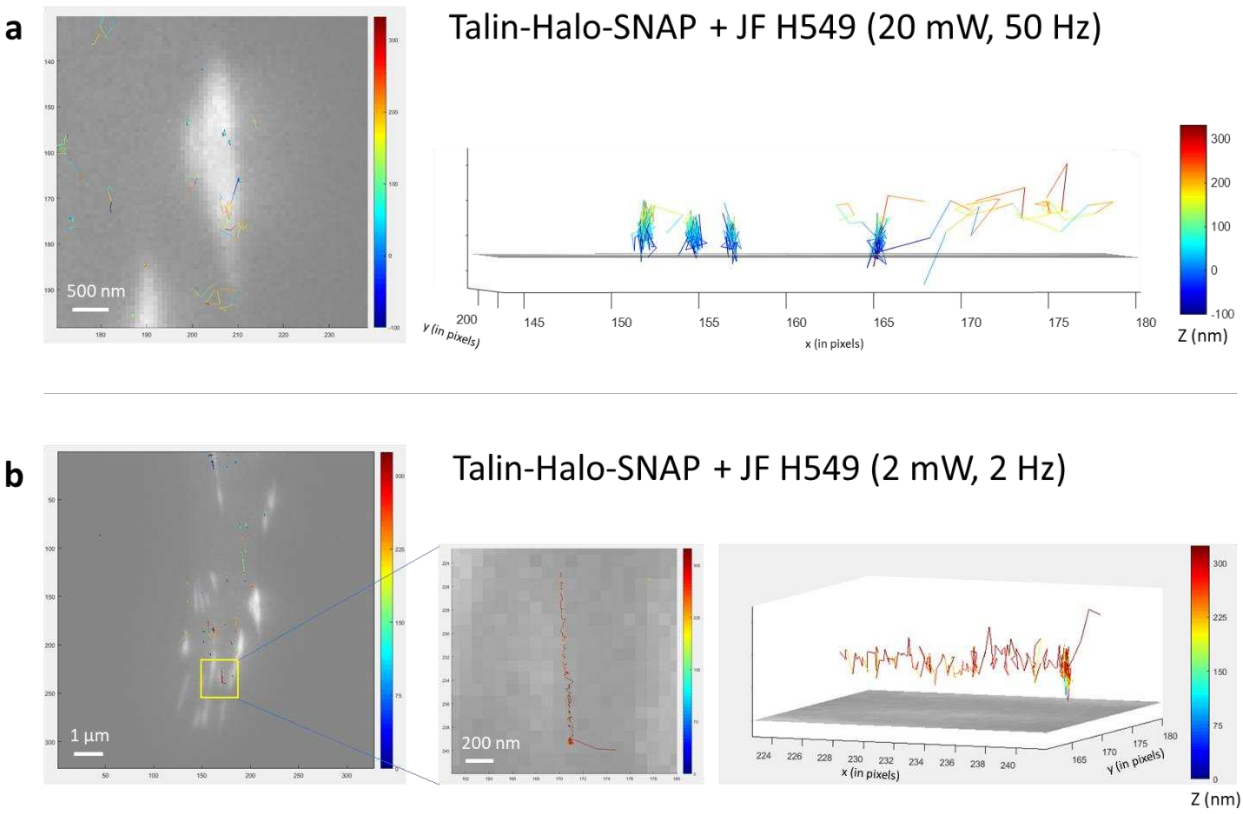

*Figure 40**. Examples of 3D single-molecule tracking of talin in living cells using astigmatism-based sptPALM with optimized Halo/SNAP labeling.** Two complementary acquisition strategies were used to capture distinct molecular dynamics. (**a**) Fast 3D tracking (20 mW at 50 Hz, 20 ms exposure) reveals color-coded trajectories of Talin-Halo-SNAP labeled with JF-H549, overlaid on a YFP-Paxillin image as a reference for focal adhesions (FAs). Molecules are observed to diffuse at higher Z positions before immobilizing at lower Z planes, indicating recruitment into FA structures. (**b**) Slow 3D tracking (2 mW at 2 Hz, 500 ms exposure) highlights the versatility of the labeling, enabling exceptionally long trajectories. These reveal immobilization phases followed by slow retrograde flows of talin, consistent with previously described dynamics, and demonstrate the ability of JF dyes to capture slow molecular motions over extended time windows. (pixel size = 160 nm).*

By combining astigmatism-based sptPALM with my optimized Halo/SNAP labeling strategy, we achieved the first successful 3D tracking of talin in living cells. This demonstration established a methodological foundation for live-cell single-molecule 3D tracking of focal adhesion proteins. It also laid the groundwork for ongoing efforts to integrate this approach with even higher-resolution techniques such as MINFLUX.

From there, the project was further developed within the lab: additional protein constructs were generated for 3D studies, and our group leader Gregory Giannone, together with Tianchi Chen and a new PhD student, Lorenzo Bergamo, established a collaboration with Daniel Müller's team (ETH Zurich) to adapt this protocol for MINFLUX applications. At that point, my direct

involvement in the 3D tracking line of work was terminated, and I concentrated the remainder of my thesis on developing the 4Polar3D approach.

2. Development and validation of protein constructs designed for polarization experiments

2. 1. Rationale when designing protein constructs for polarization experiments

The accurate determination of molecular orientation in live cells critically depends on the design of protein constructs that carry rigidly bound fluorescent reporters. Flexible linkers or loosely attached fluorophores introduce additional degrees of freedom that decouple the reporter dipole orientation from the orientation of the protein domain itself. In such cases, the retrieved information would primarily reflect the behavior of the fluorophore, not that of the target protein, defeating the purpose of orientation microscopy. Therefore, it is essential to minimize the rotational freedom of the fluorophore relative to its host protein, while preserving the protein's natural conformations and functions (Martins et al., 2025). This requirement is particularly stringent in our context, where the goal is not only structural visualization, but also live single-molecule detection, imaging, and tracking.

Several strategies have historically been employed to achieve rigid labeling. In the case of actin, for example, Rimoli et al., 2022 used 4polar-STORM with phalloidin-AF647, exploiting phalloidin's strong and specific binding to F-actin. While this approach provides highly rigid labeling, its use is limited to fixed samples and is unsuitable for live-cell studies due to phalloidin's toxicity and perturbation of actin dynamics. For live-cell experiments, genetically encoded reporters are preferred, as they allow controlled valency, straightforward expression, and minimal perturbation. In this context, Manos Mavrakis recently demonstrated in live actin studies that fluorescent proteins can be rigidly fused to target proteins. In this work, they developed GFP-based actin orientation reporters optimized for ensemble fluorescence polarization microscopy in living cells (Martins et al., 2025). These constructs incorporate fluorescent proteins with constrained rotational freedom, enabling accurate quantification of actin filament orientation at the population level. While this work demonstrates the feasibility of designing rigidly bound

reporters, it was tailored for ensemble imaging and does not directly extend to single-molecule localization or tracking approaches.

2. 2. Designing protein constructs fused with Eos and constrained Eos

Building on these advances, we designed constructs tailored for my PhD to probe the orientation of proteins central to focal adhesion (FA) mechanotransduction, namely talin, integrins, and actin. The photoconvertible fluorescent protein mEos3.2 was chosen as the reporter because of its brightness, photostability, reduced oligomerization, and suitability for single-molecule localization microscopy (PALM) and single-protein tracking (sptPALM). Importantly, mEos3.2 is also compatible with polarization-sensitive detection, making it an optimal choice for single-molecule orientation localization microscopy (SMOLM).

I will first describe the strategies used for all the constructs we designed and then move onto validation of construct localization and dynamics via sptPALM.

2. 2. 1. Designing Talin constructs for defining orientation of distinct talin domains

As explained in the introduction, due to its importance in the mechanosensitivity of FAs, we want to define the shape that talin proteins adopt inside FAs in different mechanical contexts. To do so, as talin is a large multimodular protein, we decided to insert our fluorescent reporter in several positions along talin scaffold in order to interrogate the orientation of distinct talin segments using polarization experiments. Furthermore, as distinct talin rod domains unfold for different level of forces (Yao et al., 2016), we decided to strategically target specific regions of the talin molecule with distinct sensitivity to force.

Firstly, we have chosen a C-terminus-tagged (“Cterm”) talin as a control. We expected this construct to have a homogenous distribution of orientations, as the label is located at the C-terminus of talin, and the fluorophore itself is not sterically constrained - at least by mechanical engagement of talin. Secondly, we chose to tag the R3 region, as it is the first one to unfold with force around 5pN. Inversely, we wanted to tag the R12 region, as it is one of the last ones to unfold - with forces ~25 pN (Yao et al., 2016). Lastly, we targeted the ‘neck’ of talin, that is, the unstructured region connecting the FERM domain and the rod domain of talin. As an

unstructured region, we expected talin tagged at the neck to reflect the overall orientation of the talin molecule, as it will extend and orient with the main force direction.

To ensure mEos3.2 insertions inside the polypeptide chains do not affect talin function, we collaborated with Ben Goult (University of Liverpool, UK), a structural biologist, expert in talin structure and mechanobiological functions, to define sites of insertion in mouse talin. Indeed when inserting mEos3.2 or any fluorescent reporter in talin, one must pay attention not to insert it in highly conserved regions, nor regions that are folding so that the folding is not disturbed. Furthermore to avoid affecting the mechanobiological unfolding of talin rod domains, we decided, based on all the structural information available, to design insertions in loops between α-helices inside a rod domain. To ensure enough flexibility for domains to fold, we chose to use 4-serines linkers as a conservative start in the initial designs. The insertion sites for the four constructs we designed are the following:

Talin Cterm-mEos3.2 (mEos3.2 at the C-terminus with an 8-serine linker)

Talin Neck-mEos3.2 (mEos3.2 after P470 with 4-serine linkers on both sides)

Talin R3-mEos3.2 (mEos3.2 after P881 with 4-serine linkers on both sides)

Talin R12-mEos3.2 (mEos3.2 after P2226 with 4-serine linkers on both sides)

The summary of insertion sites is shown on the molecular structure of talin in Figure 41.

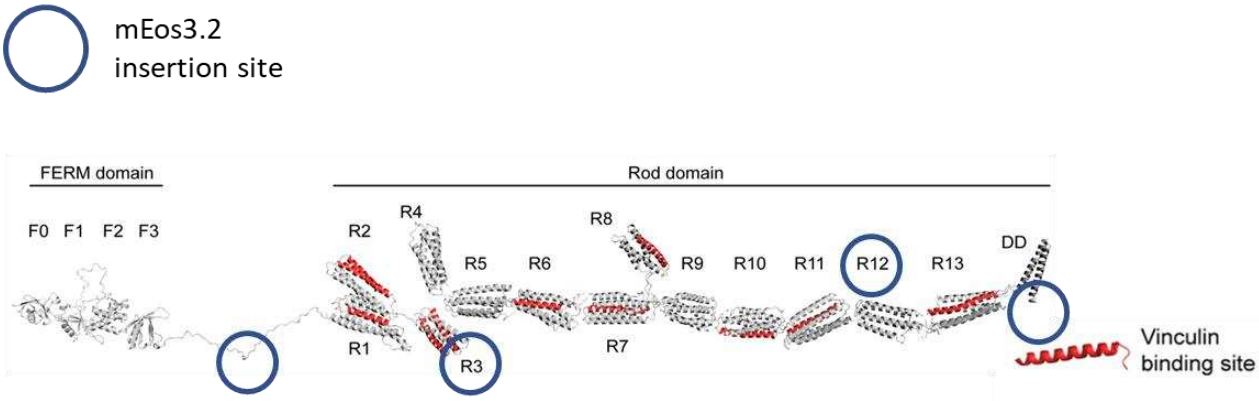

*Figure 41**. Schematic representation of mEos3.2 insertion sites in the talin molecule for polarization microscopy experiments.** Talin constructs were engineered to report protein orientation at specific mechanosensitive regions. Talins with four tagging sites were designed: C-terminal (mEos3.2 fused with an 8-serine linker), Neck (after P470 with 4-serine linkers on both sides of mEos3.2), R3 (after P881 with 4-serine linkers), and R12 (after P2226 with 4-serine linkers). mEos3.2 was chosen for its high photostability and brightness, enabling live-cell single-molecule polarization imaging. Structural model adapted from Goult et al., 2013.*

2. 2. 2. Towards more rigidly bound mEos

With an aim of designing a protein construct with a rigidly bound fluorophore (which can therefore more accurately report protein orientation using 4Polar3D), we initiated a collaboration with Manos Mavrakis (Institut Fresnel, Marseille), a cell biologist with a strong expertise in tailoring genetically encoded reporters of actin filament organization for fluorescence polarization microscopy by constraining the mobility of the fluorescent proteins (Martins et al., 2025). To constrain mobility of mEos3.2, we developed a talin construct tagged at the talin Neck (after P470) with a constrained mEos3.2 and with the removal of 4-serine linkers. During his mEos3.2 truncation screen, Manos Mavrakis concluded that we can remove up to 4 residues from the N-terminus and all 9 residues from the C-terminus of mEos3.2 without losing fluorescence (Figure 42). Therefore, we created Talin-Neck-mEos3.2ΔN4ΔC9 as a more constrained counterpart for Talin Neck-mEos3.2.

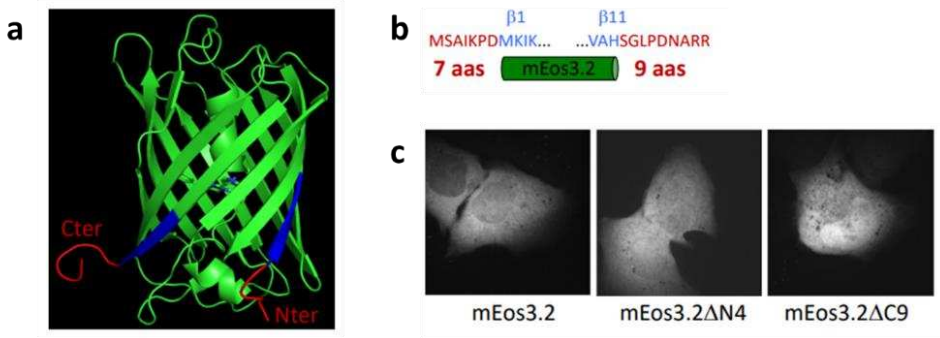

d

	are all CMV:	sequence	fluor
EOS1	mEos3.2	MSAIKPDMKIKLR... AVAHSGLPDNARR β1 β11	+
EOS2	mEos3.2ΔN2	MAIKPDMKIKLR... AVAHSGLPDNARR β1 β11	+
EOS3	mEos3.2ΔN3	MIKPDMKIKLR... AVAHSGLPDNARR β1 β11	+
EOS4	mEos3.2ΔN4	MKPDMKIKLR... AVAHSGLPDNARR β1 β11	+
EOS5	mEos3.2ΔN5	MPDMKIKLR... AVAHSGLPDNARR β1 β11	-
EOS6	mEos3.2ΔN6	MDMKIKLR... AVAHSGLPDNARR β1 β11	-
EOS7	mEos3.2ΔN7	MMKIKLR... AVAHSGLPDNARR β1 β11	-
EOS8	mEos3.2ΔC1	MSAIKPDMKIKLR... AVAHSGLPDNAR β1 β11	+
EOS9	mEos3.2ΔC2	MSAIKPDMKIKLR... AVAHSGLPDNA β1 β11	+
EOS10	mEos3.2ΔC3	MSAIKPDMKIKLR... AVAHSGLPDN β1 β11	+
EOS11	mEos3.2ΔC4	MSAIKPDMKIKLR... AVAHSGLPD β1 β11	+
EOS12	mEos3.2ΔC5	MSAIKPDMKIKLR... AVAHSGLP β1 β11	+
EOS13	mEos3.2ΔC6	MSAIKPDMKIKLR... AVAHSGL β1 β11	+
EOS14	mEos3.2ΔC7	MSAIKPDMKIKLR... AVAHSG β1 β11	+
EOS15	mEos3.2ΔC8	MSAIKPDMKIKLR... AVAHS β1 β11	+
EOS16	mEos3.2ΔC9	MSAIKPDMKIKLR... AVAH β1 β11	+

Figure 42. ***Truncation analysis of mEos3.2 revealing fluorescence retention after N- and C-terminal deletions.*** *(**a**) mEos3.2 structure highlighting C- and N-termini (red) and start of β-barrel (blue). (**b**) Partial amino acid sequence with truncated residues marked in red. (**c**) Fluorescence signal in cells expressing full-length mEos3.2, mEos3.2ΔN4, and mEos3.2ΔC9. (**d**) Summary of fluorescence presence across all truncated variants.*

Of course, these were just preliminary tests to observe presence of fluorescence. To validate whether these constructs were still functional, we studied in living cells, their proper localization inside FAs and performed sptPALM experiments to determine talin dynamics was unaffected

2. 2. 3. Designing Actins constructs for SMLOM

Studying actin orientation is crucial because the geometry and organization of actin filaments directly underlie a range of essential biological processes, including mechanotransduction. In Rimoli et al., 2022 they emphasize that the precise spatial arrangement of actin filaments is a determinant for cell mechanics, which in turn drives processes such as immune responses, tissue development, cell adhesion, and motility. Actin filament alignment and its remodeling in space and time are necessary to understand how cells exert forces, respond to their environment, and coordinate structural changes. Moreover, the orientation and conformational state of actin filaments, beyond just their location, provide critical insights into the functional state of actin assemblies and interactions with proteins like myosin II, integrins, and talin involved in mechanotransduction.

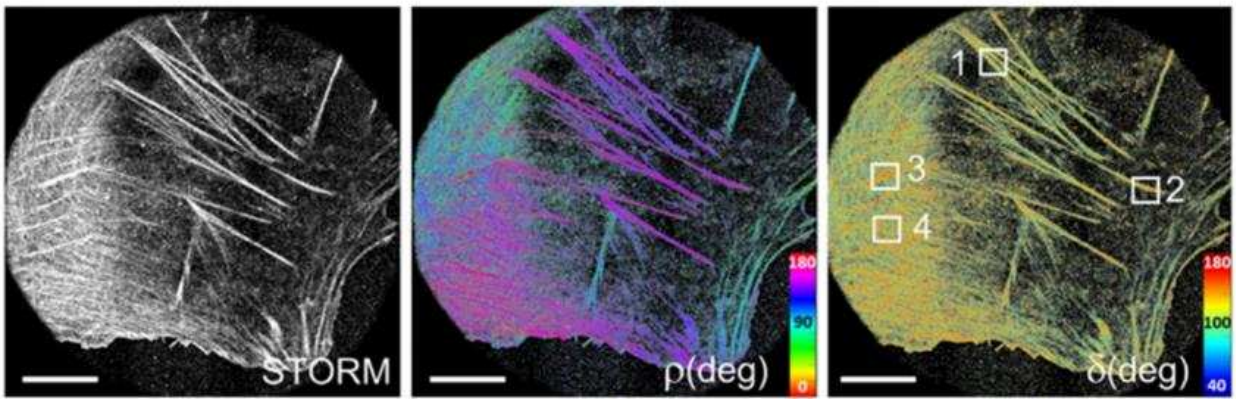

Figure 43. ***Actin fibers orientation obtained with 4-polar STORM****. (left) Wide field view single molecule (AF488) localization STORM image of F-actin labeled with AF-488 phalloidin, (middle) Corresponding 4polar-STORM stick image with color-coded in plane orientation measurements, (right) Corresponding 4polar-STORM stick image with color-coded wobbling angle measurements. Scale bar: 7 μm. (Rimoli et al., 2022)*

In the mentioned paper they studied actin filament organization exclusively with fixed samples using 4-polarSTORM (Figure 43Figure 43). To do so, they used AF488-phalloidin to label F-actin. However, studying actin orientation in living cells is particularly valuable because biological processes involving actin, such as cell migration, force generation, and adhesion turnover, are dynamic and time-sensitive. Observing actin orientation in real-time allows capturing these rapid

changes and understanding how orientation responds to signaling or mechanical cues. Live-cell orientation imaging can provide functional readouts, such as the role of myosin II activity in stress fiber organization, which was shown in this study to directly impact actin filament alignment and 3D orientation. Therefore, accessing to live-cell orientation imaging to study the spatiotemporal dynamics of actin cytoskeletal organization, would enable us to link structure to function in the context of living, responsive systems (Rimoli et al., 2022).

To do so, it was necessary to create actin constructs with a rigidly bound fluorescent reporter compatible with single-molecule live cell imaging. With Manos Mavrakis, we developed two actin reporters for SMLOM with constrained mEos3.2: mEos3.2ΔC8-humanβ-actin and mEos3.2ΔC9-humanβ-actin in which mEos3.2 was shortened at the C-terminus respectively by 8 and 9 amino acids. As in the case of the talin constructs, Manos performed preliminary experiments and concluded that mEos3.2 bound to actin can be shortened by a maximum of 9 AA on the C terminus, while still preserving its fluorescent properties. I proceeded with further testing inside living cells and compare these newly designed reporters to mEos2-βactin, used previously in our team.

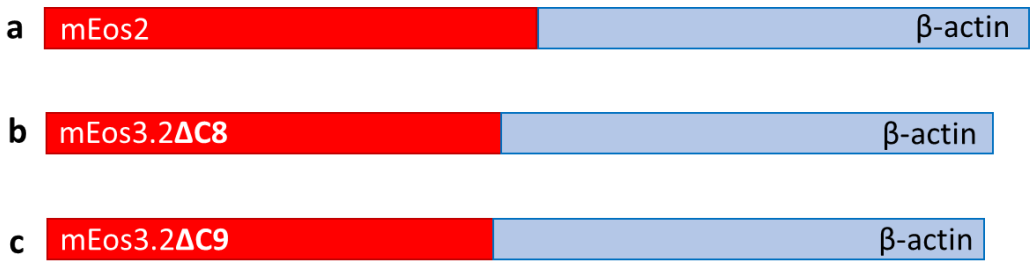

Figure 44. ***Actin constructs developed for polarization microscopy****. Actin constructs were engineered to improve fluorophore rigidity while preserving functional incorporation into filaments. (**a**) mEos2–human β-actin (control; N-terminal fusion). (**b**) mEos3.2ΔC8–human β-actin (C-terminal truncation of mEos3.2 by 8 amino acids). (**c**) mEos3.2ΔC9–human β-actin (C-terminal truncation by 9 amino acids).*

2. 2. 4. Designing integrins for defining conformational changes during activation

As previously mentioned, integrins are transmembrane proteins connecting to the ECM on the extracellular side, and to talin intracellularly (Kanchanawong et al., 2010). As the extracellular domain of integrins undergoes a huge conformational change during activation (Sala et al., 2024; Chen et al., 2024a; Lu et al., 2022), studying its orientation under different levels of contractility could provide new insights linking integrin activation with mechanosensing and

mechanotransduction. For integrins, we therefore focused on designing constructs that can be used to reveal conformational changes of the extracellular domain of integrins.

To this end, with the help of Manos Mavrakis, we developed and optimized integrin constructs to report the orientation of β3-integrin extracellular domain. The starting point for the design was based on insertion of fluorescent reporters within the loop of integrin hybrid domain generated in Wehrle-Haller lab (Soto-Ribeiro et al., 2019).

Specifically, we engineered a mouse integrin fusion protein with full-length mEos3.2 inserted at position K97 (Figure 46Figure 46a), without any linkers, located within the extracellular domain. This region is known to undergo significant conformational rearrangements upon activation (Shattil et al., 2012), making it a promising site for monitoring orientation changes. We hypothesize that C-terminal tagging, due to its flexible cytoplasmic tail, may lead to a more isotropic orientation distribution of the fluorophore. This is why we decided to compare the behavior of the newly made K97 construct with the C-terminally tagged β3-integrin already used in the team (Rossier et al., 2012). A visual comparison of the predicted orientation changes for both the K97- and C-terminally tagged constructs is presented in Figure 45Figure 45.

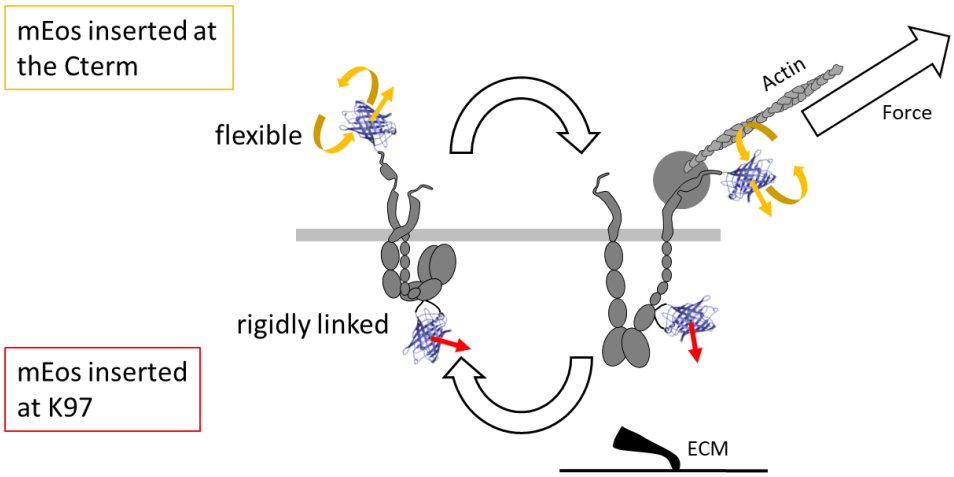

Figure 45. ***Schematic representation of mEos insertion sites on integrin and its significance for conformational change reporting****. Schematic shows β3-integrin in its inactive (bent) and active (extended) conformations. Two labeling strategies are represented: K97 extracellular domain insertion (without linker) of mEos3.2, positioned to track conformational changes upon activation, and C-terminal cytoplasmic tail tagging. Arrows indicate hypothetical fluorophore dipole orientation changes in each configuration. The K97 insertion site is expected to report extracellular domain rearrangements more directly than C-terminal tagging.*

To further increase the rigidity of the fluorescent reporter, and thereby obtain a more accurate proxy for integrin extracellular domain orientation, we also developed integrin constructs incorporating a truncated version of mEos3.2. In these constructs, 8 and 9 amino acids were removed from the N- and C-terminus of mEos3.2, respectively, while maintaining the insertion site at position K97 in the extracellular domain (Figure 46b). To enhance rigidity even further, we engineered additional variants in which we deleted amino acids 98–101 (Figure 46c) and 98–102 (Figure 46d) from the integrin sequence itself, immediately downstream of the insertion site. These modifications were designed to reduce local flexibility around the fluorophore and improve its alignment with the integrin backbone.

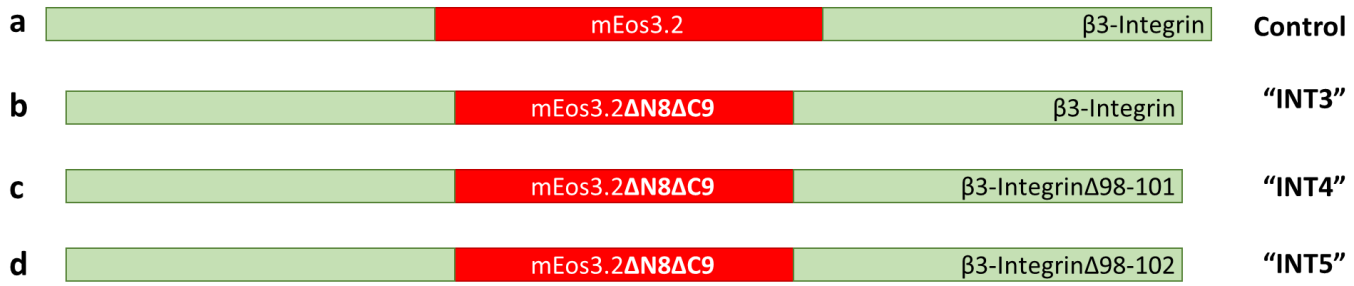

Figure 46. ***Schematic representation of β3-integrin constructs with rigidified mEos3.2 variants for polarization microscopy****. (**a**) β3IntegrinK97-mEos3.2-β3Integrin (full-length mEos3.2 at residue K97, no linker) (**b**) β3IntegrinK97-mEos3.2ΔN8ΔC9-β3Integrin (truncated fluorophore with 8 N-terminal and 9 C-terminal residues deleted). (**c**) β3IntegrinK97-mEos3.2ΔN8ΔC6-β3IntegrinΔ98-101 (additional deletion of integrin residues 98-101 downstream of insertion). (**d**) β3IntegrinK97-mEos3.2ΔN8ΔC6-β3IntegrinΔ98-102 (deletion of residues 98-102) (all mouse integrins).*

As a C-terminus tagged construct for our first polarization experiments, we started using a 6His-β3Integrin-mEos2 (human), a protein construct which was used previously in the team to reveal integrin protein dynamics (Rossier et al., 2012). However, later on, we worked on the development of a mouse form of a C-terminus tagged integrin, to create a more reliable model that respects species context, as we use mouse embryonic fibroblasts (MEFs). These results are shown in Appendix 1.

2. 3. Validation of protein constructs using cellular localization and protein dynamic analysis

To validate the engineered protein constructs for my experiments, we needed to test their fluorescence properties, efficient photoconversion and photoactivation, and correct cellular

localization. Reliable fluorescence is essential to guarantee sufficient signal-to-noise ratios for precise single molecule detection and tracking. Effective photoconversion or photoactivation ensures that individual molecules can be sparsely and selectively visualized over time, which is critical for resolving single-molecule trajectories in densely packed environments. Moreover, correct co-localization of the constructs with the FAs confirms that the proteins maintain their native targeting and functionality, avoiding artifacts that could compromise the biological relevance of the data generated using the newly designed constructs. Together, this dual-validation establish the constructs as robust tools for high-precision single-molecule studies of dynamic processes within the cellular context.

2. 3. 1. Talin constructs show consistent behavior across multiple tagging sites

To investigate the behavior of newly designed talin constructs and assess their suitability for our polarization microscopy orientation studies, we performed single-protein tracking of all four talin constructs after mEos3.2 (full length) photo-activation (sptPALM). MEFs were co-transfected with Talin-mEos3.2 (tagged at the Neck, R3, R12 or C terminus) constructs and YFP-paxillin, as a FA reporter. After a 48h incubation at 37 ˚C, 5% CO_2, cells were spread on fibronectin-coated coverslips in regular medium to promote robust FA formation. After 2-4h of spreading, cells were transferred into a Ringer solution, a salt-rich medium that mimics extracellular concentrations and provides an optimal environment for single molecule imaging. Cells were imaged using total internal reflection fluorescence microscopy (TIRF), allowing selective visualization of the basal membrane where FAs reside.

To validate mEos3.2 photophysical properties were conserved, we used 405nm laser light illumination to induce mEos3.2 photoconversion for all 4 new talin constructs. Using similar laser power for 405nm-induced photoconversion and 561nm for mEos3.2 fluorescence excitation as used in our sptPALM pipeline, we could readily detect numerous single molecule mEos3.2 fluorescent signals (Figure 47). Photoconversion response to 405nm intensity appeared normal and permitted to finely tune the number of photoconverted molecules in the field of view

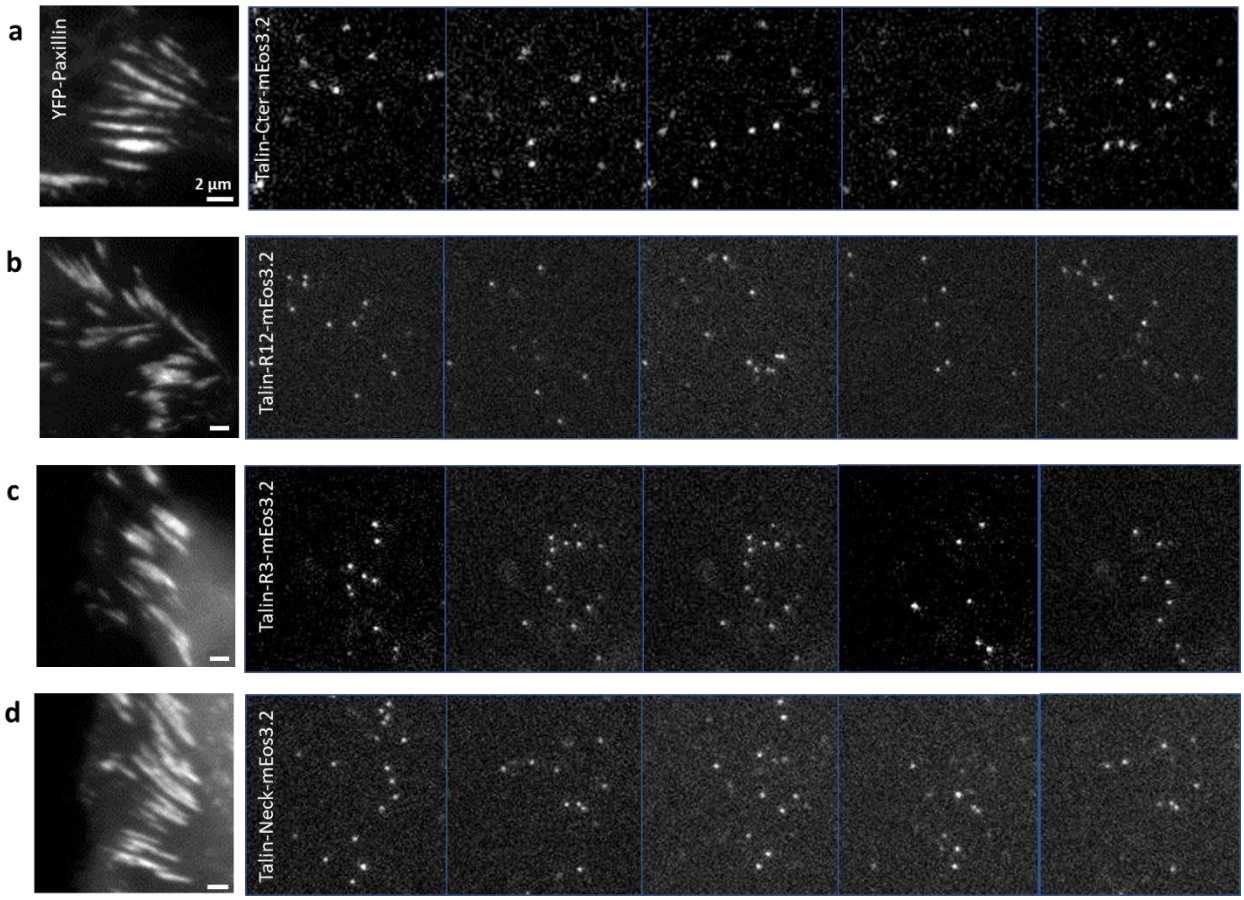

Figure 47. ***Single-particle tracking PALM (sptPALM) acquisition of talin constructs with mEos3.2 at distinct tagging positions show good SNR and sparse detections.*** *MEFs were co-transfected with YFP-paxillin (FA marker) and one of four Talin constructs: Talin-Cterm-mEos3.2 (control) (**a**), -R12-mEos3.2 (**b**), -R3-mEos3.2 (**c**), or -Neck-mEos3.2 (**d**). After 48 h at 37 °C, cells were plated on fibronectin-coated coverslips for 2–4 h, transferred into Ringer's solution, and imaged using TIRF microscopy. Left: YFP-paxillin fluorescence showing FA morphology. Right: representative sptPALM frames (20 ms exposure) of mEos3.2-tagged talins. Scale bar: 2 µm. These acquisitions enabled quantitative mapping of talin dynamics inside and outside FAs.*

Using sparse activation, we reconstructed thousands of talin localizations and trajectories inside and outside FAs (Figure 48). For trajectories lasting at least 260ms (≥13 points), we computed the mean square displacement (MSD), which describes the diffusion properties of a molecule. We sorted trajectories according to their diffusion modes. These diffusion modes are represented with a color coding in Figure 48 on the right side (red-immobile, green-confined, purple-diffusive).

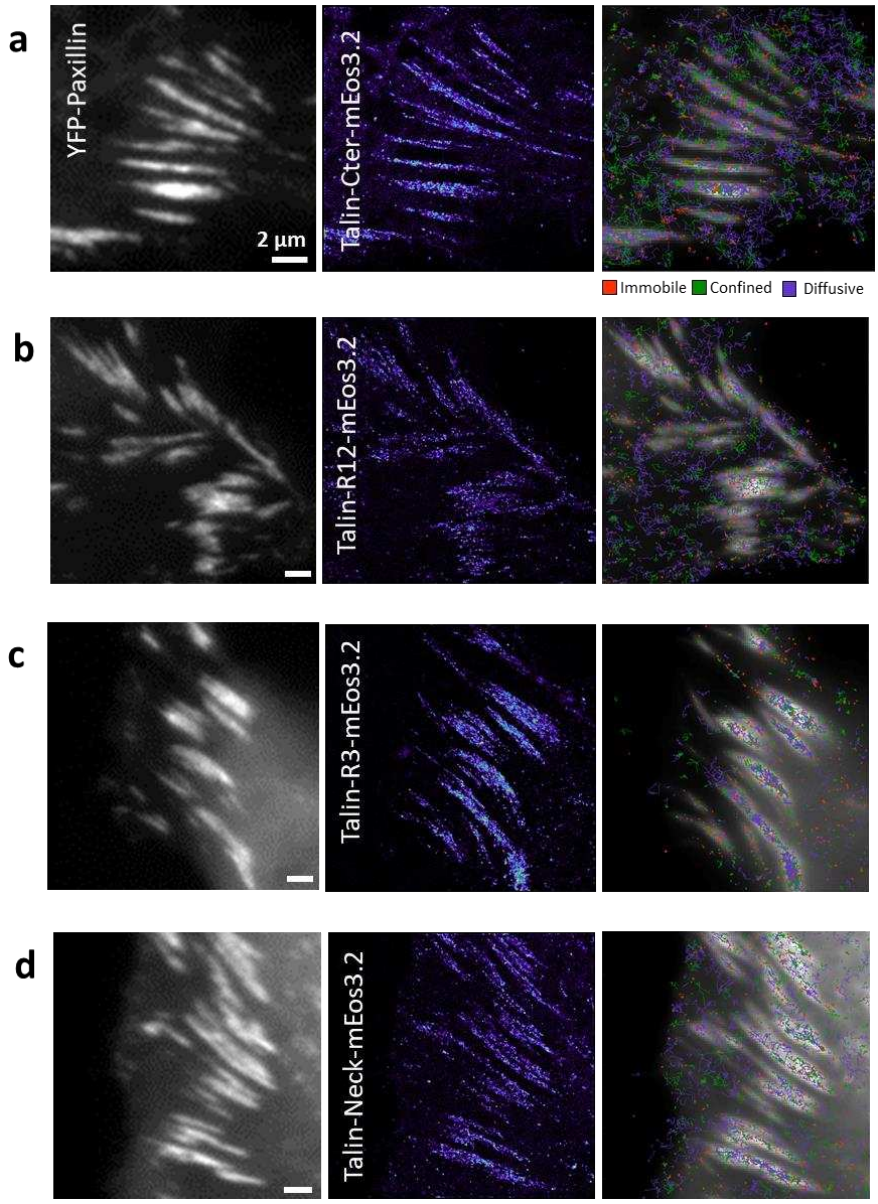

Figure 48. ***Super-resolution reconstructions and diffusion mode classification of talin constructs in MEFs.*** *MEFs were prepared and imaged as in Figure 47. Left: diffraction-limited YFP-paxillin image of FAs. Middle: sptPALM super-resolution image of talin molecule localizations over a 400 s sequence. Right: trajectories color-coded by diffusion mode (red - immobile, green - confined, purple - diffusive) overlaid on FA map (grey). (**a**) Talin-Cterm–mEos3.2, (**b**) Talin-R12–mEos3.2, (**c**) Talin-R3–mEos3.2; (**d**) Talin-Neck–mEos3.2. Scale bar: 2 µm. Visual inspection revealed that most trajectories occurred within FAs, predominantly in immobile and confined states.*

This kind of representation is very useful to gain first impressions about molecular behavior, as it allows direct visual correlation between FA location and diffusion modes. Visual inspection suggested that the majority of the detections for all four constructs are found within FA. We could see that detections both inside and outside FAs are primarily immobile and confined. However, to obtain a quantitative and statistically comparable result, we generated binary masks

of FAs using the YFP-paxillin fluorescent signal, enabling direct comparison of diffusive behavior inside vs. outside of FAs.

Extracting diffusion coefficients for all talin constructs and comparing their distribution inside (Figure 49a) vs outside (Figure 49b) FAs, talin constructs were all found primarily immobile both inside and outside FAs, with a smaller fraction displaying measurable diffusion. Importantly, our control construct (C-term tagged) and the three newly designed tagging positions displayed very similar distributions, indicating comparable mobility profiles.

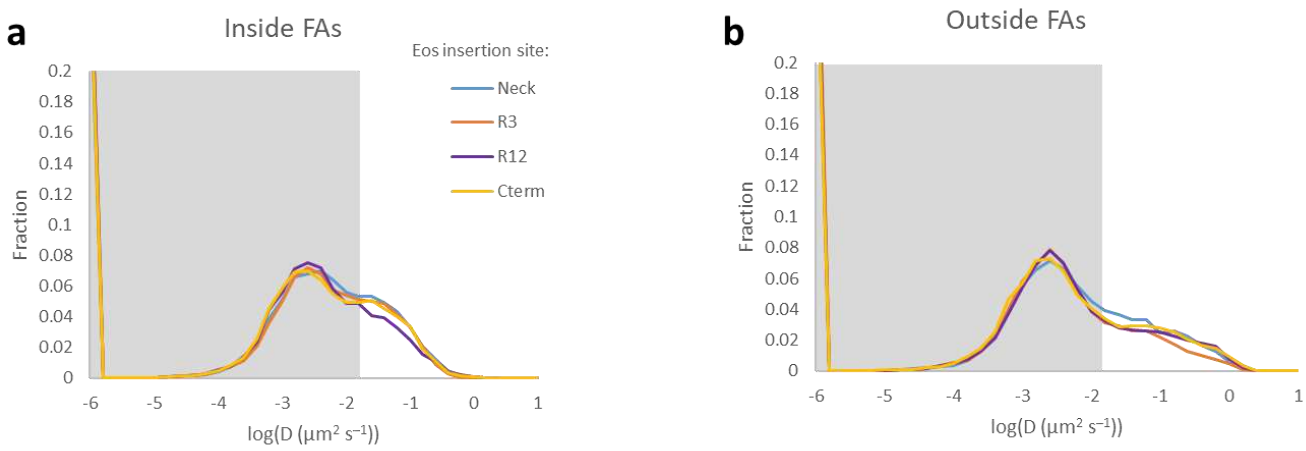

Figure 49. ***Diffusion coefficient distributions of talin constructs inside and outside focal adhesions show very similar behavior****. Based on the performed sptPALM experiments, distributions of log(D) for trajectories ≥ 260 ms were calculated and are shown inside (**a**) and outside (**b**) FAs (mean for all cells). The grey areas including D values inferior to 0.008 µm²s⁻¹ correspond to immobile trajectories. Number of cells: Neck, n = 16; R3, n = 13; R12, n = 10; Cterm, n = 15. All constructs displayed similar diffusion profiles, indicating that tag position does not markedly alter talin mobility.*

To further compare behavior of new talin constructs, we quantified the fraction of molecules assigned to each diffusion mode (diffusive, confined, or immobile) inside and outside FAs (Figure 50), as well as the diffusion coefficient of the freely diffusing subpopulation (Figure 51). Inside FAs, immobile molecules accounted for 60-70% of total detections, while diffusive molecules represented 18-24%. Outside FAs, these proportions were 65-70% and 19-24%, respectively. D_{diff} showed no difference between constructs inside FAs. Outside FAs, talins tagged at the R12 and Cterm showed similar D_{diff}, while the median values of talins tagged at the Neck and R3 were slightly lower (~0.05 and ~0.1 $\mu m^2 s^{-1}$ respectively).

Although some differences in dynamic behavior were observed, they were not statistically significant. This suggests that any variation likely reflects tag-specific local effects rather than

fundamental changes in talin mobility and is unlikely to impact the reliability of the polarization experiments for determining talin orientation.

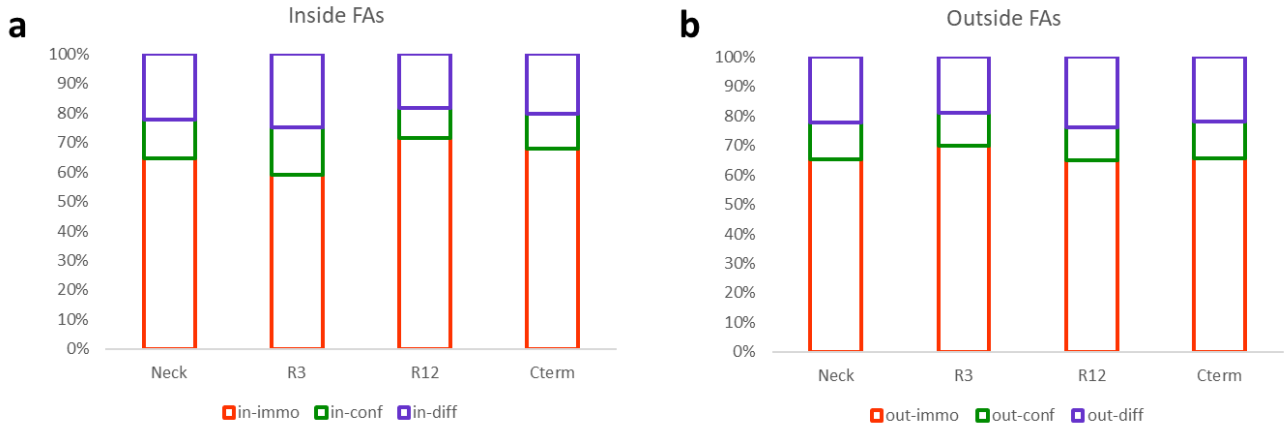

Figure 50. ***Percentage of diffusion modes for talin constructs inside and outside focal adhesions reveals no significant difference among constructs too****. Percentage of trajectories classified as diffusive, confined, or immobile inside (**a**) and outside (**b**) FAs, as defined by binary masks from YFP-paxillin images. Classification was derived from MSD analysis of trajectories ≥ 260 ms. Number of cells: Neck, n = 16; R3, n = 13; R12, n = 10; Cterm, n = 15. Across all constructs, immobile molecules represented the majority population, with comparable distributions in both FA and non-FA regions, supporting their use in our further experiments.*

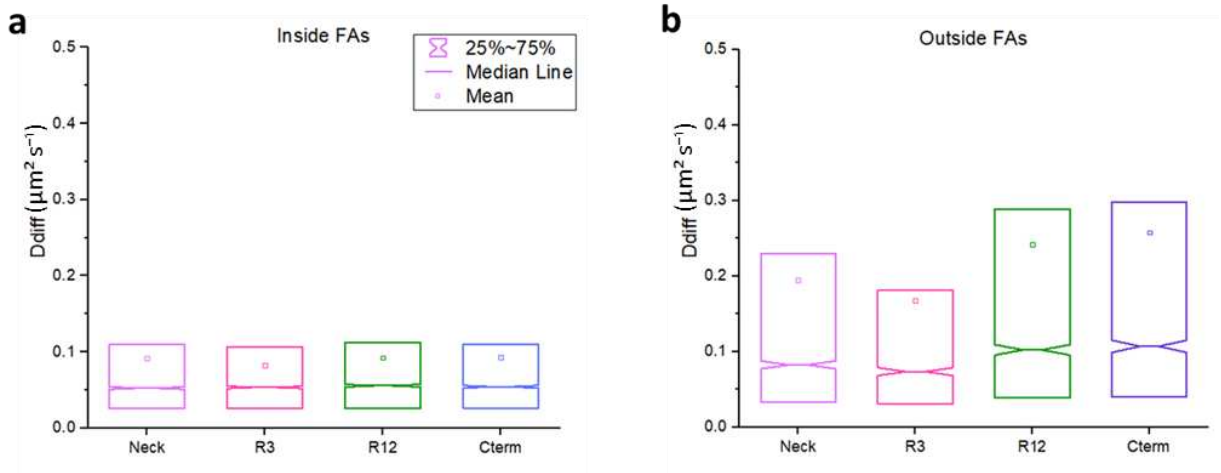

Figure 51. ***Talin constructs tagged at different positions show similar D_{diff} inside and outside focal adhesions****. Diffusion coefficients were calculated for trajectories classified as freely diffusive (≥ 260 ms) inside (**a**) and outside (**b**) FAs, as defined by binary masks from YFP-paxillin images. Number of cells: Neck, n = 16; R3, n = 13; R12, n = 10; Cterm, n = 15. Inside FAs, D_{diff} values were similar across constructs. Outside FAs, Neck- and R3-tagged talins showed slightly lower median D_{diff} (~0.05 and ~0.1 μm² s⁻¹, respectively) than R12 and Cterm variants, but without statistical significance.*

To summarize, these results suggest that all talin constructs - tagged at the Neck, R3, R12, and C terminus, demonstrated similar diffusion characteristics inside and outside focal adhesions. These findings validate their use in dynamic tracking experiments and confirm that the tagging

position does not introduce significant artifacts. The new constructs are similar to the historically used C-terminally tagged talin and are therefore suitable for comparative mechanobiology studies.

2. 3. 2. Truncated mEos3.2 impairs talin imaging performance

With the aim of creating a more rigidly constrained mEos3.2 when fused to talin - hypothetically providing a more accurate proxy for talin's orientation in polarization microscopy - we designed and tested a truncated variant, Talin-mEos3.2ΔN4ΔC9-talin, in comparison with the well-characterized Talin-Cterm-mEos3.2 construct used as a control. We performed sptPALM experiments in the same manner as for previous talin constructs. MEFs were prepared in the same way as for previous talin samples, imaged using TIRF microscopy, enabling selective excitation of molecules in FAs and numerous sparse Talin-mEos3.2 were tracked (Figure 52).

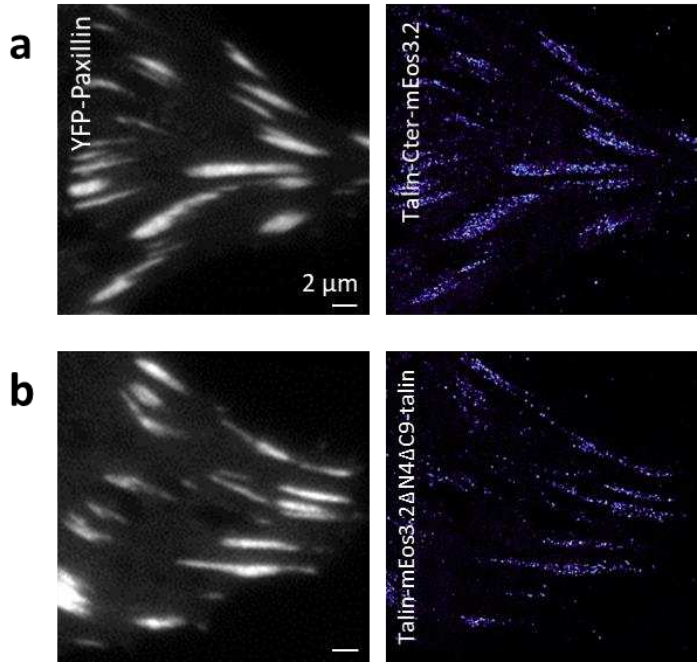

Figure 52. ***Truncated mEos3.2 inserted in talin requires higher excitation and is unsuitable for polarization microscopy.*** *MEFs were co-transfected with YFP-paxillin and either Talin-Cterm-mEos3.2 (control) or Talin-Neck-mEos3.2ΔN4ΔC9. After 48 h, cells were plated on fibronectin-coated coverslips for 2–4 h, transferred into Ringer's solution, and imaged by TIRF-based sptPALM (20 ms exposure, 400 s acquisition). Left: diffraction-limited YFP–paxillin FAs image. Right: super-resolution reconstruction of talin molecule localizations. Scale bar: 2 µm. The truncated construct retained fluorescence but required ~5× higher laser power than the control, increasing photobleaching risk and limiting suitability for polarization microscopy.*

Although the truncated construct was fluorescent and photoactivatable, and found primarily inside FAs (Figure 52b), Talin-mEos3.2ΔN4ΔC9-talin required significantly higher 405nm laser

powers than the control (~5×), which greatly increases the phototoxicity responses and accelerates mEos3.2 photobleaching, reducing tracks duration. Moreover, as our polarization experiments split the signal into four channels in the detection path, the reduced molecular brightness of the truncated mEos3.2 variant would further compromise signal-to-noise ratio and orientation determination quality. Given these practical limitations and their likely impact on quantitative imaging performance, we decided not to proceed with further behavioral analysis of this construct or its use in subsequent experiments.

2. 3. 3. Truncated mEos3.2-actin constructs support functional dynamics and improved rigidity

To enable the study of actin filament orientation in living cells - moving beyond fixed-cell approaches described in the literature (e.g. Rimoli et al., 2022), we designed two truncated mEos3.2-actin constructs: mEos3.2ΔC8-Actin and mEos3.2ΔC9-Actin, aimed at increasing rigidity and thus providing a more stable fluorescence dipole. Results obtained in living cells with these two constructs were compared with the ones using mEos2-Actin, a protein construct previously used in the team (Rossier et al., 2012).

We performed single-protein tracking of actin constructs after mEos photo-activation (sptPALM). MEFs co-transfected with mEos-Actin constructs and GFP–Actin used as an actin organization reporter. Localization of the exogenous constructs confirm incorporation into the actin cytoskeleton (actin stress fibers, actin lamellipodia). After a 48h incubation at 37 ˚C, cells were spread on fibronectin-coated coverslips in regular medium to promote stress fibers formation. After 2-4h of spreading, cells were transferred into a Ringer solution, and imaged using TIRF, allowing selective excitation of the ventral actin cytoskeleton, mainly actin stress fibers extremities anchored to focal adhesions at the basal membrane. Numerous sparse actin detections were localized inside stress fibers (Figure 53) and tracked. Using our sptPALM analysis pipeline, we obtained the distribution of actin coefficients of diffusion plotted in Figure 54.

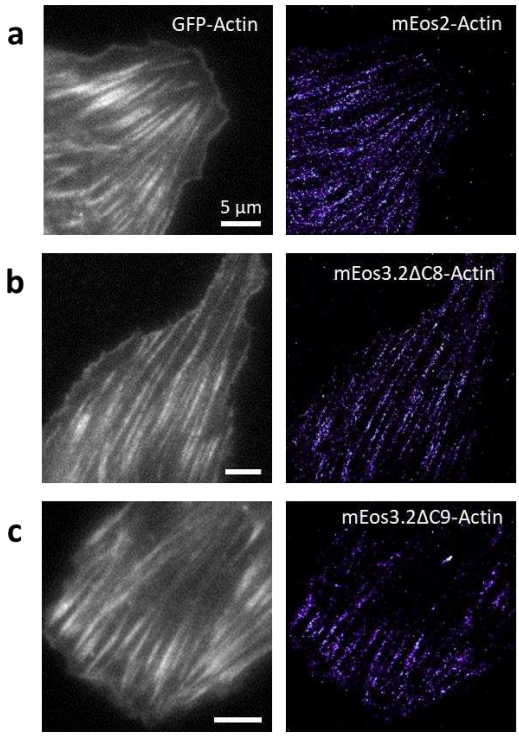

Figure 53. ***Truncated mEos3.2-actin constructs incorporate robustly into stress fibers.*** *MEFs were co-transfected with GFP-actin (stress fiber marker) and one of three constructs: mEos2-actin (control) (**a**), mEos3.2ΔC8-actin (**b**), or mEos3.2ΔC9-actin (**c**). After 48 h, cells were plated on fibronectin-coated coverslips in regular medium for 2-4 h, transferred into Ringer's solution, and imaged by TIRF-based sptPALM (20 ms exposure, 400 s acquisition). Left: diffraction-limited GFP-actin image showing stress fibers and FAs. Right: super-resolution reconstruction of actin localizations. Scale bar: 5 µm. Truncated constructs showed robust incorporation into stress fibers.*

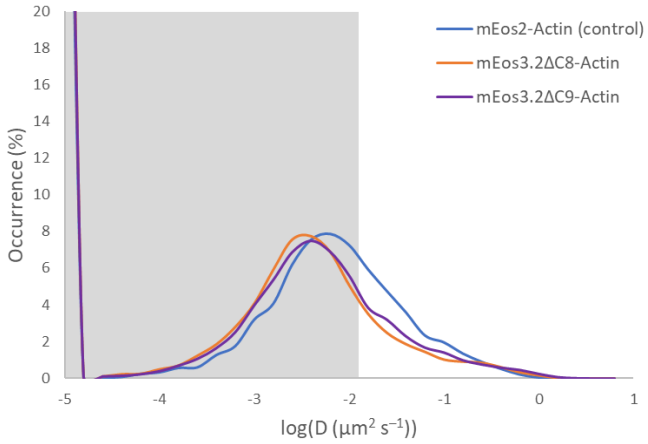

Figure 54. ***Actin constructs with truncated mEos3.2 show reduced diffusivity compared to mEos2-actin.*** *Log(D) distributions (mean for all cells) for mEos2-actin (control; n = 7 cells), mEos3.2ΔC8-actin (n = 21), and mEos3.2ΔC9–β-actin (n = 19). Grey shading indicates immobile trajectories (D < 0.008 µm² s⁻¹). Both truncated constructs displayed a shift toward lower diffusivity relative to the control, suggesting increased probe rigidity and stronger filament integration.*

Both truncated mEos3.2-actin constructs showed a clear shift towards less diffusive behavior compared to the mEos2-Actin control, suggesting a possibly stronger integration into the actin network. The distributions, however, maintained a similar overall shape, indicating that the general dynamic range of actin filament mobility was preserved. This suggests that truncation increases rigidity without fundamentally altering actin filament turnover or mobility patterns.

To further characterize actin dynamics and assess the performance of our newly developed constructs, we analyzed slow actin retrograde flow inside stress fibers (Figure 55) - a continuous rearward movement of actin molecules oriented from the leading edge toward the cell nucleus, driven by myosin II–mediated contractility. To quantify actin dynamics from super-resolved time-lapse movies, I generated kymographs along stress fibers. The slopes of intensity traces in these kymographs were measured to calculate retrograde flow of actin (example given in Figure 55a). Retrograde flow speed was expressed in nm/s, with one dot representing one tracked molecule. Both truncated constructs exhibited retrograde flow speeds within the range expected for intact stress fibers as found in Rossier et al., 2012 and Orré et al., 2021, indicating that filament incorporation and force transmission remained functionally intact despite these truncations.

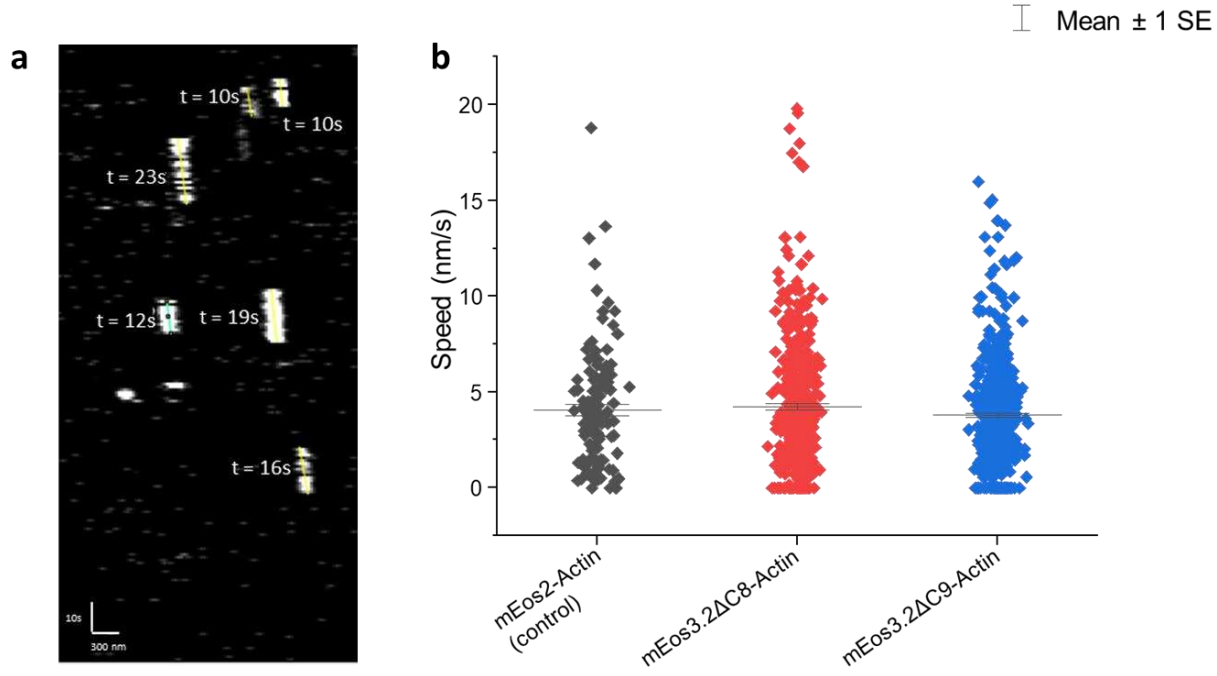

Figure 55. ***Truncated actin constructs preserve physiological retrograde flow speeds****. Retrograde flow was quantified from sptPALM trajectories as the rearward displacement rate of actin molecules inside stress fibers. (**a**) Example of kymographs used for speed calculation, (**b**) retrograde flow speed of actin constructs. Each point represents one molecule. Number of molecules: mEos2-actin, 122; mEos3.2ΔC8-actin, 387; mEos3.2ΔC9-actin, 546.*

Both truncated constructs exhibited retrograde flow speeds within the expected physiological range, indicating preserved incorporation into force-bearing actin bundles.

Taken together, the reduced diffusion, preserved distribution profile, and maintained retrograde flow speeds strongly support that both truncated mEos3.2-actin constructs integrate effectively into the actin cytoskeleton while putatively offering increased dipole stability for polarization-based orientation measurements. Both mEos3.2ΔC8–Actin and mEos3.2ΔC9–Actin exhibited comparable retrograde flow velocities, indicating that truncation at either position does not significantly affect actin incorporation or behavior. Given our objective to maximize the rigidity of the fluorescent reporter, and the fact that both constructs perform equivalently in terms of actin dynamics, subsequent experiments should focus on mEos3.2ΔC9-Actin as the preferred construct for future use.

2. 3. 4. Only full-length extracellularly labeled integrin supports robust single-molecule imaging

To check the quality of the newly engineered integrin constructs, MEFs were co-transfected with β3IntegrinK97-mEos3.2-β3Integrin constructs and YFP-paxillin, as a FA reporter. The rest of the experiment preparation was performed in the same manner as for our previous sptPALM experiments. Cells were imaged using TIRF, allowing selective visualization of the basal membrane where FAs are located.

Among the newly engineered constructs, the full-length mEos3.2 insertion at position K97 in the extracellular domain performed best. This construct showed sufficient brightness for single-molecule detection, enabling imaging at standard laser power. Its performance made it a viable tool for probing conformational changes associated with integrin activation (Figure 56a). In contrast, the truncated versions of mEos3.2 (Figure 56b-d), required significantly higher laser power for detection and yielded notably fewer localizations. This poor performance is likely due to compromised fluorophore stability or folding caused by the terminal deletions. Unfortunately additional backbone deletions at residues 98–101 or 98–102 did not appear to improve mEos3.2 photophysical performances. In some instances, backbone deletions even prevented normal integrin addressing to the plasma membrane as seen with organelles retention in Figure 56c.

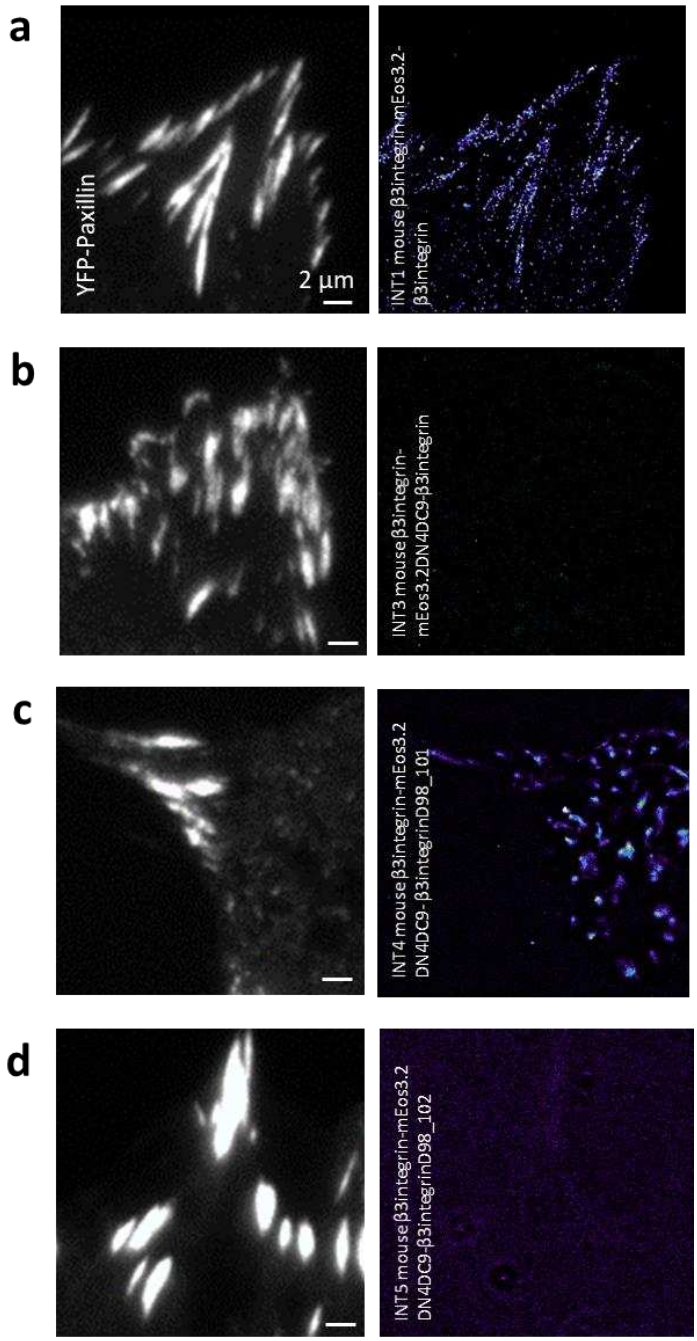

Figure 56. ***Full-length mEos3.2 at K97 supports brighter and denser integrin imaging than truncated variants.*** *MEFs were co-transfected with YFP-paxillin and one of the following mouse β3-integrin constructs: (**a**) β3IntegrinK97-mEos3.2-β3Integrin (full-length mEos3.2 at K97, no linker; control), (**b**) β3IntegrinK97-mEos3.2ΔN4ΔC9-β3Integrin, (**c**) β3IntegrinK97-mEos3.2ΔN4ΔC9-β3IntegrinΔ98-101, (**d**) β3IntegrinK97-mEos3.2ΔN4ΔC9-β3IntegrinΔ98-102. Cells were imaged 2-4 h after plating on fibronectin-coated coverslips in Ringer's solution using TIRF-based sptPALM (400 s acquisition). Left: YFP-paxillin FA image. Right: super-resolution image of integrin localizations. Scale bar: 2 µm. The full-length construct displayed superior brightness and localization density.*

Quantitative analysis confirmed the superiority of the β3IntegrinK97-mEos3.2(FL)-β3Integrin construct (from here on referred to as K97-FL). We performed sptPALM experiments under identical conditions to those used in all previous experiments and compared this construct to our control 6His-β3Integrin-mEos2 (a C-terminus tagged human integrin previously used in the lab (Rossier et al., 2012)).

We extracted diffusion coefficients and fraction of diffusive, confined and immobile populations inside and outside FAs. Inside FAs (Figure 57a, Figure 58a), both the K97-FL and the control were predominantly immobile, with ~10% of trajectories showing diffusion, indicating comparable dynamic behavior in the adhesion context. Outside of FAs (Figure 57b, Figure 58b) the K97-FL construct exhibited slightly higher diffusivity than the control under basal conditions (without Mn^{2+} activation) and showed a more pronounced shift towards the diffusive population upon Mn^{2+} activation. As we will focus mainly on integrin orientation inside FAs as FAs are the primary sites of integrin activation, these differences outside adhesions were not considered limiting for our purposes.

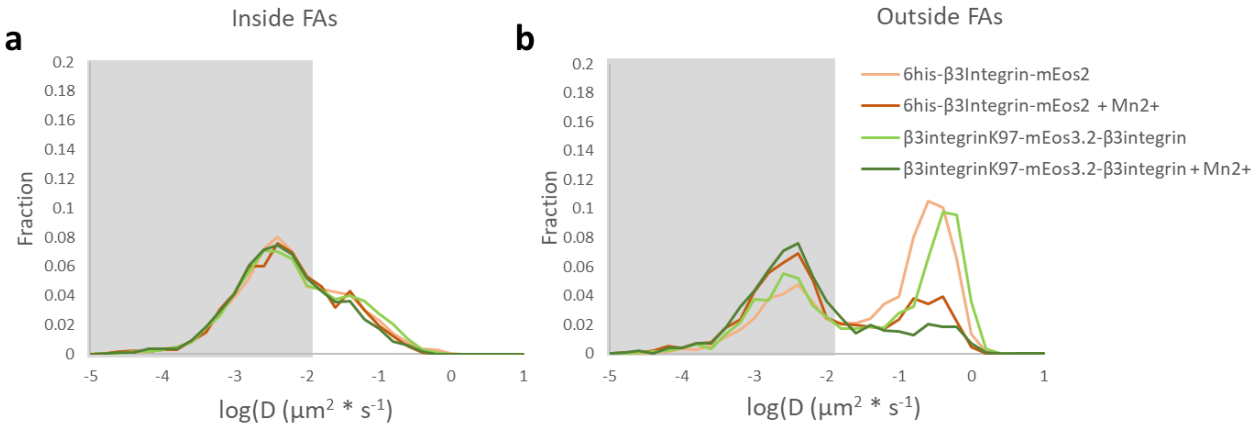

Figure 57. ***K97 tagged and C-terminally tagged integrin show comparable immobility inside focal adhesions****. Log(D) distributions (mean for all cells) for β3IntegrinK97-mEos3.2-β3Integrin and control 6His-β3Integrin-mEos2 (human C-terminally tagged), measured inside (**a**) and outside (**b**) FAs. Grey shading indicates immobile trajectories (D < 0.008 µm² s⁻¹). Inside FAs, both constructs showed predominantly immobile behavior; outside FAs, the K97 construct displayed slightly higher diffusivity, but seemed to be more responsive to Mn^{2+} activation.*

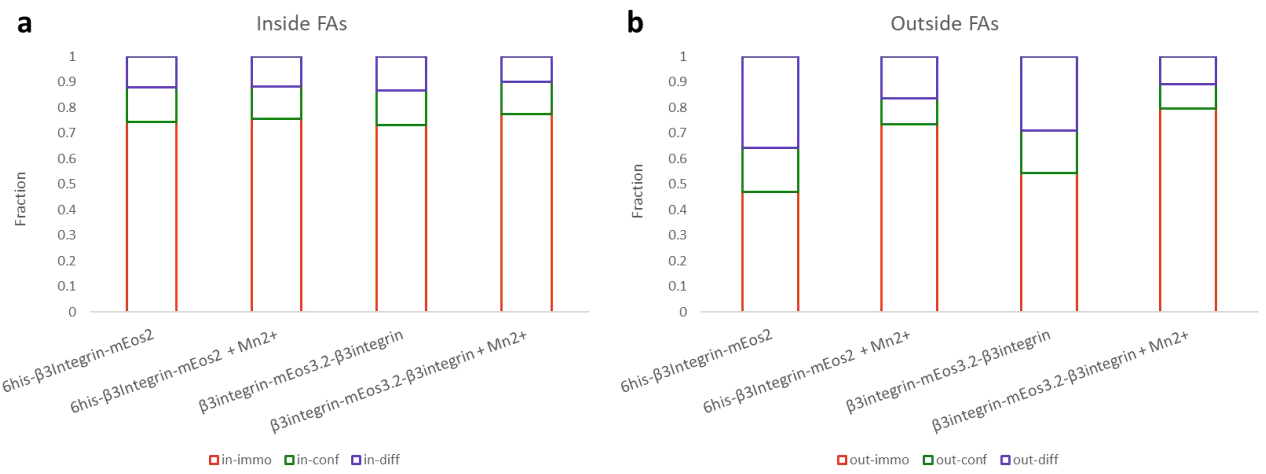

Figure 58. ***K97 integrin shows a slightly larger shift toward immobile population upon Mn^{2+} activation than C-terminally tagged integrin.*** *Fraction of trajectories classified as diffusive, confined, or immobile for β3IntegrinK97-mEos3.2-β3Integrin and 6His-β3Integrin-mEos2. Inside FAs, both constructs were largely immobile. Outside FAs, the K97 construct showed a slightly larger shift toward the immobile population upon Mn^{2+} activation.*

In conclusion, the K97-mEos3.2(FL)-β3-integrin construct provides the necessary brightness, photostability, and dynamic behavior compatibility for robust single-molecule imaging in FAs, while preserving potential orientation-reporting of the extracellular domain capability. Its performance, comparable to the established 6His-β3Integrin-mEos2 inside FAs, and superior to all truncated variants, supports its use as the primary tool for probing integrin conformational changes in mechanosensing studies.

3. 4Polar3D reveals changes in orientation in FA proteins

In order to investigate how mechanosensitive focal adhesion (FA) proteins are oriented in situ, and to determine whether intramolecular orientation changes occur under different activation or contractility conditions, we implemented SMOLM (single-molecule orientation and localization microscopy) modality called 4Polar3D (Kumar et al., 2025) method combined to the use of mEos3.2-tagged constructs specifically generated for this project (Chapter 2 in Results). 4Polar3D approach allows simultaneous extraction of fluorophore 3D orientation (in-plane ρ, out-of-plane η, wobbling δ) and nanometric localization, enabling correlation of molecular orientation with FA position.

To do so, MEFs co-transfected with protein-mEos3.2 constructs and YFP-paxillin, as a FA reporter. After a 48h incubation at 37 ˚C, 5% CO_2, cells were spread on fibronectin-coated coverslips in

regular medium to promote robust FA formation. In live cell experiments, after 2h of spreading, cells were transferred into a Ringer solution, a salt-rich medium that mimics extracellular concentrations and provides an optimal environment for imaging. When using fixed cells, the cells were fixed according to the standard PFA fixation protocol described in the methods, and imaged in PBS 1X. Using TIRF, numerous sparse mEos3.2 were photoactivated during streams of 20 000 frames at ~5.4Hz (185 ms exposure time), corresponding to complete imaging sequence of 1h duration unless the fluorophores bleached or cell retracted during live imaging. Images of YFP-Paxillin were also acquired as a reference of FAs. View of the acquisition windows are shown in Figure 59.

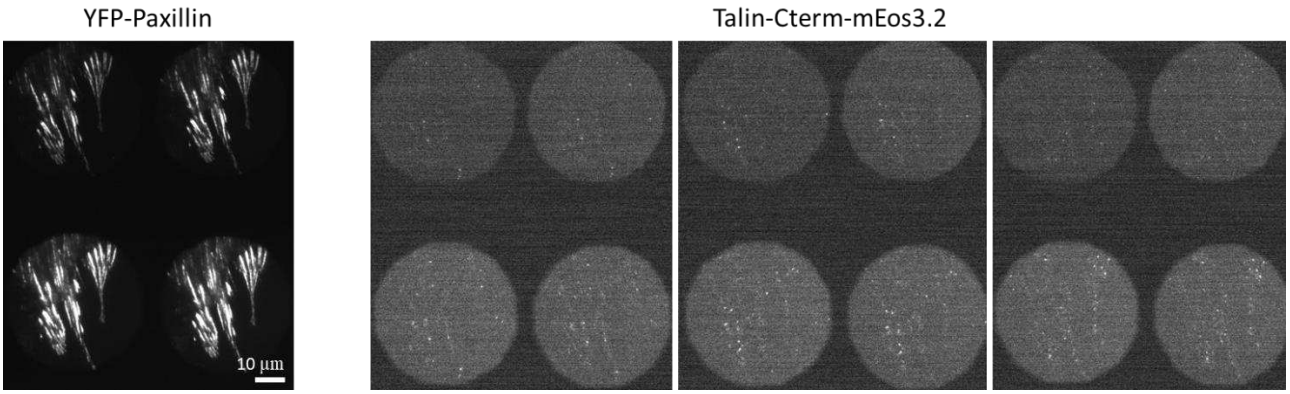

Figure 59. ***Acquisition window during 4Polar3D single-molecule polarization microscopy experiments.*** *Acquisition windows confirm suitable single-molecule sparsity for 4Polar3D orientation imaging. MEFs co-transfected with YFP-paxillin and talin-mEos3.2 constructs. They were imaged under TIRF using 4Polar3D single-molecule polarization microscopy. Left: diffraction-limited YFP-paxillin image used to delineate FA regions. Right: representative acquisition snapshots of talin-Cterm-mEos3.2 emissions during streams of ~20,000 frames at ~5.4 Hz (185 ms exposure), recorded in Ringer solution for live cells or PBS 1X for fixed samples, as specified in Methods. Scale bar: 10 µm.*

3. 1. Integrin polarization experiments reveal Mn^{2+}-induced changes in out-of-plane orientation

As a first application, and a proof-of-concept experiment, we sought to test whether 4Polar3D could detect conformational changes in integrins upon activation. We imaged two β3 integrin constructs: one labeled extracellularly at K97 (β3IntegrinK97-mEos3.2-β3Integrin) and one tagged at the cytoplasmic C-terminus (6His-β3Integrin-mEos2). After processing the data, as described in Methods, we were able to retrieve the in plane (ρ) and out of plane (η) orientation, as well as wobbling (δ), for each detection (example of 6His-β3Integrin-mEos2 shown in Figure 60a).

Upon Mn^{2+} addition, which locks integrins in an extended, high-affinity conformation, we observed a clear change in mean η (out-of-plane orientation) for the extracellularly labeled construct, while the C-terminally tagged construct showed minimal orientation change (Figure 60b). Mn^{2+} induced a shift in η distribution toward more upright conformations for the extracellular label, consistent with integrin extension, whereas C-terminal η remained stable. We noticed no visible differences in ρ or δ.

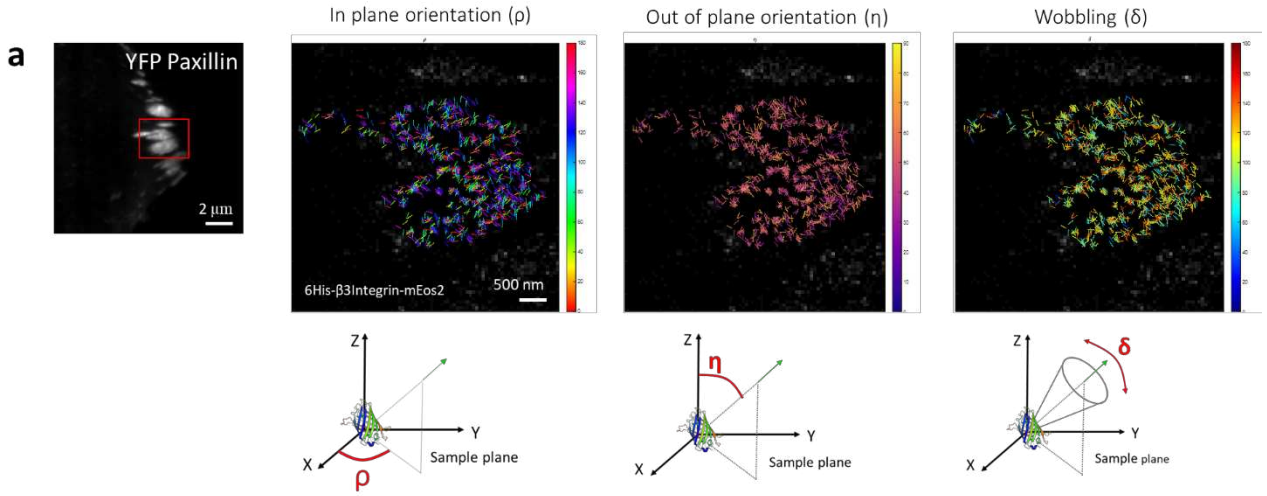

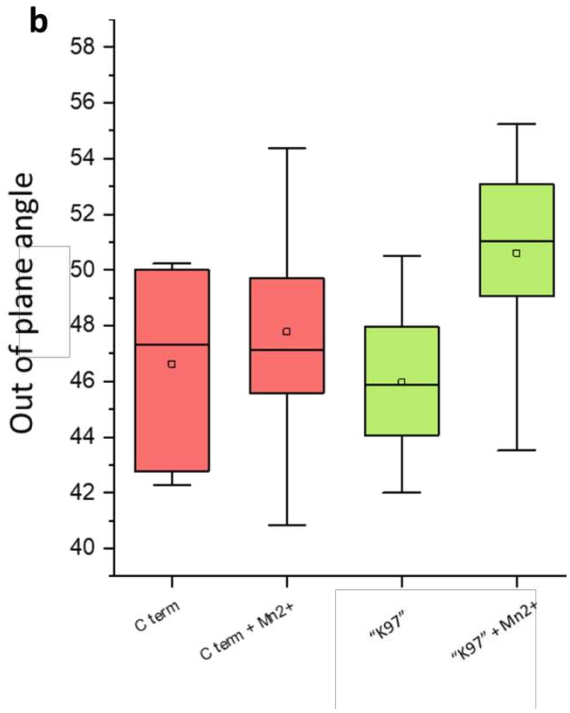

Figure 60. ***Mn^{2+} activation selectively increases the out-of-plane tilt (η) of the extracellularly labeled β3 integrin, while the cytoplasmic C-terminus tagged integrin remains unchanged.*** *MEFs expressing either β3IntegrinK97-mEos3.2-β3Integrin (extracellular K97 label) or 6His-β3Integrin-mEos2 (C-terminal cytoplasmic tag) were imaged live with 4Polar3D (185 ms exposure, TIRF). (**a**) from left to right – YFP-Paxillin image as a FA reference, 6His-β3Integrin-mEos2 in-plane orientation ρ map of single molecules (0-180°), out-of-plane orientation η map (0-90°), and wobbling angles δ (0–180°). Sticks orientations shows ρ. (**b**) η distributions were calculated from polarization-resolved single-molecule emissions over ~20,000 frames per stream. Upon Mn^{2+} treatment (see Methods), β3IntegrinK97 showed a clear shift of η (consistent with integrin extension), whereas the C-terminally tagged construct showed minimal change.*

These initial results constituted a first proof of concept for detecting at the single molecule level, orientation changes in living cells.

However as integrins exhibit rapid dynamics switches between immobilization and diffusion states, the extended exposures required for 4Polar3D (185 ms vs. 20ms used in regular sptPALM) due to four-way signal splitting inherent to our polarization imaging experiments, potentially lead to motion blur explaining the reason why the single molecule fluorescence signal was often dim, thus reducing measurement reliability. For these sensitivity considerations, we redirected our focus to talin, a less mobile FA protein expected to exhibit orientation heterogeneity depending on labeling site and contractility level, and whose low mobility is advantageous for long-exposure orientation measurements.

3. 2. In-plane orientation (ρ) reveals axial gradients along the talin molecule in basal conditions

To determine what does talin's orientation look like and whether it varies along its length, we imaged MEFs expressing mEos3.2-tagged talin at four positions - Neck, R3, R12, and C terminus (Figure 62a) using 4Polar3D single-molecule polarization microscopy. As illustrated in Figure 61 for talin-neck-mEos3.2, this approach yields multiple data representations from the same acquisition:

(a) a super-resolved image reconstruction from mEos3.2 detections overlaid with YFP–paxillin as an FA reporter,

(b) a temporal map with detections color-coded by frame number (blue to red) and sticks indicating in-plane orientation (ρ),

(c) an in-plane orientation ρ map with sticks showing dipole direction with color coding ρ (scale 0°-180°),

(d) an out-of-plane orientation η map with sticks orientation showing ρ but color coding η (scale 0°-90°),

(e) a wobbling δ map showing the fluorophore wobbling angle (0°-180°) with sticks orientation indicating ρ.

This multi-parameter output enables simultaneous spatial localization, in-plane and out-of-plane orientation measurement, and assessment of fluorophore rotational mobility.

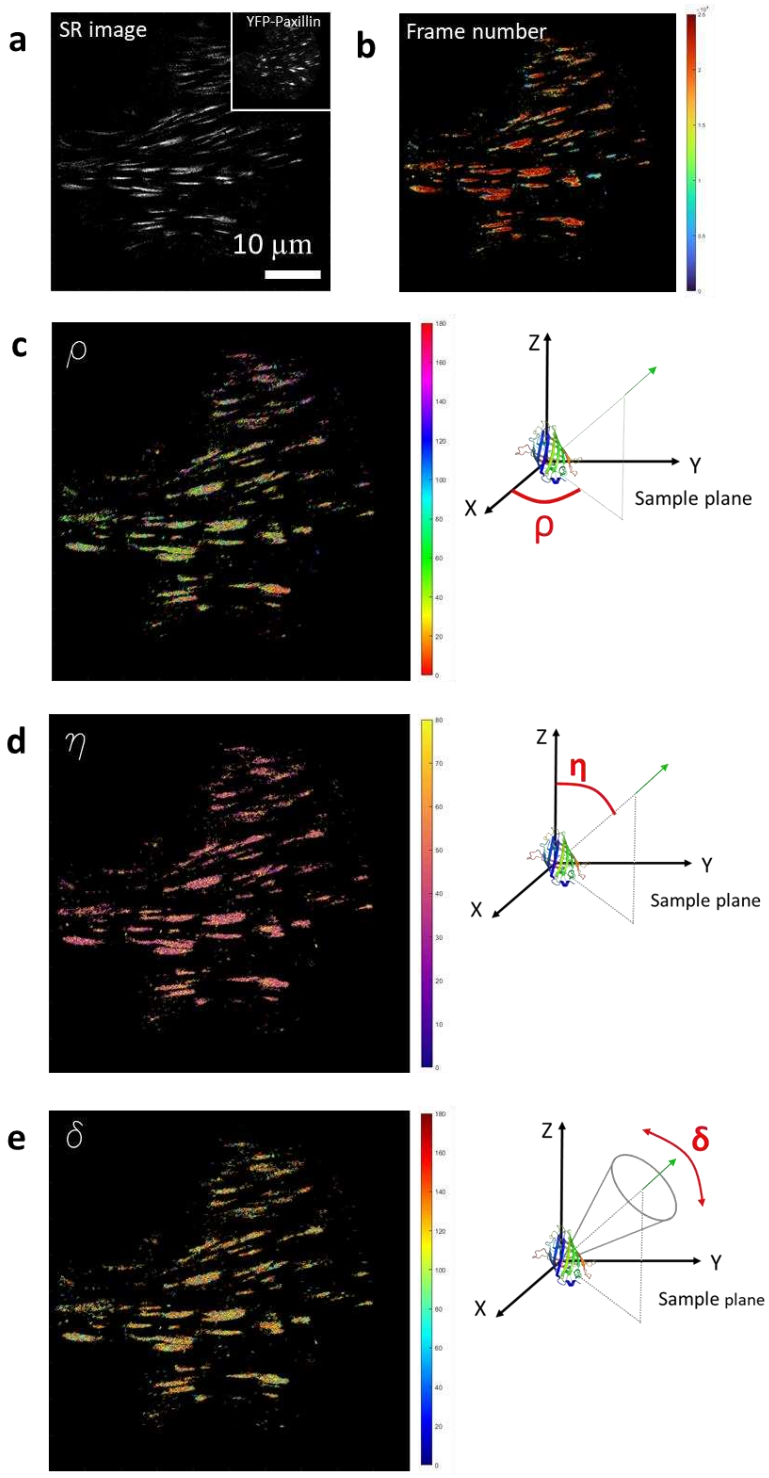

Figure 61. ***Visual data obtained via single molecule polarization microscopy – example of talin-neck-mEos3.2.****; (**a**) mEos3.2 super-resolution reconstruction, insertion: YFP-paxillin (FA reporter), (**b**) detections color-coded by frame index (blue→red), (**c**) in-plane orientation ρ map (0-180°), (**d**) out-of-plane orientation η map (0-90°), and (**e**) wobbling angles δ (0–180°). Sticks orientations shows ρ for b-e. Streams comprised 20,000 frames at ~5.4 Hz (185 ms exposure) under TIRF. Scale bar: 10 µm.*

Fixed cells were used initially as a controlled condition, as they are easier to image, due to lack of protein dynamics and cell migration present in living cells.

To assess whether talin and its specific domains adopt random or preferred orientations, we first aligned each sample by rotating the ρ detections so that the mean focal adhesion (FA) axis was set to 0°. Because dipole orientations are symmetric, we then mirrored the data accordingly. The resulting distributions were plotted in radial histograms (Figure 62b), allowing straightforward visual comparison of orientation differences.

In fixed cells, we observed a progressive increase in ρ heterogeneity from the Neck toward the C-terminus (Figure 62b). Quantitatively, Neck-tagged talin molecules were strongly aligned with the FA axis, whereas C-terminally tagged talins were more isotropically distributed. R3 and R12 showed intermediate alignment, with R12 exhibiting greater homogeneity than R3.

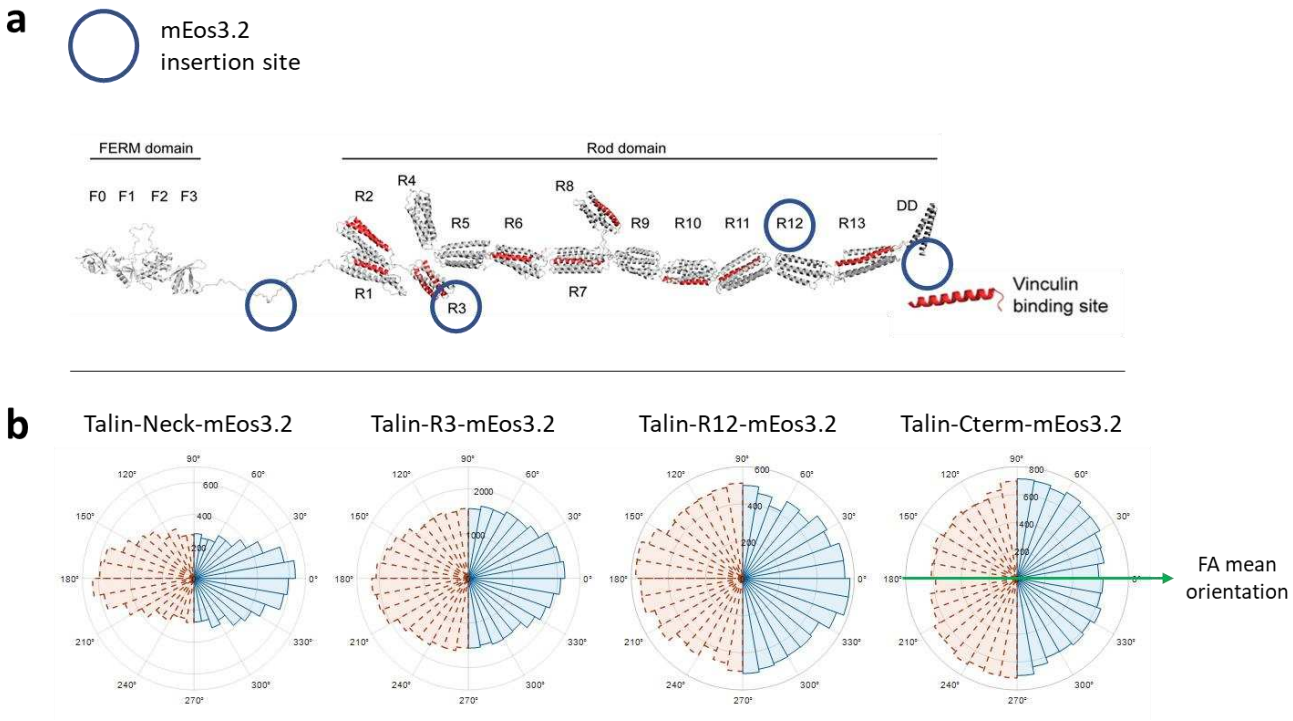

Figure 62. ***In fixed cells, talin's in-plane orientation (ρ) is strongly aligned at the neck and progressively more isotropic toward the C-terminus.*** *(**a**) Schematic of mEos3.2 insertion positions (Neck, R3, R12, C-term). (**b**) For each construct, single-molecule ρ detections were rotated so the mean FA axis is 0° and mirrored to account for dipole symmetry. MEFs were PFA-fixed (protocol in Methods) and imaged in PBS 1X under TIRF (185 ms exposure). Number of cells: Neck n=3, R3 n=5, R12 n=5, C-term n=5. The Neck construct shows the narrowest ρ distribution (strong alignment), with broader distributions at R3/R12 and the broadest at C-term.*

In order to define a parameter quantifying preferred orientation of mEos3.2 dipole visible in the radial distribution plots, we computed a polarization ratio: the ratio of detection counts at the

dominant ρ peak to those at the orthogonal angle. This metric quantifies directional alignment even when the main orientation is tilted relative to the FA axis. In Figure 63, we show a comparison of the polarization ratio across all four talin constructs (imaged in fixed cells) calculated at the cellular level by pooling detections from all FAs. While a more refined analysis at the single-FA (ROI-by-ROI) level would offer more spatial resolution, such an approach was hindered by insufficient detection counts per FA, making the ratio less robust due to noise.

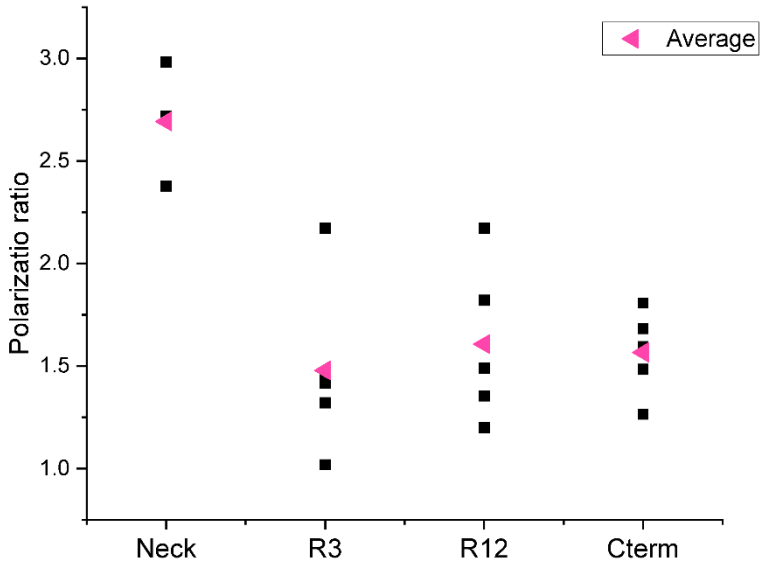

Figure 63. ***A polarization-ratio metric confirms stronger directional alignment at the talin neck in fixed cells****. Per-cell polarization ratio (peak ρ intensity / orthogonal intensity) was computed by pooling detections across all FAs in a cell (single-FA analysis was underpowered due to low counts). Squares denote individual cells. Number of cells: Neck n=3, R3 n=5, R12 n=5, C-term n=5. Neck shows the highest ratios, R3 and R12 are lower and closer to C-term, and R3 exhibits greater inter-cell variability than R12.*

Using this metric, we observe a clear trend between talin tagged at the Neck and the C terminus, with the 'Neck' clearly having a preferential orientation, and the C terminus-tagged displaying more isotropic orientation. Concerning orientations adopted by mEos3.2-tagged talin rod domains R3 and R12, they display similar average polarization ratios as the talin-Cterm. However, the spread of the polarization ratio for R3 and R12 seems to be higher than that for the C-term tagged talin. This could be a result of capturing R3 and R12 tagged construct in folded/unfolded states, whereas those kind of changes do not exist at the C terminus.

These fixed-cell results suggest a clear difference between the talin neck and the more distal regions of the molecule. The neck adopts a favored orientation aligned with the FA axis, whereas the rod domains (R3 and R12) and the C-terminus display more isotropic distributions. This

indicates the existence of a gradient of polarization along talin, with orientation amplitude decreasing from the neck toward the C-terminal end. Mechanistically, this makes sense: the neck is a short, unstructured polypeptide chain directly linking the FERM head to the rod, and thus is likely to align under mechanical tension, whereas rod domains are composed of folding/unfolding modules that can adopt a wider range of orientations.

However, these observations were made in fixed cells, raising the possibility that fixation might bias or constrain protein orientations. To validate that these differences are not fixation artifacts and indeed reflect the native organization of talin under mechanical load, we performed the same experiment in living cells.

At the level of living cells, the trend seen in fixed samples seems to generally be followed (Figure 64, Figure 65), but with some notable differences: R3 displayed a higher polarization ratio in live cells compared to fixed, possibly due to reduced conformational relaxation compared to PFA-fixed samples. Interestingly, the wide range of polarization ratios for R3 in live cells could reflect variable contractility states, as R3 unfolds under low force (~5 pN, Yao et al., 2016).

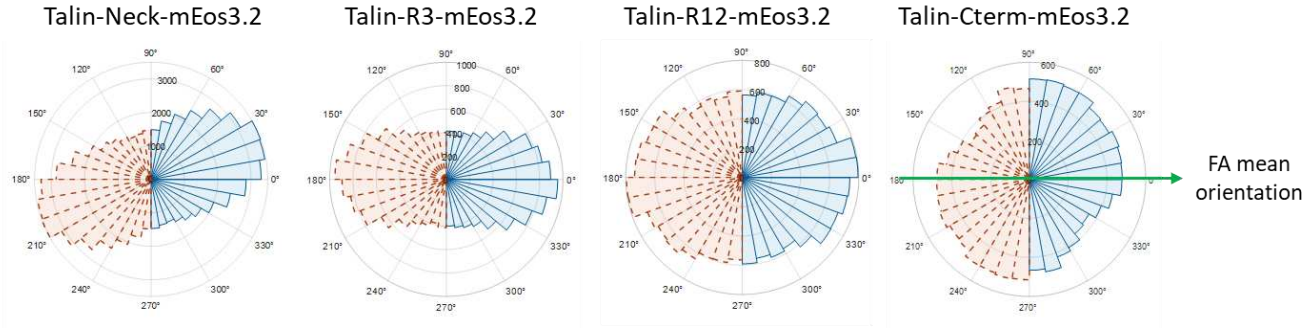

Figure 64. ***Live-cell ρ distributions reproduce the axial gradient observed in fixed cells, with alignment strongest at the neck****. MEFs expressing talin-mEos3.2 constructs were imaged live in Ringer under TIRF with 4Polar3D (185 ms exposure). Per-cell ρ distributions were rotated to the mean FA axis (0°) and mirrored as in fixed samples. Number of cells: Neck n=5, R3 n=5, R12 n=7, C-term n=3. Overall gradients match fixed-cell trends.*

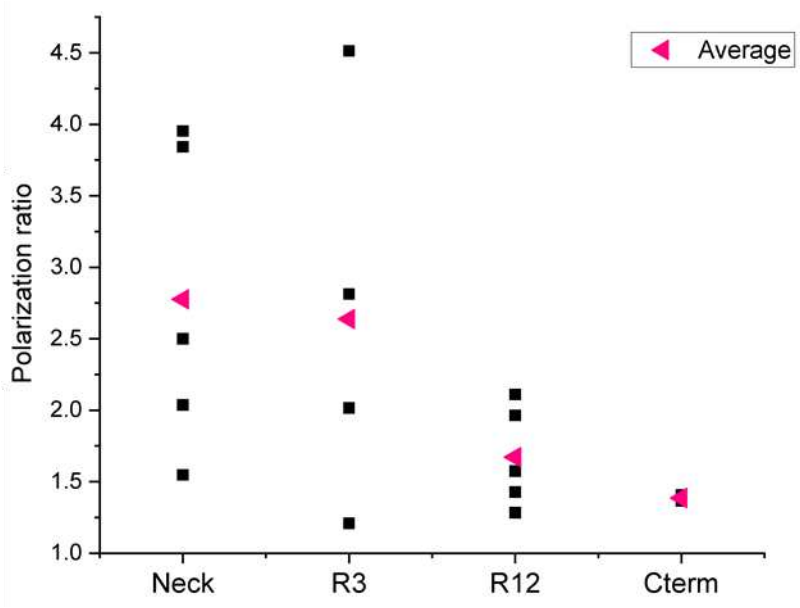

*Figure 65.**In live cells, polarization ratios remain highest at the neck and are elevated (and more variable) for R3 compared to fixed conditions**. Per-cell polarization ratios were computed as in Figure 63. Numbers of cells: Neck n=5, R3 n=5, R12 n=7, C-term n=3. The elevated and variable ratios for R3 may reflect force-dependent conformational heterogeneity in live cells.*

Talin displays a structural orientation gradient, with stronger alignment at the 'neck' and increased isotropy towards the C-terminus. This trend is observed in both fixed and live cells, although live-cell data reveal higher polarization ratios for R3, potentially reflecting force-dependent conformational changes. These findings validate the use of SMOLM for probing intramolecular orientation in mechanosensitive proteins.

3. 3. Out-of-plane orientation (η) shows no site-specific difference in talins, but fixation affects distribution

In order to assess whether the out-of-plane orientation (η) of talin varies depending on the tagging site, and whether fixation alters this parameter, we analyzed η distributions for all four constructs (Neck, R3, R12, C-term) in both fixed and live MEFs.

To do so, η was extracted from 4Polar3D measurements in the same acquisitions used for ρ analysis, with detections pooled per construct. We compared fixed-cell datasets (Figure 66a), with live-cell datasets (Figure 66b), to isolate potential fixation-induced biases.

The results showed no significant differences in η between constructs in either fixed or live conditions. However, mean η values were consistently higher in fixed cells, suggesting that chemical fixation slightly increases the apparent off-plane tilt.

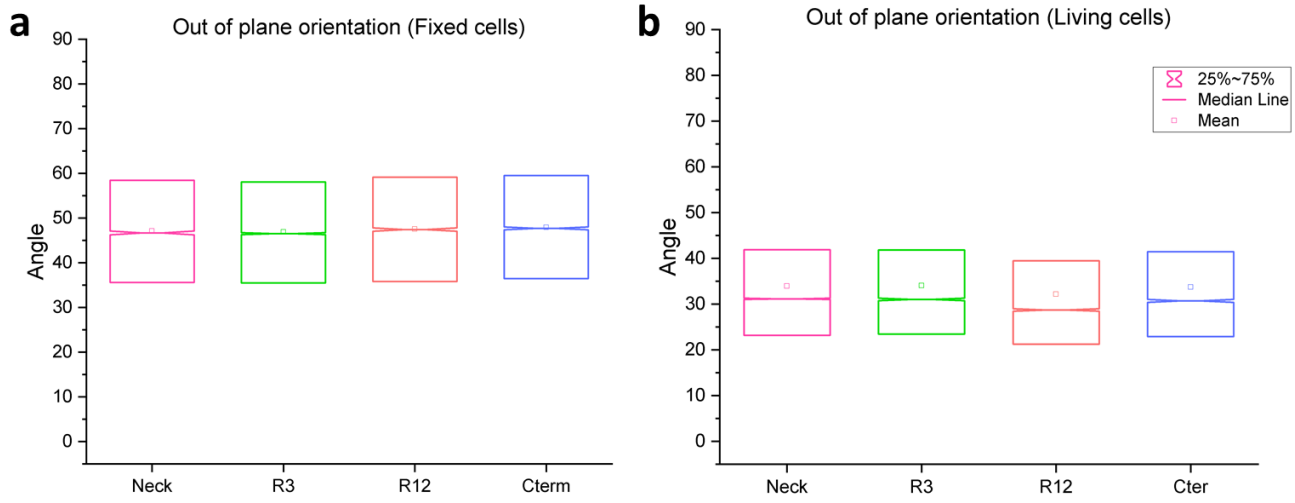

Figure 66. ***Out-of-plane orientation (η) shows no site-specific differences across talin constructs, but fixation increases η****. (**a**) Fixed-cell η distributions and (**b**) live-cell η distributions for Neck, R3, R12, and C-term tagged talins from 4Polar3D acquisitions (185 ms exposure). Across constructs, η is similar, but mean η is higher after PFA fixation, indicating a small off-plane bias induced by fixation.*

We also quantified the wobbling angle (δ), defined as the angular range explored by the fluorophore emission dipole. This parameter is critical, as high wobbling compromises the reliability of orientation measurements. In fixed cells, all constructs displayed mean δ values below 80° (Figure 67a), while in live cells δ values were around or below 100° (Figure 67b).

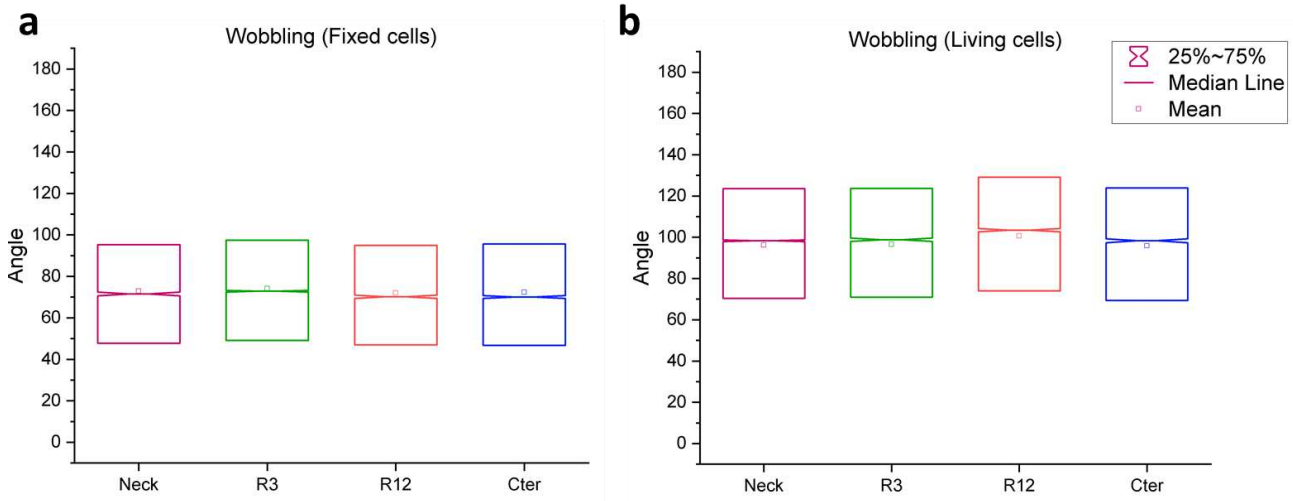

Figure 67. ***Wobbling (δ) remains within an orientation-retrieval-compatible range; fixation decreases δ****. δ distributions for (**a**) fixed and (**b**) live MEFs show δ <~80° in fixed cells and around or below ~100° in live cells across constructs (4Polar3D, 185 ms exposure). These values are compatible with robust orientation analysis (see Methods). Lower δ in fixed cells likely reflects fixation crosslinking-induced restriction of rotational mobility.*

These δ values compare favorably to established benchmarks: for example, 4polar-STORM imaging of AF488-phalloidin on actin filaments yielded δ = 86° ± 27° (Rimoli et al., 2022), a condition shown to permit accurate orientation retrieval. Thus, the wobbling measured here remains within a range compatible with high-quality orientation determination. The slightly lower δ in fixed cells can be attributed to molecular crosslinking during PFA fixation, which restricts rotational freedom.

Based on this data, we can conclude that neither η or δ depend on talin's tagging position, but fixation increases η and decreases δ, effects likely related to crosslinking-induced structural constraints.

3. 4. Drug-induced contractility changes as a tool to probe talin dynamics

Because talin's molecular orientation may be modulated by intracellular tension, we aimed to perturb actomyosin contractility pharmacologically and assess the resulting FA responses. This step served two purposes: first, to validate the effectiveness of selected drugs in altering contractility; and second, to establish conditions for subsequent orientation measurements under defined mechanical states.

We selected three drugs with distinct effects on the contractile state: CalyculinA (myosin phosphatase inhibitor that increases contractility), Y-27632 (Rho-associated kinase inhibitor that decreases contractility), and para-amino-blebbistatin (myosin II inhibitor that strongly decreases contractility).

3. 4. 1. Focal adhesion responses confirm pharmacological drug effects on contractility

To define the experimental conditions of use of the drugs we wanted to use to induce/inhibit contractility, I first performed a series of timelapses. To test each drug, I transfected the cells with YFP-Paxillin, as a FA reporter, and applied the drug at t0 and acquired an image every 2 minutes for 1h.

In case of CalyculinA (20 nM) (Figure 68), both the size of FAs and the intensity of the YFP-Paxillin signal was increasing (after ~15 minutes). Under the effect of RHOK inhibitor Y-27632 (15 µM) (Figure 69), already after 10 minutes, the FA size was reduced, and it kept decreasing with time. After 30 minutes, the cells started forming new protrusions and were spreading further. With the use of para-amino-blebbistatin (Figure 70), we saw the same rate of FA size reduction, but no new protrusion sites being formed.

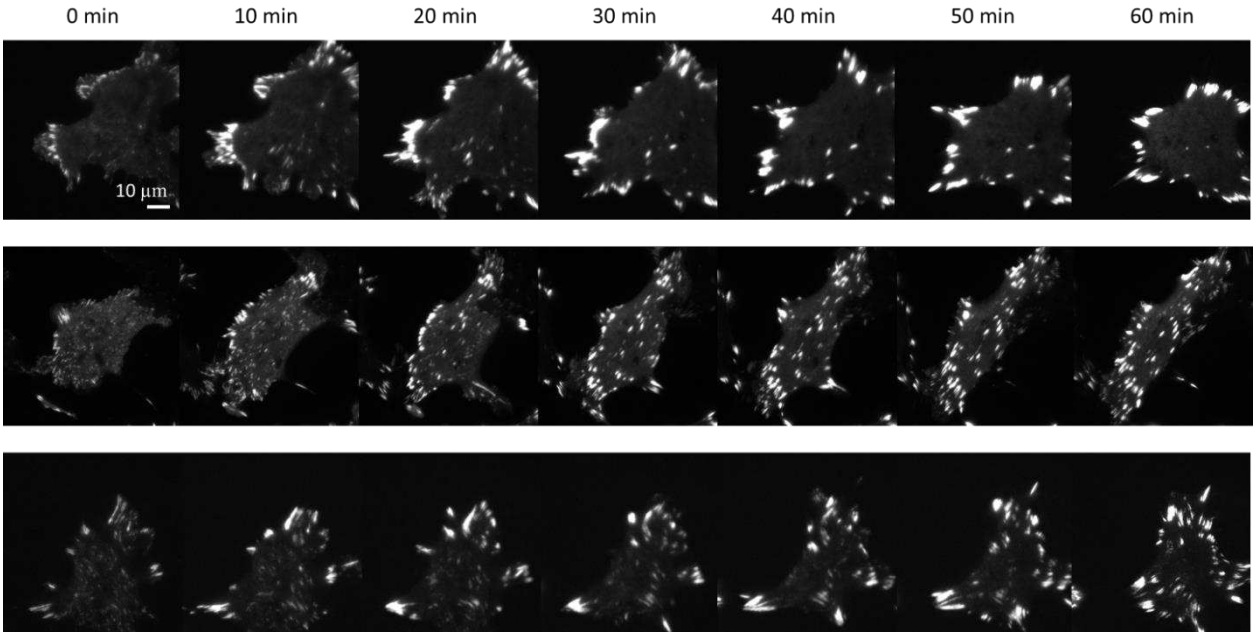

Figure 68. ***CalyculinA induces FA growth and paxillin recruitment over 60 minutes, validating increased contractility****. Live MEFs expressing YFP-paxillin were imaged every 2 min for 1 h under TIRF with CalyculinA added at t=0 (20 nM). Example time-lapses show increased FA area and YFP-paxillin intensity over time. Contrast was kept constant across the stream. Scale bar: 10 µm.*

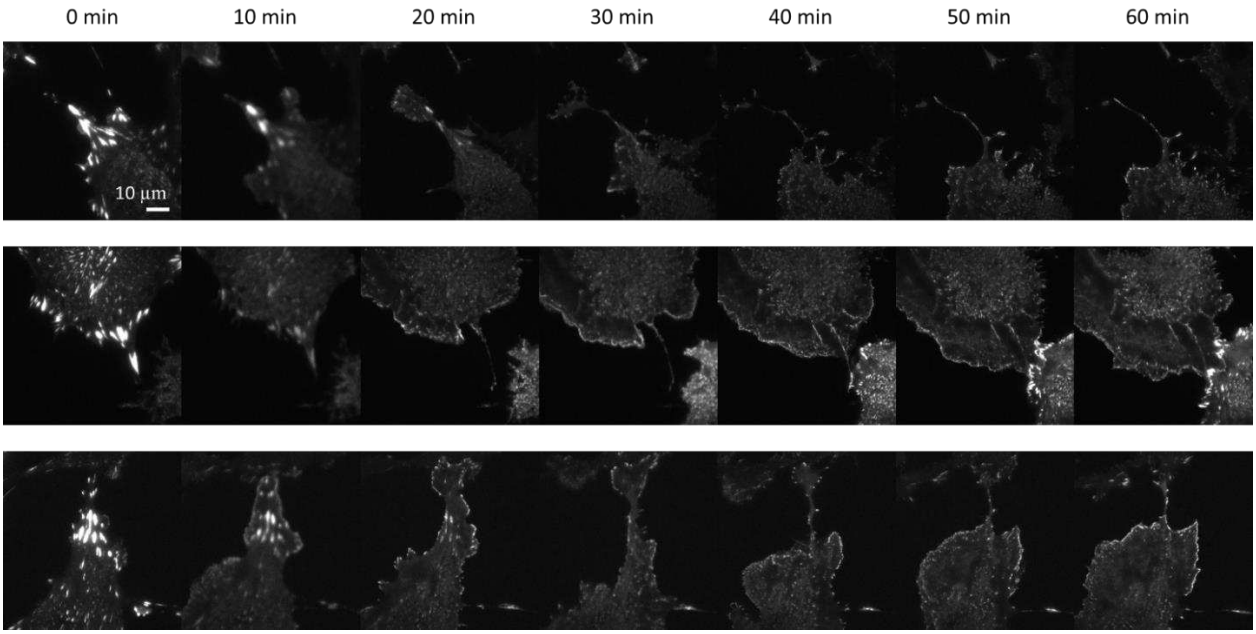

Figure 69. ***RhoK inhibition by Y-27632 reduces FA size and promotes protrusive spreading****. Live YFP-paxillin MEFs were imaged every 2 min for 60 min under TIRF; Y-27632 was applied at t=0 (15 μM). FA size decreased within ~10 min and continued to decline; by ~30 min cells exhibited new protrusions and further spreading. Contrast constant across the stream. Scale bar: 10 μm.*

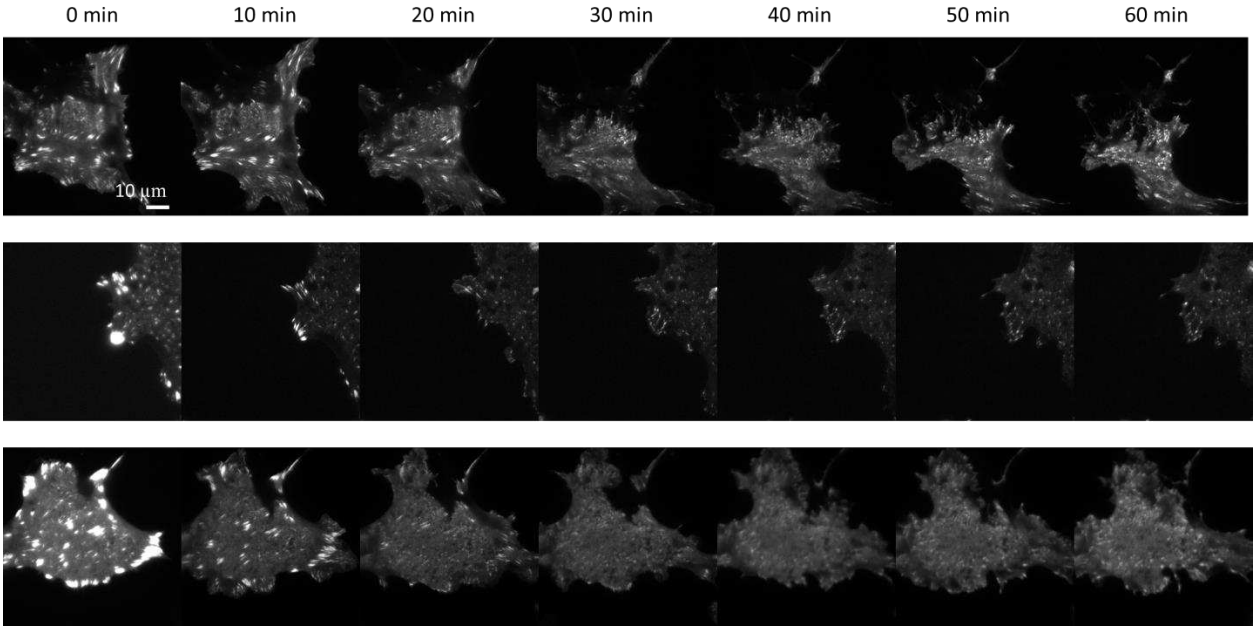

Figure 70. ***Para-amino-blebbistatin rapidly decreases FA size without inducing new protrusions****. YFP-paxillin MEFs were imaged every 2 min for 60 min under TIRF after drug addition at t=0 (50 μM). FA area decreased at a rate comparable to Y-27632, but without the emergence of new protrusion sites. Contrast constant across the stream. Scale bar: 10 μm.*

To understand these the effect of these drugs better, I performed the following measurements per frame and plotted them in Figure 71:

- Total area of FAs in pixels (with a lower threshold of 100 pixels to account only for FAs detections), to see quantitatively how does it change.
- Intensity density – to see how the intensity, and therefore the recruitment of YFP-Paxillin changed over time.
- Number of regions of interest (ROIs) per frame (i.e. number of FA) to check how does the number of FAs evolve upon use of different drugs.

Under CalyculinA treatment, both the total FA area and intensity density increased progressively over time for most cells, accompanied by increase in ROI number. In contrast, Y-27632 led to a rapid decrease in FA area and intensity density within the first 10 minutes, followed by a partial recovery at later time points that coincided with the formation of new protrusions and additional FAs in some cells. Para-amino-blebbistatin produced a similar initial loss of FA area and signal intensity, but without the subsequent recovery or increase in ROI number. These quantitative measurements thus confirm the expected pharmacological effects of each drug on focal adhesion stability in MEFs.

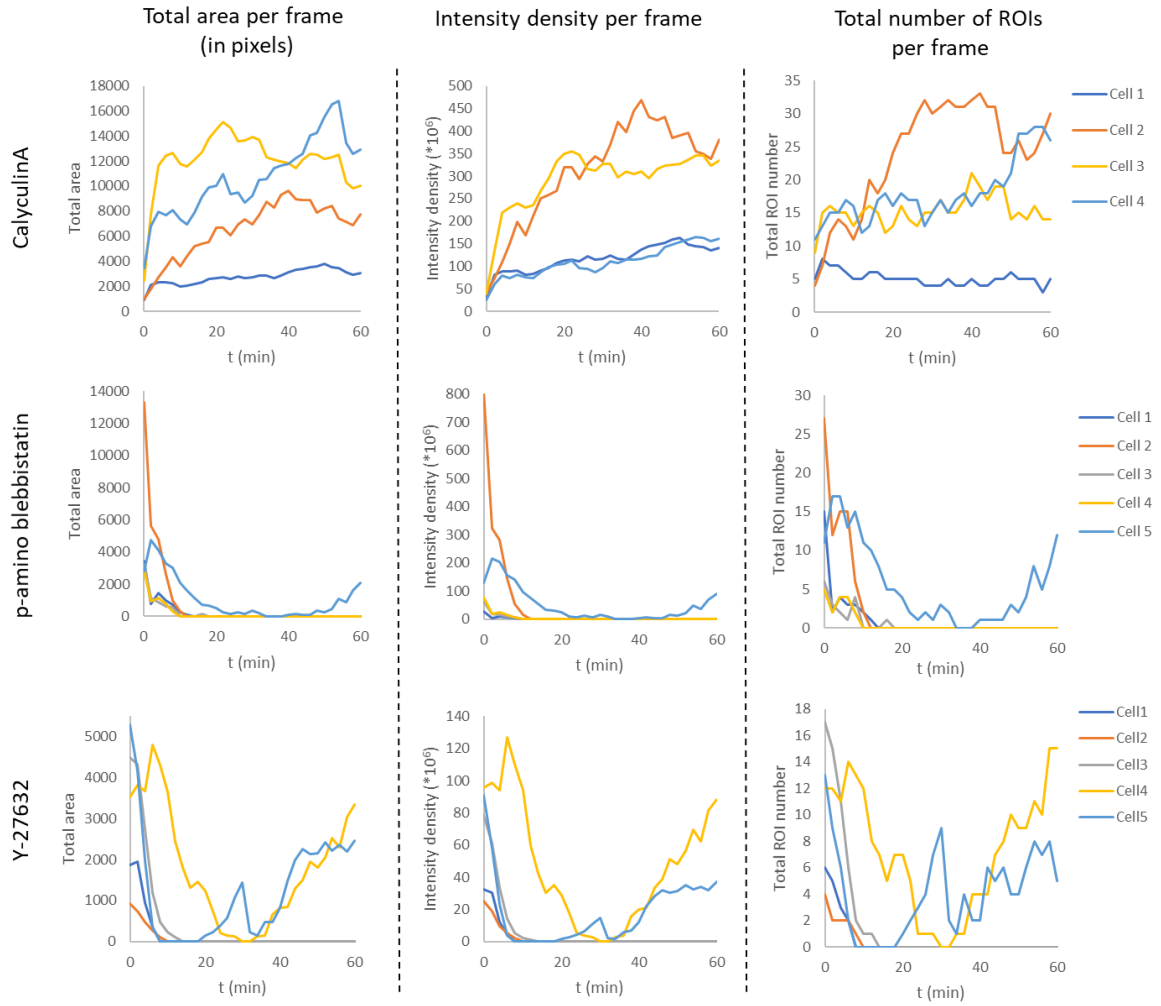

Figure 71. ***Quantitative analysis of focal adhesion dynamics under pharmacological treatments in live MEFs****. MEFs transfected with YFP-paxillin were plated on fibronectin-coated coverslips and imaged by TIRF microscopy every 2 min for 60 min. Drugs were applied at t=0 at the following concentrations: CalyculinA (20 nM), para-amino-blebbistatin (50 µM), or Y-27632 (15 µM). Per-frame measurements of (i) total FA area (pixels), (ii) YFP-paxillin intensity density, and (iii) number of FAs (ROIs) were plotted to assess focal adhesion responses over time. CalyculinA treatment led to progressive increases in FA area, intensity, and number of ROIs for most cells. Y-27632 caused rapid FA area and intensity loss, followed by partial recovery and formation of new protrusions. Para-amino-blebbistatin induced similar initial FA shrinkage but no recovery or additional ROI formation. These measurements quantitatively confirm the differential effects of contractility-modulating drugs on focal adhesion stability and dynamics.*

3. 4. 2. Single particle tracking under the effect of drugs shows moderate to intense effects on talin dynamics

In order to investigate how pharmacologically induced changes in actomyosin contractility alter talin behavior, we performed single-particle tracking photoactivated localization microscopy (sptPALM) on MEFs expressing one of four mEos3.2-tagged talin constructs (Neck, R3, R12 or C-

terminus tagged). This allowed us to probe whether specific mechanical perturbations differentially affect talin mobility in FAs and surrounding membrane regions.

In the following subsections, we detail the effects of each drug, beginning with CalyculinA (increased contractility), followed by Y-27632 and para-amino-blebbistatin (decreased contractility), describing both qualitative changes in reconstructed trajectories and quantitative shifts in diffusion parameters.

3. 4. 2. 1. Increased contractility through CalyculinA mildly restricts talin mobility only at talin-neck

To check if and how does CalyculinA affect talin dynamics, MEFs expressing mEos3.2-tagged talin constructs (Neck, R3, R12 or C-terminal tagged) were treated with 20 nM CalyculinA for 30 min or with a Ringer solution containing the same amount of DMSO (control). Each dataset included a widefield YFP-paxillin image to generate FA masks, followed by 400 s sptPALM acquisitions at 20 ms/frame under TIRF illumination. Localizations were linked into trajectories and classified into immobile ($D < 0.008$ $\mu m^2/s$), confined, or freely diffusive modes using mean square displacement analysis. Data were analyzed separately inside and outside FA masks.

Qualitatively, super-resolved reconstructions and color-coded trajectories (Figure 72) showed no visible differences for R3, R12, or C-term tagged constructs after treatment. For talin-neck, there appeared to be a modest reduction in purple (diffusive) trajectories both inside and outside FAs.

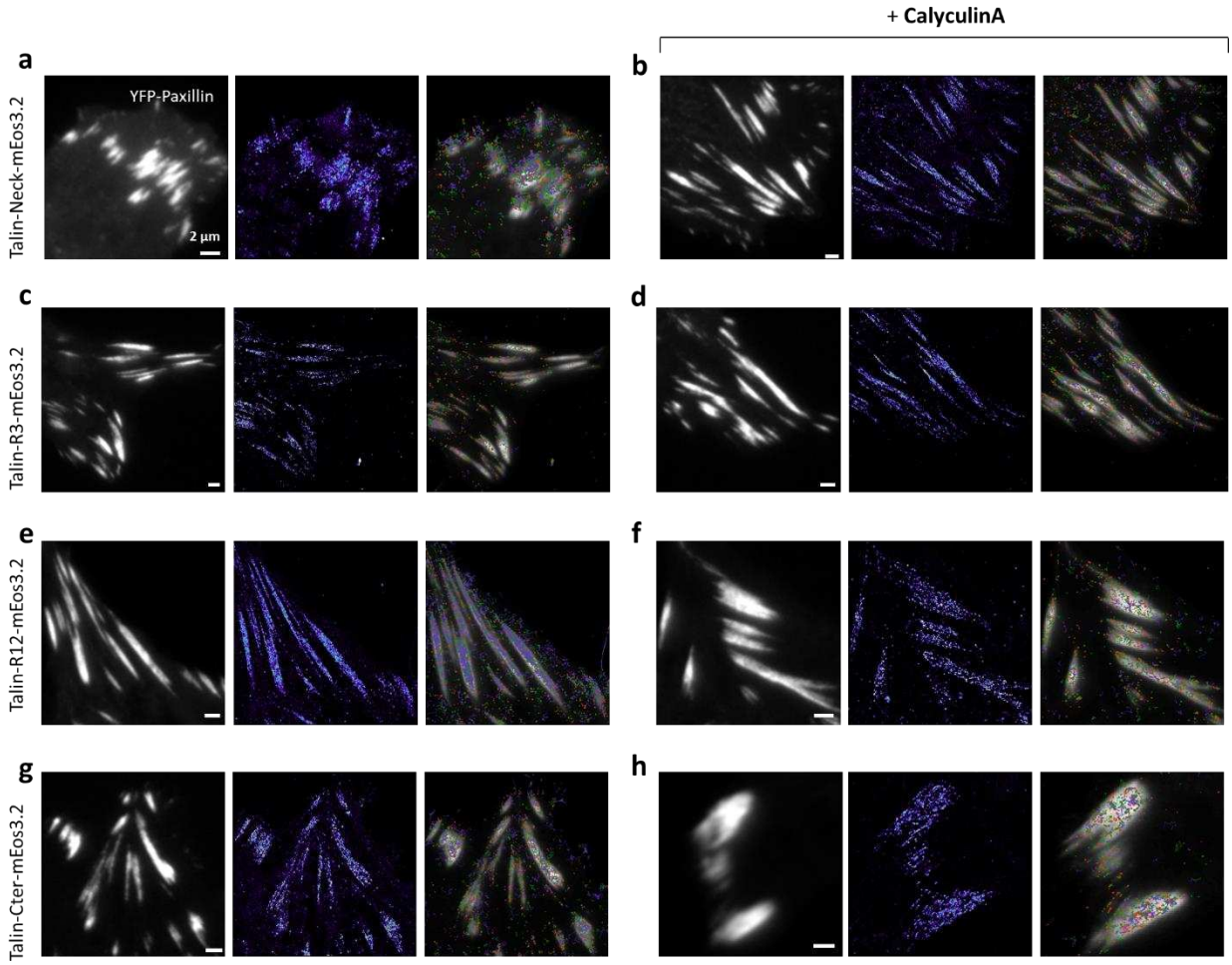

Figure 72. ***CalyculinA produces no overt trajectory-level change for most talin constructs; talin-neck shows a modest reduction of visually diffusive tracks****. MEFs expressing mEos3.2-tagged talin (Neck, R3, R12, C-term) were treated with 20 nM CalyculinA for 30 min, then imaged by sptPALM under TIRF (400 s, 50 ms/frame). Left: YFP-paxillin image and FA masks. Middle: super-resolution reconstructions from sptPALM localizations. Right: color-coded trajectories overlaid on FA map (purple-diffusive, green-confined, red-immobile). Panels: (**a**) Neck control, (**b**) Neck + CalA, (**c**) R3 control, (**d**) R3 + CalA, (**e**) R12 control, (**f**) R12 + CalA, (**g**) C-term control, (**h**) C-term + CalA. Scale bar: 2 µm.*

Quantitatively inside FAs (Figure 73, Figure 74, Figure 75), the log(D) distribution only for talin-neck shifted toward lower diffusion values after CalyculinA treatment (Figure 73), suggesting a slight increase in slower-moving tracks. From Figure 74, we can see that the fraction of diffusive molecules showed a noticeable change only in the case of R12 tagged talin after CalyculinA treatment (a decrease of ~9%). D_{diff} (D of freely diffusive molecules) showed no statistical difference between control and treatment (Figure 75).

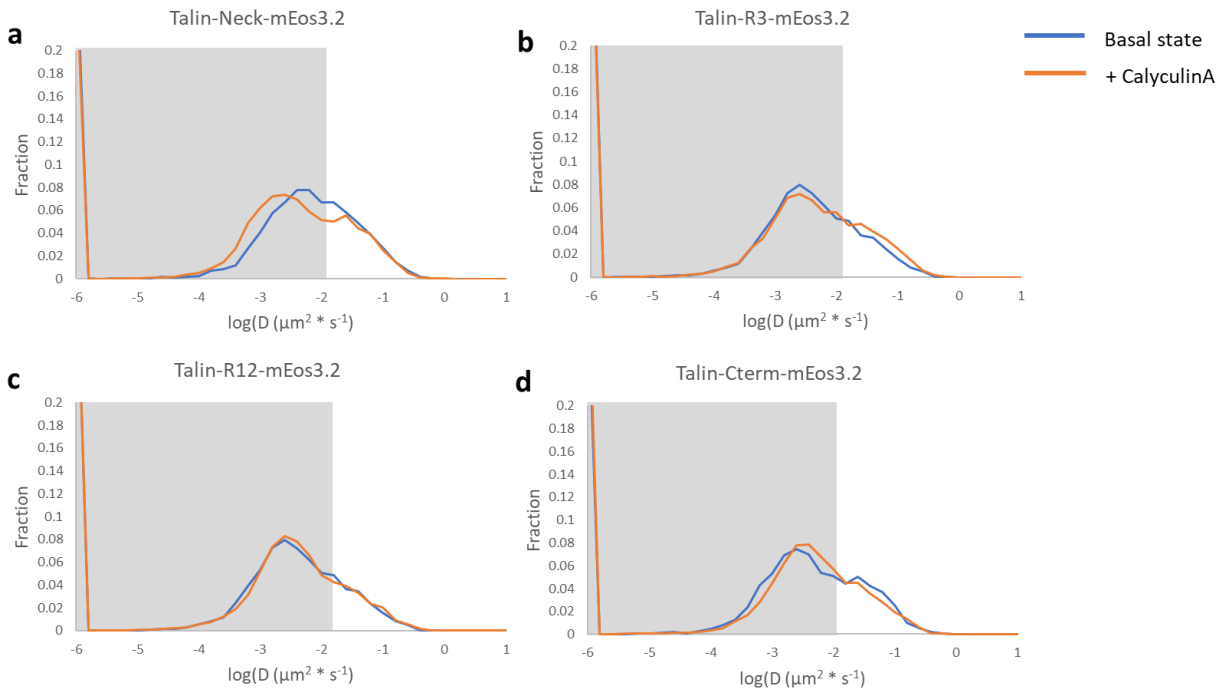

Figure 73. ***Inside FAs, only talin-neck shows a slight shift of log(D) toward lower values after CalyculinA treatment****. Log(D) distributions (mean across cells) for trajectories ≥260 ms inside FA masks; grey shading marks immobile threshold (D < 0.008 µm²/s). n=3 control cells and n=4 CalyculinA-treated cells per construct (Neck, R3, R12, C-term).*

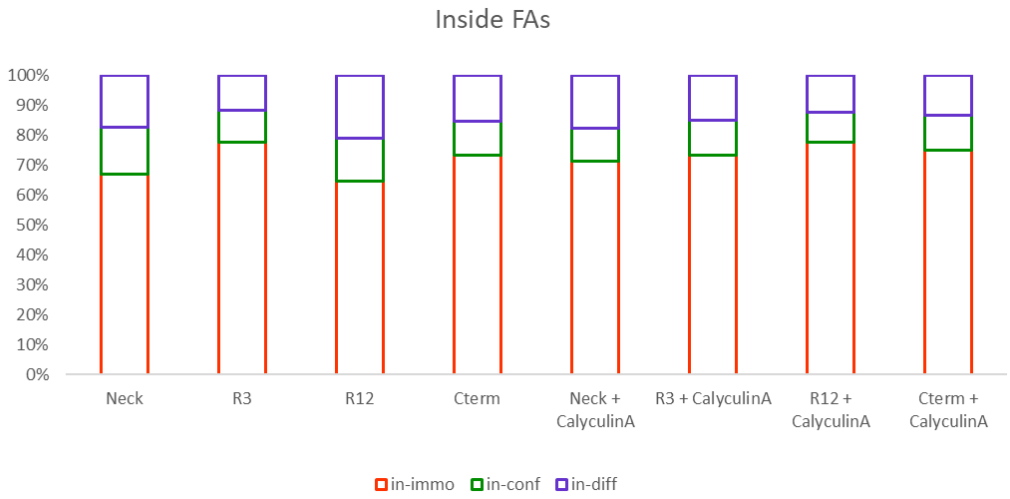

Figure 74. ***Inside FAs, fractional populations change minimally after CalyculinA; only R12 shows a noticeable drop in diffusive fraction (~9%)****. Mean percentages for all cells of diffusive, confined, and immobile trajectories (≥260 ms) inside FA masks. n=3 control and n=4 treated cells per construct*

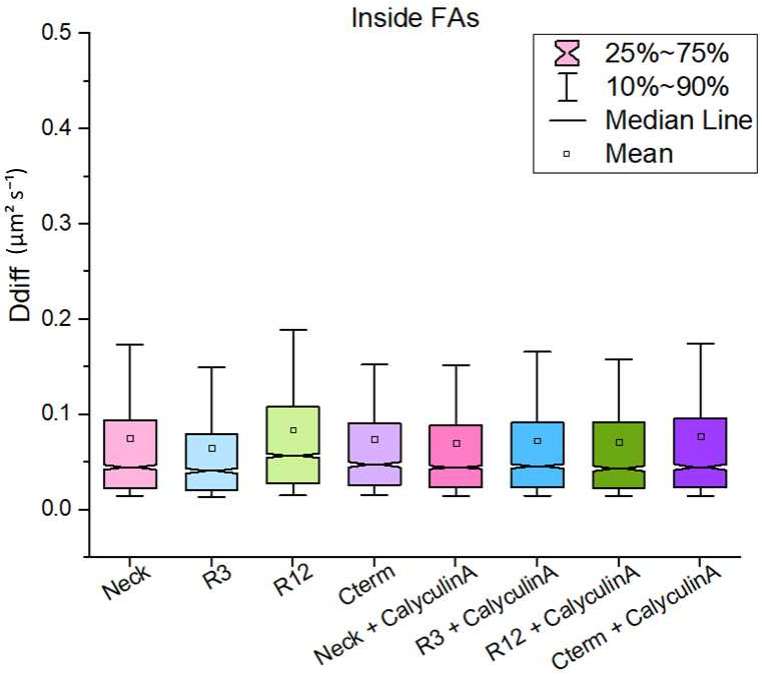

Figure 75. ***Inside FAs, the diffusion coefficient of the freely diffusive population (D_{diff}) is not significantly altered by CalyculinA****. Median D_{diff} for all cells for freely diffusive trajectories (classification via MSD), comparing control vs. CalyculinA for each construct; n=3 control and n=4 treated cells.*

Taken together, these results showed that, inside FAs, overall mobility of talin constructs was largely unaffected by acute contractility enhancement.

Outside FAs, we also examined whether CalyculinA-induced contractility changes altered talin mobility. For each construct, we analyzed the log(D) distribution (Figure 76), the fractions of diffusive, confined, and immobile tracks (Figure 77), and the diffusion coefficient of the freely diffusive population (D_{diff}) (Figure 78).

The most visible change was for talin-neck, where the log(D) distribution shifted toward lower values after treatment, suggesting a subtle bias toward slower dynamics. In terms of fractional populations, the diffusive fraction decreased by ~1.8%, −1.2%, 6.5%, and 1.2% for the neck, R3, R12, and C-terminal constructs, respectively, with only the R12 decrease being clearly noticeable. D_{diff} values remained statistically unchanged for all constructs.

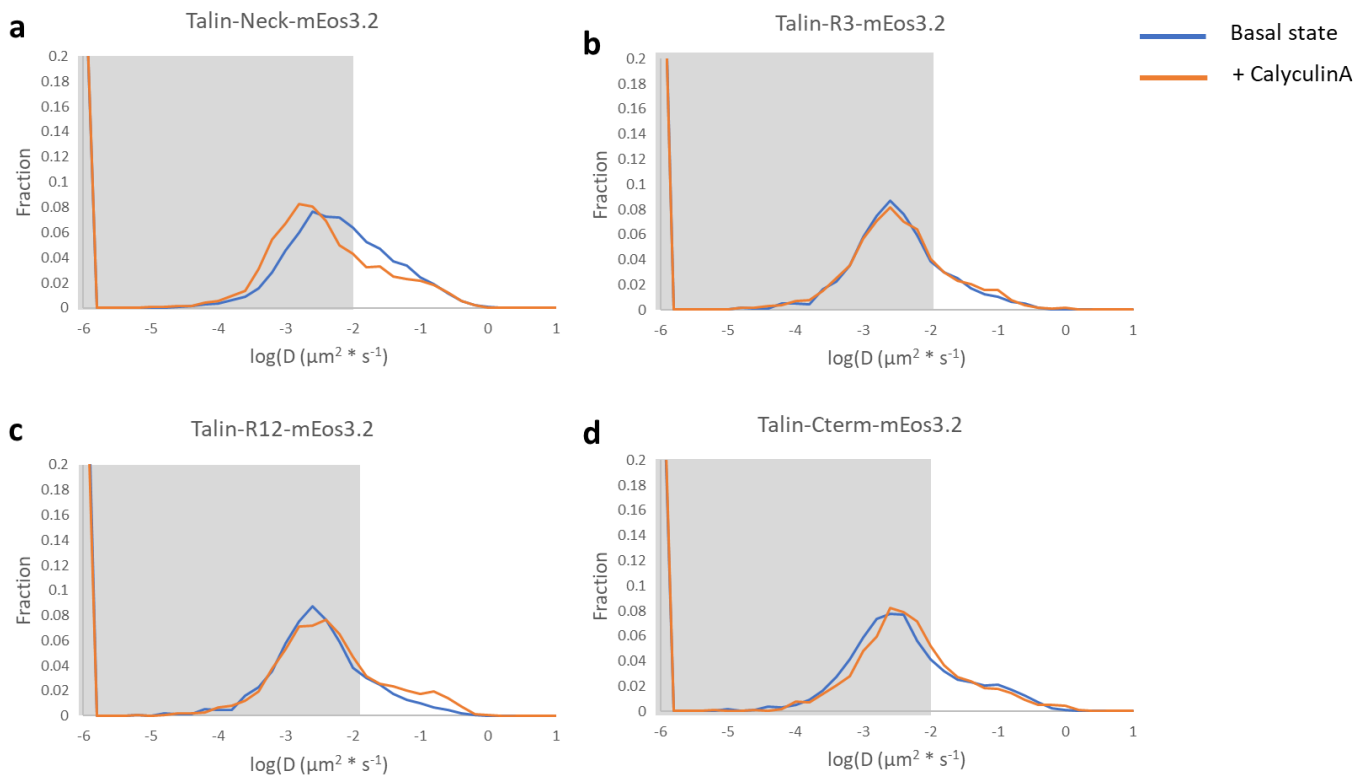

Figure 76. ***Outside FAs, talin-neck log(D) shifts slightly toward lower values after CalyculinA, while other constructs remain largely unchanged****. Per-cell log(D) distributions (mean across cells) for trajectories ≥260 ms outside FA masks; grey shading indicates D < 0.008 µm²/s. n=3 control and n=4 treated cells per construct.*

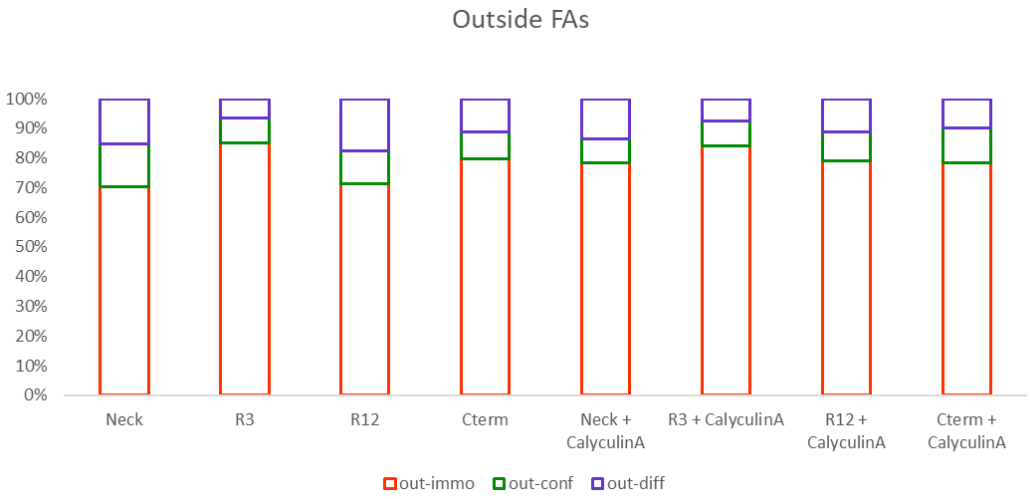

Figure 77. ***Outside FAs, only R12 exhibits a noticeable reduction in the diffusive fraction (~6.5%) after CalyculinA; other constructs change by ≤~2%****. Mean percentages of diffusive, confined, and immobile trajectories (≥260 ms) outside FA masks. Diffusive fraction changes (CalA minus control): Neck −1.8%, R3 +1.2%, R12 −6.5%, C-term −1.2%. n=3 control and n=4 treated cells per construct.*

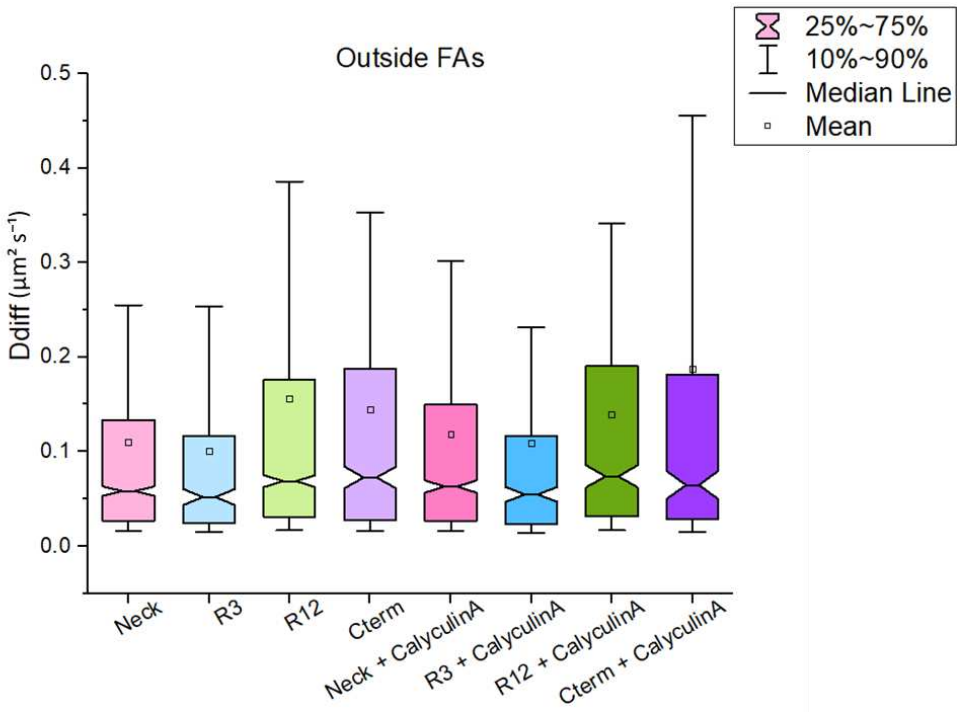

Figure 78. ***Outside FAs, D_{diff} remains statistically unchanged across all talin constructs after CalyculinA.*** *A Median D_{diff} for all cells for freely diffusive trajectories (classification via MSD), outside FAs, comparing control vs. CalyculinA for each construct; n=3 control and n=4 treated cells.*

To conclude, outside FAs, CalyculinA produced only minor changes in talin mobility. Talin-neck showed a small shift in log(D) toward lower values, and R12 exhibited a ~6.5% reduction in its diffusive fraction. Other constructs showed negligible changes in both fractional populations and D_{diff}, indicating that enhanced contractility exerts minimal influence on talin dynamics outside FAs.

These findings, of course, do not discourage further use of CalyculinA in our studies, as the dynamics of the protein do not necessarily have to correlate with its orientation.

3. 4. 2. 2. Reduced contractility via RhoK inhibition slightly enhances talin diffusion across FAs

In order to assess whether lowering actomyosin contractility alters talin mobility, MEFs expressing one of four mEos3.2-tagged talin constructs (Neck, R3, R12 or C-terminus tagged) and YFP-Paxillin were treated with 15 µM Y-27632 for 15 min, or with DMSO-containing Ringer solution as control. Imaging and data analysis was performed in the same manner as for CalyculinA.

Qualitatively, super-resolved reconstructions and color-coded trajectories (Figure 79) showed a modest increase in purple (diffusive) tracks for all constructs after Y-27632 treatment, consistent with the expectation of reduced mechanical restraint.

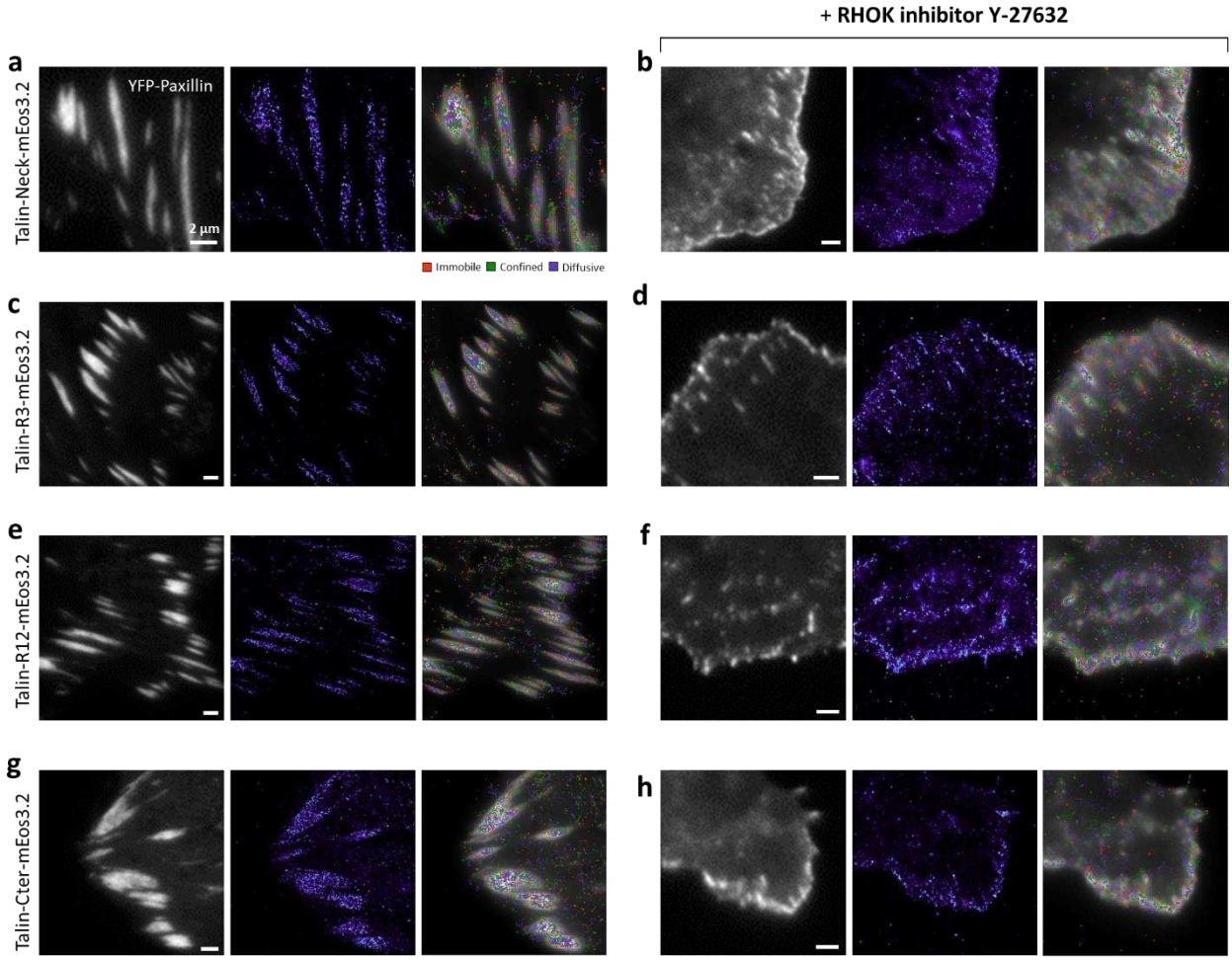

Figure 79. ***RhoK inhibition (using Y-27632) modestly increases diffusive talin trajectories within FAs across constructs****. MEFs expressing mEos3.2-tagged talin (Neck, R3, R12, C-term) were treated with 20 µM Y-27632 for 15 min, then imaged by sptPALM under TIRF (400 s, 50 ms/frame). Left: YFP-paxillin FA map. Middle: super-resolution reconstructions. Right: trajectories color-coded by mode (purple-diffusive, green-confined, red-immobile). Panels (a-h) correspond to control vs. treated for each construct. Scale bar: 2 µm.*

For each construct and condition, we computed log(D) distributions, the fractions of diffusive/confined/immobile trajectories, and the diffusion coefficient of the freely diffusing subpopulation (D_{diff}). This quantitative analysis restricted to inside FAs showed a small decrease in confinement and immobilization upon Y-27632 treatment when we look at the coefficient of diffusion distribution for each construct (Figure 80). The fraction of immobile molecules also slightly decreased upon Y-27632 treatment (Figure 81) (by ~3.5%, 4%, 7% and 6.3% for neck, R3,

R12 and Cterm, respectively). D_{diff} (D of freely diffusing molecules) showed no statistically different results between the control and the treatment with Y-27632 (Figure 82).

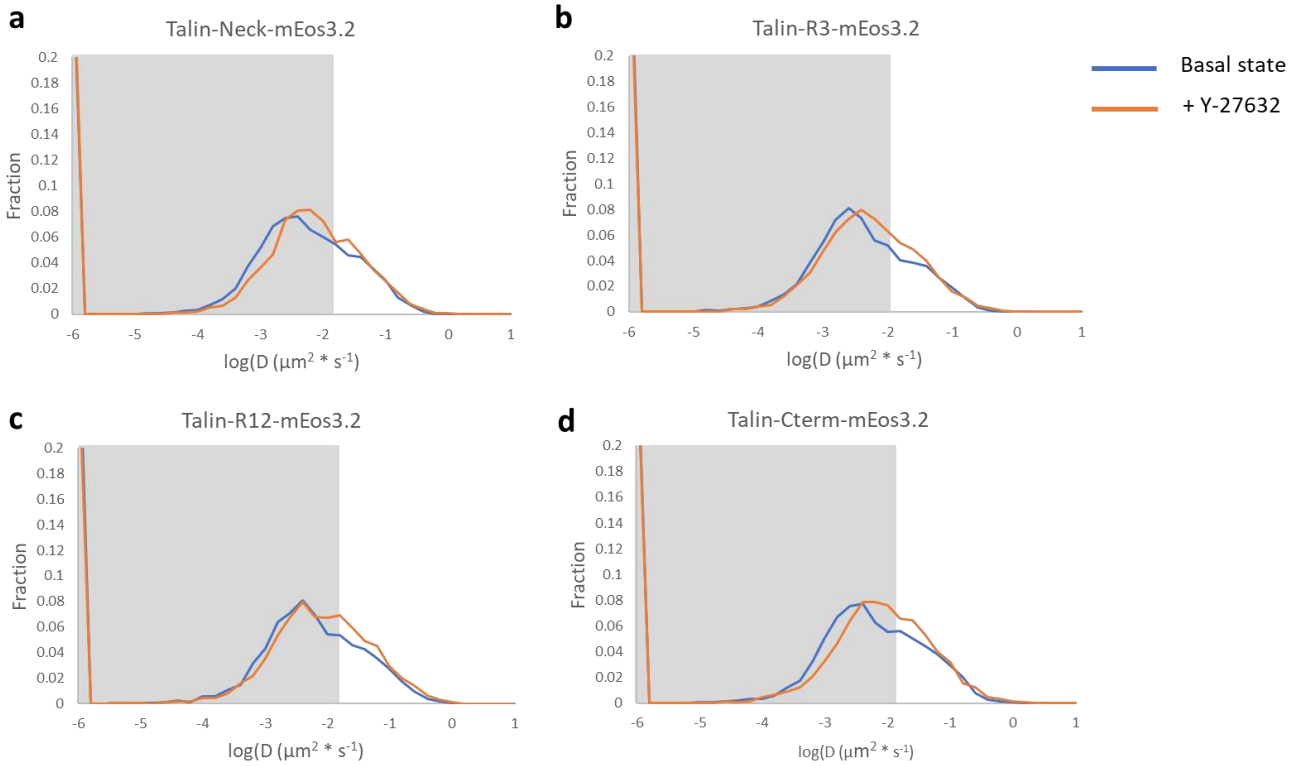

Figure 80. ***Inside FAs, Y-27632 slightly shifts log(D) distributions toward higher values, consistent with mildly faster talin mobility****. Log(D) distributions (mean across cells) for trajectories ≥260 ms within FA masks; grey shading marks immobile threshold (D < 0.008 μm²/s). n=3 control and n=4 treated cells per construct.*

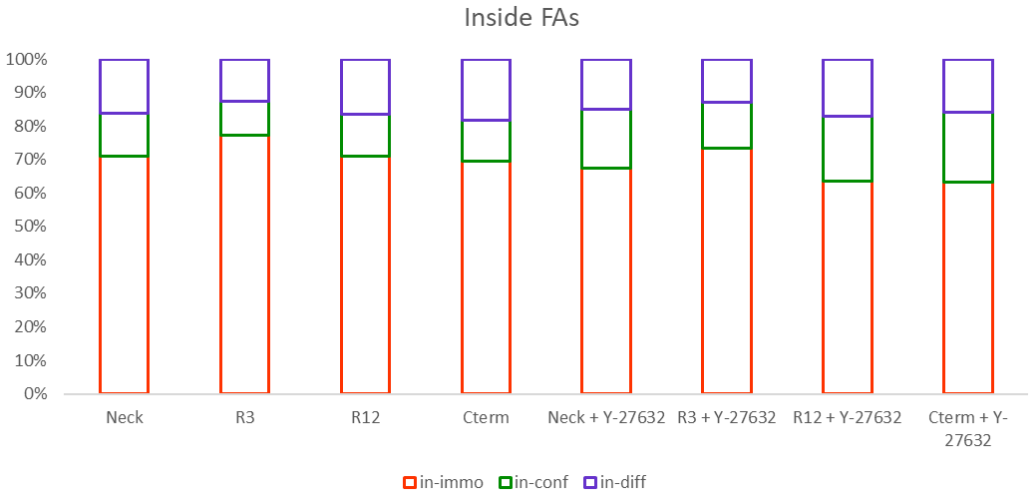

Figure 81. ***Inside FAs, Y-27632 modestly reduces the immobile fraction and increases the diffusive fraction across constructs****. Per-cell mean percentages of diffusive, confined, and immobile trajectories (≥260 ms) inside FA masks.*

The immobile fraction decreases by ~3.5% (Neck), ~4% (R3), ~7% (R12), and ~6.3% (C-term) relative to control. n=3 control and n=4 treated cells per construct

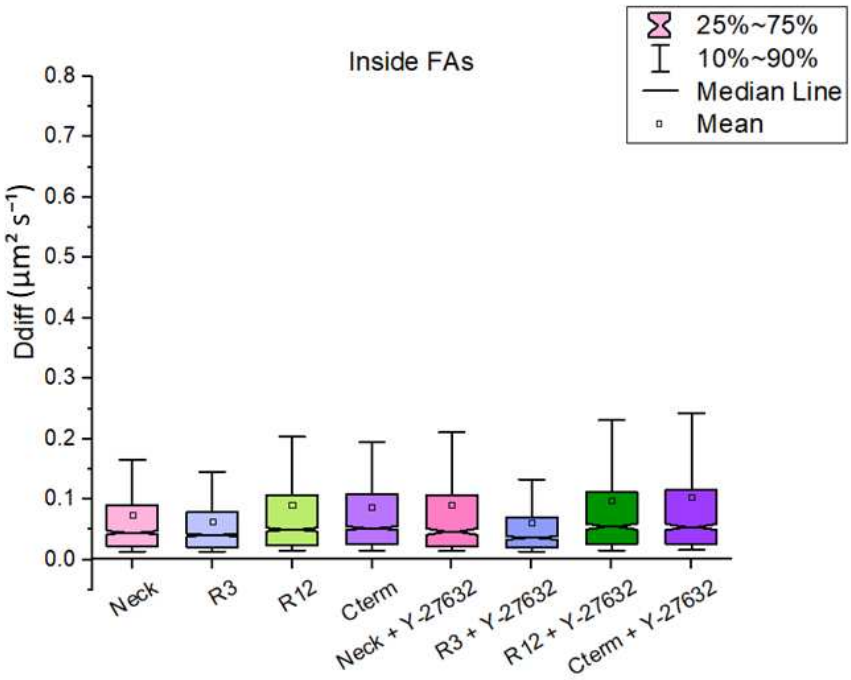

Figure 82. ***Inside FAs, the diffusion coefficient of freely diffusive talin (D_{diff}) is not significantly altered by Y-27632.*** *Median Ddiff for all cells for freely diffusive trajectories (classification via MSD), inside FA masks, control vs. Y-27632. n=3 control and n=4 treated cells per construct.*

In order to test whether lowering actomyosin contractility relaxes talin dynamics more strongly outside focal adhesions (FAs) than inside them, we quantified talin mobility specifically outside FA masks following Rho-kinase inhibition with Y-27632.

Outside FAs, Y-27632 shifted the diffusion coefficient distribution toward higher values across all four tagging positions (Figure 83) and increased the diffusive and confined fractions with a corresponding reduction of immobile trajectories (Figure 84). More precisely, the fraction of diffusive molecules outside FAs after RhoK inhibition increased by ~4%, 6.5%, 8.7% and 10.6%, for Neck, R3, R12 and Cterm respectively. The immobile population decreased by ~11%, 12.6%, 16% and 19.7% for the same constructs. Importantly, the mobility increase was more pronounced outside than inside FAs: D_{diff} rose outside FAs with Y-27632 (Figure 84) (between 0.5 and 1 µm²/s, depending on the construct), whereas inside FAs D_{diff} showed no detectable change (Figure 82).

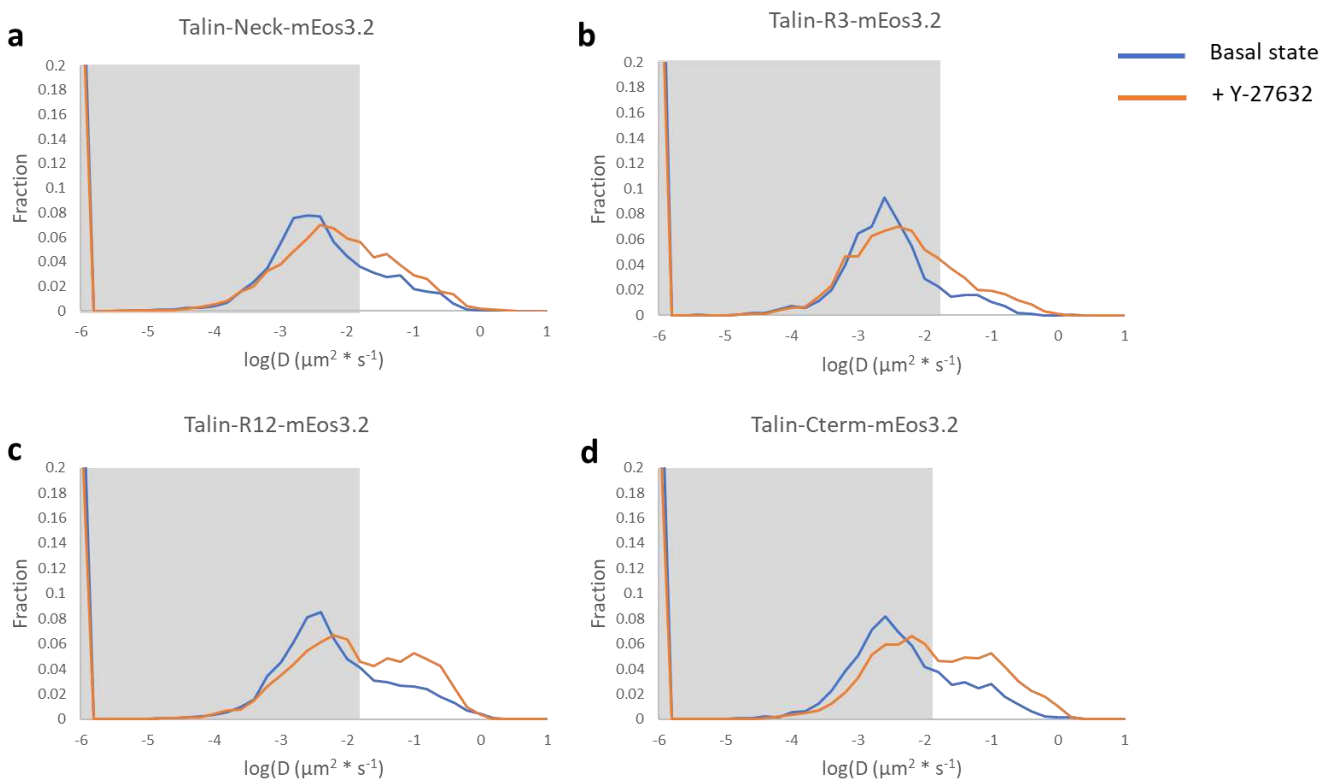

Figure 83. ***Outside FAs, Y-27632 shifts talin log(D) distributions toward faster diffusion****. Distributions of log(D) (mean across cells) for trajectories ≥ 260 ms recorded outside FA masks; grey shading marks the immobile threshold (D < 0.008 µm² s⁻¹). n = 3 control and n = 4 Y-27632-treated cells per construct.*

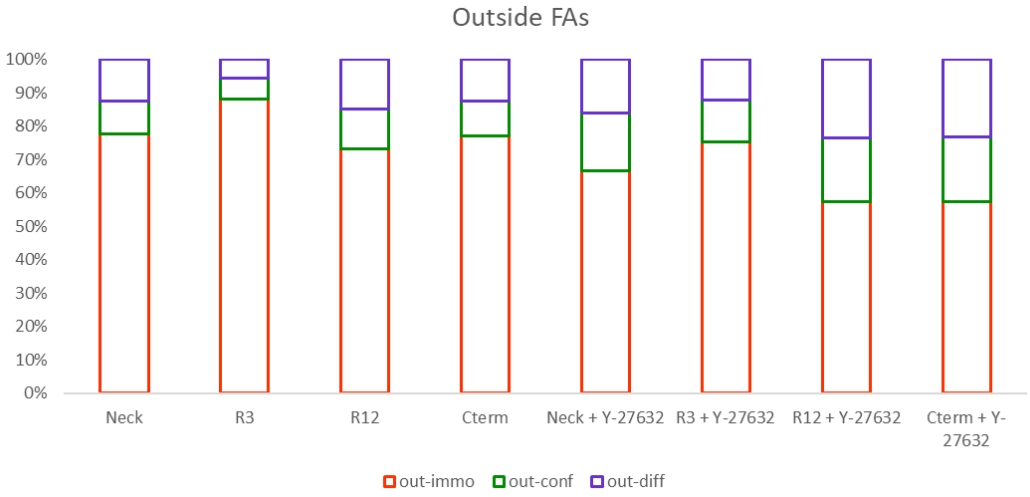

Figure 84. ***Outside FAs, Y-27632 increases the diffusive and confined fractions and decreases the immobile fraction across all talin tagging positions****. Bars show mean percentages for all cells for trajectories ≥ 260 ms outside FA masks. The fraction of diffusive molecules outside FAs after RhoK inhibition increased by ~4%, 6.5%, 8.7% and 10.6%, for Neck, R3, R12 and Cterm respectively. The immobile population decreased by ~11%, 12.6%, 16% and 19.7% for the same constructs. n = 3 control and n = 4 Y-27632-treated cells per construct.*

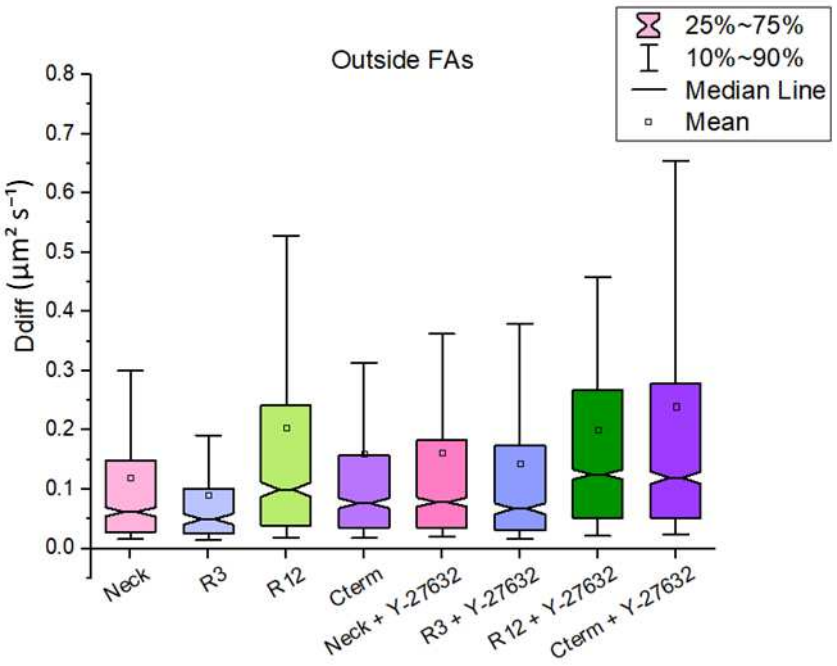

Figure 85. ***Outside FAs, the diffusion coefficient of freely diffusing talin (Ddiff) increases with Y-27632 across constructs, contrasting with the lack of change inside FAs*** *(see Figure 82). n = 3 control and n = 4 Y-27632-treated cells per construct.*

These changes suggest that RhoK inhibition somewhat reduces force transmission through talin, slightly increasing its mobility both inside and outside FAs. This confirmed that we can use it to study talin orientation in decreased contractility conditions using Y-27632 RhoK inhibitor.

3. 4. 2. 3. Talin becomes highly diffusive under the effect of para-amino-blebbistatin

In order to probe talin dynamics under myosin II inhibition and to evaluate whether extreme loss of contractility produces large, measurable changes in molecular mobility, we treated cells with para-amino-blebbistatin, a photostable derivative of blebbistatin that directly inhibits myosin II ATPase activity and strongly reduces cellular tension. The goal was to compare these results to the moderate Y-27632 effect and to decide which lowered-contractility condition should be used in our single-molecule polarization (4Polar3D) measurements.

To do so, MEFs expressing one of four mEos3.2-tagged talin constructs (Neck, R3, R12, C-terminus) and YFP-paxillin were treated with 50 µM para-amino-blebbistatin (control = DMSO in Ringer) 30 minutes prior to imaging. Imaging and data analysis was performed in the same manner as for CalyculinA and Y-27632.

Visual inspection of super-resolved reconstructions and color-coded trajectories (Figure 86) reveals a marked increase in purple (diffusive) tracks for all constructs following para-amino-blebbistatin treatment, even within FA boundaries.

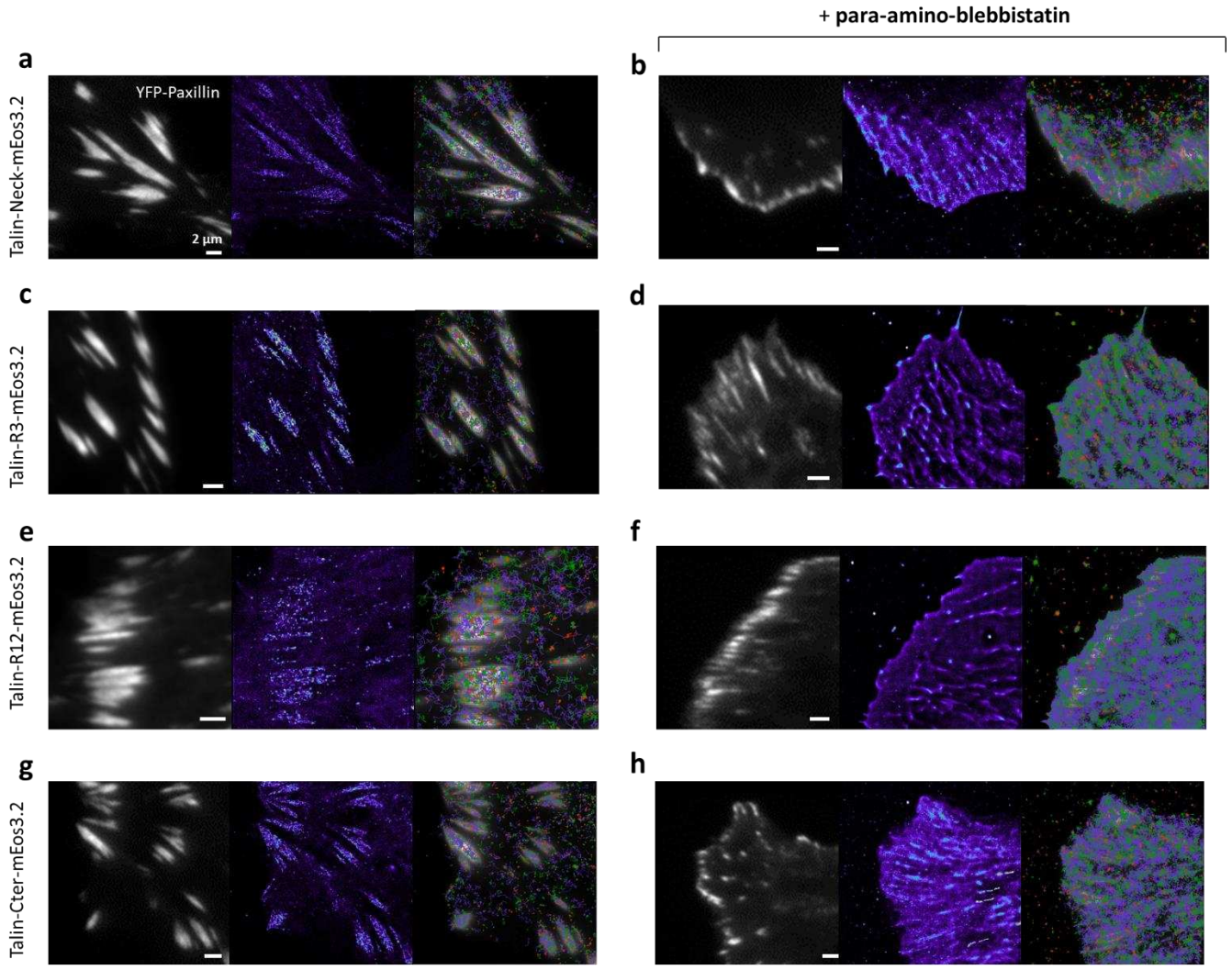

Figure 86. ***Para-amino-blebbistatin treatment produces abundant diffusive talin trajectories****. MEFs expressing talin-mEos3.2 constructs were treated with 50 µM para-amino-blebbistatin (or DMSO control) in Ringer solution and imaged by sptPALM under TIRF (400 s, 50 ms/frame). Left: YFP-paxillin widefield image; Middle: sptPALM super-resolution reconstruction; Right: trajectories color-coded by diffusion mode (purple-diffusive, green-confined, red-immobile) over FA masks. Panels: (**a**) Neck control, (**b**) Neck + para-amino-blebbistatin, (**c**) R3 control, (**d**) R3 + para-amino-blebbistatin, (**e**) R12 control, (**f**) R12 + para-amino-blebbistatin, (**g**) C-term control, (**h**) C-term + para-amino-blebbistatin. Scale bar: 2 µm.*

Quantitatively, the log(D) distributions inside FAs (Figure 87) shift substantially toward higher values upon treatment, indicating a larger pool of fast-moving detections. The fraction of immobile and confined molecules inside FAs decreases dramatically after para-amino-

blebbistatin (Figure 87), and the diffusive population increased. This is observed for all constructs and is the strongest effect among the three drugs tested. Inside FAs, after p-amino-blebbistatin application, we saw a ~14%, 17.5%, 27.5% and 20.5% increase in diffusive population for talins tagged at the neck, R3, R12 and Cterm respectively.

D_{diff}, the diffusion coefficient of the freely diffusive population inside FAs (Figure 88), increases substantially for most constructs; notably, the C-terminus tagged talin displays an approximate median D_{diff} increase of ~0.27 $\mu m^2 s^{-1}$. This magnitude of change confirms a large enhancement of the freely diffusing subpopulation inside adhesions.

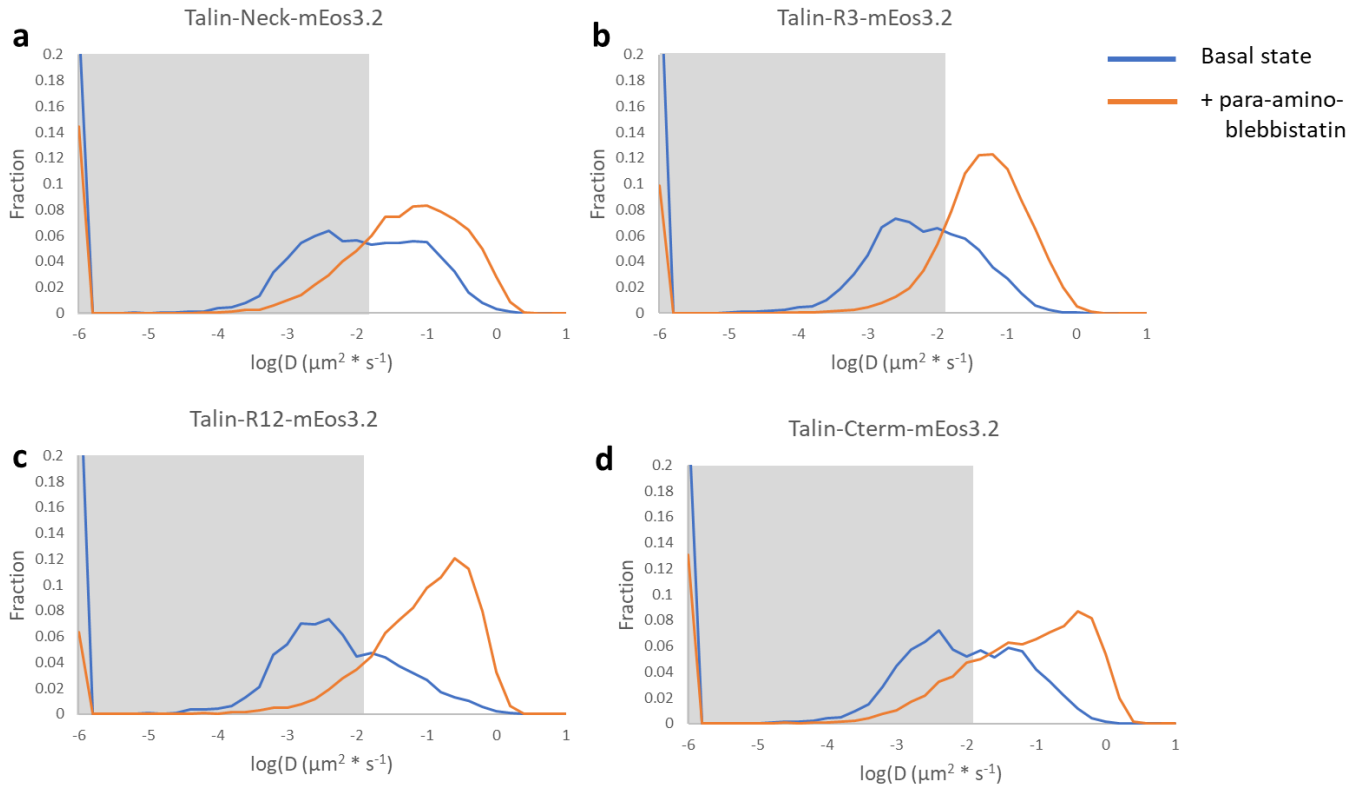

Figure 87. ***Inside focal adhesions, para-amino-blebbistatin treatment markedly shifts the distribution of diffusion coefficients toward higher values across all talin constructs.*** *Shown are histograms of log(D) for trajectories of ≥260 ms duration inside FA masks, comparing control (blue) and para-amino-blebbistatin–treated (orange) cells. The grey shaded area corresponds to immobile trajectories ($D < 0.008\ \mu m^2 s^{-1}$). For each construct, the treatment induces a rightward shift in the distribution, reflecting increased molecular mobility. Cell counts: n = 3 control, n = 4 treated; exceptions are R12 (n = 4 control) and R3 (n = 5 treated).*

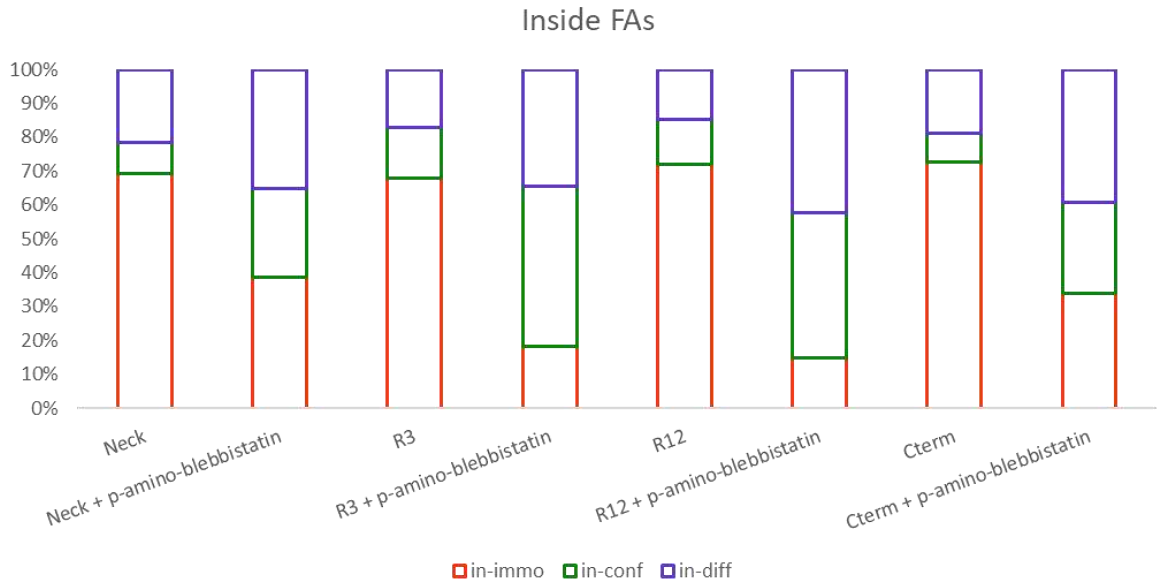

Figure 88. ***Para-amino-blebbistatin strongly reduces the immobile and confined fractions of talin inside FAs, with a corresponding increase in the diffusive population****. Bars represent mean percentages (for all cells) of trajectories (≥260 ms) classified as diffusive, confined, or immobile inside FA masks. Across all constructs, treatment leads to pronounced depletion of the immobile fraction.*

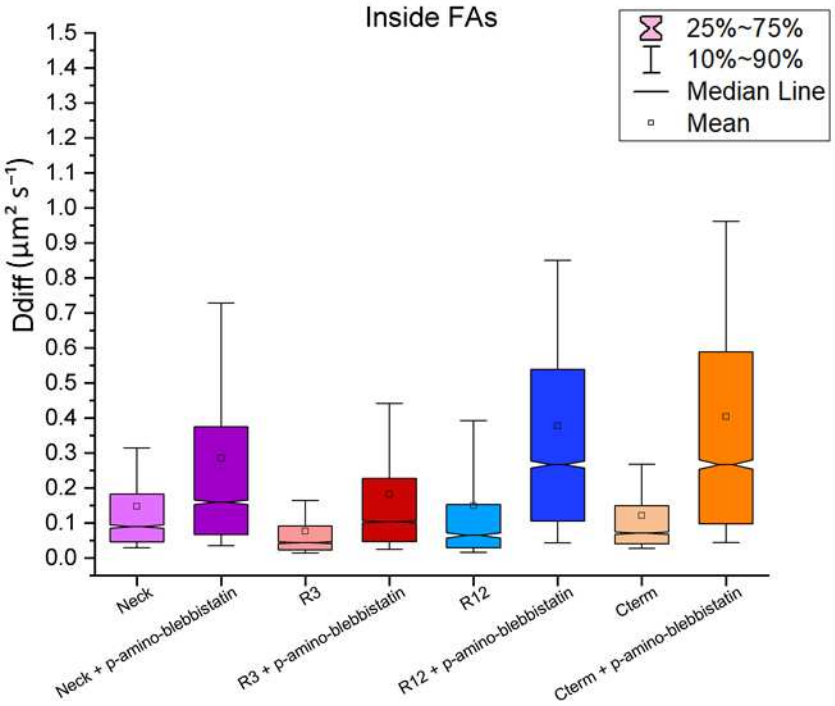

Figure 89. ***Freely diffusive talin molecules inside FAs display markedly higher diffusion coefficients after para-amino-blebbistatin treatment****.* D_{diff} *values for trajectories classified as diffusive inside FA masks, obtained by MSD analysis. All constructs exhibit a positive shift post-treatment, with the largest median increase observed for C-terminally tagged talin (~0.27 μm² s⁻¹). Cell counts as in Figure 87.*

Outside FAs, the effect is even stronger: the log(D) distributions for all constructs shift markedly toward higher values (Figure 90).

The diffusive fraction outside FAs increases a dramatically after para-amino-blebbistatin treatment (Figure 91): by approximately ~9%, 21%, 22% and 23% for neck, R3, R12 and Cterm, respectively. These increases indicate a mass conversion of molecules from immobile/confined states into a diffusive pool. Correspondingly, D_{diff} outside FAs increases markedly, with per-construct median increases on the order of ~0.1-0.4 $\mu m^2 s^{-1}$ depending on the tagging site (Figure 92). Together, these data show that para-amino-blebbistatin produces the largest mobility change of the three drugs tested, both inside and outside adhesions.

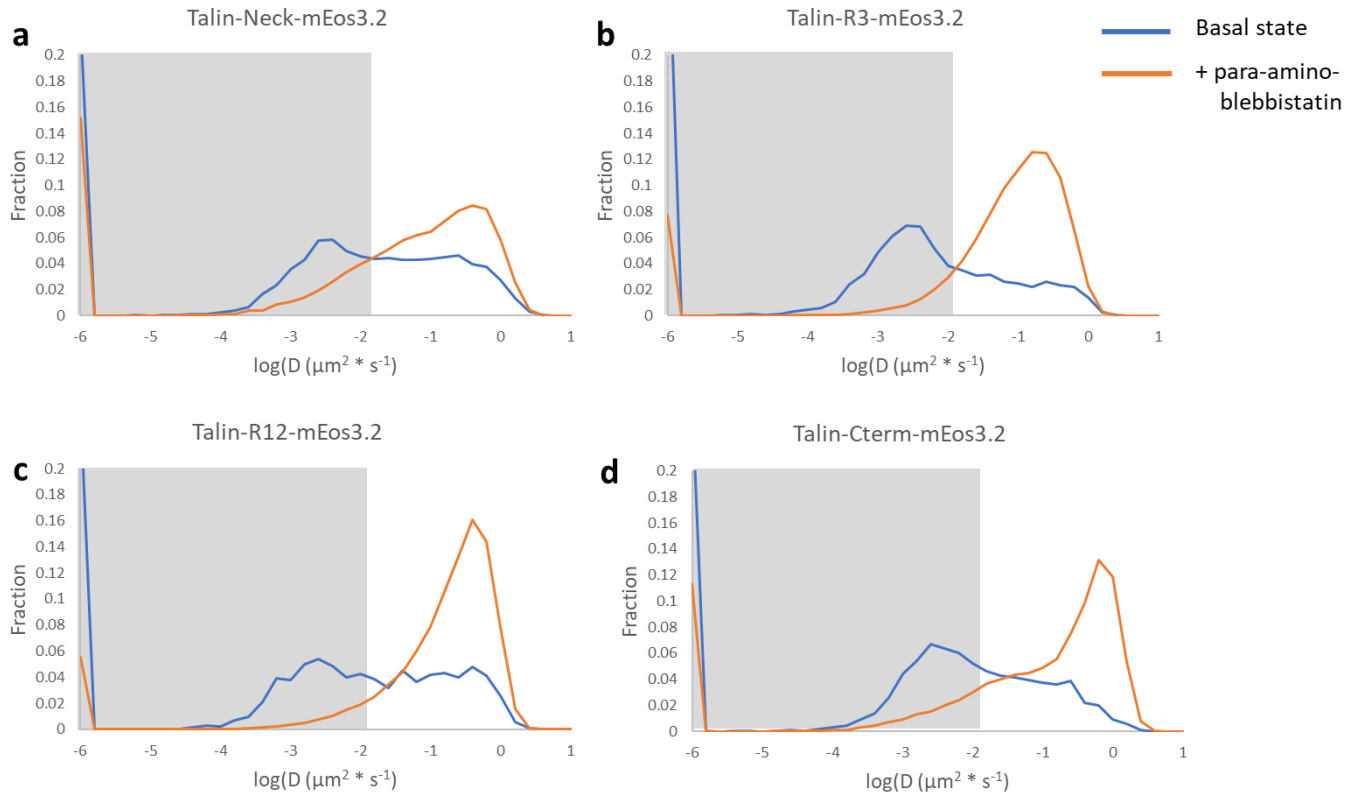

Figure 90. ***Outside FAs, para-amino-blebbistatin induces a pronounced shift in log(D) distributions toward faster dynamics for all constructs****. Log(D) for trajectories ≥260 ms outside FA masks are shown, with control (blue) and para-amino-blebbistatin (orange). Grey shading marks the immobile pool of molecules (D < 0.008 μm² s⁻¹). This shift reflects a substantial redistribution of talin molecules from immobilized to faster diffusive states.*

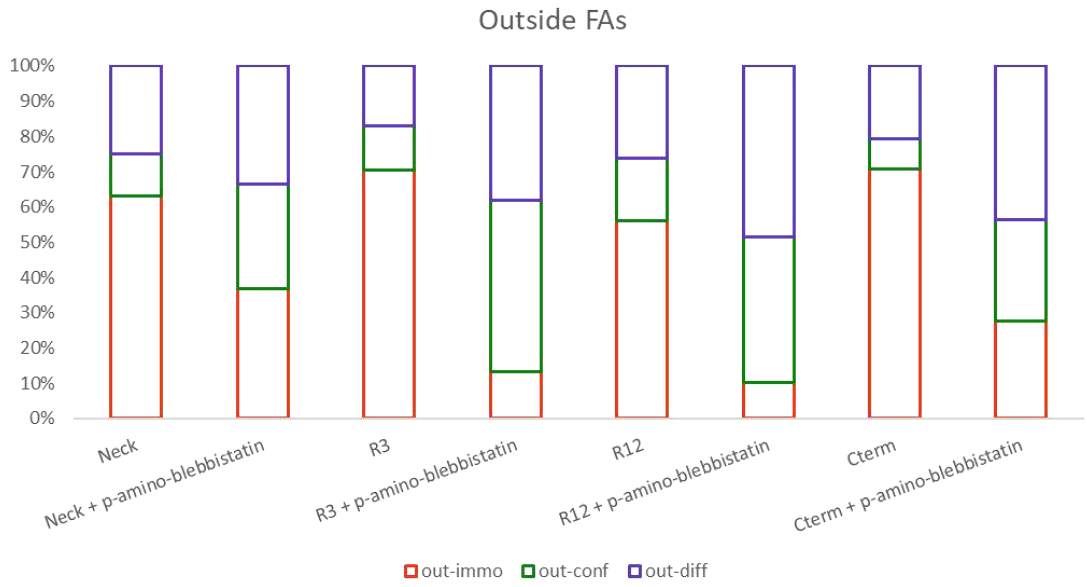

Figure 91. ***Para-amino-blebbistatin drastically decreases the immobile fraction of talin outside FAs, accompanied by increases in both confined and diffusive populations.*** *Percentages of trajectories (≥260 ms) outside FA masks are shown for each diffusion mode (immobile, confined, diffusive). Immobile fraction reductions are approximately −30% (Neck), −15% (R3), −10% (R12), and −40% (C-term). n = 3 control, n = 4 treated.*

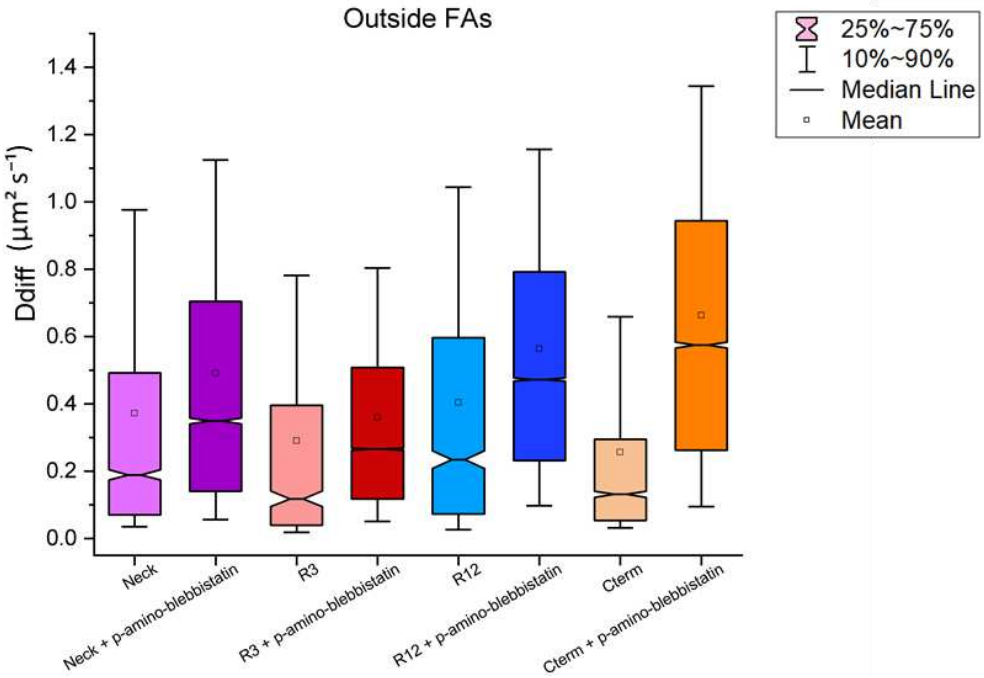

Figure 92. ***Outside FAs, the freely diffusive population of talin exhibits large increases in D_{diff} after para-amino-blebbistatin treatment.*** *D_{diff} values for trajectories classified as diffusive outside FA masks. All constructs show an increase of ~0.1–0.4 μm² s⁻¹, consistent with substantial loosening of molecular confinement. n = 3 control, n = 4 treated.*

These data demonstrate that para-amino-blebbistatin produces a severe loss of talin immobilization and confinement, dramatically increasing the diffusive pool. While this confirms that strong myosin II inhibition effectively uncouples talin from force-bearing interactions, the resulting high mobility is problematic for single-molecule polarization microscopy performed with our 185 ms exposure time: motion blur and the high fraction of short, rapidly moving detections reduce the reliability of orientation retrieval (ρ, η, δ) and increase uncertainty in recovered orientation distributions. Therefore, although para-amino-blebbistatin is an effective tool to use in order to probe the mechanics of talin disengagement, it is generally incompatible with our current 4Polar3D live-cell orientation measurements.

We then concluded that Y-27632 or vinculin KO conditions provide a better balance between altering contractility and preserving sufficient molecular dwell time for reliable orientation readout.

3. 5. Next step: observing talin orientation under the effect of pharmacological drugs and in Vinculin KO cells

3. 5. 1. Photoselection issue

Our next step was to explore orientation in conditions with enhanced contractility with the use of CalyculinA, or in VinculinKO cells, due to their effect on mechanical tension transmitted through talin (Ringer et al., 2017). As a first step in our new batch of experiments, we wanted to reproduce the data obtained in basal state (no drugs, WT MEFs), and to, of course, have it as a control. To do so, we performed the experiment according to the same protocols as described in chapter 3.2. of the results (*In-plane orientation (ρ) reveals axial gradients along the talin molecule in basal conditions*) (MEFs transfected with one of four talin-mEos3.2 + YFP-Paxillin, TIRF, 20 000 frames, 185s exposure time).

Unfortunately, during this set of experiments, we encountered a strong photoselection, due to a polarization bias in the excitation beam. This means we primarily excited mEos3.2 at an in-plane angle (ρ) of ~90˚ in most cases. This photoselection is clearly apparent in Figure 93, where both in the figures with sticks that color code ρ (upper panel), as well as the polar histograms of raw ρ (not rotated to follow the mean orientation of the FAs) (lower panel), displayed a preferential

orientation. Therefore, before comparing drug-treated vs. control cells, or wild-type vs. knockout conditions, we needed to quantify and minimize the contribution of photoselection in our imaging setup.

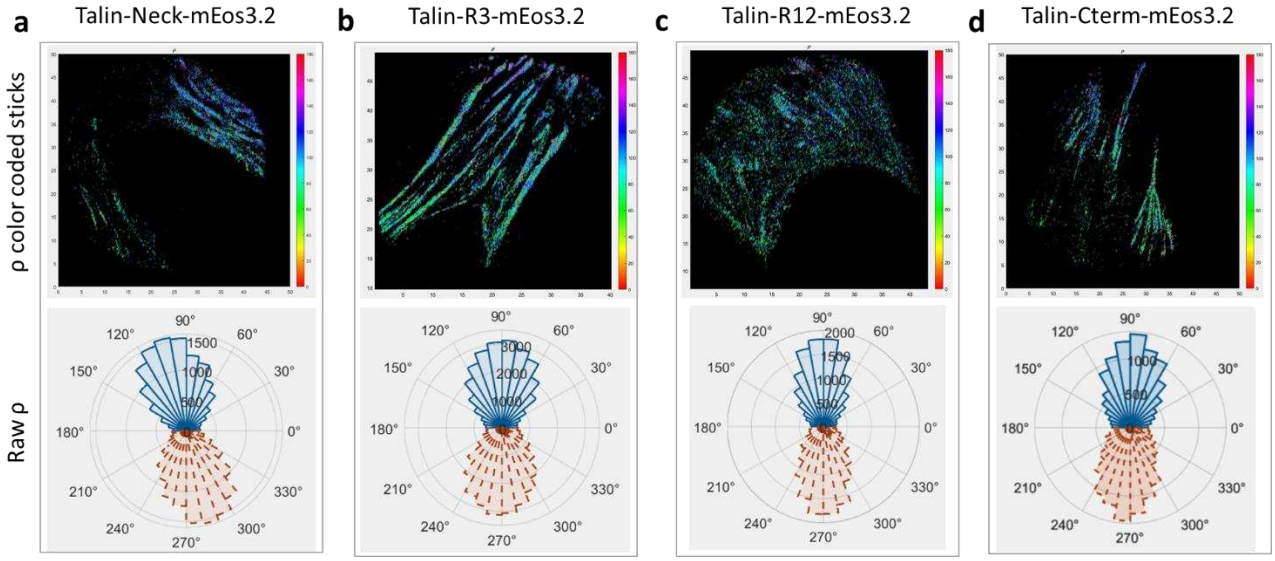

*Figure 93**. Raw in-plane orientation (ρ) in live MEFs reveals excitation photoselection prior to correction**. Representative 4polar3D-TIRF acquisitions of MEFs expressing talin-mEos3.2 tagged at (**a**) Neck, (**b**) R3, (**c**) R12, and (**d**) C-terminus. Top of each panel: stick-plot of single-molecule detections color-coded by ρ (0–180°); sticks are oriented with the measured in-plane angle of each detection. Bottom of each panel: polar histograms of raw ρ (no rotation to FA axis and no correction), showing a pronounced accumulation near ~90°. Imaging was performed in live cells by TIRF to restrict excitation to the basal membrane; four polarization-resolved channels were registered and analyzed as described in the 4polar3D Methods. This systematic angular bias motivated the correction strategy developed in Figure 94.*

In order to recover the true in-plane orientation (ρ) of talin in live MEFs despite the strong photoselection observed in this dataset (Figure 93), we had established, in collaboration with Sophie Brasslet, a post-hoc correction based on a reference population expected to be approximately randomly oriented with respect to the excitation polarization. To do so, we segmented FAs from YFP-paxillin images and collected single-molecule detections located outside FA masks from 10 WT MEF cells acquired on 10 independent experimental days (4polar3D-TIRF). Pooling these outside-FA detections reduces day-to-day optical variability and increases sampling of orientations that are not constrained by FA architecture. From the pooled outside-FA dataset, we derived a correction function that maps the biased raw ρ histogram toward a more homogeneous (uniform) ρ distribution. This calibration was then applied to the raw ρ values of each cell. Figure 94 illustrates the procedure: the outside-FA reference (blue)

defines the bias, the raw distribution from a representative cell (red) shows the preferential angle of the specific cell (i.e. photo bias), and the corrected distribution (orange) shows how the cell data looks like after our correction. We then used these corrected ρ values for all subsequent analyses.

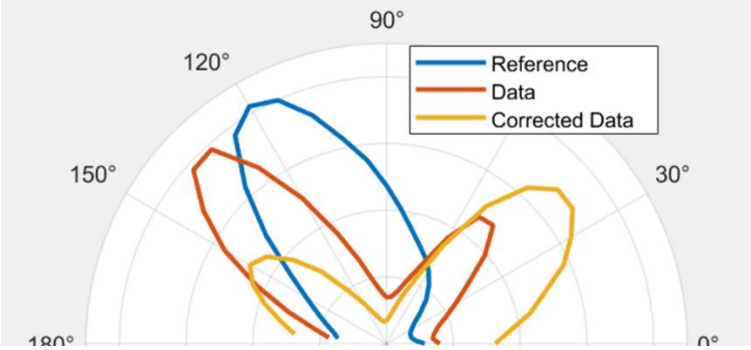

*Figure 94**. Photoselection correction using an outside-FA reference population**. To estimate and remove excitation-induced angular bias, we pooled single-molecule detections located outside FA masks from 10 WT MEF cells acquired on 10 different days (blue; "reference," assumed approximately random with respect to the FA axis). A correction was derived from this reference so that its ρ distribution becomes homogeneous (uniform); applying the same mapping to the raw ρ distribution of an example cell (red) yields the corrected distribution (orange), which no longer exhibits strong photoselection. This reference-based calibration was subsequently applied to all cells before group-level analyses.*

In Figure 95, we present the new dataset acquired in living cells, analyzed using the same representation as in the earlier experiments described in chapter 3.2. in results, but this time with correction for photoselection bias. For talin tagged at the neck, a preferred orientation is still discernible, although the effect is considerably weaker compared to the previous dataset. By contrast, the R3 construct now displays a largely homogeneous orientation distribution, indicating that the apparent anisotropy observed earlier has diminished. Similarly, both the R12- and C-terminal–tagged constructs exhibit homogeneous ρ distributions.

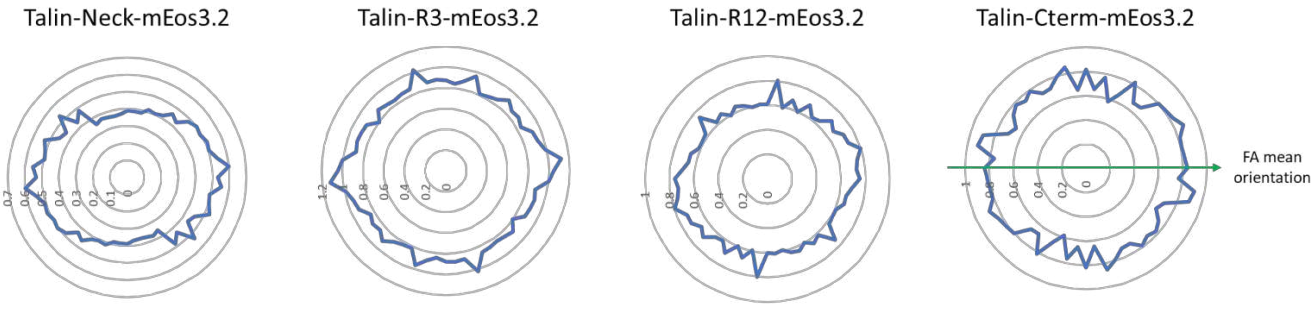

*Figure 95**. In-plane orientation (ρ) of talin in live MEFs after photoselection correction partially recovers orientation gradient along the talin molecule seen in the first set of experiments**. For each construct (Neck, R3, R12, C-term), corrected single-molecule ρ values from live-cell 4polar3D-TIRF acquisitions were rotated so that the FA long axis lies at 0° for each cell, then aggregated across cells (n = 8 per construct). Compared with the raw, biased distributions*

(Figure 93), the corrected data reveal construct-dependent trends: Neck-tagged talin retains a detectable preferential alignment with the FA axis, whereas R3, R12, and C-terminal tags display more homogeneous orientations.

Altogether, these results indicate that the photoselection correction was effective, but might not be sufficient for making definitive conclusions. In the following experimental conditions (3.5.2 & 3.5.3) acquired with the photoselection bias, the results should be considered as indicative for further experiments.

3. 5. 2. CalyculinA increases preferential orientation in talin tagged at the C-terminus

In order to examine whether acute enhancement of actomyosin contractility affects talin orientation, we used CalyculinA.

MEFs expressing mEos3.2-tagged talin constructs (Neck, R3, or C-terminal tagged) were treated with 20 nM CalyculinA for 30 min or with a Ringer solution containing the same amount of DMSO (control) and imaged using 4Polar3D in the same way as all the previous samples (20 000 frames at ~5.4Hz).

After processing the data and performing the post-hoc photoselection correction (Figure 96), we observed that talins tagged at the neck and the R3 showed quite a homogenous in plane orientation. Interestingly, the C terminus tagged talin showed the most preferential orientation.

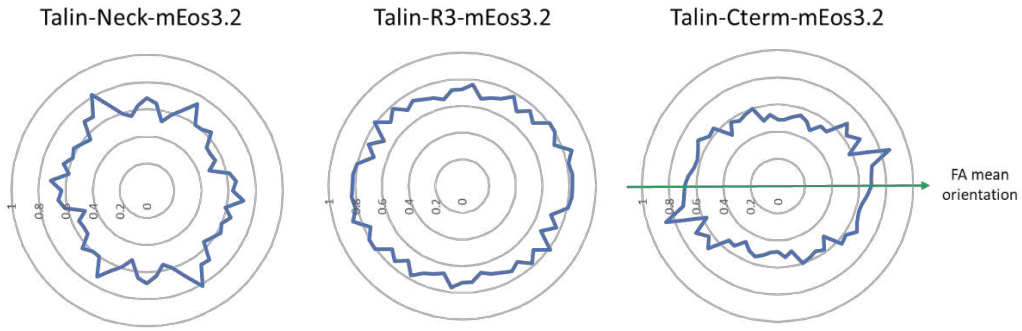

*Figure 96**. Calyculin A enhances preferential alignment for C-terminally tagged talin after photoselection correction**. Corrected and FA-aligned ρ distributions are shown for Neck, R3, and C-terminal tags in live MEFs treated with Calyculin A (n = 3, 4, 4, respectively). Under increased contractility, Neck- and R3-tagged talin remain broadly distributed, while the C-terminal tag exhibits the strongest preferential orientation relative to the FA axis. These measurements were performed with the same 4polar3D-TIRF pipeline and corrected using the outside-FA reference described in Figure 94.*

These results could potentially be pointing to a possible release of talin-integrin interaction, which is why we could observe a more homogenous orientation distribution at the talin-neck and -R3.

3. 5. 3. Rescuing vinculin seems to rescue talin-neck orientation too

For the purpose of studying the determinants of protein orientation in FAs, we also used MEF Vinculin knock-out (KO) cells. Vinculin is required for cell polarization and migration (Thievessen et al., 2015), and its removal causes an effect on mechanical tension transmitted through talin (Ringer et al., 2017), therefore we expected to see this effect when examining talin orientation too.

We transfected talins tagged at the neck and C terminus in VinculinKO cells, and both in cells where vinculin was rescued by GFP-vinculin cotransfection (as a control). We chose them as two extreme cases in their orientational responses.

In the case of talin-neck-mEos3.2 (Figure 97a), we observed that talin gets more aligned with the mean orientation of FAs with the rescue of vinculin, whereas for the talin tagged at the C terminus showed a similar level of homogeneity both with the knockout of vinculin and in the case of its rescue. Those preliminary data need of course to be confirmed in the coming future but suggest that vinculin already demonstrated to be a molecular determinant for force transmission through talin, participates as well in controlling talin shape we are able to unveil with the use of polarization-resolved SMLOM.

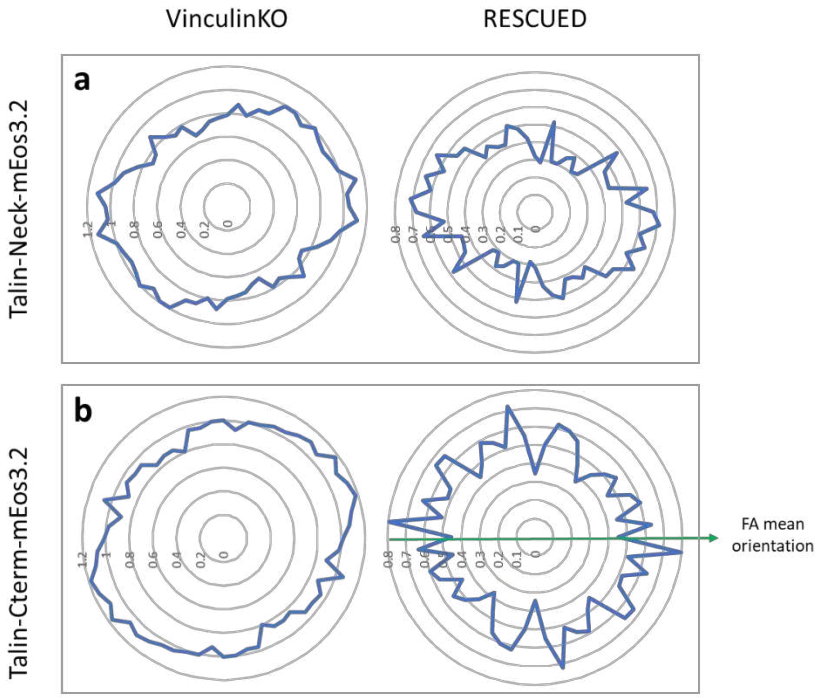

Figure 97. ***Vinculin depletion and rescue modulate talin neck alignment after photoselection correction****. Corrected, FA-aligned ρ distributions for talin-mEos3.2 tagged at (**a**) the Neck and (**b**) the C-terminus in Vinculin-KO MEFs versus vinculin-rescued controls (n = 3 (Neck in Vinculin KO); 2 (Neck, control); 4 (Cterm in Vinculin KO); 3 (Cterm, control)). Rescuing vinculin increases the preferential alignment of Neck-tagged talin, whereas the C-terminal tag remains comparatively homogeneous in both conditions, consistent with distinct mechanical coupling across the talin rod. All data were acquired by live-cell 4polar3D-TIRF and corrected using the outside-FA reference.*

Though this last set of experiments suggested some conclusions, it is visible that the effects we used to see seem to be diminished. That is, although the photoselection correction approach has its validity, it might not be the best approach in our case. This is why these experiments need to be repeated in better optical conditions, where the photoselection will be reduced at start.

Discussion and perspectives

In order to integrate the experimental results from this thesis into the broader context of mechanobiology, it is essential to place them in relationship with existing models of integrin adhesion site (IAS) mechanics, previous single-molecule studies, and in vitro force spectroscopy data. This section therefore discusses the meaning of our observations, the methodological choices made, and their implications for future work, while also speculating on possible mechanisms of action underlying the measured orientations.

This thesis was centered around understanding the mechanical and spatial behavior of key adhesion proteins, with particular attention to talin orientation, using advanced optical and single-molecule methods in living cells. Our work sheds light on how protein conformation and alignment contribute to mechanotransduction at integrin adhesion sites (IAS)-the cellular interface where force sensing and structural coupling to the extracellular matrix occur.

Decoding Talin Orientation via Single-Molecule Polarization Microscopy

The most innovative aspect of this project lies in the application of single-molecule fluorescence polarization microscopy to decipher the orientation and rotational freedom of proteins in living cells. Talin, as a mechanosensitive scaffold with force-unfolding domains, is known to undergo conformational and orientational changes under tension. Previous indirect evidence for such orientation changes came from FRET-based tension sensors (Austen et al., 2015; Kumar et al., 2016) and single-molecule magnetic tweezers assays (Yao et al., 2016), but these approaches could not directly visualize angular preferences in the native cellular environment. Here, by developing tailored constructs of talin tagged at defined mechanical domains, and by employing rigidly bound mEos3.2 and the 4polar3D technique, we gained access to angular data of talin molecules at the single-molecule level in their native cellular environment.

The polarization results obtained provide key evidence that talin orientation reflects its mechanical state, tag position, and biochemical context, and even responds to genetic perturbations. In particular:

- Talins tagged at the neck and R3 displayed more distinct preferential alignment with the focal adhesion axis, consistent with being under mechanical strain.

- In contrast, C-terminal and R12-tagged talins showed more uniform angular distributions, likely reflecting their distal positions and reduced force transmission.
- The knockout of vinculin, a known talin interactor, reduced the orientation preference, particularly at the neck, suggesting vinculin's role in stabilizing force-bearing conformations.

These findings reinforce the working model in which talin behaves as an anisotropic molecular rod whose different domains experience different mechanical regimes depending on their position along the molecule and their connectivity to integrin and actin networks. The neck region, being proximal to integrins, is likely to be mechanically "locked in" during force transmission, whereas the distal C-terminal tail may retain greater rotational freedom.

While these observations provide important insight into the mechanical behavior of talin, results obtained under altered contractility conditions, namely vinculin knockout and CalyculinA treatment, should be interpreted with caution. In both cases, the correction for photoselection was limited, and the optical bias may have influenced the observed orientation distributions. Although some trends were consistent with expected mechanical responses, the precise quantification of angles in these datasets may not fully reflect biological reality. Improved photoselection correction or more isotropic excitation schemes would be necessary for more definitive conclusions.

These observations are not merely structural but mechanistic, they demonstrate that orientation encodes tension and conformational status. While this hypothesis had been supported by in vitro unfolding data and molecular simulations (e.g. Yao et al., 2016), this thesis provides the first live-cell, single-molecule evidence for such a relationship.

Methodological Innovations and Technical Challenges

The development of this pipeline was itself a major achievement. The following contributions are of particular note:

- Construct design: mEos3.2 was inserted at key points along talin to report on the behavior of defined structural elements, informed by mechanical unfolding profiles and domain structure.

- Orientation quantification in living samples: Using the 4polar3D microscope setup—developed by our collaborator Sophie Brasselet and her team (Institut Fresnel, Marseille) and combining it with our established expertise in live-cell imaging, we were able to determine the in-plane (ρ), out-of-plane (η), and wobbling (δ) parameters of individual fluorophores directly in the native context of living cells.
- Photoselection correction: An important component of the data processing, allowing us to correct for the optical bias introduced by polarized excitation. Though partial, this correction improved interpretability of the angular distributions.
- Ratio-based quantification: By computing the polarization ratio - signal intensity at the most detected angle versus its orthogonal, we provided a cell-level quantification of alignment, which correlated well with domain and construct behavior.

Despite these advances, the approach was not without limitations. The photoselection artifact proved more significant than initially expected. While correction techniques allowed qualitative interpretation, true quantification will require further optical improvements. Additionally, signal-to-noise issues restricted per-FA (i.e. region of interest) analysis, limiting our ability to draw more detailed mechanistic conclusions. Addressing these will be crucial for future applications. This could involve increasing labeling density without increasing background (e.g. through improved Halo/SNAP ligands or genetic knock-in approaches) and enhancing detection sensitivity.

Broader Applications and Future Directions

The insights gained from this study are both biologically meaningful and technologically expandable. Polarization microscopy is still a relatively underutilized approach, particularly in mechanobiology. Yet, it offers a unique axis of information – orientation, that is directly linked to molecular function and force.

The work presented here opens several future directions:

Combining Orientation with Spatial and Temporal Resolution

While ρ, η, and δ provide angular information, combining these with 3D spatial tracking and temporal data (via sptPALM) will enable complete reconstruction of force-induced motion and reorientation of individual proteins over time. This integration is within reach at IINS, our institute, given our access to SAF, astigmatism, and soon hopefully a MINFLUX setup.

Multiscale Integration of Data

A key challenge in adhesion biology is understanding how single-molecule events translate to cell-scale behavior. Polarization-based orientation could be combined with membrane deformation assays, traction force microscopy, or live-cell mechanical stimulation, to build a multiscale model of force transmission.

Alternative and Complementary Approaches

In parallel to the work conducted in this thesis, a complementary technique called POLCAM (Polarization Camera-based Orientation Microscopy) was recently developed by another group (Bruggeman et al., 2024). POLCAM is a SMOLM-based method that uses a micro-polarizer array integrated into the camera sensor to simultaneously capture four polarization-resolved images. This enables robust estimation of single-molecule orientation and wobble, without the need for beam-splitting optics, offering a compact and high-throughput alternative for orientation microscopy. While current implementations have focused on fixed samples, POLCAM's simplicity and real-time processing pipeline suggest strong potential for future live-cell applications, particularly in mechanobiology. Its ability to detect rotational immobilization and nanoscale orientational heterogeneity could complement the methods developed here and expand the toolkit available for probing force-transducing proteins in adhesion complexes.

Protein-Specific and Mutational Analyses

Future studies should extend this framework to integrins and other mechanosensors, and include mutants to probe the structural determinants of angular behavior. For instance, does blocking talin's ability to bind vinculin abolish alignment? What happens when integrins are locked in an inactive state?

In addition to talin, the methods developed in this thesis can be directly applied to study the orientation and conformational transitions of integrins themselves. Integrins undergo large-scale conformational rearrangements between bent, extended-closed, and extended-open states, which correlate with their activation and force engagement. Polarization-resolved imaging of integrins tagged at defined positions could provide critical information about their angular preferences within adhesion sites, their orientation relative to the membrane, and their dynamic transitions during force transmission. Such studies could reveal whether specific integrin

conformations correlate with force-bearing states, clustering, or intracellular recruitment of adaptors - key parameters in understanding integrin activation and adhesion regulation. As mentioned before, our current system that allows the minimal exposure time of 185 ms would need to be improved for this purpose.

Applications at IINS and Beyond

At the Interdisciplinary Institute for Neuroscience (IINS) in Bordeaux, where this work was partially conducted, the potential of polarization microscopy is enormous. The institute already hosts state-of-the-art single-molecule and super-resolution techniques, with expertise in optics, neuroscience, and cell biology. The orientation work can now be extended to:

- Neurosynaptic proteins and the mechanical regulation of synapse formation.
- Membrane tension sensors and mechanosensitive ion channels.

Final Perspective

Taken together, these results support a revised working model in which talin's orientation within FAs is not uniform along its length but reflects a gradient of mechanical constraint, highest at the N-terminal neck and decreasing toward the C-terminus. This gradient is dynamically modulated by binding partners (e.g., vinculin) and contractility state, and can be perturbed by pharmacological or genetic manipulation.

This thesis represents a significant technical and conceptual step toward measuring how molecules behave mechanically in their native context. The central takeaway is that orientation is not an epiphenomenon - it is a direct readout of protein state and force. By resolving it, we access a layer of biology that had remained hidden.

As methods continue to evolve, the combination of orientation, spatial localization, and dynamic tracking will provide a comprehensive picture of mechanotransduction at the molecular level. In the context of diseases like cancer, fibrosis, or immune dysfunction, understanding how proteins like talin respond to force in real time could inform targeted interventions, mechanically tuned therapies, or new diagnostic paradigms.

Thus, this thesis not only contributes technical innovation and biological discovery, but also defines a roadmap for future research—one that continues to merge the precision of physics, the complexity of biology, and the creativity of interdisciplinary science.

Bibliography

Albiges-Rizo, C., O. Destaing, B. Fourcade, E. Planus, and M.R. Block. 2009. Actin machinery and mechanosensitivity in invadopodia, podosomes and focal adhesions. *J. Cell Sci.* 122. doi:10.1242/jcs.052704.

Alonso, M.A. 2023. Geometric descriptions for the polarization of nonparaxial light: a tutorial. *Adv. Opt. Photonics*. 15. doi:10.1364/aop.475491.

Anderson, J.M., J. Li, and T.A. Springer. 2022. Regulation of integrin α5β1 conformational states and intrinsic affinities by metal ions and the ADMIDAS. *Mol. Biol. Cell*. 33. doi:10.1091/mbc.E21-11-0536.

Anthis, N.J., K.L. Wegener, F. Ye, C. Kim, B.T. Goult, E.D. Lowe, I. Vakonakis, N. Bate, D.R. Critchley, M.H. Ginsberg, and I.D. Campbell. 2009. The structure of an integrin/talin complex reveals the basis of inside-out signal transduction. *EMBO J.* 28:3623–3632. doi:10.1038/emboj.2009.287.

Atherton, P., B. Stutchbury, D. Jethwa, and C. Ballestrem. 2016. Mechanosensitive components of integrin adhesions: Role of vinculin. *Exp. Cell Res.* 343:21–27. doi:10.1016/j.yexcr.2015.11.017.

Austen, K., P. Ringer, A. Mehlich, A. Chrostek-Grashoff, C. Kluger, C. Klingner, B. Sabass, R. Zent, M. Rief, and C. Grashoff. 2015. Extracellular rigidity sensing by talin isoform-specific mechanical linkages. *Nat. Cell Biol.* 17. doi:10.1038/ncb3268.

Axelrod, D. 1981. Cell-substrate contacts illuminated by total internal reflection fluorescence. *J. Cell Biol.* 89:141–145. doi:10.1083/jcb.89.1.141.

Bachir, A.I., A.R. Horwitz, W.J. Nelson, and J.M. Bianchini. 2017. Actin-based adhesion modules mediate cell interactions with the extracellular matrix and neighboring cells. *Cold Spring Harb. Perspect. Biol.* 9. doi:10.1101/cshperspect.a023234.

Bachir, A.I., J. Zareno, K. Moissoglu, E.F. Plow, E. Gratton, and A.R. Horwitz. 2014. Integrin-associated complexes form hierarchically with variable stoichiometry in nascent adhesions. *Curr. Biol.* 24. doi:10.1016/j.cub.2014.07.011.

Bachmann, M., S. Kukkurainen, V.P. Hytönen, and B. Wehrle-Haller. 2019. Cell adhesion by integrins. *Physiol. Rev.* 99:1655–1699. doi:10.1152/physrev.00036.2018.

Balaban, N.Q., U.S. Schwarz, D. Riveline, P. Goichberg, G. Tzur, I. Sabanay, D. Mahalu, S. Safran, A. Bershadsky, L. Addadi, and B. Geiger. 2001. Force and focal adhesion assembly: A close relationship studied using elastic micropatterned substrates. *Nat. Cell Biol.* 3. doi:10.1038/35074532.

Balzarotti, F., Y. Eilers, K.C. Gwosch, A.H. Gynnå, V. Westphal, F.D. Stefani, J. Elf, and S.W. Hell. 2017. Nanometer resolution imaging and tracking of fluorescent molecules with minimal photon fluxes. *Science (80-.).* 355. doi:10.1126/science.aak9913.

Barczyk, M., S. Carracedo, and D. Gullberg. 2010. Integrins. *Cell Tissue Res.* 339:269–280. doi:10.1007/s00441-009-0834-6.

Barnett, S.F.H., and B.T. Goult. 2022. The MeshCODE to scale—visualising synaptic binary information. *Front. Cell. Neurosci.* 16. doi:10.3389/fncel.2022.1014629.

Battaglia, R.A., S. Delic, H. Herrmann, and N.T. Snider. 2018. Vimentin on the move: New developments in cell migration. *F1000Research*. 7. doi:10.12688/f1000research.15967.1.

Betzig, E., G.H. Patterson, R. Sougrat, O.W. Lindwasser, S. Olenych, J.S. Bonifacino, M.W. Davidson, J. Lippincott-Schwartz, and H.F. Hess. 2006. Imaging intracellular fluorescent proteins at nanometer resolution. *Science (80-.).* 313:1642–1645. doi:10.1126/science.1127344.

Blanchoin, L., R. Boujemaa-Paterski, C. Sykes, and J. Plastino. 2014. Actin dynamics, architecture, and mechanics in cell motility. *Physiol. Rev.* 94:235–263. doi:10.1152/physrev.00018.2013.

Bouchet, B.P., R.E. Gough, Y.C. Ammon, D. van de Willige, H. Post, G. Jacquemet, A.F. Maarten Altelaar, A.J.R. Heck, B.T. Goult, and A. Akhmanova. 2016. Talin-KANK1 interaction controls the recruitment of cortical microtubule stabilizing complexes to focal adhesions. *Elife*. 5:1–23. doi:10.7554/eLife.18124.

Bourg, N., C. Mayet, G. Dupuis, T. Barroca, P. Bon, S. Lécart, E. Fort, and S. Lévêque-Fort. 2015. Direct optical nanoscopy with axially localized detection. *Nat. Photonics*. 9. doi:10.1038/nphoton.2015.132.

Brangwynne, C.P., F.C. MacKintosh, S. Kumar, N.A. Geisse, J. Talbot, L. Mahadevan, K.K. Parker, D.E. Ingber, and D.A. Weitz. 2006. Microtubules can bear enhanced compressive loads in living cells because of lateral reinforcement. *J. Cell Biol.* 173. doi:10.1083/jcb.200601060.

Brasselet, S., and M.A. Alonso. 2024. Polarization microscopy: from ensemble structural imaging to single-molecule 3D orientation and localization microscopy. *Optica*. 10:1486. doi:10.1364/optica.502119.

Brill-Karniely, Y., Y. Ideses, A. Bernheim-Groswasser, and A. Ben-Shaul. 2009. From branched networks of actin filaments to bundles. *ChemPhysChem*. 10:2818–2827. doi:10.1002/cphc.200900615.

Broeken, J., B. Rieger, and S. Stallinga. 2014. Simultaneous measurement of position and color of single fluorescent emitters using diffractive optics. *Opt. Lett.* 39. doi:10.1364/ol.39.003352.

Brosseau, C., and A. Dogariu. 2006. Symmetry properties and polarization descriptors for an arbitrary electromagnetic wavefield. *In* Progress in Optics.

Brouhard, G.J., and L.M. Rice. 2018. Microtubule Dynamics: an interplay of biochemistry and mechanics. *Nat. Rev. Mol. Cell Biol.* 19:451–463. doi:10.1038/s41580-018-0009-y.

Bruggeman, E., O. Zhang, L.-M. Needham, M. Körbel, S. Daly, M. Cheetham, R. Peters, T. Wu, A.S. Klymchenko, S.J. Davis, E.K. Paluch, D. Klenerman, M.D. Lew, K. O'Holleran, and S.F. Lee. 2024. POLCAM: Instant molecular orientation microscopy for the life sciences. *bioRxiv*. 21:2023.02.07.527479. doi:10.1101/2023.02.07.527479.

Burridge, K., and E.S. Wittchen. 2013. The tension mounts: Stress fibers as force-generating mechanotransducers. *J. Cell Biol.* 200:9–19. doi:10.1083/jcb.201210090.

Butcher, D.T., T. Alliston, and V.M. Weaver. 2009. A tense situation: Forcing tumour progression. *Nat. Rev. Cancer*. 9. doi:10.1038/nrc2544.

Calderwood, D.A., I.D. Campbell, and D.R. Critchley. 2013. Talins and kindlins: Partners in integrin-mediated adhesion. *Nat. Rev. Mol. Cell Biol.* 14:503–517. doi:https://doi.org/10.1038/nrm3624.

Calderwood, D.A., Y. Fujioka, J.M. De Pereda, B. García-Alvarez, T. Nakamoto, B. Margolis, C.J. McGlade, R.C. Liddington, and M.H. Ginsberg. 2003. Integrin β cytoplasmic domain interactions with phosphotyrosine-binding domains: A structural prototype for diversity in integrin signaling. *Proc. Natl. Acad. Sci. U. S. A.* 100:2272–2277. doi:10.1073/pnas.262791999.

Calderwood, D.A., B. Yan, J.M. De Pereda, B.G. Alvarez, Y. Fujioka, R.C. Liddington, and M.H. Ginsberg. 2002. The phosphotyrosine binding-like domain of talin activates integrins. *J. Biol. Chem.* 277:21749–21758. doi:10.1074/jbc.M111996200.

Cao, H., Q. He, R. von Eyben, J. Bloomstein, D.K. Nambiar, V. Viswanathan, S. Aggarwal, S. Kwok, R. Liang, A.J. Koong, J.S. Lewis, C. Kong, N. Xiao, and Q.T. Le. 2020. The role of Glial cell derived neurotrophic factor in head and neck cancer. *PLoS One*. 15. doi:10.1371/journal.pone.0229311.

Carlsson, L., L.E. Nyström, I. Sundkvist, F. Markey, and U. Lindberg. 1977. Actin polymerizability is influenced by profilin, a low molecular weight protein in non-muscle cells. *J. Mol. Biol.* 115:465–483. doi:10.1016/0022-2836(77)90166-8.

Case, L.B., M.A. Baird, G. Shtengel, S.L. Campbell, H.F. Hess, M.W. Davidson, and C.M. Waterman. 2015. Molecular mechanism of vinculin activation and nanoscale spatial organization in focal adhesions. *Nat. Cell Biol.* 17:880–892. doi:10.1038/ncb3180.

Chang, Y.C., H. Zhang, J. Franco-Barraza, M.L. Brennan, T. Patel, E. Cukierman, and J. Wu. 2014. Structural and mechanistic insights into the recruitment of talin by RIAM in integrin signaling. *Structure*. 22:1810–1820. doi:10.1016/j.str.2014.09.020.

Chazeau, A., and G. Giannone. 2016. Organization and dynamics of the actin cytoskeleton during dendritic spine morphological remodeling. *Cell. Mol. Life Sci.* 73:3053–3073. doi:10.1007/s00018-016-2214-1.

Chazeau, A., A. Mehidi, D. Nair, J.J. Gautier, C. Leduc, I. Chamma, F. Kage, A. Kechkar, O. Thoumine, K. Rottner, D. Choquet, A. Gautreau, J. Sibarita, and G. Giannone. 2014. Nanoscale segregation of actin nucleation and elongation factors determines dendritic spine protrusion. *EMBO J.* 33:2745–2764. doi:10.15252/embj.201488837.

Chen, Y., Z. Li, F. Kong, L.A. Ju, and C. Zhu. 2024a. Force-Regulated Spontaneous Conformational Changes of Integrins α5β1and αVβ3. *ACS Nano*. 18. doi:10.1021/acsnano.3c06253.

Chen, Z., X. Han, B. Che, H. Feng, Y. Zhou, L. Deng, and X. Wang. 2024b. Focal adhesion-mediated directional cell migration guided by gradient-stretched substrate. *iScience*. 27:110446. doi:10.1016/j.isci.2024.110446.

Choi, C.K., M. Vicente-Manzanares, J. Zareno, L.A. Whitmore, A. Mogilner, and A.R. Horwitz. 2008. Actin and α-actinin orchestrate the assembly and maturation of nascent adhesions in a myosin II motor-independent manner. *Nat. Cell Biol.* 10:1039–1050. doi:10.1038/ncb1763.

Ciobanasu, C., B. Faivre, and C. Le Clainche. 2014. Actomyosin-dependent formation of the mechanosensitive talin-vinculin complex reinforces actin anchoring. *Nat. Commun.* 5. doi:10.1038/ncomms4095.

Cole, N.B. 2013. Site-specific protein labeling with SNAP-tags. *Curr. Protoc. Protein Sci.* 2013. doi:10.1002/0471140864.ps3001s73.

Cook, A., F. Walterspiel, and C. Deo. 2023. HaloTag-Based Reporters for Fluorescence Imaging and Biosensing. *ChemBioChem*. 24. doi:10.1002/cbic.202300022.

Cruz, C.A.V., H.A. Shaban, A. Kress, N. Bertaux, S. Monneret, M. Mavrakis, J. Savatier, and S. Brasselet. 2016. Quantitative nanoscale imaging of orientational order in biological filaments by polarized superresolution microscopy. *Proc. Natl. Acad. Sci. U. S. A.* 113:E820–E828. doi:10.1073/pnas.1516811113.

Curcio, V., L.A. Alemán-Castañeda, T.G. Brown, S. Brasselet, and M.A. Alonso. 2020. Birefringent Fourier filtering for single molecule coordinate and height super-resolution imaging with

dithering and orientation. *Nat. Commun.* 11:1–13. doi:10.1038/s41467-020-19064-6.
Dahal, N., S. Sharma, B. Phan, A. Eis, and I. Popa. 2022. Mechanical regulation of talin through binding and history-dependent unfolding. *Sci. Adv.* 8. doi:10.1126/sciadv.abl7719.
Dedden, D., S. Schumacher, C.F. Kelley, M. Zacharias, C. Biertümpfel, R. Fässler, and N. Mizuno. 2019. The Architecture of Talin1 Reveals an Autoinhibition Mechanism. *Cell*. 179:120-131.e13. doi:10.1016/j.cell.2019.08.034.
Dempsey, G.T., J.C. Vaughan, K.H. Chen, M. Bates, and X. Zhuang. 2011. Evaluation of fluorophores for optimal performance in localization-based super-resolution imaging. *Nat. Methods*. 8. doi:10.1038/nmeth.1768.
Deng, W., R.L. Carr, R.R. Kaul, M. Pavlova-deb, A. Haage, P. Roca-cusachs, and G. Tanentzapf. 2025. Consolidation of cell-ECM adhesion through direct talin-mediated actin linkage is essential for mouse embryonic morphogenesis.
Despotović, S.Z., Đ.N. Milićević, A.J. Krmpot, A.M. Pavlović, V.D. Živanović, Z. Krivokapić, V.B. Pavlović, S. Lević, G. Nikolić, and M.D. Rabasović. 2020. Altered organization of collagen fibers in the uninvolved human colon mucosa 10 cm and 20 cm away from the malignant tumor. *Sci. Rep.* 10. doi:10.1038/s41598-020-63368-y.
Di, X., X. Gao, L. Peng, J. Ai, X. Jin, S. Qi, H. Li, K. Wang, and D. Luo. 2023. Cellular mechanotransduction in health and diseases: from molecular mechanism to therapeutic targets. *Signal Transduct. Target. Ther.* 8. doi:10.1038/s41392-023-01501-9.
Dominguez, R., and K.C. Holmes. 2011. Actin structure and function. *Annu. Rev. Biophys.* 40:169–186. doi:10.1146/annurev-biophys-042910-155359.
Dransfield, I., C. Cabañas, A. Craig, and N. Hogg. 1992. Divalent cation regulation of the function of the leukocyte integrin LFA-1. *J. Cell Biol.* 116:219–226. doi:10.1083/jcb.116.1.219.
Dupont, S., L. Morsut, M. Aragona, E. Enzo, S. Giulitti, M. Cordenonsi, F. Zanconato, J. Le Digabel, M. Forcato, S. Bicciato, N. Elvassore, and S. Piccolo. 2011. Role of YAP/TAZ in mechanotransduction. *Nature*. 474. doi:10.1038/nature10137.
Eldirany, S.A., I.B. Lomakin, M. Ho, and C.G. Bunick. 2021. Recent insight into intermediate filament structure. *Curr. Opin. Cell Biol.* 68:132–143. doi:10.1016/j.ceb.2020.10.001.
Elosegui-Artola, A., R. Oria, Y. Chen, A. Kosmalska, C. Pérez-González, N. Castro, C. Zhu, X. Trepat, and P. Roca-Cusachs. 2016. Mechanical regulation of a molecular clutch defines force transmission and transduction in response to matrix rigidity. *Nat. Cell Biol.* 18. doi:10.1038/ncb3336.
Ferrand, P., P. Gasecka, A. Kress, X. Wang, F.Z. Bioud, J. Duboisset, and S. Brasselet. 2014. Ultimate use of two-photon fluorescence microscopy to map orientational behavior of fluorophores. *Biophys. J.* 106. doi:10.1016/j.bpj.2014.04.011.
Fischer, L.S., C. Klingner, T. Schlichthaerle, M.T. Strauss, R. Böttcher, R. Fässler, R. Jungmann, and C. Grashoff. 2021. Quantitative single-protein imaging reveals molecular complex formation of integrin, talin, and kindlin during cell adhesion. *Nat. Commun.* 12. doi:10.1038/s41467-021-21142-2.
Fletcher, D.A., and R.D. Mullins. 2010. Cell mechanics and the cytoskeleton. *Nature*. 463:485–492. doi:10.1038/nature08908.
Florine-Casteel, K. 1990. Phospholipid order in gel- and fluid-phase cell-size liposomes measured by digitized video fluorescence polarization microscopy. *Biophys. J.* 57. doi:10.1016/S0006-3495(90)82639-4.

Franz, F., R. Tapia-Rojo, S. Winograd-Katz, R. Boujemaa-Paterski, W. Li, T. Unger, S. Albeck, C. Aponte-Santamaria, S. Garcia-Manyes, O. Medalia, B. Geiger, and F. Gräter. 2023. Allosteric activation of vinculin by talin. *Nat. Commun.* 14. doi:10.1038/s41467-023-39646-4.

Galkin, V.E., A. Orlova, D.S. Kudryashov, A. Solodukhin, E. Reisler, G.F. Schröder, and E.H. Egelman. 2011. Remodeling of actin filaments by ADF/cofilin proteins. *Proc. Natl. Acad. Sci. U. S. A.* 108:20568–20572. doi:10.1073/pnas.1110109108.

Gao, J., Y. Bao, S. Ge, P. Sun, J. Sun, J. Liu, F. Chen, L. Han, Z. Cao, J. Qin, G.C. White, Z. Xu, and Y.Q. Ma. 2019. Sharpin suppresses β1-integrin activation by complexing with the β1 tail and kindlin-1. *Cell Commun. Signal.* 17:1–13. doi:10.1186/s12964-019-0407-6.

Gardel, M.L., I.C. Schneider, Y. Aratyn-Schaus, and C.M. Waterman. 2010. Mechanical integration of actin and adhesion dynamics in cell migration. *Annu. Rev. Cell Dev. Biol.* 26. doi:10.1146/annurev.cellbio.011209.122036.

Geiger, B., J.P. Spatz, and A.D. Bershadsky. 2009. Environmental sensing through focal adhesions. *Nat. Rev. Mol. Cell Biol.* 10:21–33. doi:10.1038/nrm2593.

Giannone, G., G. Jiang, D.H. Sutton, D.R. Critchley, and M.P. Sheetz. 2003. Talin1 is critical for force-dependent reinforcement of initial integrin-cytoskeleton bonds but not tyrosine kinase activation. *J. Cell Biol.* 163:409–419. doi:10.1083/jcb.200302001.

Gingras, A.R., W.H. Ziegler, R. Frank, I.L. Barsukov, G.C.K. Roberts, D.R. Critchley, and J. Emsley. 2005. Mapping and consensus sequence identification for multiple vinculin binding sites within the talin rod. *J. Biol. Chem.* 280:37217–37224. doi:10.1074/jbc.M508060200.

Gittes, F., B. Mickey, J. Nettleton, and J. Howard. 1993. Flexural rigidity of microtubules and actin filaments measured from thermal fluctuations in shape. *J. Cell Biol.* 120. doi:10.1083/jcb.120.4.923.

Goksoy, E., Y.Q. Ma, X. Wang, X. Kong, D. Perera, E.F. Plow, and J. Qin. 2008. Structural Basis for the Autoinhibition of Talin in Regulating Integrin Activation. *Mol. Cell*. 31:124–133. doi:10.1016/j.molcel.2008.06.011.

Goldmann, W.H., and G. Isenberg. 1991. Kinetic determination of talin-actin binding. *Biochem. Biophys. Res. Commun.* 178:718–723. doi:10.1016/0006-291X(91)90167-6.

Gough, R.E., and B.T. Goult. 2018. The tale of two talins – two isoforms to fine-tune integrin signalling. *FEBS Lett.* 592:2108–2125. doi:10.1002/1873-3468.13081.

Goult, B.T., N. Bate, N.J. Anthis, K.L. Wegener, A.R. Gingras, B. Patel, I.L. Barsukov, I.D. Campbell, G.C.K. Roberts, and D.R. Critchley. 2009. The structure of an interdomain complex that regulates Talin activity. *J. Biol. Chem.* 284:15097–15106. doi:10.1074/jbc.M900078200.

Goult, B.T., M. Bouaouina, P.R. Elliott, N. Bate, B. Patel, A.R. Gingras, J.G. Grossmann, G.C.K. Roberts, D.A. Calderwood, D.R. Critchley, and I.L. Barsukov. 2010. Structure of a double ubiquitin-like domain in the talin head: A role in integrin activation. *EMBO J.* 29:1069–1080. doi:10.1038/emboj.2010.4.

Goult, B.T., N.H. Brown, and M.A. Schwartz. 2021. Talin in mechanotransduction and mechanomemory at a glance. *J. Cell Sci.* 134:1–7. doi:10.1242/jcs.258749.

Goult, B.T., T. Zacharchenko, N. Bate, R. Tsang, F. Hey, A.R. Gingras, P.R. Elliott, G.C.K. Roberts, C. Ballestrem, D.R. Critchley, and I.L. Barsukov. 2013. RIAM and vinculin binding to talin are mutually exclusive and regulate adhesion assembly and turnover. *J. Biol. Chem.* 288:8238–8249. doi:10.1074/jbc.M112.438119.

Gregor, M., S. Osmanagic-Myers, G. Burgstaller, M. Wolfram, I. Fischer, G. Walko, G.P. Resch, A.

Jörgl, H. Herrmann, and G. Wiche. 2014. Mechanosensing through focal adhesion-anchored intermediate filaments. *FASEB J.* 28:715–729. doi:10.1096/fj.13-231829.

Grimm, J.B., A.K. Muthusamy, Y. Liang, T.A. Brown, W.C. Lemon, R. Patel, R. Lu, J.J. Macklin, P.J. Keller, N. Ji, and L.D. Lavis. 2017. A general method to fine-tune fluorophores for live-cell and in vivo imaging. *Nat. Methods*. 14. doi:10.1038/nmeth.4403.

Guo, Y., J. Yan, and B.T. Goult. 2024. Mechanotransduction through protein stretching. *Curr. Opin. Cell Biol.* 87:102327. doi:10.1016/j.ceb.2024.102327.

Gustavsson, A.-K., P.N. Petrov, and W.E. Moerner. 2018a. Light sheet approaches for improved precision in 3D localization-based super-resolution imaging in mammalian cells [Invited]. *Opt. Express*. 26. doi:10.1364/oe.26.013122.

Gustavsson, A.K., P.N. Petrov, M.Y. Lee, Y. Shechtman, and W.E. Moerner. 2018b. 3D single-molecule super-resolution microscopy with a tilted light sheet. *Nat. Commun.* 9:1–8. doi:10.1038/s41467-017-02563-4.

Han, M.K.L., and J. de Rooij. 2016. Converging and Unique Mechanisms of Mechanotransduction at Adhesion Sites. *Trends Cell Biol.* 26:612–623. doi:10.1016/j.tcb.2016.03.005.

Hemmings, L., D.J.G. Rees, V. Ohanian, S.J. Bolton, A.P. Gilmore, B. Patel, H. Priddle, J.E. Trevithick, R.O. Hynes, and D.R. Critchley. 1996. Talin contains three actin-binding sites each of which is adjacent to a vinculin-binding site. *J. Cell Sci.* 109:2715–2726. doi:10.1242/jcs.109.11.2715.

Henning Stumpf, B., A. Ambriović-Ristov, A. Radenovic, and A.S. Smith. 2020. Recent Advances and Prospects in the Research of Nascent Adhesions. *Front. Physiol.* 11:1–16. doi:10.3389/fphys.2020.574371.

Herrmann, H., and U. Aebi. 2016. Intermediate filaments: Structure and assembly. *Cold Spring Harb. Perspect. Biol.* 8:1–22. doi:10.1101/cshperspect.a018242.

Hoelzel, C.A., and X. Zhang. 2020. Visualizing and Manipulating Biological Processes by Using HaloTag and SNAP-Tag Technologies. *ChemBioChem*. 21. doi:10.1002/cbic.202000037.

Hoffman, B.D., C. Grashoff, and M.A. Schwartz. 2011. Dynamic molecular processes mediate cellular mechanotransduction. *Nature*. 475:316–323. doi:10.1038/nature10316.

Hohmann, T., and F. Dehghani. 2019. The cytoskeleton—a complex interacting meshwork. *Cells*. 8. doi:10.3390/cells8040362.

Holmes, K.C., D. Popp, W. Gebhard, and W. Kabsch. 1990. 347044a0. 347:6.

Hotulainen, P., and P. Lappalainen. 2006. Stress fibers are generated by two distinct actin assembly mechanisms in motile cells. *J. Cell Biol.* 173:383–394. doi:10.1083/jcb.200511093.

Huang, B., W. Wang, M. Bates, and X. Zhuang. 2008. Three-dimensional super-resolution imaging by stochastic optical reconstruction microscopy. *Science (80-.).* 319. doi:10.1126/science.1153529.

Humphrey, J.D., E.R. Dufresne, and M.A. Schwartz. 2014. Mechanotransduction and extracellular matrix homeostasis. *Nat. Rev. Mol. Cell Biol.* 15:802–812. doi:10.1038/nrm3896.

Hytönen, V.P., and V. Vogel. 2008. How force might activate talin's vinculin binding sites: SMD reveals a structural mechanism. *PLoS Comput. Biol.* 4. doi:10.1371/journal.pcbi.0040024.

Izeddin, I., M. El Beheiry, J. Andilla, D. Ciepielewski, X. Darzacq, and M. Dahan. 2012a. PSF shaping using adaptive optics for three-dimensional single-molecule super-resolution imaging and tracking. *Opt. Express*. 20. doi:10.1364/oe.20.004957.

Izeddin, I., J. Boulanger, V. Racine, C.G. Specht, A. Kechkar, D. Nair, A. Triller, D. Choquet, M.

Dahan, and J.B. Sibarita. 2012b. Wavelet analysis for single molecule localization microscopy. *Opt. Express*. 20:2081. doi:10.1364/oe.20.002081.

Juanes, M.A., D. Isnardon, A. Badache, S. Brasselet, M. Mavrakis, and B.L. Goode. 2019. The role of APC-mediated actin assembly in microtubule capture and focal adhesion turnover. *J. Cell Biol.* 218. doi:10.1083/JCB.201904165.

Kadry, Y.A., and D.A. Calderwood. 2020. Chapter 22: Structural and signaling functions of integrins. *Biochim. Biophys. Acta - Biomembr.* 1862:183206. doi:10.1016/j.bbamem.2020.183206.

Kanchanawong, P., G. Shtengel, A.M. Pasapera, E.B. Ramko, M.W. Davidson, H.F. Hess, and C.M. Waterman. 2010. Nanoscale architecture of integrin-based cell adhesions. *Nature*. 468:580–584. doi:10.1038/nature09621.

Kang, M., Y. Otani, Y. Guo, J. Yan, B.T. Goult, and A.K. Howe. 2024. The focal adhesion protein talin is a mechanically gated A-kinase anchoring protein. *Proc. Natl. Acad. Sci. U. S. A.* 121. doi:10.1073/pnas.2314947121.

Kinosita, K., S. Kawato, and A. Ikegami. 1977. A theory of fluorescence polarization decay in membranes. *Biophys. J.* 20. doi:10.1016/S0006-3495(77)85550-1.

Kong, F., A.J. García, A.P. Mould, M.J. Humphries, and C. Zhu. 2009. Demonstration of catch bonds between an integrin and its ligand. *J. Cell Biol.* 185. doi:10.1083/jcb.200810002.

Kovács, M., J. Tóth, C. Hetényi, A. Málnási-Csizmadia, and J.R. Seller. 2004. Mechanism of blebbistatin inhibition of myosin II. *J. Biol. Chem.* 279. doi:10.1074/jbc.M405319200.

Kress, A., P. Ferrand, H. Rigneault, T. Trombik, H.T. He, D. Marguet, and S. Brasselet. 2011. Probing orientational behavior of MHC class i protein and lipid probes in cell membranes by fluorescence polarization-resolved imaging. *Biophys. J.* 101:468–476. doi:10.1016/j.bpj.2011.05.021.

Kress, A., X. Wang, H. Ranchon, J. Savatier, H. Rigneault, P. Ferrand, and S. Brasselet. 2013. Mapping the local organization of cell membranes using excitation- polarization-resolved confocal fluorescence microscopy. *Biophys. J.* 105:127–136. doi:10.1016/j.bpj.2013.05.043.

Kuhlman, P.A., C.A. Hughes, V. Bennett, and V.M. Fowler. 1996. A new function for adducin: Calcium/calmodulin-regulated capping of the barbed ends of actin filaments. *J. Biol. Chem.* 271:7986–7991. doi:10.1074/jbc.271.14.7986.

Kumar, A., M. Ouyang, K. Van den Dries, E.J. McGhee, K. Tanaka, M.D. Anderson, A. Groisman, B.T. Goult, K.I. Anderson, and M.A. Schwartz. 2016. Talin tension sensor reveals novel features of focal adhesion force transmission and mechanosensitivity. *J. Cell Biol.* 213. doi:10.1083/jcb.201510012.

Kumar, C.S.S., C.A.V. Cruz, M. Sison, A.G. Vesga, J. Rey-, V. Curcio, L.A. Alemán-castañeda, M.A. Alonso, and R. Poincloux. 2025. 4polar3D : Single molecule 3D orientation imaging of dense actin networks using ratiometric polarization splitting. *bioRxiv*. doi:https://doi.org/10.1101/2025.07.13.664601.

Kumar, S., I.Z. Maxwell, A. Heisterkamp, T.R. Polte, T.P. Lele, M. Salanga, E. Mazur, and D.E. Ingber. 2006. Viscoelastic retraction of single living stress fibers and its impact on cell shape, cytoskeletal organization, and extracellular matrix mechanics. *Biophys. J.* 90:3762–3773. doi:10.1529/biophysj.105.071506.

Lakowicz, J.R. 2006. Principles of Fluorescence Spectroscopy. 1–954 pp.

Lawson, C., S.T. Lim, S. Uryu, X.L. Chen, D.A. Calderwood, and D.D. Schlaepfer. 2012. FAK

promotes recruitment of talin to nascent adhesions to control cell motility. *J. Cell Biol.* 196:223–232. doi:10.1083/jcb.201108078.

Legerstee, K., B. Geverts, J.A. Slotman, and A.B. Houtsmuller. 2019. Dynamics and distribution of paxillin, vinculin, zyxin and VASP depend on focal adhesion location and orientation. *Sci. Rep.* 9. doi:10.1038/s41598-019-46905-2.

Lelek, M., M.T. Gyparaki, G. Beliu, F. Schueder, J. Griffié, S. Manley, R. Jungmann, M. Sauer, M. Lakadamyali, and C. Zimmer. 2021. Single-molecule localization microscopy. *Nat. Rev. Methods Prim.* 1. doi:10.1038/s43586-021-00038-x.

Levet, F., and J.B. Sibarita. 2023. PoCA: a software platform for point cloud data visualization and quantification. *Nat. Methods*. 20. doi:10.1038/s41592-023-01811-4.

Li, J., and T.A. Springer. 2018. Energy landscape differences among integrins establish the framework for understanding activation. *J. Cell Biol.* 217. doi:10.1083/jcb.201701169.

Li, X., B.T. Goult, C. Ballestrem, and T. Zacharchenko. 2023. The structural basis of the talin-KANK1 interaction that coordinates the actin and microtubule cytoskeletons at focal adhesions. *Open Biol.* 13. doi:10.1098/rsob.230058.

Lichtman, J.W., and J.A. Conchello. 2005. Fluorescence microscopy. *Nat. Methods*. 2:910–919. doi:10.1038/nmeth817.

Liu, J., Y. Wang, W.I. Goh, H. Goh, M.A. Baird, S. Ruehland, S. Teo, N. Bate, D.R. Critchley, M.W. Davidson, and P. Kanchanawong. 2015. Talin determines the nanoscale architecture of focal adhesions. *Proc. Natl. Acad. Sci. U. S. A.* 112. doi:10.1073/pnas.1512025112.

Liu, S., P. Hoess, and J. Ries. 2022. Super-Resolution Microscopy for Structural Cell Biology. *Annu. Rev. Biophys.* 51:301–326. doi:10.1146/annurev-biophys-102521-112912.

Lu, F., L. Zhu, T. Bromberger, J. Yang, Q. Yang, J. Liu, E.F. Plow, M. Moser, and J. Qin. 2022. Mechanism of integrin activation by talin and its cooperation with kindlin. *Nat. Commun.* 13. doi:10.1038/s41467-022-30117-w.

Lu, P., K. Takai, W.M. Valerie, and W. Zena. 2011. ExtracellularMatrix Degradation and Remodeling in Development and Disease. *Cold Spring Harb. Lab. Press.* doi:10.1101/cshperspect.a005058.

Maity, A., J. Wulffelé, I. Ayala, A. Favier, V. Adam, D. Bourgeois, and B. Brutscher. 2024. Structural Heterogeneity in a Phototransformable Fluorescent Protein Impacts its Photochemical Properties. *Adv. Sci.* 11. doi:10.1002/advs.202306272.

Margadant, F., L.L. Chew, X. Hu, H. Yu, N. Bate, X. Zhang, and M. Sheetz. 2011. Mechanotransduction in vivo by repeated talin stretch-relaxation events depends upon vinculin. *PLoS Biol.* 9. doi:10.1371/journal.pbio.1001223.

Martel, V., C. Racaud-Sultan, S. Dupe, C. Marie, F. Paulhe, A. Galmiche, M.R. Block, and C. Albiges-Rizo. 2001. Conformation, Localization, and Integrin Binding of Talin Depend on Its Interaction with Phosphoinositides. *J. Biol. Chem.* 276:21217–21227. doi:10.1074/jbc.M102373200.

Martins, C.S., F. Iv, S.K. Suman, T.C. Panagiotou, C. Sidor, M. Ruso-López, C.N. Plancke, S. Omi, M. Gomes, A. Llewellyn, S.R. Bandi, L. Ramond, F. Arbizzani, C.V. Rimoli, F. Schnorrer, F. Robin, A. Wilde, L. LeGoff, J.-D. Pedelacq, S. Cabantous, S.A. Rincon, C. Chandre, S. Brasselet, and M. Mavrakis. 2025. Genetically encoded reporters of actin filament organization in living cells and tissues. *Cell*. 2024.04.26.591305. doi:10.1016/j.cell.2025.03.003.

Mattheyses, A.L., S.M. Simon, and J.Z. Rappoport. 2010. Imaging with total internal reflection

fluorescence microscopy for the cell biologist. *J. Cell Sci.* 123. doi:10.1242/jcs.056218.
Mavrakis, M., Y. Azou-Gros, F.C. Tsai, J. Alvarado, A. Bertin, F. Iv, A. Kress, S. Brasselet, G.H. Koenderink, and T. Lecuit. 2014. Septins promote F-actin ring formation by crosslinking actin filaments into curved bundles. *Nat. Cell Biol.* 16:322–334. doi:10.1038/ncb2921.
McKinney, S.A., C.S. Murphy, K.L. Hazelwood, M.W. Davidson, and L.L. Looger. 2009. A bright and photostable photoconvertible fluorescent protein. *Nat. Methods*. 6:131–133. doi:10.1038/nmeth.1296.
Nermut, M. V., N.M. Green, P. Eason, S.S. Yamada, and K.M. Yamada. 1988. Electron microscopy and structural model of human fibronectin receptor. *EMBO J.* 7:4093–4099. doi:10.1002/j.1460-2075.1988.tb03303.x.
Nishida, N., C. Xie, M. Shimaoka, Y. Cheng, T. Walz, and T.A. Springer. 2006. Activation of Leukocyte β2 Integrins by Conversion from Bent to Extended Conformations. *Immunity*. 25:583–594. doi:10.1016/j.immuni.2006.07.016.
Nobes, C.D., and A. Hall. 1995. Rho, Rac, and Cdc42 GTPases regulate the assembly of multimolecular focal complexes associated with actin stress fibers, lamellipodia, and filopodia. *Cell*. 81:53–62. doi:10.1016/0092-8674(95)90370-4.
Nordenfelt, P., T.I. Moore, S.B. Mehta, J.M. Kalappurakkal, V. Swaminathan, N. Koga, T.J. Lambert, D. Baker, J.C. Waters, R. Oldenbourg, T. Tani, S. Mayor, C.M. Waterman, and T.A. Springer. 2017. Direction of actin flow dictates integrin LFA-1 orientation during leukocyte migration. *Nat. Commun.* 8. doi:10.1038/s41467-017-01848-y.
Oakes, P.W., E. Wagner, C.A. Brand, D. Probst, M. Linke, U.S. Schwarz, M. Glotzer, and M.L. Gardel. 2017. Optogenetic control of RhoA reveals zyxin-mediated elasticity of stress fibres. *Nat. Commun.* 8. doi:10.1038/ncomms15817.
Ohi, R., and M. Zanic. 2016. Ahead of the Curve: New Insights into Microtubule Dynamics. *F1000Research*. 5:1–8. doi:10.12688/f1000research.7439.1.
Oria, R., T. Wiegand, J. Escribano, A. Elosegui-Artola, J.J. Uriarte, C. Moreno-Pulido, I. Platzman, P. Delcanale, L. Albertazzi, D. Navajas, X. Trepat, J.M. García-Aznar, E.A. Cavalcanti-Adam, and P. Roca-Cusachs. 2017. Force loading explains spatial sensing of ligands by cells. *Nature*. 552. doi:10.1038/nature24662.
Orré, T., A. Joly, Z. Karatas, B. Kastberger, C. Cabriel, R.T. Böttcher, S. Lévêque-Fort, J.B. Sibarita, R. Fässler, B. Wehrle-Haller, O. Rossier, and G. Giannone. 2021. Molecular motion and tridimensional nanoscale localization of kindlin control integrin activation in focal adhesions. *Nat. Commun.* 12. doi:10.1038/s41467-021-23372-w.
Orré, T., O. Rossier, and G. Giannone. 2019. The inner life of integrin adhesion sites: From single molecules to functional macromolecular complexes. *Exp. Cell Res.* 379:235–244. doi:10.1016/j.yexcr.2019.03.036.
Oudjedi, L., J.-B. Fiche, S. Abrahamsson, L. Mazenq, A. Lecestre, P.-F. Calmon, A. Cerf, and M. Nöllmann. 2016. Astigmatic multifocus microscopy enables deep 3D super-resolved imaging. *Biomed. Opt. Express*. 7. doi:10.1364/boe.7.002163.
Owen, L.M., A.S. Adhikari, M. Patel, P. Grimmer, N. Leijnse, M.C. Kim, J. Notbohm, C. Franck, and A.R. Dunn. 2017. A cytoskeletal clutch mediates cellular force transmission in a soft, three-dimensional extracellular matrix. *Mol. Biol. Cell*. 28. doi:10.1091/mbc.E17-02-0102.
Park, J.S., I.B. Lee, H.M. Moon, J.S. Ryu, S.Y. Kong, S.C. Hong, and M. Cho. 2020. Fluorescence-Combined Interferometric Scattering Imaging Reveals Nanoscale Dynamic Events of Single

Nascent Adhesions in Living Cells. *J. Phys. Chem. Lett.* 11. doi:10.1021/acs.jpclett.0c02103.
Paszek, M.J., C.C. Dufort, M.G. Rubashkin, M.W. Davidson, K.S. Thorn, J.T. Liphardt, and V.M. Weaver. 2012. Scanning angle interference microscopy reveals cell dynamics at the nanoscale. *Nat. Methods*. 9. doi:10.1038/nmeth.2077.
Plak, K., H. Pots, P.J.M. Van Haastert, and A. Kortholt. 2016. Direct Interaction between TalinB and Rap1 is necessary for adhesion of Dictyostelium cells. *BMC Cell Biol.* 17:1–8. doi:10.1186/s12860-015-0078-0.
Pollard, T.D. 1986. Rate constants for the reactions of ATP- and ADP-actin with the ends of actin filaments. *J. Cell Biol.* 103:2747–2754. doi:10.1083/jcb.103.6.2747.
Pollard, T.D., and John A. Cooper. 2009. Actin, a Central Player in Cell Shape and Movement. *Science (80-.).* 326:1208–1212. doi:10.1126/science.1175862.
Racine, V., M. Sachse, J. Salamero, V. Fraisier, A. Trubuil, and J.B. Sibarita. 2007. Visualization and quantification of vesicle trafficking on a three-dimensional cytoskeleton network in living cells. *J. Microsc.* 225:214–228. doi:10.1111/j.1365-2818.2007.01723.x.
Rath, N., and M.F. Olson. 2012. Rho-associated kinases in tumorigenesis: Re-considering ROCK inhibition for cancer therapy. *EMBO Rep.* 13. doi:10.1038/embor.2012.127.
Réfrégier, P., M. Roche, and S. Brasselet. 2011. Precision analysis in polarization-resolved second harmonic generation microscopy. *Opt. Lett.* 36. doi:10.1364/ol.36.002149.
Rezniczek, G.A., J.M. De Pereda, S. Reipert, and G. Wiche. 1998. Linking integrin α6β4-based cell adhesion to the intermediate filament cytoskeleton: Direct interaction between the β4 subunit and plectin at multiple molecular sites. *J. Cell Biol.* 141. doi:10.1083/jcb.141.1.209.
Rimoli, C.V., C.A. Valades-Cruz, V. Curcio, M. Mavrakis, and S. Brasselet. 2022. 4polar-STORM polarized super-resolution imaging of actin filament organization in cells. *Nat. Commun.* 13:1–13. doi:10.1038/s41467-022-27966-w.
Ringer, P., A. Weißl, A.L. Cost, A. Freikamp, B. Sabass, A. Mehlich, M. Tramier, M. Rief, and C. Grashoff. 2017. Multiplexing molecular tension sensors reveals piconewton force gradient across talin-1. *Nat. Methods*. 14:1090–1096. doi:10.1038/nmeth.4431.
Rio, A., R. Perez-jimenez, R. Liu, P. Roca-cusachs, J.M. Fernandez, and M.P. Sheetz. 2009. Stretching Single Talin Rod. *Science (80-.).* 323:638–641.
Rocha, D.N., E.D. Carvalho, J.B. Relvas, M.J. Oliveira, and A.P. Pêgo. 2022. Mechanotransduction: Exploring New Therapeutic Avenues in Central Nervous System Pathology. *Front. Neurosci.* 16. doi:10.3389/fnins.2022.861613.
Rodius, S., O. Chaloin, M. Moes, E. Schaffner-Reckinger, I. Landrieu, G. Lippens, M. Lin, J. Zhang, and N. Kieffer. 2008. The talin rod IBS2 α-helix interacts with the β3 integrin cytoplasmic tail membrane-proximal helix by establishing charge complementary salt bridges. *J. Biol. Chem.* 283:24212–24223. doi:10.1074/jbc.M709704200.
Rossier, O., V. Octeau, J.-B. Sibarita, C. Leduc, B. Tessier, D. Nair, V. Gatterdam, O. Destaing, C. Albigès-Rizo, R. Tampé, L. Cognet, D. Choquet, B. Lounis, and G. Giannone. 2012. Integrins β1 and β3 exhibit distinct dynamic nanoscale organizations inside focal adhesions. *Nat. Cell Biol.* 14. doi:10.1038/ncb2588.
Ruoslahti, E., and F.G. Giancotti. 1989. Integrins and tumor cell dissemination. *Cancer Cells*. 1:119–126.
Rust, M.J., M. Bates, and X. Zhuang. 2006. Sub-diffraction-limit imaging by stochastic optical reconstruction microscopy (STORM). *Nat. Methods*. 3:793–795. doi:10.1038/nmeth929.

Sala, S., A. Caillier, and P.W. Oakes. 2024. Principles and regulation of mechanosensing. *J. Cell Sci.* 137. doi:10.1242/jcs.261338.

Sawada, Y., M. Tamada, B.J. Dubin-Thaler, O. Cherniavskaya, R. Sakai, S. Tanaka, and M.P. Sheetz. 2006. Force Sensing by Mechanical Extension of the Src Family Kinase Substrate p130Cas. *Cell*. 127:1015–1026. doi:10.1016/j.cell.2006.09.044.

Schiller, H.B., C.C. Friedel, C. Boulegue, and R. Fässignssler. 2011. Quantitative proteomics of the integrin adhesome show a myosin II-dependent recruitment of LIM domain proteins. *EMBO Rep.* 12. doi:10.1038/embor.2011.5.

Schlichthaerle, T., C. Lindner, and R. Jungmann. 2021. Super-resolved visualization of single DNA-based tension sensors in cell adhesion. *Nat. Commun.* 12. doi:10.1038/s41467-021-22606-1.

Schmidt, R., T. Weihs, C.A. Wurm, I. Jansen, J. Rehman, S.J. Sahl, and S.W. Hell. 2021. MINFLUX nanometer-scale 3D imaging and microsecond-range tracking on a common fluorescence microscope. *Nat. Commun.* 12. doi:10.1038/s41467-021-21652-z.

Seetharaman, S., and S. Etienne-Manneville. 2019. Microtubules at focal adhesions – a double-edged sword. *J. Cell Sci.* 132. doi:10.1242/jcs.232843.

Sergé, A., N. Bertaux, H. Rigneault, and D. Marguet. 2008. Dynamic multiple-target tracing to probe spatiotemporal cartography of cell membranes. *Nat. Methods*. 5. doi:10.1038/nmeth.1233.

Shattil, S.J., C. Kim, and M.H. Ginsberg. 2012. The final steps of integrin activation: the end game Sanford. *Changes*. 29:997–1003. doi:10.1038/nrm2871.The.

Shechtman, Y., A.-K. Gustavsson, P.N. Petrov, E. Dultz, M.Y. Lee, K. Weis, and W.E. Moerner. 2017. Observation of live chromatin dynamics in cells via 3D localization microscopy using Tetrapod point spread functions. *Biomed. Opt. Express*. 8. doi:10.1364/boe.8.005735.

Shechtman, Y., S.J. Sahl, A.S. Backer, and W.E. Moerner. 2014. Optimal point spread function design for 3D imaging. *Phys. Rev. Lett.* 113. doi:10.1103/PhysRevLett.113.133902.

Shimaoka, M., J. Takagi, and T.A. Springer. 2002. Conformational regulation of integrin structure and function. *Annu. Rev. Biophys. Biomol. Struct.* 31:485–516. doi:10.1146/annurev.biophys.31.101101.140922.

Shtengel, G., Y. Wang, Z. Zhang, W.I. Goh, H.F. Hess, and P. Kanchanawong. 2014. Imaging cellular ultrastructure by PALM, iPALM, and correlative iPALM-EM. *In* Methods in Cell Biology.

Smith, M.J., W.R. Hardy, J.M. Murphy, N. Jones, and T. Pawson. 2006. Screening for PTB Domain Binding Partners and Ligand Specificity Using Proteome-Derived NPXY Peptide Arrays. *Mol. Cell. Biol.* 26:8461–8474. doi:10.1128/mcb.01491-06.

Soto-Ribeiro, M., B. Kastberger, M. Bachmann, L. Azizi, K. Fouad, M.C. Jacquier, D. Boettiger, D. Bouvard, M. Bastmeyer, V.P. Hytönen, and B. Wehrle-Haller. 2019. β1D integrin splice variant stabilizes integrin dynamics and reduces integrin signaling by limiting paxillin recruitment. *J. Cell Sci.* 132. doi:10.1242/jcs.224493.

Stallinga, S. 2015. Effect of rotational diffusion in an orientational potential well on the point spread function of electric dipole emitters. *J. Opt. Soc. Am. A*. 32. doi:10.1364/josaa.32.000213.

Sun, N., D.R. Critchley, D. Paulin, Z. Li, and R.M. Robson. 2008. Human α-synemin interacts directly with vinculin and metavinculin. *Biochem. J.* 409:657–667. doi:10.1042/BJ20071188.

Sun, Z., A. Lambacher, and R. Fässler. 2014. Nascent adhesions: From fluctuations to a

hierarchical organization. *Curr. Biol.* 24:R801–R803. doi:10.1016/j.cub.2014.07.061.
Svitkina, T.M., and G.G. Borisy. 1999. Arp2/3 complex and actin depolymerizing factor/cofilin in dendritic organization and treadmilling of actin filament array in lamellipodia. *J. Cell Biol.* 145:1009–1026. doi:10.1083/jcb.145.5.1009.
Swaminathan, V., and M. Gloerich. 2021. Decoding mechanical cues by molecular mechanotransduction. *Curr. Opin. Cell Biol.* 72:72–80. doi:10.1016/j.ceb.2021.05.006.
Takagi, J., and T.A. Springer. 2002. Integrin activation and structural rearrangement. *Immunol. Rev.* 186:141–163. doi:10.1034/j.1600-065X.2002.18613.x.
Tamkun, J.W., D.W. DeSimone, D. Fonda, R.S. Patel, C. Buck, A.F. Horwitz, and R.O. Hynes. 1986. Structure of integrin, a glycoprotein involved in the transmembrane linkage between fibronectin and actin. *Cell*. 46:271–282. doi:10.1016/0092-8674(86)90744-0.
Tapia-Rojo, R., A. Alonso-Caballero, and J.M. Fernandez. 2020. Direct observation of a coil-to-helix contraction triggered by vinculin binding to talin. *Sci. Adv.* 6. doi:10.1126/sciadv.aaz4707.
Theocharis, A.D., S.S. Skandalis, C. Gialeli, and N.K. Karamanos. 2016. Extracellular matrix structure. *Adv. Drug Deliv. Rev.* 97:4–27. doi:10.1016/j.addr.2015.11.001.
Thievessen, I., N. Fakhri, J. Steinwachs, V. Kraus, R.S. McIsaac, L. Gao, B.C. Chen, M.A. Baird, M.W. Davidson, E. Betzig, R. Oldenbourg, C.M. Waterman, and B. Fabry. 2015. Vinculin is required for cell polarization, migration, and extracellular matrix remodeling in 3D collagen. *FASEB J.* 29. doi:10.1096/fj.14-268235.
Toprak, E., and P.R. Selvin. 2007. New fluorescent tools for watching nanometer-scale conformational changes of single molecules. *Annu. Rev. Biophys. Biomol. Struct.* 36. doi:10.1146/annurev.biophys.36.040306.132700.
Tsuruta, D., and J.C.R. Jones. 2003. The vimentin cytoskeleton regulates focal contact size and adhesion of endothelial cells subjected to shear stress. *J. Cell Sci.* 116:4977–4984. doi:10.1242/jcs.00823.
Turkowyd, B., D. Virant, and U. Endesfelder. 2016. From single molecules to life: microscopy at the nanoscale. *Anal. Bioanal. Chem.* 408:6885–6911. doi:10.1007/s00216-016-9781-8.
Uehata, M., T. Ishizaki, H. Satoh, T. Ono, T. Kawahara, T. Morishita, H. Tamakawa, K. Yamagami, J. Inui, M. Maekawa, and S. Narumiya. 1997. Calcium sensitization of smooth muscle mediated by a Rho-associated protein kinase in hypertension. *Nature*. 389. doi:10.1038/40187.
Ulmer, T.S., D.A. Calderwood, M.H. Ginsberg, and I.D. Campbell. 2003. Domain-specific interactions of talin with the membrane-proximal region of the integrin β3 subunit. *Biochemistry*. 42:8307–8312. doi:10.1021/bi034384s.
Uyeda, T.Q.P., P.D. Abramson, and J.A. Spudich. 1996. The neck region of the myosin motor domain acts as a lever arm to generate movement. *Proc. Natl. Acad. Sci. U. S. A.* 93:4459–4464. doi:10.1073/pnas.93.9.4459.
Valli, J., A. Garcia-Burgos, L.M. Rooney, B.V. de Melo e Oliveira, R.R. Duncan, and C. Rickman. 2021. Seeing beyond the limit: A guide to choosing the right super-resolution microscopy technique. *J. Biol. Chem.* 297:100791. doi:10.1016/j.jbc.2021.100791.
Várkuti, B.H., M. Képiró, I.Á. Horváth, L. Végner, S. Ráti, Á. Zsigmond, G. Hegyi, Z. Lenkei, M. Varga, and A. Málnási-Csizmadia. 2016. A highly soluble, non-phototoxic, non-fluorescent blebbistatin derivative. *Sci. Rep.* 6. doi:10.1038/srep26141.

Vicente-Manzanares, M., X. Ma, R.S. Adelstein, and A.R. Horwitz. 2009. Non-muscle myosin II takes centre stage in cell adhesion and migration. *Nat. Rev. Mol. Cell Biol.* 10:778–790. doi:10.1038/nrm2786.

Vleugel, M., M. Kok, and M. Dogterom. 2016. Understanding force-generating microtubule systems through in vitro reconstitution. *Cell Adhes. Migr.* 10:475–494. doi:10.1080/19336918.2016.1241923.

Wakimoto, T., S. Matsunaga, A. Takai, and N. Fusetani. 2002. Insight into binding of calyculin A to protein phosphatase 1: Isolation of hemicalyculin A and chemical transformation of calyculin A. *Chem. Biol.* 9. doi:10.1016/S1074-5521(02)00118-7.

Wehrle-Haller, B. 2012. Assembly and disassembly of cell matrix adhesions. *Curr. Opin. Cell Biol.* 24:569–581. doi:10.1016/j.ceb.2012.06.010.

Wiedenmann, J., S. Ivanchenko, F. Oswald, F. Schmitt, C. Röcker, A. Salih, K.D. Spindler, and G.U. Nienhaus. 2004. EosFP, a fluorescent marker protein with UV-inducible green-to-red fluorescence conversion. *Proc. Natl. Acad. Sci. U. S. A.* 101:15905–15910. doi:10.1073/pnas.0403668101.

Wolfenson, H., I. Lavelin, and B. Geiger. 2013. Dynamic Regulation of the Structure and Functions of Integrin Adhesions. *Dev. Cell*. 24:447–458. doi:10.1016/j.devcel.2013.02.012.

Yang, J., L. Zhu, H. Zhang, J. Hirbawi, K. Fukuda, P. Dwivedi, J. Liu, T. Byzova, E.F. Plow, J. Wu, and J. Qin. 2014. Conformational activation of talin by RIAM triggers integrin-mediated cell adhesion. *Nat. Commun.* 5:5880. doi:10.1038/ncomms6880.

Yao, M., B.T. Goult, B. Klapholz, X. Hu, C.P. Toseland, Y. Guo, P. Cong, M.P. Sheetz, and J. Yan. 2016. The mechanical response of talin. *Nat. Commun.* 7. doi:10.1038/ncomms11966.

Yoshigi, M., L.M. Hoffman, C.C. Jensen, H.J. Yost, and M.C. Beckerle. 2005. Mechanical force mobilizes zyxin from focal adhesions to actin filaments and regulates cytoskeletal reinforcement. *J. Cell Biol.* 171. doi:10.1083/jcb.200505018.

Zaidel-Bar, R., C. Ballestrem, Z. Kam, and B. Geiger. 2003. Early molecular events in the assembly of matrix adhesions at the leading edge of migrating cells. *J. Cell Sci.* 116. doi:10.1242/jcs.00792.

Zamir, E., B. Geiger, and Z. Kam. 2008. Quantitative multicolor compositional imaging resolves molecular domains in cell-matrix adhesions. *PLoS One*. 3:9–11. doi:10.1371/journal.pone.0001901.

Zhang, M., H. Chang, Y. Zhang, J. Yu, L. Wu, W. Ji, J. Chen, B. Liu, J. Lu, Y. Liu, J. Zhang, P. Xu, and T. Xu. 2012. Rational design of true monomeric and bright photoactivatable fluorescent proteins. *Nat. Methods*. 9:727–729. doi:10.1038/nmeth.2021.

Zhanghao, K., X. Chen, W. Liu, M. Li, Y. Liu, Y. Wang, S. Luo, X. Wang, C. Shan, H. Xie, J. Gao, X. Chen, D. Jin, X. Li, Y. Zhang, Q. Dai, and P. Xi. 2019. Super-resolution imaging of fluorescent dipoles via polarized structured illumination microscopy. *Nat. Commun.* 10. doi:10.1038/s41467-019-12681-w.

Zhao, Q., H. Zhou, S. Chi, Y. Wang, J. Wang, J. Geng, K. Wu, W. Liu, T. Zhang, M.Q. Dong, J. Wang, X. Li, and B. Xiao. 2018. Structure and mechanogating mechanism of the Piezo1 channel. *Nature*. 554. doi:10.1038/nature25743.

Zhu, L., J. Yang, T. Bromberger, A. Holly, F. Lu, H. Liu, K. Sun, S. Klapproth, J. Hirbawi, T. V. Byzova, E.F. Plow, M. Moser, and J. Qin. 2017. Structure of Rap1b bound to talin reveals a pathway for triggering integrin activation. *Nat. Commun.* 8:1–11. doi:10.1038/s41467-017-01822-8.

Appendix 1

Development of a reliable C-terminus tagged mouse β3 integrin

Previous work in our lab had already shown that INT2 (a mouse β3 integrin fused to mEos3.2; no His-tag) exhibited higher diffusivity than the human 6His-tagged β3 integrin construct previously used in the lab (Rossier et al., 2012). These differences were consistently observed both inside and outside focal adhesions (FAs) and under basal and Mn^{2+}-activated conditions. This unexpected finding suggested that factors beyond integrin activation state - such as the presence of purification tags, the species of origin, or linker composition, could significantly influence integrin dynamics.

This motivated us to perform a systematic development and comparison of β3 integrin constructs in mouse embryonic fibroblasts (MEFs), in collaboration with Manos Mavrakis (Institut Fresnel, Marseille). Our goal was to disentangle the respective contributions of the His-tag, linker length, and species origin to integrin mobility, and thereby identify a construct that most faithfully reflects physiologically relevant behavior under basal and Mn^{2+}-activated conditions.

To do so, we started from a well-established construct consisting of a human β3 integrin fused at its C-terminus to mEos3.2 through a 12-amino-acid linker and carrying an N-terminal 6Histidine tag (Figure 101a), a protein construct which was used previously in the team for integrin dynamics studies (Rossier et al., 2012). In parallel, we tested a related construct available in the lab, 'INT2', which is a mouse β3 integrin fused to mEos3.2 with the same 12-aa linker but lacking the 6His tag (Figure 101d).

For all constructs, mouse embryonic fibroblasts (MEFs) were co-transfected with β3Integrin-mEos variants and YFP-paxillin as an FA reporter. After 48 h at 37 °C, cells were plated on fibronectin-coated coverslips, incubated 2–4 h in regular medium to promote FA formation, and transferred to Ringer's solution before imaging. Imaging was performed under TIRF, followed by sptPALM acquisition (400 s, 50 ms/frame). Widefield YFP-paxillin images were used to generate FA masks, and single-molecule localizations were reconstructed, linked into trajectories (≥260 ms, ≥13 points), and classified as immobile, confined, or freely diffusive using MSD analysis. This unified workflow was applied to all integrin constructs described below.

As expected from prior work, INT2 was more diffusive than the human 6His construct both inside and outside FAs, and under basal as well as Mn^{2+}-activated conditions (Figure 98). The fraction of diffusive integrins was also larger for INT2 (Figure 99), and the diffusion coefficients of its mobile population were higher (Figure 100).

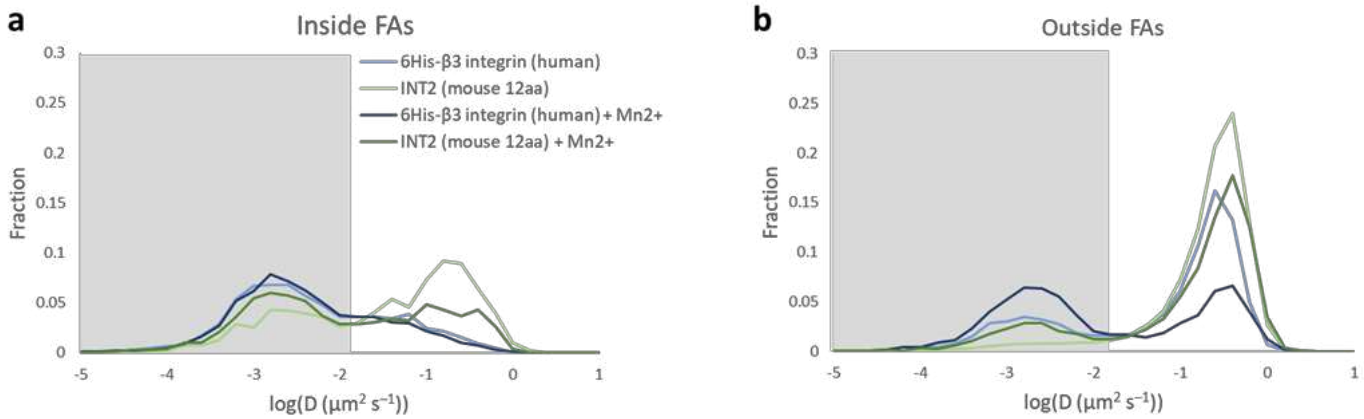

Figure 98. ***Mouse β3 integrin (INT2) is more diffusive than human 6His-tagged β3 integrin, both at baseline and after Mn^{2+} activation****. MEFs expressing either 6His-β3Integrin-mEos2 (human, 12-aa linker) or INT2 (mouse, 12-aa linker, no His-tag) were plated on fibronectin-coated coverslips and imaged by sptPALM under TIRF (400 s, 50 ms/frame). Cells were treated with or without Mn^{2+} to induce integrin activation. Shown are log(D) distributions of trajectories ≥ 260 ms inside (**a**) and outside (**b**) FA masks. Grey shading indicates immobile trajectories (D < 0.008 μm²/s). Number of cells: 5 (6His), 4 (6His + Mn^{2+}), 7 (INT2), 4 (INT2 + Mn^{2+}).*

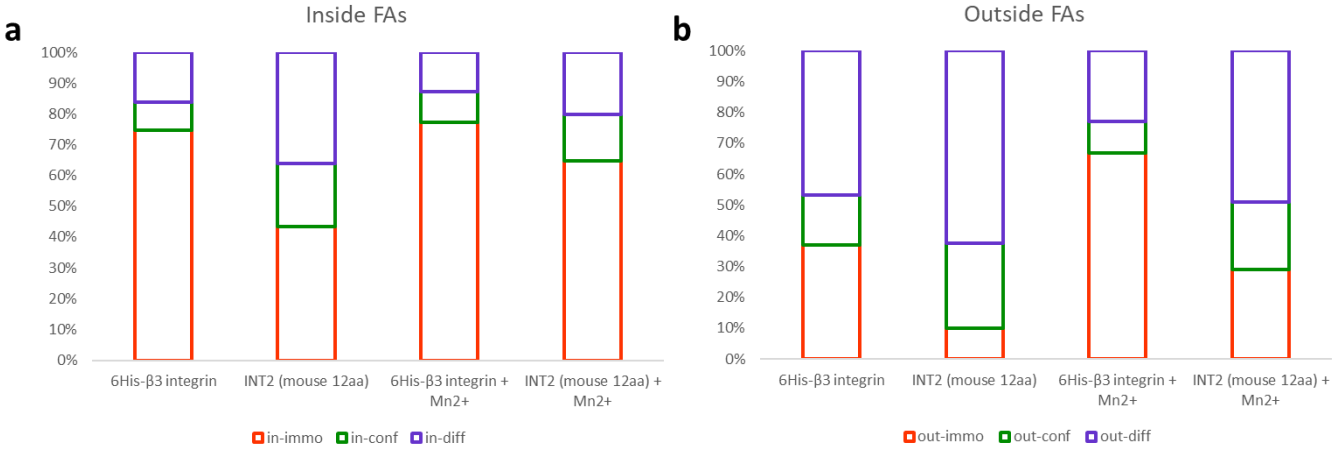

Figure 99. ***INT2 (mouse) displays a higher proportion of diffusive trajectories compared to human 6His-β3 integrin, independent of Mn^{2+} activation.*** *Mean percentages of immobile, confined, and diffusive trajectories (≥ 260 ms) are shown inside (**a**) and outside (**b**) FAs for the same constructs as in Figure 98. Number of cells as in Figure 98. Compared to the 6His-tagged construct, INT2 consistently exhibited fewer immobile and more diffusive molecules, both under basal and Mn^{2+}-activated conditions.*

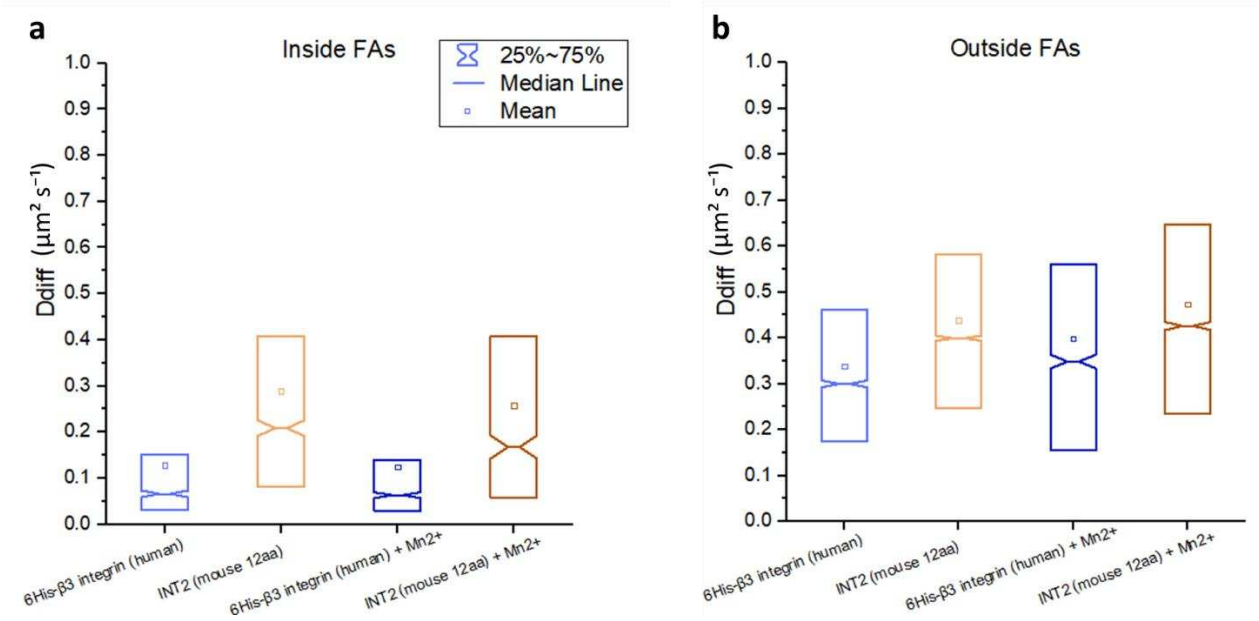

Figure 100. ***The diffusion coefficient of diffusive integrins (D_{diff}) is higher in INT2 compared to 6His-tagged β3 integrin.*** *Median D_{diff} values of trajectories classified as freely diffusive (≥ 260 ms) inside (**a**) and outside (**b**) FAs for the same conditions as in Figure 98. INT2 showed elevated Ddiff in both regions.*

As the 6His tag is used for purification purposes, and has no biological use, we hypothesized that the observed difference could be attributable to the presence of this tag. This is why we: generated a human form without the histidine tag (Figure 101b), and both human and mouse β3 integrins fused to mEos3.2 through an alternative 14-aa linker (Figure 101c, e). This strategy allowed us to dissect the contribution of the tag and the linker to integrin dynamics.

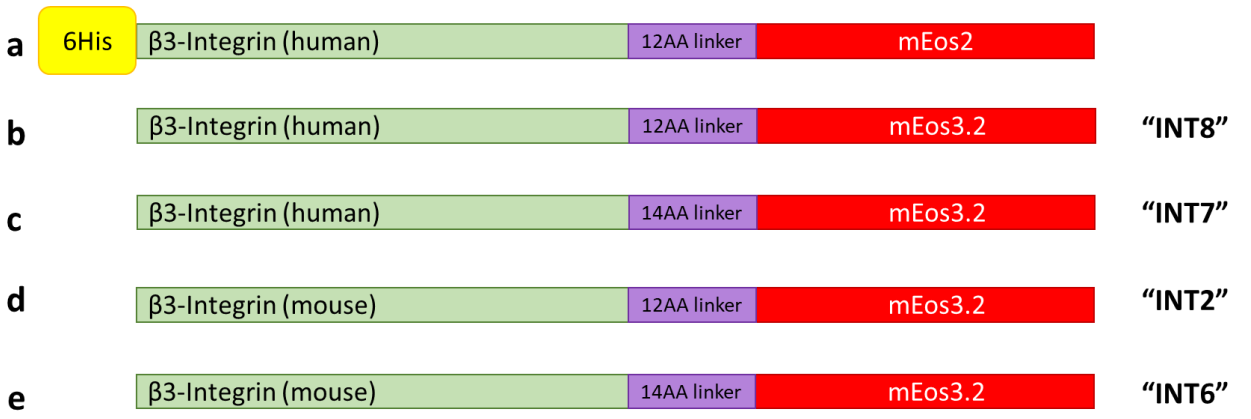

Figure 101. ***Schematic overview of β3 integrin constructs used to test the influence of His-tag and linker length****. (**a**) 6Histidine-β3Integrin-mEos2 (human, 12aa linker), (**b**) β3Integrin-mEos3.2 (human, 12aa linker), (**c**) β3Integrin-mEos3.2 (human, 14aa linker), (**d**) β3Integrin-mEos3.2 (mouse, 12aa linker), (**e**) β3Integrin-mEos3.2 (mouse, 14aa linker).*

Representative reconstructions and trajectories for all constructs are shown in Figure 102.

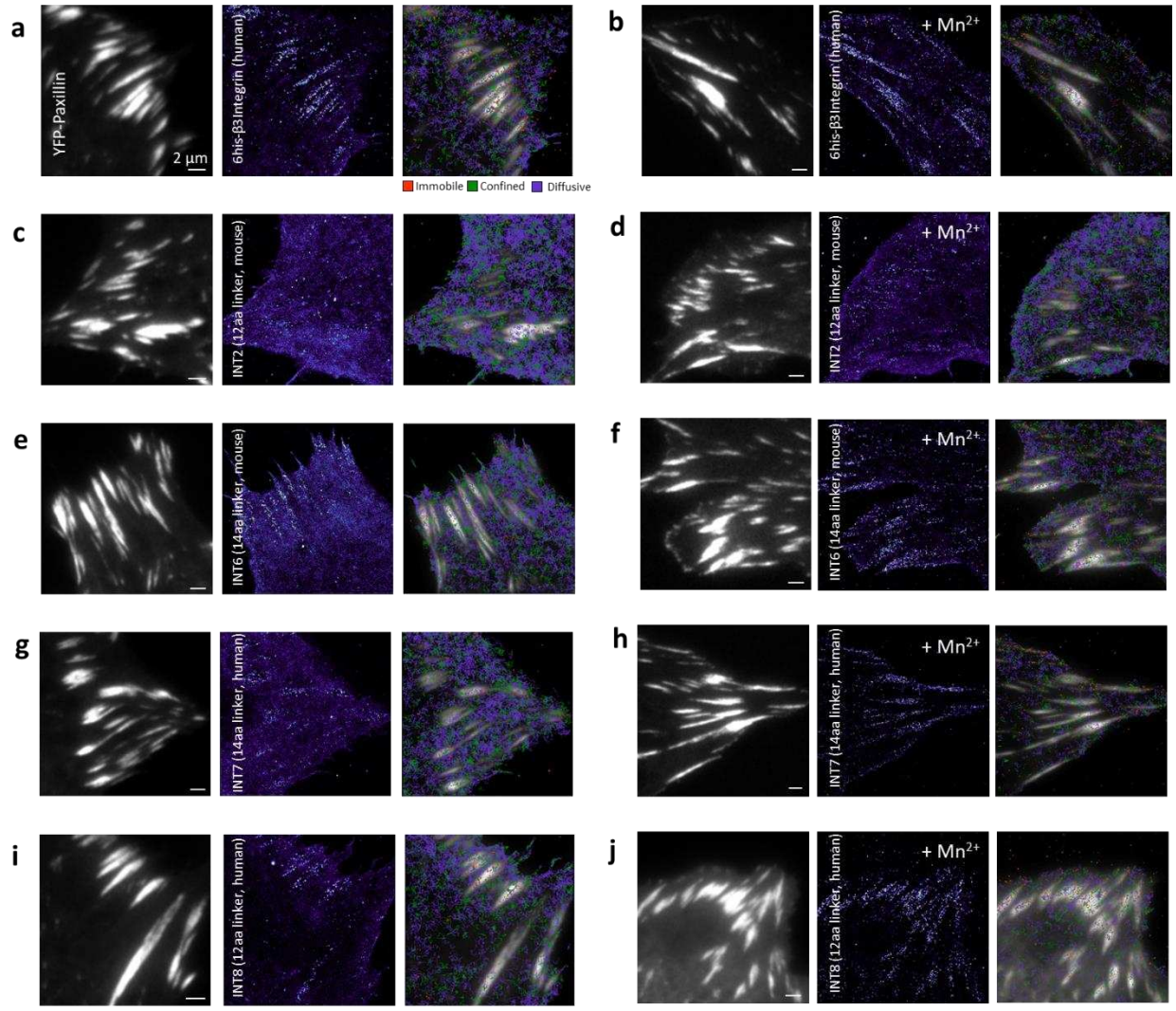

Figure 102. ***Super-resolution reconstructions and trajectory classification of β3 integrin constructs under basal and Mn²⁺-activated conditions****. MEFs were co-transfected with β3Integrin-mEos constructs and YFP-paxillin, plated on fibronectin-coated coverslips, and imaged by sptPALM under TIRF (400 s, 50 ms/frame). Each panel: left, diffraction-limited YFP-paxillin image depicting FAs; middle, super-resolved reconstruction of integrin localizations; right, color-coded trajectories overlaid on FA images (purple, diffusive; green, confined; red, immobile). Panels: (**a**) 6His-human, (**b**) 6His-human + Mn²⁺, (**c**) INT2 mouse, (**d**) INT2 + Mn²⁺, (**e**) INT6 mouse, (**f**) INT6 + Mn²⁺, (**g**) INT7 human, (**h**) INT7 + Mn²⁺, (**i**) INT8 human, (**j**) INT8 + Mn²⁺. Scale bar: 2 µm.*

We, once again, extracted single-molecule diffusion coefficients and compared their distribution inside (Figure 103a) vs outside (Figure 103b) FAs. When comparing *INT8* (a human β3 integrin construct with a 12aa linker) to the historical 6His-tagged β3 integrin (also human, with a 12aa linker), we observed that the 6His-tagged construct exhibits lower diffusivity in both regions. Interestingly, upon Mn^{2+} induced activation, the diffusion coefficient distributions of both constructs become nearly indistinguishable. This suggests that the 6His tag may alter integrin

diffusivity in the basal state but not under activating conditions. Furthermore, the *INT7* construct, which uses an alternative 14-amino-acid linker, shows overall higher diffusion than both *INT8* and the 6His-tagged integrin, highlighting the potential impact of linker length and composition.

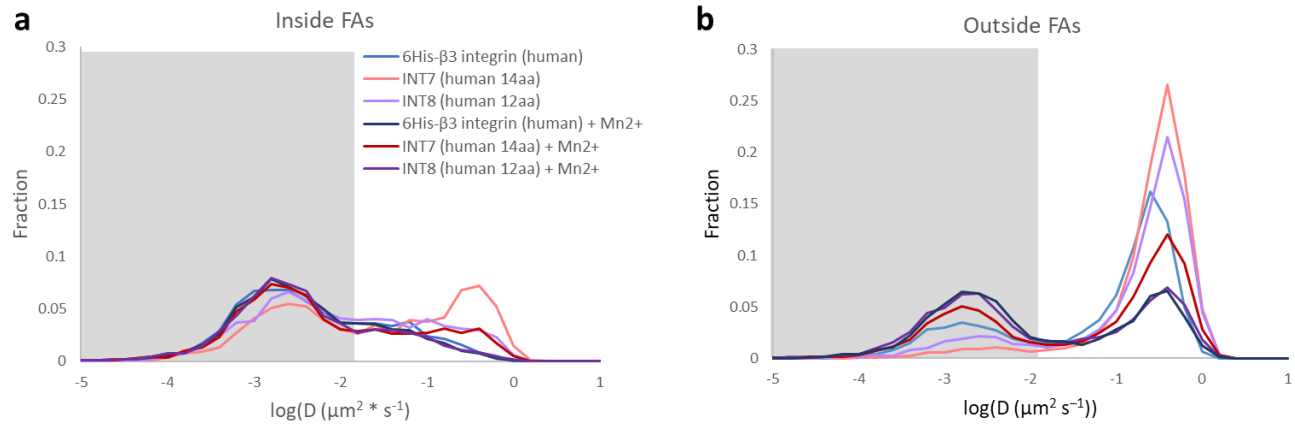

Figure 103. ***Both N-terminal His-tag and linker length influence human β3 integrin diffusivity, with Mn^{2+} activation reducing construct-dependent differences****. Distributions of log(D) for human β3 integrin constructs inside (**a**) and outside (**b**) FAs, comparing the 6His-tagged form (12-aa linker), the tag-free INT8 (12-aa linker), and INT7 (14-aa linker). Number of cells: 4 per construct. Under basal conditions, the 6His construct showed reduced diffusivity relative to INT8, while INT7 exhibited the highest mobility. Upon Mn^{2+} activation, diffusion coefficient distributions converged across all constructs, with INT8 remaining more diffusive than INT7 and 6His construct.*

We next compared the diffusion behavior of *INT2*, a mouse β3 integrin construct with the 12-aa linker, to that of *INT8*, its human counterpart. In both regions - inside and outside of FAs, *INT2* exhibited higher diffusivity than INT8 (Figure 104a, b). Notably, Mn^{2+} activation induced only a modest shift in the diffusion coefficient distribution of *INT2*, especially when compared to the more pronounced effect observed in *INT8.* These results suggest that species-specific sequence differences in the integrin tail or membrane context may influence basal diffusivity and responsiveness to activation.

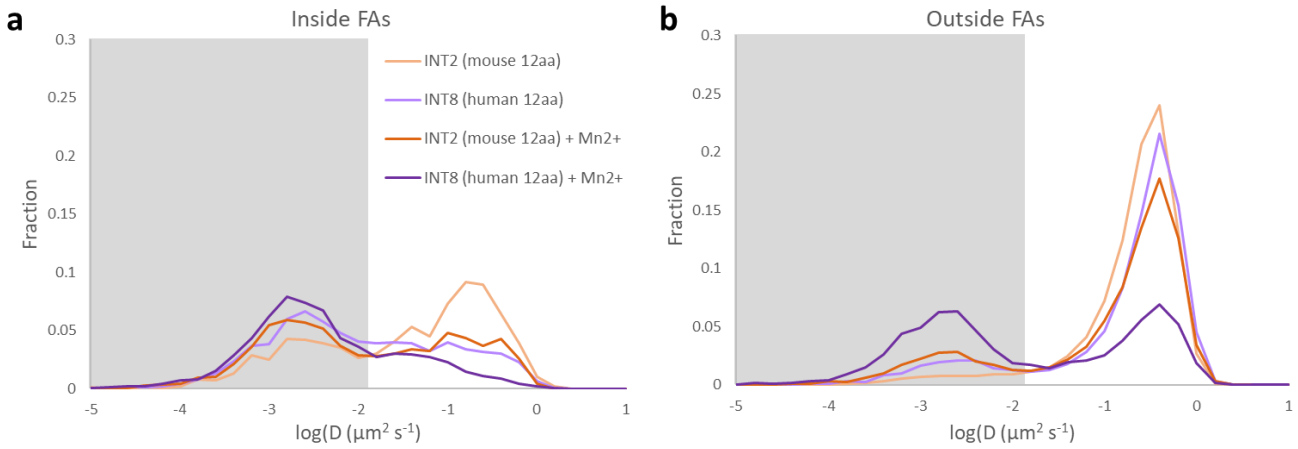

Figure 104. ***Species origin modulates β3 integrin diffusivity for 12-aa linker constructs, with mouse integrin remaining more mobile and less activation-responsive than human****. Distributions of log(D) for mouse INT2 (12-aa linker) and human INT8 (12-aa linker) inside (**a**) and outside (**b**) FAs, with and without Mn^{2+} activation. Number of cells: 4 per construct. INT2 displayed higher basal diffusivity than INT8 in both regions, and Mn^{2+} activation induced only a modest shift in INT2 compared to the stronger immobilization observed for INT8. These results suggest species-specific differences in tail sequence or membrane context that influence integrin mobility and responsiveness to activation.*

We then examined *INT6*, the mouse β3 integrin construct with the 14aa linker, and compared it to *INT7*, the corresponding human version. Interestingly, both constructs exhibited remarkably similar diffusion behavior, both inside and outside of focal adhesions (Figure 105a, b). This stands in contrast to the differences observed between other mouse and human constructs, making *INT6* and *INT7* unique in their matched diffusivity profiles. These results suggest that the 14-amino-acid linker may buffer species-specific differences and promote a conserved dynamic behavior at the membrane.

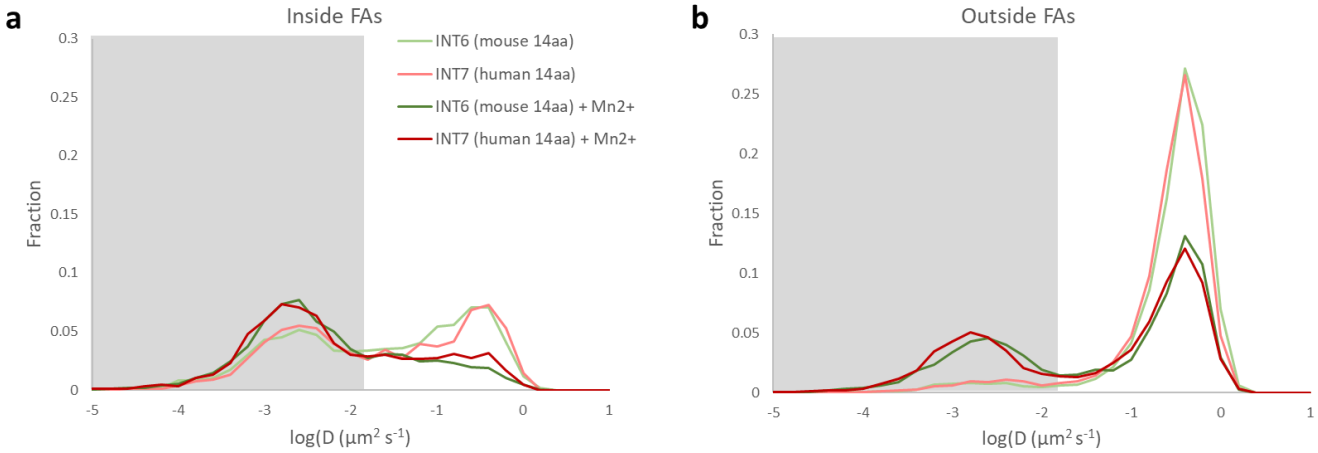

Figure 105. ***Linker length overrides species-specific differences, yielding nearly identical dynamics for human and mouse β3 integrins with 14-aa linkers****. Distributions of log(D) for mouse INT6 (14-aa linker) and human INT7 (14-aa*

*linker) inside (**a**) and outside (**b**) FAs, with and without Mn^{2+} activation. Number of cells: 4 per construct. Unlike the divergent behavior of their 12-aa linker counterparts, INT6 and INT7 exhibited nearly indistinguishable diffusion profiles under both basal and Mn^{2+}-activated conditions, indicating that the 14-aa linker buffers species-dependent effects.*

To further compare the behavior of all C-terminally tagged integrin constructs, we analyzed the proportion of immobile, confined, and freely diffusive molecules both inside and outside focal adhesions (Figure 106, Figure 107). For clarity and easier interpretation, we focused on the percentage of molecules classified as diffusive, and how this population shifts upon Mn^{2+} activation. These comparisons are summarized in Table 2 and Table 3, providing a direct overview of the activation-dependent changes in integrin mobility across constructs.

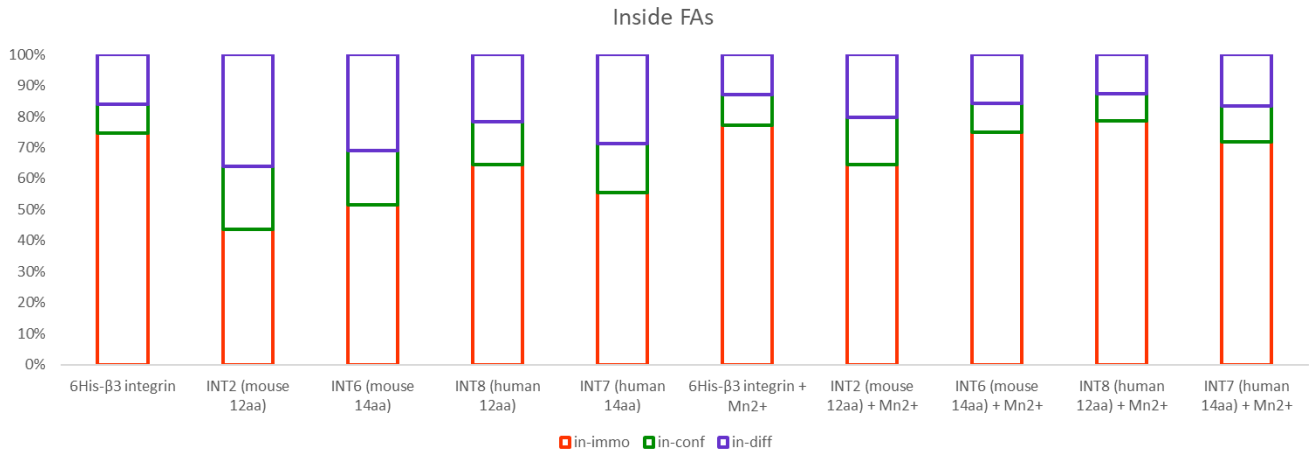

*Figure 106. **Inside FAs, Mn^{2+} activation decreases diffusion most strongly in mouse constructs INT2 and INT6**. Percentages of immobile, confined, and diffusive trajectories (≥ 260 ms) inside FA masks for all β3 integrin constructs). Number of cells: 4 per construct.*

% of diffusion decrease					
Construct name	6His-β3 integrin (human)	INT2 (mouse 12aa)	INT6 (mouse 14aa)	INT8 (human 12aa)	INT7 (human 14aa)
%	3.22	15.96	15.03	8.87	12.18

*Table 2. **Quantification of diffusion decreases inside FAs**. Percentage of molecules whose mobility decreased upon Mn^{2+} activation across integrin constructs. INT2 and INT6 showed the largest decreases (~16% and ~15%), while the human 6His construct was minimally affected (~3%).*

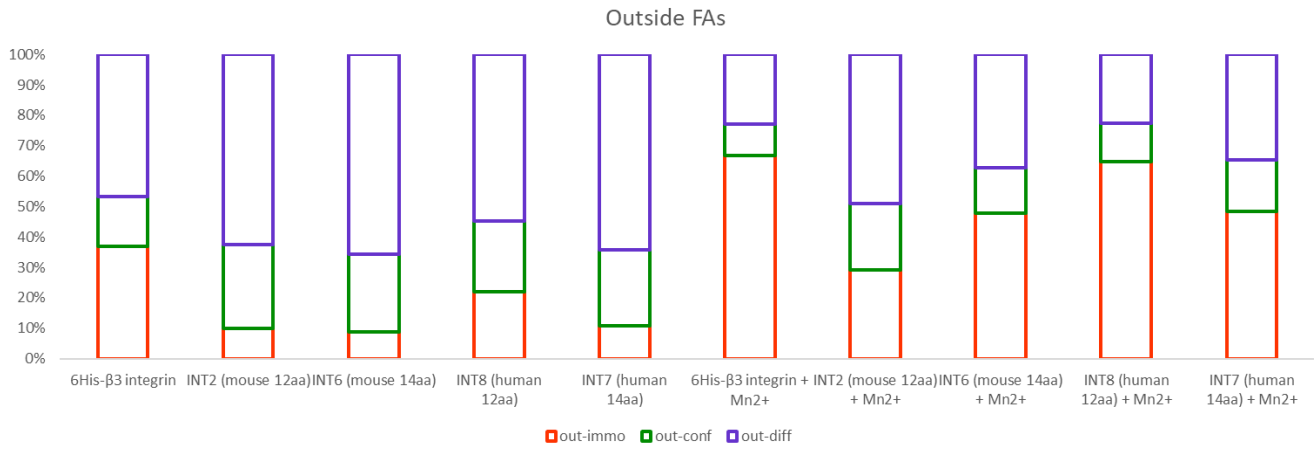

Figure 107. ***Outside FAs, both human and mouse 14-aa linker constructs show strong decreases in diffusion upon Mn^{2+} activation, alongside human 12-aa linker****. Percentages of immobile, confined, and diffusive trajectories outside FA masks for all β3 integrin constructs. Number of cells: 4 per construct. The largest decreases in diffusivity were observed for INT8 (human, 12-aa linker), INT7 (human, 14-aa linker,), and INT6 (mouse, 14-aa linker), whereas INT2 (mouse, 12-aa linker) showed the weakest response.*

% of diffusion decrease					
Construct name	6His-β3 integrin (human)	INT2 (mouse 12aa)	INT6 (mouse 14aa)	INT8 (human 12aa)	INT7 (human 14aa)
%	23.69	13.46	28.38	32.29	29.65

Table 3. ***Quantification of diffusion decreases outside FAs****. Values report the percentage of integrin molecules whose diffusion decreased upon Mn^{2+} activation. INT8 (human, 12-aa linker), INT7 (human, 14-aa linker), and INT6 (mouse, 14-aa linker) showed the strongest decreases (32%, 30%, and 28%, respectively), whereas INT2 (mouse, 12-aa linker) exhibited the smallest change (13%).*

Inside FAs (Table 2), *INT2* and *INT6* (both mouse constructs) showed the largest reductions in diffusivity (15.96% and 15.03%, respectively), while the 6His-tagged human β3 integrin showed minimal response (3.22%). In contrast, outside FAs (Table 3), the human constructs *INT8* and *INT7* displayed the strongest diffusion decrease (32.29% and 29.65%), followed by INT6 (28.38%). Interestingly, *INT2* exhibited the smallest change outside FAs (13.46%), further supporting earlier observations that Mn^{2+} has a less pronounced effect on the mouse integrin constructs. These data suggest that both species origin and linker composition influence how integrin mobility is modulated by activation, and that these effects differ between areas of the cell.

To compare the mobility behavior of individual integrin molecules across constructs, we quantified and plotted the diffusion coefficient (D_{diff}) distributions for each molecule under basal and Mn^{2+}-activated conditions, both inside (Figure 108a) and outside (Figure 108b) FAs. Inside

FAs, we observed that the 6His-β3 integrin construct (human) exhibited the lowest D_{diff} values, indicating a slow diffusion. In contrast, mouse constructs *INT2* and *INT6*, as well as the human 14aa linker construct *INT7*, showed higher diffusion coefficients, suggesting faster mobility. Upon Mn^{2+} activation, most constructs demonstrated a notable decrease in D_{diff}, reflecting increased immobilization, with the exception of *INT2*, where the effect was more modest. Outside FAs, D_{diff} values were generally higher for all constructs, as expected, with the human constructs *INT8* and *INT7*, as well as *INT6* (mouse 14aa), displaying the highest diffusivity. Interestingly, Mn^{2+} activation led to a more substantial decrease in D_{diff} in this region, especially for *INT8* and *INT7*, consistent with a strong activation-dependent shift in mobility. These data reinforce the differential behavior of integrin constructs across adhesion contexts and highlight the impact of linker composition, species origin, and activation state on single-molecule dynamics.

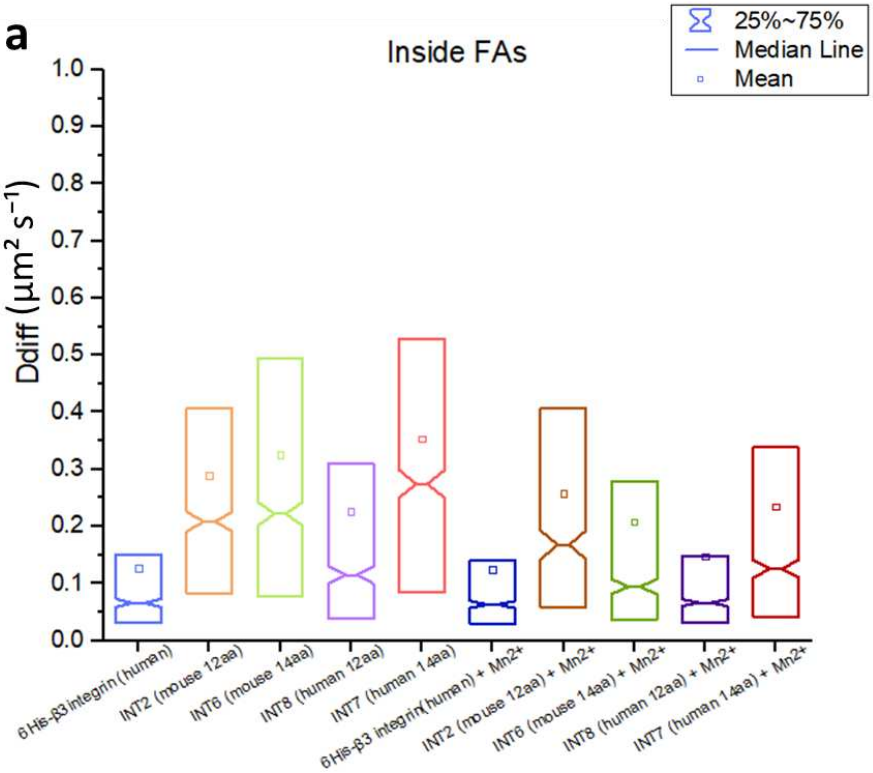

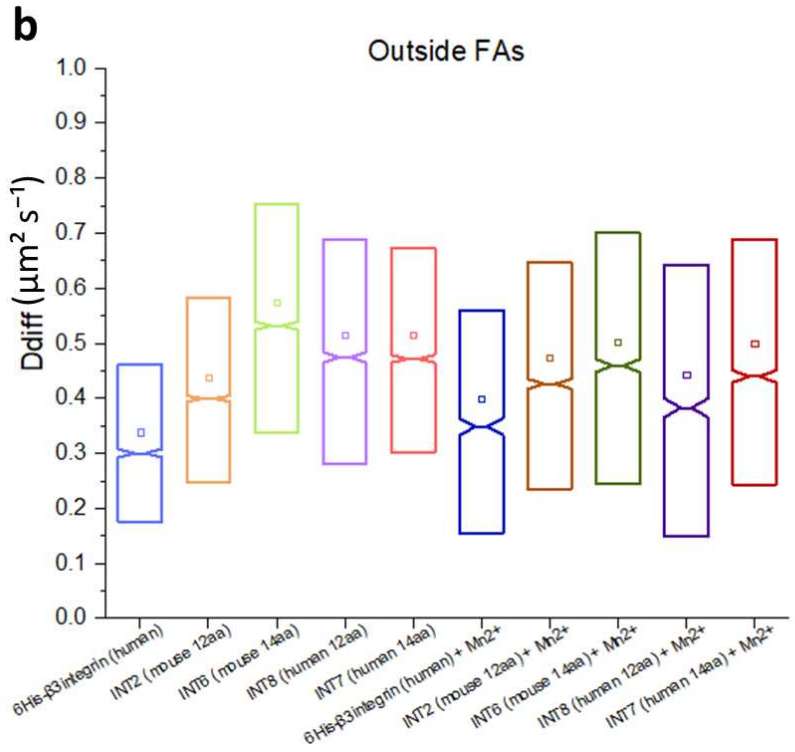

Figure 108. ***D_{diff} analysis confirms construct- and activation-dependent differences in integrin mobility****. Diffusion coefficients (D_{diff}) of trajectories classified as freely diffusive were computed inside (**a**) and outside (**b**) focal-adhesion (FA) masks for each construct under basal conditions and after Mn^{2+} activation (n = 4 cells per construct). Inside FAs, the 6His-tagged human β3 integrin tends toward the slowest diffusive population, while INT2 (mouse, 12-aa linker), INT6 (mouse, 14-aa), and INT7 (human, 14-aa) exhibit higher D_{diff}; Mn^{2+} shifts Ddiff downward for most constructs, with a comparatively small effect on INT2. Outside FAs, D_{diff} increases for all constructs; under basal conditions 6His and INT2 show to be the slower, compared to INT6, INT7 and INT8 which show higher, similar values. Mn^{2+} activation reduces D_{diff} for INT6 and INT8, whereas it remains mostly unchanged for others.*

Taken together, these results demonstrate that both the presence of an N-terminal His-tag and the choice of linker length substantially influence the mobility of β3 integrin constructs. Inside FAs, mouse constructs with a 14-aa linker (INT6) and human constructs with the same linker (INT7) showed the most physiologically consistent behavior, with robust Mn^{2+}-induced decreases in diffusivity. In contrast, the 6His-tagged human integrin displayed lower responsiveness to activation, suggesting that the His-tag introduces artifacts that dampen dynamic regulation. Moreover, species-specific differences were evident in constructs with a 12-aa linker, as mouse INT2 remained more diffusive and less responsive to Mn^{2+} compared to the human INT8 counterpart. Interestingly, the 14-aa linker largely abolished these species differences, producing nearly identical diffusion profiles for INT6 and INT7 across adhesion contexts.

Overall, these data identify INT6 (mouse, 14-aa linker) as the most reliable C-terminally tagged β3 integrin construct for further studies in MEFs. Its behavior not only reflects physiologically relevant shifts in mobility upon Mn^{2+} activation but also closely parallels the human INT7 construct, thereby providing a robust cross-species model. Thus, by carefully optimizing tag placement and linker composition, we established a construct that avoids artifacts associated with the 6His tag and exhibits reproducible, activation-sensitive dynamics suitable for mechanotransduction studies.

Appendix 2

Carla Silva Martins, Cyntia Taveneau, Gerard Castro-Linares, Mikhail Baibakov, Nicolas Buzhinsky, Mar Eroles, **Violeta Milanović**, Shizue Omi, Jean-Denis Pedelacq, Francois Iv, Léa Bouillard, Alexander Llewellyn, Maxime Gomes, Mayssa Belhabib, Mira Kuzmić, Pascal Verdier-Pinard, Stacey Lee, Ali Badache, Sanjay Kumar, Cristel Chandre, Sophie Brasselet, Felix Rico, Olivier Rossier, Gijsje H. Koenderink, Jerome Wenger, Stéphanie Cabantous, Manos Mavrakis; **Human septins organize as octamer-based filaments and mediate actin-membrane anchoring in cells**. J Cell Biol 6 March 2023; 222 (3): e202203016. doi: https://doi.org/10.1083/jcb.202203016.

As part of my contribution to this paper, I performed single-particle tracking PALM (sptPALM) to characterize the nanoscale dynamics of human septin complexes in living cells. Analysis of the trajectories we generated revealed low diffusion coefficients and confined motion, indicating that septin assemblies behaved as stable, membrane-associated filaments, rather than as freely diffusing monomers or small oligomers. These findings provided crucial dynamical evidence supporting the structural and biochemical data that septins are largely immobilized along actin stress fibers.

JCB Journal of Cell Biology

ARTICLE

Human septins organize as octamer-based filaments and mediate actin-membrane anchoring in cells

Carla Silva Martins[1,10], Cyntia Taveneau[2], Gerard Castro-Linares[3], Mikhail Baibakov[1], Nicolas Buzhinsky[4], Mar Eroles[4], Violeta Milanović[5], Shizue Omi[1], Jean-Denis Pedelacq[6], Francois Iv[1], Léa Bouillard[1], Alexander Llewellyn[1], Maxime Gomes[1], Mayssa Belhabib[1], Mira Kuzmić[7], Pascal Verdier-Pinard[7], Stacey Lee[8], Ali Badache[7], Sanjay Kumar[8], Cristel Chandre[9], Sophie Brasselet[1], Felix Rico[4], Olivier Rossier[5], Gijsje H. Koenderink[3], Jerome Wenger[1], Stéphanie Cabantous[10], and Manos Mavrakis[1]

Septins are cytoskeletal proteins conserved from algae and protists to mammals. A unique feature of septins is their presence as heteromeric complexes that polymerize into filaments in solution and on lipid membranes. Although animal septins associate extensively with actin-based structures in cells, whether septins organize as filaments in cells and if septin organization impacts septin function is not known. Customizing a tripartite split-GFP complementation assay, we show that all septins decorating actin stress fibers are octamer-containing filaments. Depleting octamers or preventing septins from polymerizing leads to a loss of stress fibers and reduced cell stiffness. Super-resolution microscopy revealed septin fibers with widths compatible with their organization as paired septin filaments. Nanometer-resolved distance measurements and single-protein tracking further showed that septin filaments are membrane bound and largely immobilized. Finally, reconstitution assays showed that septin filaments mediate actin–membrane anchoring. We propose that septin organization as octamer-based filaments is essential for septin function in anchoring and stabilizing actin filaments at the plasma membrane.

Introduction

Septins comprise a family of cytoskeletal proteins conserved from algae and protists to mammals (Cao et al., 2007; Momany et al., 2008; Nishihama et al., 2011; Pan et al., 2007). Septins were discovered in budding yeast as mutants that result in cytokinesis defects (Hartwell, 1971; Hartwell et al., 1970) and were later shown to be also required for animal cell division (Echard et al., 2004; Estey et al., 2010; Founounou et al., 2013; Kechad et al., 2012; Kinoshita et al., 1997; Neufeld and Rubin, 1994; Surka et al., 2002). However, septins are expressed in practically all human tissues, including non-dividing neurons (Karlsson et al., 2021). Septins play roles in a wide range of biological processes in non-dividing cells and tissues, including cell motility, sperm integrity, neuron development, tissue morphogenesis, and host–pathogen interactions (Fares et al., 1995; Finger et al., 2003; Gilden et al., 2012; Ihara et al., 2005; Kim et al., 2010; Kissel et al., 2005; Kuo et al., 2012; Mostowy et al., 2010; Mostowy et al., 2011; Nguyen et al., 2000; Shindo and Wallingford, 2014; Steels et al., 2007; Tada et al., 2007; Tooley et al., 2009; Xie et al., 2007). The embryonic lethality of mouse and *Drosophila* septin knock-outs (Adam et al., 2000; Fuchtbauer et al., 2011; Menon et al., 2014; Roseler et al., 2011) emphasizes their essential contribution to animal physiology, yet the precise molecular basis of septin function remains elusive.

Biochemical isolation of native septins revealed that septins exist as stable heteromeric complexes that can polymerize into filaments (Field et al., 1996; Frazier et al., 1998; Hsu et al., 1998; Kim et al., 2011; Kinoshita et al., 2002; Sellin et al., 2011). The isolation of recombinant septin complexes established that septin complexes are palindromes, with each septin in two copies and in a specific position within the complex. Each

[1]Institut Fresnel, CNRS UMR7249, Aix Marseille Univ, Centrale Marseille, Marseille, France; [2]Biomedicine Discovery Institute, Department of Biochemistry and Molecular Biology, Monash University, Clayton, Australia; [3]Department of Bionanoscience, Kavli Institute of Nanoscience Delft, Delft University of Technology, Delft, The Netherlands; [4]CNRS, INSERM, LAI, Turing Centre for Living Systems, Aix-Marseille Univ, Marseille, France; [5]University Bordeaux, CNRS, Interdisciplinary Institute for Neuroscience, IINS, UMR, Bordeaux, France; [6]Institut de Pharmacologie et de Biologie Structurale (IPBS), Université de Toulouse, CNRS, Université Toulouse III—Paul Sabatier (UPS), Toulouse, France; [7]Centre de Recherche en Cancérologie de Marseille (CRCM), INSERM, Institut Paoli-Calmettes, Aix Marseille Univ, CNRS, Marseille, France; [8]Department of Bioengineering, University of California, Berkeley, CA, USA; Department of Chemical and Biomolecular Engineering, University of California, Berkeley, CA, USA; [9]CNRS, Aix Marseille Univ, I2M, Marseille, France; [10]Centre de Recherche en Cancérologie de Toulouse (CRCT), INSERM, Université de Toulouse, UPS, CNRS, Toulouse, France.

Correspondence to Manos Mavrakis: manos.mavrakis@univ-amu.fr; Stéphanie Cabantous: stephanie.cabantous@inserm.fr

P. Verdier-Pinard's and A. Badache's current affiliation is Aix Marseille Univ, INSERM, MMG, U1251, Marseille, France.

© 2022 Silva Martins et al. This article is distributed under the terms of an Attribution–Noncommercial–Share Alike–No Mirror Sites license for the first six months after the publication date (see http://www.rupress.org/terms/). After six months it is available under a Creative Commons License (Attribution–Noncommercial–Share Alike 4.0 International license, as described at https://creativecommons.org/licenses/by-nc-sa/4.0/).

Downloaded from http://rupress.org/jcb/article-pdf/222/3/e202203016/1445844/jcb_202203016.pdf by guest on 20 October 2025

monomer interacts with its neighbors by alternating interfaces, named NC (from the N- and C-terminal domains) and G (from the GTP-binding domain; Bertin et al., 2008; DeRose et al., 2020; Farkasovsky et al., 2005; Garcia et al., 2011; Huijbregts et al., 2009; Iv et al., 2021; John et al., 2007; Kinoshita et al., 2002; Kumagai et al., 2019; Mavrakis et al., 2014; Mendonca et al., 2019; Rosa et al., 2020; Sala et al., 2016; Sirajuddin et al., 2007; Soroor et al., 2021; Versele and Thorner, 2004). Human septins are classified in four homology groups, namely, the SEPT2 group (SEPT1, 2, 4, and 5), SEPT6 group (SEPT6, 8, 10, 11, and 14), SEPT7 group (SEPT7), and SEPT3 group (SEPT3, 9, and 12; Kinoshita, 2003). Cell-isolated human septins exist as stable hexamers and octamers (Kim et al., 2011; Sellin et al., 2011; Sellin et al., 2014), with hexamers composed of septins from the SEPT2, SEPT6, SEPT7 groups, and octamers containing additional septins from the SEPT3 group (Fig. 1 A).

The most convincing evidence that septins form filaments in vivo and thereby contribute to cell viability comes from electron microscopy and functional data in budding yeast (Bertin et al., 2012; Byers and Goetsch, 1976; McMurray et al., 2011; Ong et al., 2014; Rodal et al., 2005). The conservation of septins and the ability of mammalian septin hexamers and octamers (hereafter referred to as protomers) to form filaments in solution and on lipid membranes (DeRose et al., 2020; Iv et al., 2021; Leonardo et al., 2021; Soroor et al., 2021; Szuba et al., 2021) has led to the assumption that human septins also organize as filaments in cells, but formal evidence for this is scarce. Immunogold electron microscopy has shown septins closely apposed to cortical actin filaments and to the plasma membrane organizing in linear arrays (Hagiwara et al., 2011; Kinoshita et al., 1997). Septin protomers along actin filaments or the membrane would, however, result in a similar pattern. It is reasonable to assume that septin rings and fiber-looking segments that form in the cytoplasm of mammalian cells upon actin depolymerization correspond to septin filaments or bundles thereof (Joo et al., 2007; Kim et al., 2011; Kinoshita et al., 2002; Schmidt and Nichols, 2004). However, it is unknown if these fibers originate from direct end-to-end septin polymerization. Whether all septins in cells function as filaments, and how hexamers and octamers contribute to septin filament formation and function is not known.

Actin-binding domains on septins have not yet been identified. It is hence unclear if actin-septin binding involves direct interactions or if it occurs through myosin-II (Joo et al., 2007; Mostowy et al., 2010) or Borg proteins (Calvo et al., 2015; Farrugia et al., 2020; Joberty et al., 2001; Liu et al., 2014; Salameh et al., 2021). Similarly, although mammalian septins bind lipid membranes (Bridges et al., 2016; Dolat and Spiliotis, 2016; Szuba et al., 2021; Tanaka-Takiguchi et al., 2009; Yamada et al., 2016), whether there is direct septin-membrane binding in cells has not been shown; the identification of the membrane-binding site of septins is a matter of debate (Cavini et al., 2021). It is thus not known if septin-decorated actin fibers and membranes in cells reflect membrane-bound septins.

To elucidate the interplay between human septin organization and function in non-dividing cells, we used actin stress fibers in U2OS cells as a model system. Septins in mammalian cells have been reported to decorate stress fibers in multiple studies (Calvo et al., 2015; Connolly et al., 2011; Dolat et al., 2014; Joo et al., 2007; Kim et al., 2011; Kinoshita et al., 2002; Kinoshita et al., 1997; Liu et al., 2014; Salameh et al., 2021; Schmidt and Nichols, 2004; Surka et al., 2002; Verdier-Pinard et al., 2017; Xie et al., 1999; Zhang et al., 1999). Subsets of stress fibers are lost upon septin disruption or septin relocalization to microtubules (Calvo et al., 2015; Kinoshita et al., 2002; Kuzmic et al., 2022; Salameh et al., 2021; Schmidt and Nichols, 2004; Targa et al., 2019) suggesting an essential, yet still unclear, role of septins in stress fiber integrity. To test how septins organize in cells, we combined a tripartite split-GFP complementation assay with mutants disrupting specific septin–septin interfaces to selectively perturb hexamers or octamers, or abolish polymerization altogether. Atomic force microscopy nanoindentation was used to assess the specific contribution of hexamers vs. octamers to cell stiffness. We employed super-resolution structured illumination microscopy to decipher the higher-order assembly of septin filaments. Moreover, to determine whether septin filaments are membrane-bound and if they can bridge membrane-actin interactions, we combined nanometer-resolved distance measurements and single protein tracking in cells with cell-free reconstitution assays using supported lipid bilayers. Our findings demonstrate that all actin-associated septins in cells organize as paired membrane-bound filaments whose integrity and function depend on octamers.

Results

Septins associate with contractile stress fibers

Whether septins associate preferentially with specific types of SFs and if septin organization differs among SFs is not known. To answer these questions, we examined how septins distribute in U2OS cells, with respect to peripheral, dorsal, and ventral SFs, transverse arcs and the perinuclear actin cap (Fig. 1 A). Given that SFs are classified based on their subcellular localization and their anchoring at one or both ends by focal adhesions (FAs; Tojkander et al., 2012), we co-stained for septins, actin filaments and the FA protein, paxillin. We examined the distribution of SEPT2 and SEPT7, which are common to both hexamers and octamers, and SEPT9, which is specific to octamers (Fig. 1, A and B; and Fig. S1). U2OS cells express two SEPT9 isoforms, SEPT9_i1 and SEPT9_i3 (Kuzmic et al., 2022), both of which are detected by our SEPT9 antibodies. Both septin immunostainings and live imaging of septin-GFP fusions showed identical distributions of all three septins with respect to SFs. They all decorated myosin-II containing contractile SFs (Fig. 1 B i–iii; Fig. S1 A i, ii, and iv; and Fig. S1 B i–v), but not the non-contractile dorsal ones (Fig. 1, B iii and b; Fig. S1, A iii; and Fig. S1, B iv and a). Although septins decorated contractile SFs throughout their length, they were systematically excluded from FAs (Fig. 1, B i and a; Fig. S1, A i and c; and Fig. S1, B i and c). Septins localized to peripheral and ventral SFs, transverse arcs and perinuclear actin caps, and also associated with geodesic actin nodes on the ventral plasma membrane and with actin nodes in transverse arcs. Actin nodes were enriched in F-actin and α-actinin, while actin filaments

Downloaded from http://rupress.org/jcb/article-pdf/222/3/e202203016/1445844/jcb_202203016.pdf by guest on 20 October 2025

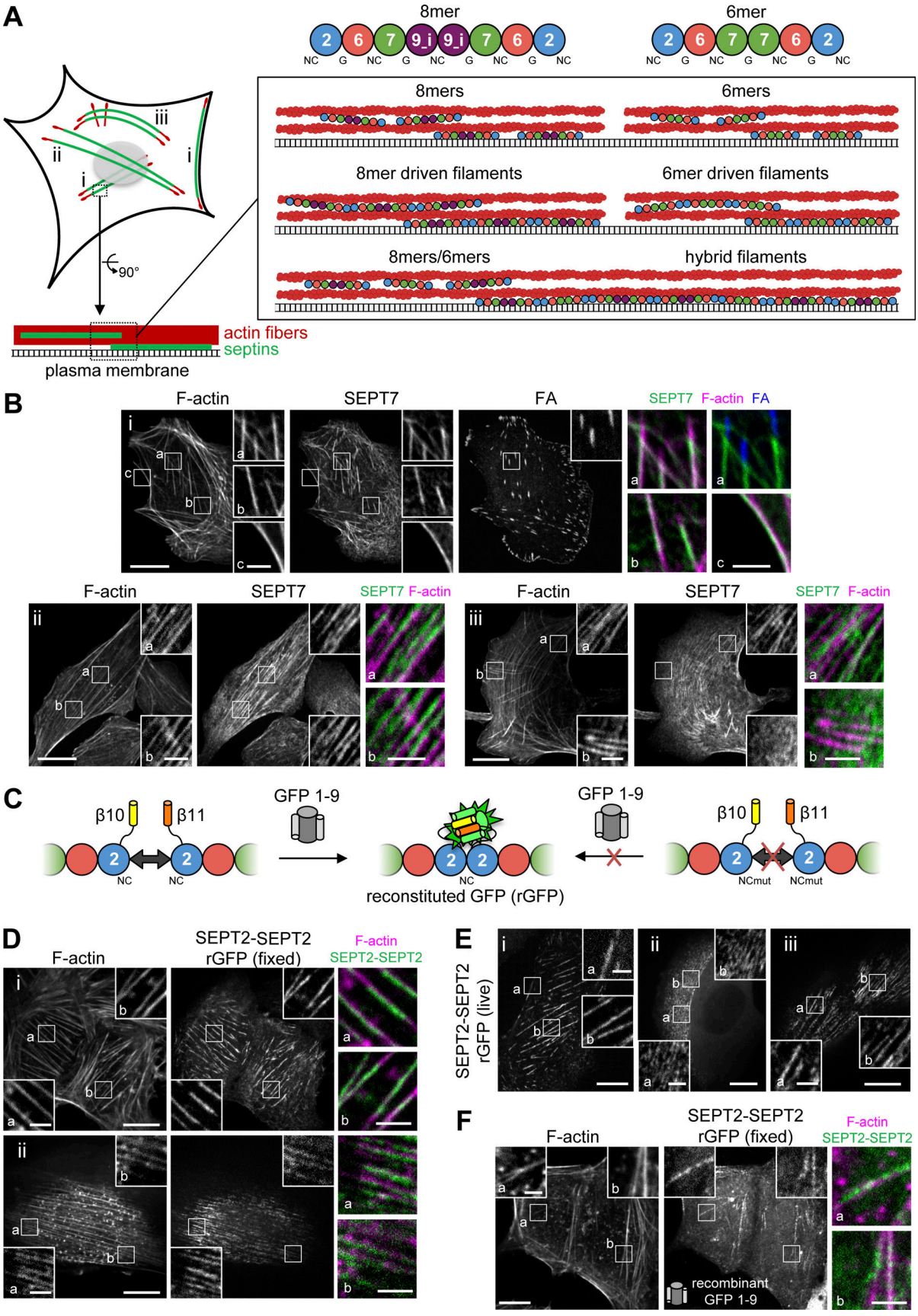

Figure 1. **A tripartite split-GFP complementation assay detects SEPT2-SEPT2 interactions on septin-decorated actin stress fibers in U2OS cells.** **(A)** The scheme on the left depicts septin-decorated stress fibers (SFs) in a mammalian cell. **(B)** Septins (green) decorate different types of actin SFs (red), notably

Downloaded from http://rupress.org/jcb/article-pdf/222/3/e202203016/1445844/jcb_202203016.pdf by guest on 20 October 2025

peripheral and ventral SFs (i), perinuclear actin caps (ii), and transverse arcs (iii), shown in the respective panels i–iii in B. The schematics on the right show human septin octamers and hexamers associating with SFs either as single protomers (top), as octamer and hexamer-driven filaments (middle), or as hybrid filaments from octamer and hexamer co-polymerization (bottom). Single protomers (top) could co-exist with filaments (middle and bottom). Septins can associate exclusively with SFs or also with the plasma membrane. (B) Representative confocal micrographs of SEPT7 immunostainings showing examples of SEPT7 localizing (i) to ventral (a and b) and peripheral (c) SFs and excluded from focal adhesions (FA; a), (ii) to perinuclear actin caps (a and b), and (iii) to transverse arcs (a) and excluded from dorsal SFs (b). Cells are co-stained for F-actin (phalloidin) and the FA protein paxillin. **(C)** Schematic representation of the tripartite split-GFP complementation assay for probing SEPT2-SEPT2 interactions. The transparency of the SEPT7 subunits is used to suggest that the polymerizing protomers can be hexamers or/and octamers. **(D and E)** Representative confocal micrographs of SEPT2-SEPT2 reconstituted GFP (rGFP) distribution in fixed cells (D) co-stained for F-actin (phalloidin) and in live cells (E). Examples in fixed cells show rGFP localizing (i) to ventral SFs (a and b) and (ii) to actin caps (a and b). Examples in live cells show rGFP localizing (i) to peripheral (a) and ventral (b) SFs, (ii) to transverse arcs (a and b), and (iii) to actin caps (a and b). **(F)** Representative confocal micrograph of SEPT2-SEPT2 rGFP in fixed cells using recombinant purified GFP1-9. The example shows rGFP localizing to ventral SFs (a and b). Scale bars in large fields of views, 10 µm. Scale bars in insets, 2 µm.

interconnecting nodes were decorated by septins and myosin-II in an aster-like pattern (Fig. S1, C and D).

The presence of SEPT9 on SFs does not exclude that septin hexamers are also present. Furthermore, the diffraction-limited optical resolution of our setup cannot distinguish septin protomers from filaments. Septin decoration of SFs may therefore reflect the presence of protomers (hexamers and/or octamers) or/and of filaments (with hexamers and octamers forming separate or hybrid filaments; Fig. 1 A).

Septins organize as filaments on contractile SFs

Both protomers have an exposed SEPT2 NC interface at their termini (Fig. 1 A; Iv et al., 2021; Mendonca et al., 2019; Soroor et al., 2021). To determine whether septins are present as filaments, we therefore designed a tripartite split-GFP complementation assay for probing SEPT2–SEPT2 interactions as a molecular readout of end-to-end septin polymerization in situ in living cells (Fig. 1 C). This protein–protein interaction assay involves the fusion of the proteins of interest to the two last beta-strands of GFP, β10 and β11: in the presence of specific protein–protein interactions in cells expressing GFP1-9 (GFP strands β1-β9), the GFP barrel is reconstituted leading to fluorescence (Cabantous et al., 2013; see Materials and methods and Fig. S2, A–C for the assay design). We generated β10- and β11-strand fusions with SEPT2 that we co-expressed using an inducible bidirectional vector in U2OS cells constitutively expressing GFP1-9 (Fig. 1 C and Fig. S2 D). To minimize the risk of not detecting SEPT2–SEPT2 interactions due to endogenous untagged SEPT2 and given that the expression levels of SEPT2-β10/β11 fusions were kept low to minimize overexpression artifacts (Fig. S2 E), we consistently knocked down endogenous SEPT2 in all subsequent experiments (Fig. S2 F).

Confocal imaging revealed the presence of the reconstituted GFP (rGFP) on peripheral and ventral SFs, transverse arcs and perinuclear actin caps (Fig. 1, D and E), with the rGFP distribution closely resembling endogenous SEPT2 immunostainings and SEPT2–GFP distribution (Fig. S1 A). The presence of SEPT2-SEPT2 rGFP on SFs was further detected in fixed wild-type U2OS cells co-expressing SEPT2-β10 and SEPT2-β11 upon incubation with recombinant purified GFP1-9 (Fig. 1 F), confirming the presence of SEPT2–SEPT2 interactions in situ on SFs. Given that recombinant animal septins form both single and paired filaments (Szuba et al., 2021), we generated structure models to examine GFP complementation both from direct SEPT2–SEPT2 interactions within a filament (Fig. 2 A), and from SEPT2 facing another SEPT2 in apposed protomers of a paired filament (Fig. 2 B). Examination of the distances and the flexibility of the SEPT2 C-termini and the linkers showed that GFP reconstitution could occur either way.

The structural models highlighted that paired protomers would lead to GFP reconstitution whether they polymerize or not. Hence to test if SEPT2-SEPT2 rGFP originates from direct SEPT2–SEPT2 interactions, we designed a double point SEPT2 NC interface mutant (SEPT2 F20D, V27D, hereafter SEPT2NC-mut) to prevent end-to-end association and thereby abolish polymerization (Fig. S3 A; Kuzmic et al., 2022; Sirajuddin et al., 2007). Reconstitution assays using purified recombinant protomers bearing these mutations confirmed that this mutant abolishes polymerization, although it can still bind actin filaments in vitro (Fig. 2, C and D; and Fig. S3, B and C). Native PAGE in cell lysates expressing SEPT2NCmut confirmed that protomers were intact: the expression of either wild-type SEPT2 or SEPT2NCmut in SEPT2 knockdown cells rescued equally well the hexamer and octamer distribution in control cells (Fig. 2 E). Strikingly, using this mutant in the context of the split SEPT2-SEPT2 assay completely abolished SF localization, as indicated by purely diffuse cytosolic fluorescence (Fig. 2, F and G; hereafter referred to as "diffuse cytosolic"). Given that wild-type SEPT2-SEPT2 rGFP was occasionally found as diffuse cytosolic, we quantified the distribution of diffuse cytosolic and non-diffuse phenotypes in cells expressing wild-type SEPT2- vs. SEPT2NCmut-β10/β11 fusions. While 95% of wild-type SEPT2-SEPT2 rGFP localized to SFs and only 5% was diffuse cytosolic, 100% of SEPT2NCmut-SEPT2NCmut rGFP was diffuse cytosolic (Fig. 2, F and G). Thus direct end-to-end septin polymerization is required for septin localization to SFs. We attributed the fact that the split-GFP assay with the NC mutant still produced fluorescence to the plasticity of septins, which are able to use both NC and G interfaces when either one is compromised (Kim et al., 2012). Our native PAGE shows the presence of SEPT2NC homodimers (Fig. 2 E), which we speculate are G-homodimers, thus enabling GFP complementation.

Septin protomers do not associate with SFs

The presence of septin filaments does not exclude that septin protomers are also present on SFs. To test whether septin protomers associate with SFs, we examined the cellular distribution of SEPT2NCmut fused to full-length GFP. Cells expressing this

Downloaded from http://rupress.org/jcb/article-pdf/222/3/e202203016/1445844/jcb_202203016.pdf by guest on 20 October 2025

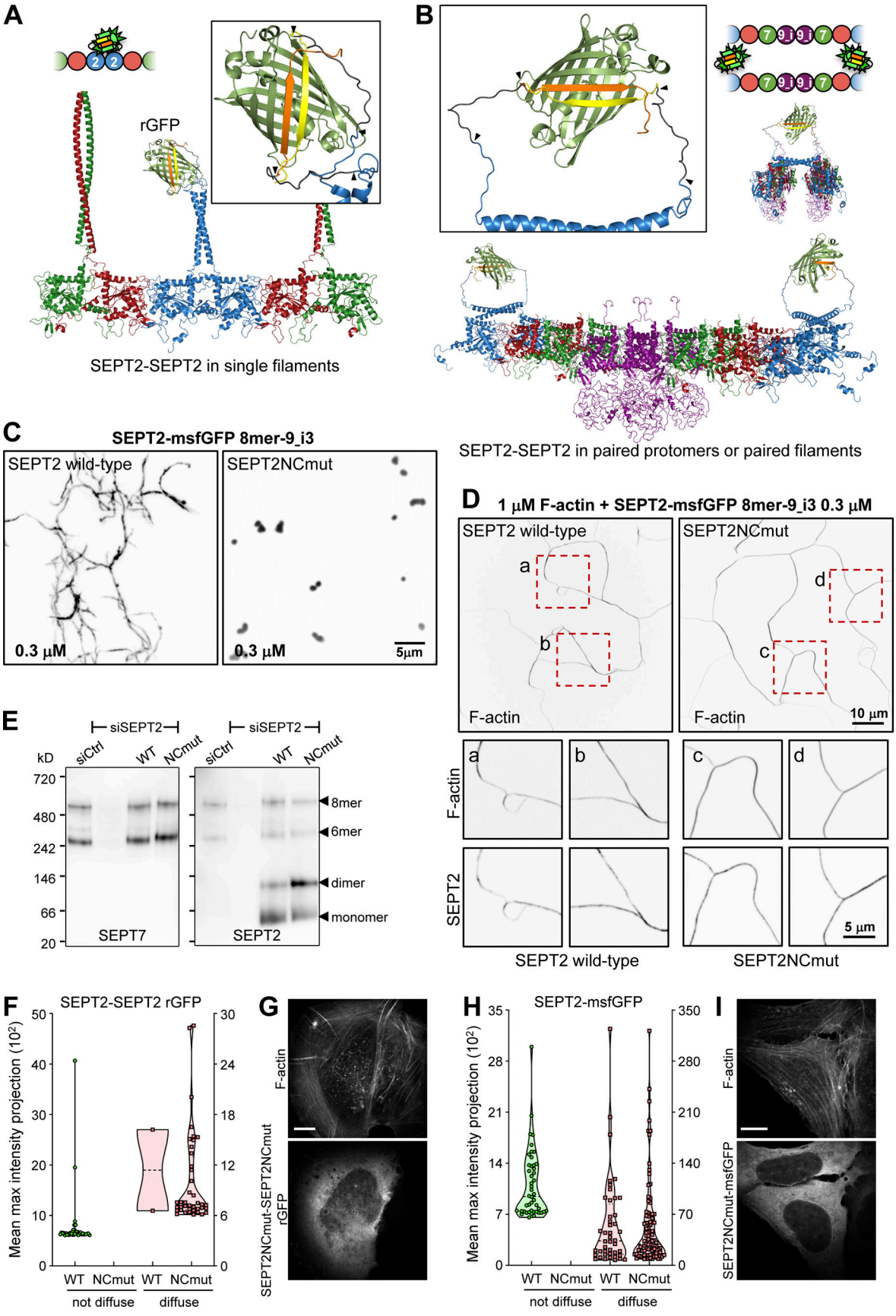

Figure 2. **All septins on SFs organize as filaments. (A and B)** Structure models of rGFP through direct SEPT2-SEPT2 interactions of two polymerizing septin protomers within a filament (A) or from SEPT2 in two apposed protomers (B). Only the end-to-end interacting halves of the protomers (hexamers or/and

Downloaded from http://rupress.org/jcb/article-pdf/222/3/e202203016/1445844/jcb_202203016.pdf by guest on 20 October 2025

octamers) are shown in A for simplicity. SEPT6 and SEPT7 coiled-coils are not shown in B for simplicity. The transparency of the terminal SEPT2 subunits in B is used to suggest that the paired protomers could be found within a filament. β10 and β11 strands are shown in yellow and orange, respectively. Linker sequences between septins and the β-strands, delimited by arrowheads, are shown in dark gray. The colors of septin subunits in the structure models correspond to the ones in the color-coded sphere representation of hexamers and octamers. The second half of the octamer is not shown in the rotated filament pair in B for the sake of simplicity. **(C)** Representative spinning disk fluorescence images of septin filament assembly upon polymerization of octamers-9_i3 in solution at the indicated final protomer concentration. Protomers contained either wild-type SEPT2 (left panel) or SEPT2NCmut (right panel). Images use an inverted grayscale. **(D)** Representative spinning disk fluorescence images of reconstituted actin filaments, polymerizing in the presence of septin octamers in solution. Protomers contained either wild-type SEPT2 (left panel) or SEPT2NCmut (right panel). Actin filaments are visualized with AlexaFluor568-conjugated phalloidin, and septins with SEPT2-msfGFP. One example of large fields of view are shown for each condition, depicting cross-linking of actin filaments; only actin labeling is shown. Insets on the bottom show higher magnifications of selected regions of interest on the top (dashed squares in red). Two regions of interest (a and b for wild-type SEPT2 and c and d for SEPT2NCmut) are shown in each case, depicting both the actin (top row) and septin (bottom row) signals. Scale bars in all large fields of views, 10 µm. Scale bars in all insets, 5 µm. **(E)** Western blot following native PAGE of U2OS cell lysates probed with anti-SEPT7 (left) and anti-SEPT2 (right) antibodies upon treatment with siRNAs targeting LacZ (siCtrl), SEPT2 (siSEPT2), and targeting SEPT2 while expressing wild-type SEPT2-msfGFP (WT) or SEPT2NCmut-msfGFP (NCmut). Molecular weight markers are shown on the left. The overexpression of the msfGFP fusions leads to SEPT2 monomers and dimers in addition to hexamers and octamers (arrowheads). **(F)** Violin plots depicting the distribution of diffuse cytosolic (red datapoints) vs. non-diffuse (green datapoints) phenotypes as a function of the intensity of the rGFP signal in GFP1-9 cells co-expressing wild-type SEPT2-β10 and -β11 or SEPT2NCmut-β10 and -β11. Data points are from a total of 40 cells each for wild-type and mutant SEPT2 distributed among the two phenotypes. **(G)** Representative example of a GFP1-9 cell co-expressing SEPT2NCmut-β10 and -β11 and co-stained for F-actin (phalloidin) showing a diffuse cytosolic phenotype. Scale bar, 10 µm. **(H)** Violin plots depicting the distribution of diffuse cytosolic (red datapoints) vs. non-diffuse (green datapoints) phenotypes as a function of the intensity of the msfGFP signal in cells expressing wild-type SEPT2-msfGFP or SEPT2NCmut-msfGFP. Data points are from a total of 90 cells each for wild-type and mutant SEPT2 distributed among the two phenotypes. **(I)** Representative example of a cell expressing SEPT2NCmut-msfGFP and co-stained for F-actin (phalloidin) showing a diffuse cytosolic phenotype. Scale bar, 10 µm. Source data are available for this figure: SourceData F2.

mutant exhibited a diffuse cytosolic localization, demonstrating that this mutant does not bind SFs (Fig. 2, H and I). Wild-type SEPT2-GFP fusions also showed diffuse cytosolic localization in addition to SF localization (Fig. S1 A v). However, while SEPT2-GFP was diffuse cytosolic in only ∼50% of cells, 100% of the cells expressing SEPT2NCmut showed this phenotype (Fig. 2, H and I). This result showed that septin protomers in cells do not associate with SFs, meaning that all septins decorating SFs are filamentous.

SF-associated septin filaments contain predominantly octamers

As SEPT2 is common to both protomers (Fig. 1 A), the results described above did not inform us on the composition of septin filaments. Recombinant hexamers and SEPT9-containing octamers have the capacity to co-polymerize in vitro (Fig. S3 D and Soroor et al., 2021). To explicitly visualize the presence of octamers on SFs, we probed SEPT7-SEPT9 and SEPT9-SEPT9 interactions as molecular signatures of octamers (Fig. 3, A and B). Expression levels of all β10/β11 fusions were kept low to minimize overexpression artifacts (Fig. S2 E), and endogenous SEPT7 and SEPT9 were consistently knocked down in all subsequent experiments (Fig. S2, G and H).

As expected, rGFP from SEPT9_i3-SEPT9_i3 localized to contractile SFs (Fig. 3 C), similarly to SEPT9 immunostainings (Fig. S1 B), confirming that septin filaments contain SEPT9_i3-octamers. Split-GFP assays probing SEPT7-SEPT9_i3 interactions confirmed these findings (Fig. 3 D), with rGFP additionally labeling cytoplasmic rings of ∼0.9 µm in diameter (Fig. 3, D ii and E). To confirm that SF-localized rGFP from SEPT7-SEPT9_i3 and SEPT9_i3-SEPT9_i3 reflect direct interactions, we designed a double point SEPT9_i3 NC interface mutant (SEPT9_i3 M263D, I270D, hereafter SEPT9_i3NCmut), a double point SEPT9_i3 G interface mutant (SEPT9_i3 W502A, H512D, hereafter SEPT9_i3Gmut) and a double point SEPT7 G interface mutant (SEPT7 W269A, H279D, hereafter SEPT7Gmut1; Fig. S3 A)(Kuzmic et al., 2022; Sirajuddin et al., 2007; Zent et al., 2011). Native PAGE in cells expressing these mutants confirmed that SEPT9_i3NCmut completely disrupted octamers (Fig. 4 A), whereas SEPT7Gmut1 completely disrupted octamers and hexamers (Fig. 4 B). Split-GFP assays using these mutants completely abolished SF localization (Fig. 4, C–H), confirming that SF localization requires intact SEPT7-SEPT9_i3 and SEPT9_i3-SEPT9_i3 interfaces. All above assays gave identical results for SEPT9_i1, confirming the presence of both SEPT9_i1- and SEPT9_i3-containing octamers in SF-associated septin filaments (Fig. 3 F, Fig. 4, A and H; and Fig. S4, A and B).

To test whether hexamers are also present on SFs, we probed SEPT7–SEPT7 interactions. Strikingly, rGFP from SEPT7–SEPT7 interactions was unexpectedly difficult to detect on SFs: although it localized to SFs (Fig. 5, A i, and B i), the majority was found on ectopic short, needle-like bundles (Fig. 5, A ii, and B ii), similar to the localization of full-length GFP-SEPT7 fusions (Fig. 5, C and D). These ectopic bundles did not localize to SFs (Fig. 5, A ii, and D) and contained SEPT2 but not SEPT9 (Fig. 5 C). These bundles thus most likely consist of hexamers, in line with the capacity of recombinant hexamers to form septin filament bundles in vitro (DeRose et al., 2020; Iv et al., 2021; Kinoshita et al., 2002; Leonardo et al., 2021). The presence of rGFP on the ectopic bundles thus showed that the split SEPT7-SEPT7 assay readily detects SEPT7–SEPT7 interactions originating from hexamers.

An observation that could explain the difficulty to detect SEPT7-SEPT7 on SFs was the dependence of SEPT7 localization on SEPT9 expression levels. We consistently detected ectopic bundles when we exogenously expressed only SEPT7, either GFP-SEPT7 or split SEPT7-SEPT7 (Fig. 5, A–D), but not when we co-expressed SEPT9 (Fig. 5, E and F). We reasoned that in the absence of exogenous SEPT9, the slightest excess of SEPT7 leads to ectopic hexamer-based bundles, also reducing the availability of SEPT7 for forming octamers to bind SFs. Exogenous co-expression of SEPT9, on the other hand, would cause incorporation of the exogenous SEPT7 into octamers, thus preventing the

Downloaded from http://rupress.org/jcb/article-pdf/222/3/e202203016/1445844/jcb_202203016.pdf by guest on 20 October 2025

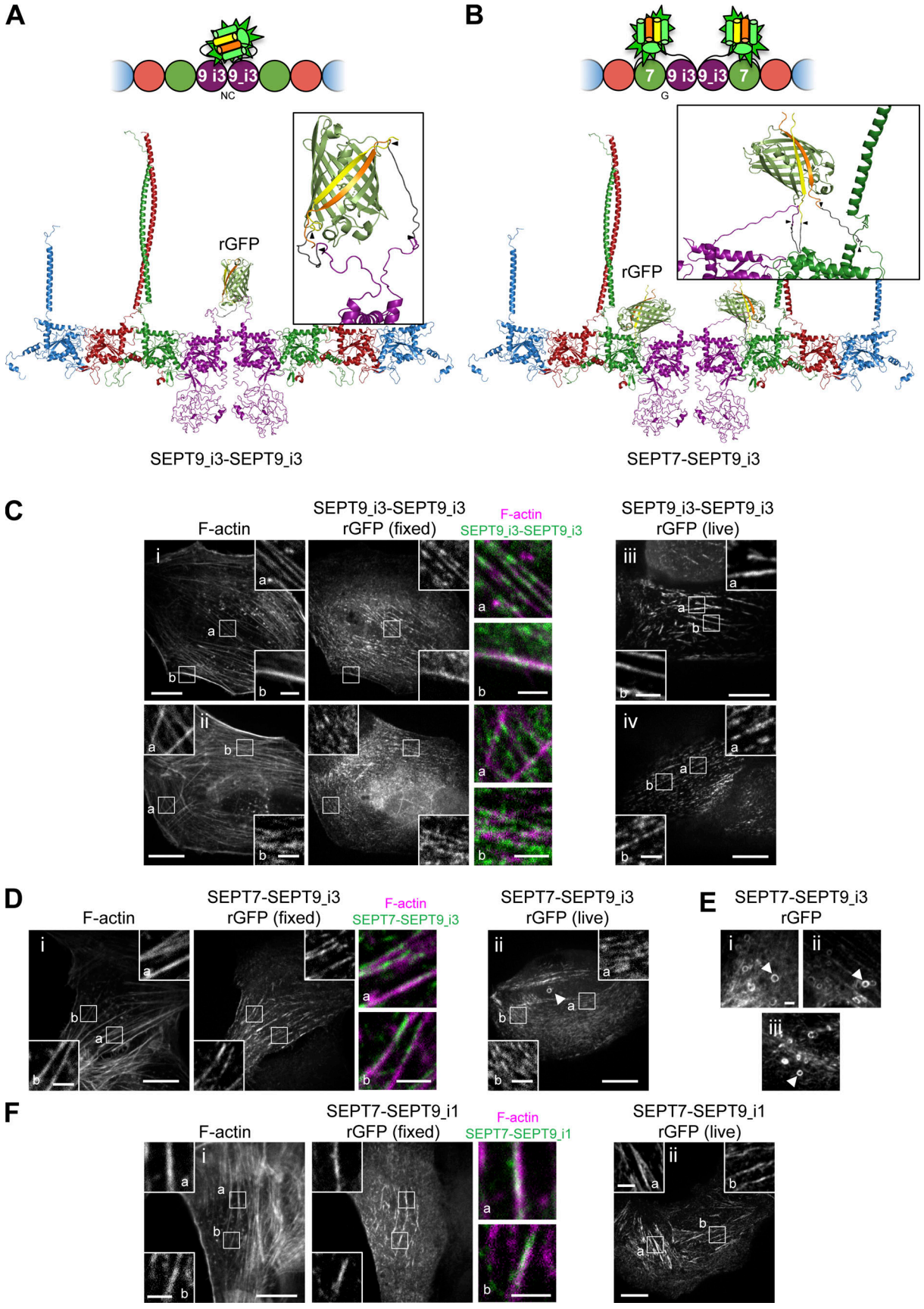

Figure 3. **SF-associated septin filaments contain octamers. (A and B)** Schematic (top) and respective structure model (bottom) of rGFP through SEPT9–SEPT9 interactions (A) and SEPT7–SEPT9 interactions (B) within an octamer. The transparency of the terminal SEPT2 subunits is used to suggest that

Downloaded from http://rupress.org/jcb/article-pdf/222/3/e202203016/1445844/jcb_202203016.pdf by guest on 20 October 2025

the protomers are found within a filament. β10 and β11 strands are shown in yellow and orange, respectively. Linker sequences between septins and the β-strands, delimited by arrowheads, are shown in dark gray. The colors of septin subunits in the structure models match the ones in the color-coded sphere representation of octamers. **(C)** Representative confocal micrographs of SEPT9_i3-SEPT9_i3 rGFP distribution in fixed cells (left and middle columns) co-stained for F-actin (phalloidin) and in live cells (right column). Examples of rGFP in fixed cells localizing (i) to ventral (a) and peripheral (b) SFs and (ii) to transverse arcs (b) and excluded from dorsal SFs (a). Examples in live cells show rGFP localizing (iii) to ventral SFs (a and b) and (iv) to actin caps (a and b). Scale bars in large fields of views, 10 µm. Scale bars in insets, 2 µm. **(D)** Representative confocal micrographs of SEPT7-SEPT9_i3 rGFP distribution in fixed cells (left and middle columns) co-stained for F-actin (phalloidin) and in live cells (right column). Example of rGFP in fixed cells localizing (i) to ventral SFs (a and b). Example in live cells showing rGFP localizing (ii) to transverse arcs (a and b). The arrowhead points to a ring. Such cytoplasmic rings were ∼0.5–1.6 µm in diameter (0.9 µm on average from 19 measured rings). Scale bars in large fields of views, 10 µm. Scale bars in insets, 2 µm. **(E)** Additional examples of rings (arrowheads) in GFP1-9 cells co-expressing β11-SEPT7 and SEPT9_i3-β10. Scale bar, 2 µm. **(F)** Representative confocal micrographs of SEPT7-SEPT9_i1 rGFP distribution in fixed cells (left and middle columns) co-stained for F-actin (phalloidin) and in live cells (right column). Examples in fixed and live cells show rGFP localizing to ventral SFs (a and b). Scale bars in large fields of views, 10 µm. Scale bars in insets, 2 µm.

formation of ectopic hexamer bundles. Consistent with this hypothesis, SEPT7-SEPT7 rGFP was readily detectable on SFs under conditions of exogenous SEPT9 co-expression (Fig. 5 F). Furthermore, it was difficult to find SEPT9-decorated SFs in cells also displaying ectopic hexamer-based bundles (Fig. 5 C). These observations raised the possibility that septin filaments on SFs contain mostly, if not exclusively, octamers.

To explore the origin of SEPT7-SEPT7 rGFP on SFs, we generated structure models of septin protomers in order to examine GFP complementation from SEPT7–SEPT7 interactions within one hexamer (Fig. 5 G), as well as from SEPT7 facing another SEPT7 in apposed hexamers or octamers in a paired filament (Fig. 5 H). Examination of the distances and the flexibility of the SEPT7 N-termini and the linkers showed that GFP reconstitution can occur either way.

To identify the sources of the SEPT7-SEPT7 rGFP signal on SFs, we aimed at perturbing hexamers while preserving octamers. To this end, we generated a single point SEPT7 G interface mutant (SEPT7 H279D, hereafter SEPT7Gmut2; Fig. S3 A) that should destabilize the SEPT7-SEPT7 G-interface when present in both SEPT7 subunits, but preserve the SEPT7-SEPT9 G-interface if SEPT7 is mutated but SEPT9 is wild-type. In line with these predictions, native PAGE showed that octamers are not affected by the expression of SEPT7Gmut2 (Fig. 4 B), and rGFP from SEPT7Gmut2-SEPT9_i3 recapitulated normal septin localization on SFs (Fig. 6 A). Importantly, rGFP from SEPT7Gmut2-SEPT7Gmut2 localized to SFs but did not show any ectopic bundles (Fig. 6 B) indicating that SEPT7Gmut2 completely abolished SEPT7–SEPT7 interactions within hexamers in the bundles. Thus our findings show that the SF-localized rGFP from SEPT7Gmut2-SEPT7Gmut2 originates from paired octamers (Fig. 5 H).

These observations altogether strongly suggest that the detected rGFP from SEPT7-SEPT7 on SFs originates from paired octamers. Split-GFP assays using the SEPT7Gmut1 mutant resulted in diffuse cytosolic distributions (Fig. 4, D and H; and Fig. 6, C–E), confirming that SF localization requires intact SEPT7 G interfaces. We concluded that septins on SFs organize as paired filaments containing mostly, or even exclusively, octamers.

Polymerization-competent septin octamers, but not hexamers, are essential for the integrity and function of SF-associated septin filaments

To further test the contribution of hexamers vs. octamers to septin filament formation, we examined septin filaments under three conditions: (a) the presence of hexamers and octamers (control condition), (b) the absence of octamers, by knocking down SEPT9, and (c) the presence of octamers only, by expressing SEPT7Gmut2. As a readout of septin filaments, we examined rGFP from SEPT2-SEPT2 in live cells while imaging stress fibers (Fig. 7, A–C). To assess the effects of the perturbations, we quantified the distribution of non-diffuse vs. diffuse cytosolic phenotypes and calculated Pearson and Manders correlation coefficients for actin-septin co-localization (Fig. 7, D and E). Strikingly, removing octamers by knocking down SEPT9 entirely removed the SEPT2-SEPT2 rGFP signal from all SFs, leaving behind a punctate pattern not localizing to SFs, suggesting that filamentous septin integrity depends entirely on octamers. On the other hand, preserving octamers in the absence of hexamers preserved septin filaments on SFs, showing that the absence of hexamers does not compromise septin filament integrity.

To test the functional contribution of octamers and hexamers to SFs, we quantified the number of cells presenting ventral SFs in cells containing hexamers and octamers, hexamers only, octamers only, and containing hexamers and octamers that cannot polymerize. Knocking down SEPT9 removed both SEPT9 and SEPT7 from all ventral SFs (compare Fig. 8, A and B). Importantly, whereas 82% of control cells, and 81% of cells with octamers only, contained ventral SFs, only 44% of cells in the absence of octamers, and 46% of cells with hexamers and octamers that could not polymerize, presented ventral SFs (Fig. 8, B and C). Total actin levels did not change among these conditions (Fig. 8 D). Thus, polymerization-competent septin octamers are essential for the integrity of SFs.

To further question the functional contribution of protomers, we turned to atomic force microscopy (AFM) nanoindentation for measuring cell stiffness. Septin depletion has been shown to reduce cell stiffness, using AFM, in cultured mammalian cells (Mostowy et al., 2011), but the specific contribution of hexamers vs. octamers was not explored. To address this question, we indented cells containing hexamers and octamers, hexamers only and octamers only with an AFM cantilever tip and determined the elastic modulus (E_0) and the fluidity (β) of the cells by fitting the experimental force-indentation curves to a viscoelastic model (Fig. 8 E, see Materials and methods). While removing hexamers did not have any effect, the depletion of octamers resulted in a statistically significant decrease in cell stiffness and a corresponding increase in cell fluidity (Fig. 8 E). Cells with significantly reduced ventral SFs in the absence of

Downloaded from http://rupress.org/jcb/article-pdf/222/3/e202203016/1445844/jcb_202203016.pdf by guest on 20 October 2025

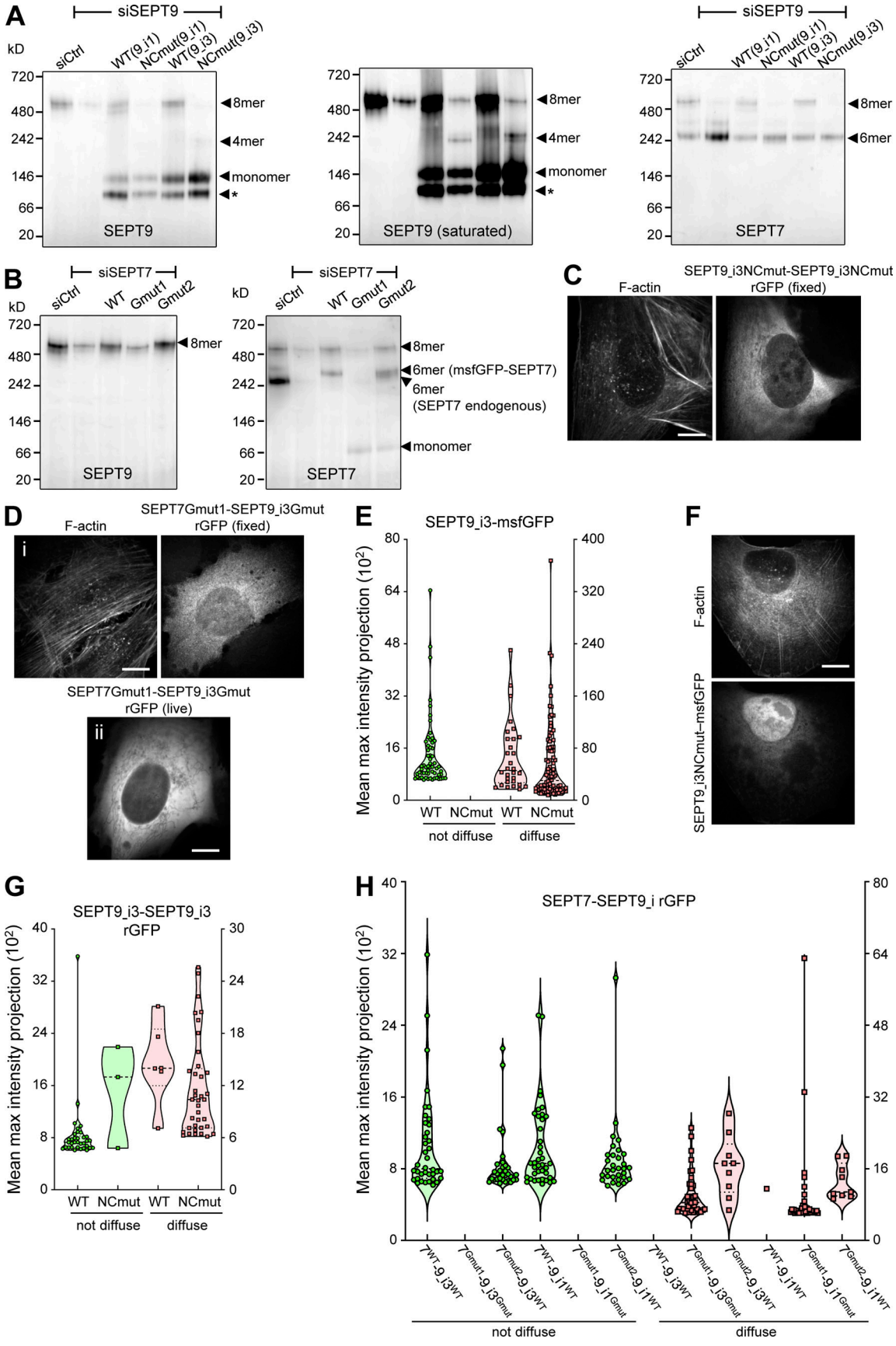

Figure 4. **Intact SEPT9 NC and G interfaces are required for septin localization to SFs. (A)** Western blot following native PAGE of U2OS cell lysates probed with anti-SEPT9 (left and middle) and anti-SEPT7 (right) antibodies upon treatment with siRNAs targeting LacZ (siCtrl), SEPT9 (siSEPT9), and targeting

Downloaded from http://rupress.org/jcb/article-pdf/222/3/e202203016/1445844/jcb_202203016.pdf by guest on 20 October 2025

SEPT9 while expressing wild-type SEPT9-msfGFP (WT) or SEPT9NCmut-msfGFP (NCmut) for both SEPT9_i1 and SEPT9_i3. The SEPT9 blot is also shown saturated on purpose for displaying weaker bands. Arrowheads point to the sizes of the indicated complexes. The asterisks point to SEPT9 degradation. Molecular weight markers are shown on the left. **(B)** Western blot following native PAGE of U2OS cell lysates probed with anti-SEPT9 (left) and anti-SEPT7 (right) antibodies upon treatment with siRNAs targeting LacZ (siCtrl), SEPT7 (siSEPT7), and targeting SEPT7 while expressing wild-type msfGFP-SEPT7 (WT), msfGFP-SEPT7Gmut1 (Gmut1), or msfGFP-SEPT7Gmut2 (Gmut2). Arrowheads point to the sizes of the indicated complexes. Molecular weight markers are shown on the left. **(C)** Representative example of a GFP1-9 cell co-expressing SEPT9_i3NCmut-β10 and -β11, co-stained for F-actin (phalloidin), showing a diffuse cytosolic phenotype. Scale bar, 10 µm. **(D)** Representative examples of a fixed (i) and a live (ii) GFP1-9 cell co-expressing β11-SEPT7Gmut1 and SEPT9_i3Gmut-β10 showing a diffuse cytosolic phenotype. The fixed cell is co-stained for F-actin (phalloidin). Scale bar, 10 µm. **(E)** Violin plots depicting the distribution of diffuse cytosolic (red datapoints) vs. non-diffuse (green datapoints) phenotypes as a function of the intensity of the msfGFP signal in cells expressing wild-type SEPT9_i3-msfGFP or SEPT9_i3NCmut-msfGFP. Data points are from a total of 90 cells each for wild-type and mutant SEPT9 distributed among the two phenotypes. **(F)** Representative example of a cell expressing SEPT9_i3NCmut-msfGFP, co-stained for F-actin (phalloidin), showing a diffuse cytosolic phenotype. Scale bar, 10 µm. **(G)** Violin plots depicting the distribution of diffuse cytosolic (red datapoints) vs. non-diffuse (green datapoints) phenotypes as a function of the intensity of the rGFP signal in GFP1-9 cells co-expressing wild-type SEPT9_i3-β10 and -β11 or SEPT9_i3NCmut-β10 and -β11. Data points are from a total of 40 cells each for wild-type and mutant SEPT9 distributed among the two phenotypes. **(H)** Violin plots depicting the distribution of diffuse cytosolic (red datapoints) vs. non-diffuse (green datapoints) phenotypes as a function of the intensity of the rGFP signal in GFP1-9 cells co-expressing the indicated combinations of β11-SEPT7 and SEPT9-β10 fusions. Data points are from a total of 40 cells each for each combination, distributed among the two phenotypes. Source data are available for this figure: SourceData F4.

octamers are predicted to generate less prestress and thus lower stiffness (Chowdhury et al., 2021; Wang et al., 2002). We concluded that polymerization-competent octamers are essential for their function in cell mechanics through the generation or/and maintenance of SFs.

Super-resolution microscopy reveals septin fibers running longitudinally along and around SFs and interconnecting SFs

Having shown that all septins associated with SFs are filamentous, we aimed at visualizing how septin filaments organize on the different types of SFs. We employed super-resolution structured illumination (SIM) microscopy in cells co-stained for SEPT7 (as a pan-septin filament marker), actin filaments, and α-actinin or non-muscle myosin heavy chain IIA (NMIIA). We examined septin filament organization on perinuclear actin caps, transverse arcs, including at arc nodes, on ventral SFs and at ventral actin nodes (Fig. 9, A–E). Regardless of the type of SF, we noticed that septin filament morphology was very different from that of the corresponding actin filament bundles. While actin filament bundles typically appeared as straight, rigid fibers, septin fibers consistently appeared less straight and with lower orientational persistence (Note: we choose to use septin "fibers" instead of "filaments" in this section to avoid confusion with single or paired septin filaments or bundles thereof; we discuss the composition of septin fibers below). Unlike core SF components like myosin and α-actinin, which displayed a sarcomere-like punctate distribution (Fig. 9, E i), septin fibers were distinctly separate from SFs, organizing in three manners: (a) septin fibers running longitudinally along SFs, either on the side of SFs with their signal segregated from the F-actin signal, or overlapping with SFs with the septin and F-actin signals merging (Fig. 9, A a, and E i and iii, a, b), (b) septin fibers running longitudinally along SFs and diagonally across their width, as if wrapping around the SFs (Fig. 9, A b, and E ii a,b), and (c) septin fibers running longitudinally along segments of SFs while interconnecting different SFs and connecting to other septin fibers (Fig. 9, C and D, and E iv b). Interconnecting septin fiber segments in between SFs frequently colocalized with F-actin signal, but in many instances there was no detectable F-actin signal along these segments.

Regardless of the type of SFs, the majority of septin fibers appeared thinner than their associated SFs. Septin fibers were often thicker on the SF segments adjacent to FAs (Fig. 9, E iii b and E iv a), but thicker septin fibers were also found on arcs, caps, and ventral SFs. Thicker septin fibers did not exceed the width of the associated SF, and appeared either as single thick fibers, or what looked like two closely apposed thin fibers (dashed rectangle in the SEPT7 channel of Fig. 9, E iii). To compare septin fiber thicknesses across the different SF types we measured the width of septin fibers for each SF type. The full width at half maximum (FWHM) was calculated from fluorescence intensity line profiles (Fig. 9 F). Widths of the thick septin fibers found on ventral SFs were plotted separately. All thin septin fiber populations had median FWHM values in a narrow range of 123–137 nm, whereas the thick ones showed an almost twofold higher median FWHM value of 231 nm (Fig. 9, F and H). There was no statistically significant difference between thin septin fiber widths on caps, asters, arcs, and ventral SFs (Fig. 9 F).

To determine whether septin fibers are single or paired filaments ("double septin filaments"), or bundles thereof, we checked the FWHM values of microtubules (MTs) in the same cells. MTs are 25-nm wide tubes and are routinely used as the gold standard for assessing the performance of super-resolution microscopy techniques. MTs were stained using whole primary and fluorophore-coupled secondary IgG antibodies, just like for septin stainings, leading to an estimated real MT width of ∼60 nm (Fig. 9 I; Weber et al., 1978). We found an average FWHM value of 115 nm for the MT width in our cells, in line with reported values (Hamel et al., 2014; Wegel et al., 2016), given that the lateral resolution of SIM is roughly half of the diffraction limit, i.e., ∼110 nm. Given that the observed size in our images is the convolution of the real object size with the point spread function (PSF) of the SIM microscope, we simulated the predicted image size as a function of the real fiber size (Fig. 9 G). The comparison of the estimated real widths of primary and secondary IgG-decorated septins, assumed to organize as single or as paired filaments with either narrow (∼5 nm) or wide (∼20 nm) spacing (Leonardo et al., 2021; Fig. 9 I), with the widths predicted from our FWHM measurements of immunostained

Downloaded from http://rupress.org/jcb/article-pdf/222/3/e202203016/1445844/jcb_202203016.pdf by guest on 20 October 2025

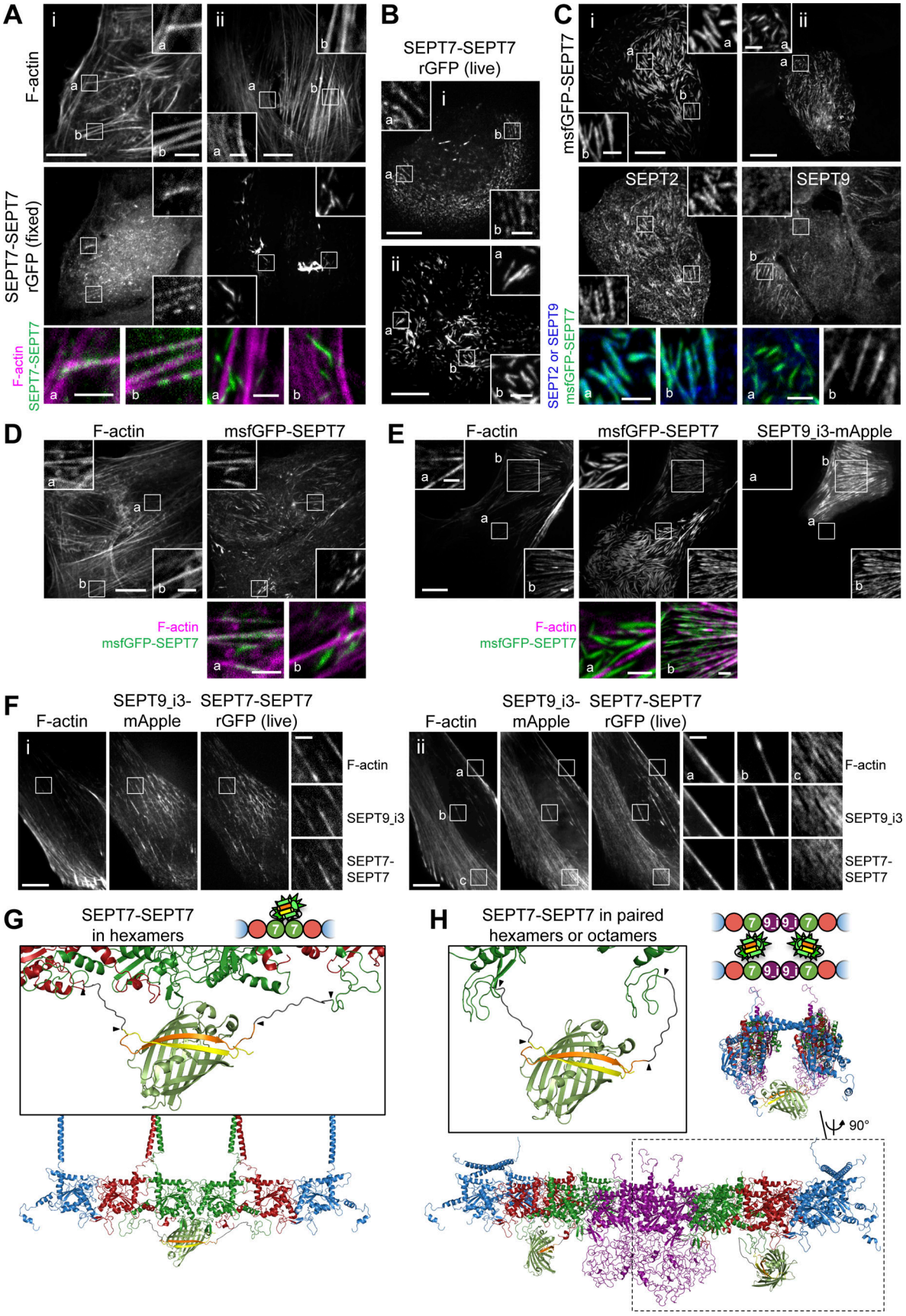

Figure 5. **Exogenous SEPT7 and SEPT9 expression affect SEPT7 distribution. (A)** Representative confocal micrographs of SEPT7-SEPT7 rGFP distribution in fixed cells co-stained for F-actin (phalloidin) localizing (i) to ventral (a and b) SFs and (ii) to ectopic bundles devoid of phalloidin staining (a and b). Scale bars

Downloaded from http://rupress.org/jcb/article-pdf/222/3/e202203016/1445844/jcb_202203016.pdf by guest on 20 October 2025

in large fields of views, 10 µm. Scale bars in insets, 2 µm. **(B)** Representative confocal micrographs of SEPT7-SEPT7 rGFP distribution in live cells localizing (i) to transverse arcs (a and b) and (ii) to ectopic bundles (a and b). Scale bars in large fields of views, 10 µm. Scale bars in insets, 2 µm. **(C)** Examples of cells expressing msfGFP-SEPT7 and co-stained for SEPT2 (i) or for SEPT9 (ii). msfGFP-SEPT7 localizing to ectopic bundles contained SEPT2 (i; a and b) but not SEPT9 (ii; a). A non-transfected cell in (ii) shows SEPT9-stained SFs (b). Scale bars in large fields of views, 10 µm. Scale bars in insets, 2 µm. **(D)** Representative confocal micrograph of a cell expressing msfGFP-SEPT7 co-stained for F-actin (phalloidin) localizing to ventral SFs (a) and to ectopic bundles devoid of phalloidin staining (b). Scale bars in large fields of views, 10 µm. Scale bars in insets, 2 µm. **(E)** Representative example of a cell (top right) co-expressing msfGFP-SEPT7 and SEPT9_i3-mApple and labeled for F-actin (SiR-actin). Example shows msfGFP-SEPT7 localizing to ventral SFs (b). A cell expressing only msfGFP-SEPT7 (bottom left) in (ii) shows msfGFP-SEPT7 localizing to ectopic bundles that are devoid of F-actin (a). Scale bars in large fields of views, 10 µm. Scale bars in insets, 2 µm. **(F)** Representative examples of GFP1-9 cells co-expressing β10- and β11-SEPT7, SEPT9_i3-mApple and labeled for F-actin (SiR-actin). Example in (i) shows rGFP localization to ventral SFs. Example in (ii) shows rGFP localization to peripheral (a), ventral SFs (b) and transverse arcs (c). Scale bars in large fields of views, 10 µm. Scale bars in insets, 2 µm. **(G and H)** Schematic (top) and respective structure model (bottom) of rGFP through SEPT7–SEPT7 interactions within a hexamer (G) or from SEPT7 in two apposed octamers within a paired filament (H). The transparency of the terminal SEPT2 subunits is used to suggest that the protomers are found within a filament. β10 and β11 strands are shown in yellow and orange, respectively. Linker sequences between septins and the β-strands, delimited by arrowheads, are shown in dark grey. The colors of septin subunits correspond to the ones in the color-coded sphere representation of hexamers and octamers. The second half of the octamer is not shown in the rotated filament pair in H for the sake of simplicity. Only SEPT7 subunits are shown in the zoom-in of the reconstituted GFP barrel in H for the sake of simplicity.

septins (Fig. 9 H), suggests that the thin septin fiber widths are compatible with single or paired septin filaments, whereas the thick septin fibers could correspond to two single or two double septin filaments. We note that these estimations assume that septin filaments in cells are present as single filaments with flexible coiled-coils, or paired filaments mediated by coiled-coil pairing (Fig. 9 I) in line with published literature (Cavini et al., 2021). The flexibility of coiled-coils combined with the presence of primary and secondary antibodies suggests that septin fibers cannot correspond to more than a few filaments even if septins interact directly through their GTP-binding domains, a condition previously observed only in the absence of coiled-coils (Bertin et al., 2010; Szuba et al., 2021).

We also wondered about the length of the SF-associated septin fibers. Short septin fibers associated with and interconnecting actin nodes had lengths on the order of 0.5–3.5 µm, whereas septin fibers on arcs, actin caps and ventral SFs were as short as 0.5–1 µm and as long as 10–15 µm (Fig. 9 J). We note that these values provide an upper bound since, given the lateral resolution limit of SIM, we cannot be sure that what appears as continuous fiber signal originates from a single fiber or from adjacent fibers overlapping at their ends.

All microtubule-associated septins organize as filaments containing predominantly octamers

To examine if our results on SF-associated septin filaments also hold for MT-associated septins, which contain specifically SEPT9_i1 (Kuzmic et al., 2022), we probed SEPT9_i1-SEPT9_i1, SEPT7-SEPT9_i1, and SEPT2–SEPT2 interactions using the split-GFP assay. Our results confirmed that MT localization requires intact SEPT7-SEPT9_i1 and SEPT9_i1-SEPT9_i1 interfaces and direct SEPT2–SEPT2 interactions (Fig. S4, A–F and Fig. 4 H), allowing us also to visualize septin filaments on MTs in situ in cells (Fig. S4 F). We further tested the importance of hexamers for septin-MT association. In line with our results on exogenously expressed SEPT7, it was difficult to find SEPT9-decorated MTs in cells also displaying ectopic hexamer-based bundles (Fig. S4 G). rGFP from SEPT7-SEPT7 was, however, readily detected on MTs upon exogenous SEPT9_i1 co-expression (Fig. S4 H), suggesting that the rGFP signal may originate from paired filaments (Fig. 5 H). rGFP from SEPT7Gmut2-SEPT7Gmut2, in the presence of exogenous SEPT9_i1, and SEPT7Gmut2-SEPT9_i1 were readily detected on MTs (Fig. S4, I and J), reflecting SEPT7-SEPT7 rGFP from paired octamers. Finally, SIM imaging revealed thin septin fibers running along MTs over several micrometers (Fig. S4 K). Different from the presence of both thin and thick actin-associated septin fibers, all MT-associated septin fibers appeared homogeneous in their width. FWHM measurements (Fig. 9 G and Fig. S4 L) predicted MT and septin fiber widths in the ranges of 65–135 and 85–130 nm, respectively, compatible with MT-associated septins organizing as paired septin filaments (Fig. 9 I). Our findings reveal that all MT-associated septins are exclusively in the form of octamers and filamentous, consistent with septins on actin SFs.

SF-associated septin filaments are closely apposed to the plasma membrane

Having shown that all SF-associated septins are filamentous, we wondered how septin function relates to septins being filamentous. Recombinant human septins can bind and cross-link actin filaments, but can also bind lipid membranes, raising the hypothesis that septin filaments in cells anchor SFs to the plasma membrane. A first indication that septins might be membrane-bound came from live cell extraction experiments. While extracting the plasma membrane after fixation entirely preserved septin localization to SFs, live-cell extraction removed septins from all SFs while preserving myosin on SFs (Fig. 10 A). Septins thus did not behave like core components of SFs, and their sensitivity to the detergent suggested they might be bound to the membrane.

To test if septins on SFs are close to the plasma membrane of the U2OS cells, we employed a metal-induced energy transfer (MIET) assay (Chizhik et al., 2014). In MIET, the fluorescence lifetime is dependent on the distance of fluorophores from a metal layer, allowing us to deduce the axial distance of fluorophores from a gold-coated coverslip surface with an axial resolution of a few nanometers (Fig. 10 B). We hypothesized that septins could either associate with the plasma membrane while interacting with SFs, or that septins interact with SFs in the absence of any septin-membrane association. To distinguish these scenarios, we compared distances of the fluorescent protein, mApple, in three conditions: (a) mApple N-terminally

Downloaded from http://rupress.org/jcb/article-pdf/222/3/e202203016/1445844/jcb_202203016.pdf by guest on 20 October 2025

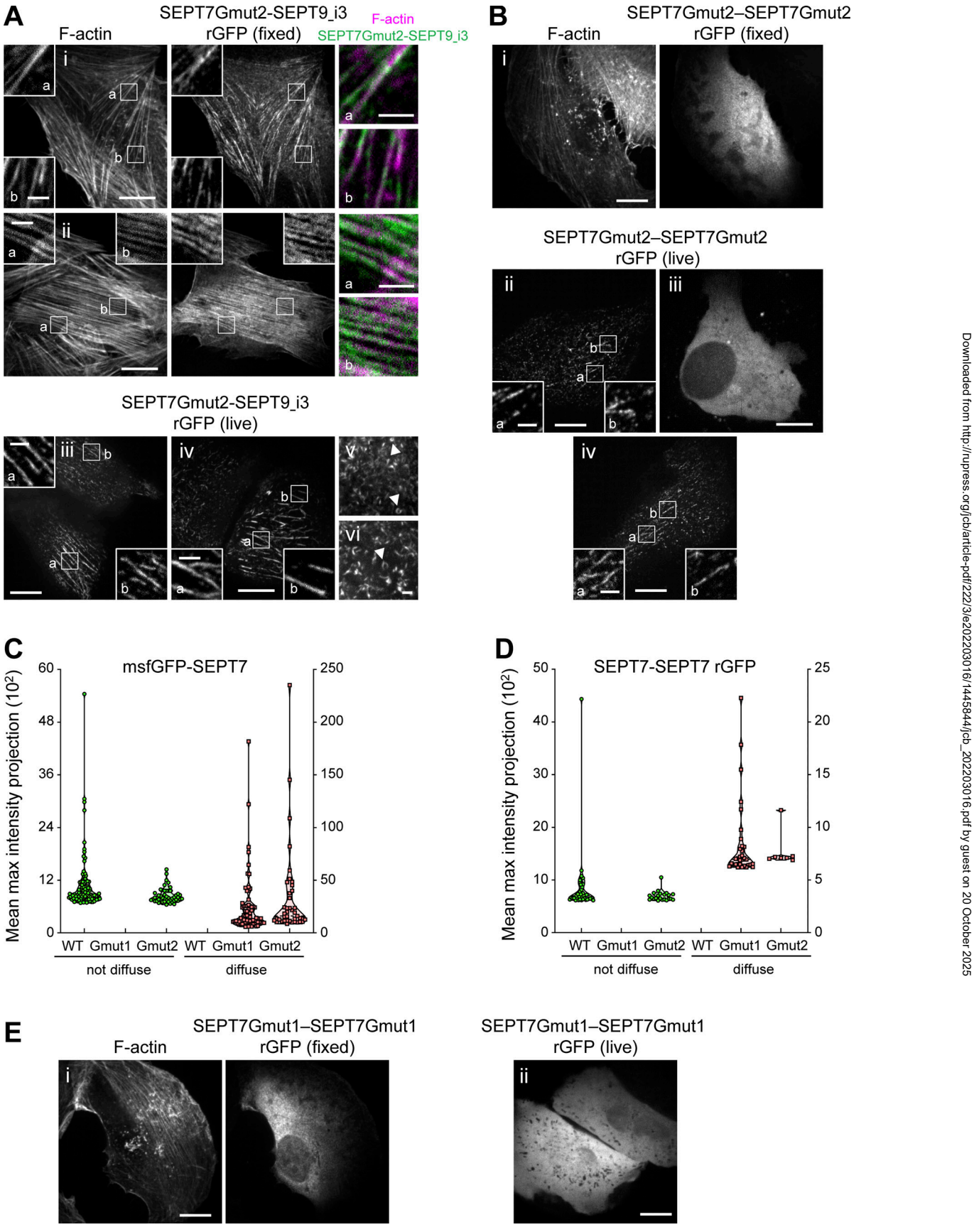

Figure 6. **Intact SEPT7 G interfaces are required for septin localization to SFs. (A)** Representative examples of fixed (i and ii) and live (iii–vi) GFP1-9 cells co-expressing β11-SEPT7Gmut2 and SEPT9_i3-β10. Fixed cells are co-stained for F-actin (phalloidin). Examples shows rGFP localizing (i and ii) to ventral SFs (a

Downloaded from http://rupress.org/jcb/article-pdf/222/3/e202203016/1445844/jcb_202203016.pdf by guest on 20 October 2025

and b), (iii) to perinuclear actin caps (a and b), (iv) to ventral SFs (a and b), and (v and vi) rings (arrowheads). Scale bars in large fields of views, 10 µm. Scale bars in insets, 2 µm. **(B)** Representative examples of GFP1-9 cells (i–iv) co-expressing β10- and β11-SEPT7Gmut2. The fixed cell is co-stained for F-actin (phalloidin). Examples show diffuse cytosolic phenotypes (i and iii) of the rGFP and rGFP localizing to SFs (ii and iv). Scale bars in large fields of views, 10 µm. Scale bars in insets, 2 µm. **(C)** Violin plots depicting the distribution of diffuse cytosolic (red datapoints) vs. non-diffuse (green datapoints) phenotypes as a function of the intensity of the msfGFP signal in cells expressing wild-type msfGFP-SEPT7 or msfGFP-SEPT7NCmut. Data points are from a total of 71 cells for wild-type, 68 cells for SEPT7Gmut1 and 90 cells for SEPT7Gmut2 distributed among the two phenotypes. **(D)** Violin plots depicting the distribution of diffuse cytosolic (red datapoints) vs. non-diffuse (green datapoints) phenotypes as a function of the intensity of the rGFP signal in GFP1-9 cells co-expressing wild-type β10- and β11-SEPT7, β10- and β11-SEPT7Gmut1, or β10- and β11-SEPT7Gmut2. Data points are from a total of 40 cells for wild-type, 33 cells for β10- and β11-SEPT7Gmut1 and 29 cells for β10- and β11-SEPT7Gmut2 distributed among the two phenotypes. **(E)** Representative examples of GFP1-9 cells (i and ii) co-expressing β10- and β11-SEPT7Gmut1 showing a diffuse cytosolic phenotype. The fixed cell is co-stained for F-actin (phalloidin). Scale bar, 10 µm.

fused to the 20 N-terminal residues of neuromodulin/GAP43 that contains palmitoylated cysteines (GAP43-mApple); as a reference for fluorophores localizing directly at the plasma membrane, (b) SEPT9_i3-mApple as a reference for ventral SF-associated septin octamers, and (c) SEPT9_i3-mApple-CAAX as a reference for septins targeted to the plasma membrane through the H-Ras CAAX motif which functions as a membrane targeting signal. Representative lifetime decay traces are shown in Fig. 10 C; and Fig. S5, A and B. Strikingly, the distance of mApple from the metal surface, derived from the lifetime-distance dependence curve (Fig. 10 D), was the same for SF-associated septins, membrane-bound mApple, and membrane-bound septins, meaning that septins are closely apposed to the plasma membrane (Fig. 10 E). Lifetime measurements of AF568-phalloidin bound to ventral SFs under the same conditions placed SFs significantly further away, by ∼25 nm, from the plasma membrane (Fig. 10 E). MIET assays being limited to probing interactions within 200 nm from the metal surface, it was not feasible to probe septin populations on transverse arcs and perinuclear actin caps, which are localized further away.

Septin filaments anchor actin filaments to lipid membranes

Since SF-associated septins are closely apposed to the membrane, we wondered if septin filaments could function to anchor stress fibers to the plasma membrane. In the absence of available septin membrane-binding and actin-binding mutants, we turned to reconstitution assays on supported lipid bilayers (SLBs), comparing only phosphatidylcholine- (PC) vs. phosphatidylinositol(4,5)-bisphosphate (PI(4,5)P_2)-containing membranes (Fig. 10 F), PI(4,5)P_2 being a septin-interacting lipid (Szuba et al., 2021). To image only truly membrane-associated structures, we used total internal reflection fluorescence (TIRF) microscopy in the absence of crowding agents. Actin filaments alone did not bind lipid membranes, whereas septin octamers alone specifically bound PI(4,5)P_2-containing membranes (Fig. S5, C and D), in line with previous reports for mammalian septin hexamers (Szuba et al., 2021). To test if septins can anchor actin to membranes, we either preformed actin–septin bundles in solution and then added them to SLBs, co-polymerized septins and actin on SLBs, or added actin to preassembled septin filaments on SLBs. In all cases, and specifically on PI(4,5)P_2-containing membranes but not on membranes composed only of PC, actin filaments and actin filament bundles were anchored to the lipid bilayers (Fig. 10 F; and Fig. S5, E and F), showing that septin filaments can indeed at the same time bind membranes and actin and thus mediate membrane-actin anchoring.

Single protein tracking reveals that septins are immobilized on actin stress fibers

To determine whether the molecular dynamics of septins at the plasma membrane are consistent with a SF-anchoring function, we combined photoactivated localization microscopy (PALM) with live-cell single protein tracking of SEPT9_i3 and actin fused to photoswitchable mEos fluorescent proteins using sptPALM (Manley et al., 2008; Rossier et al., 2012). Cells were co-transfected with mEos-fused proteins and EYFP-paxillin as a FA reporter, or GFP-actin as a SF and FA reporter. Using TIRF microscopy, we detected and tracked sparse photo-activated proteins within 200 nm above the coverslip surface at high-frequency (50 Hz acquisition), allowing us to reconstruct thousands of protein trajectories (Fig. 10, G–I). For trajectories lasting at least 260 ms, we computed the mean square displacement (MSD). We then sorted trajectories according to their diffusion modes (immobile, confined, free-diffusive), and extracted diffusion coefficients (D_{diff}, D_{conf}; Fig. 10, J and K; and Fig. S5, G and H; see Materials and methods). We first looked at the dynamic behavior of mEos2-actin in SFs labeled with GFP-actin (Fig. 10 G). mEos2-actin was found inside FAs and also linearly organized along SFs between FAs, as expected. Actin mostly displayed immobilized and confined behaviors, as illustrated by the large fractions of immobilization and confined diffusion (Fig. 10, G and K; immobile: 88.5 ± 0.5%, confined: 6.8 ± 0.3%, mean ± SEM) and a distribution of diffusion coefficients centered around 1.5–2.5.10^{-3} µm^2.s^{-1} (Fig. 10 J). In line with septin immunostainings, single SEPT9_i3-mEos3.2 molecules were rarely found inside FAs, but were linearly organized between FAs decorating SFs (Fig. 10 H). Like actin, also SEPT9_i3-mEos3.2 was found to be primarily immobilized and confined (Fig. 10, H and K; immobile: 70.0 ± 1.9%, confined: 13.9 ± 0.8%, mean ± SEM). Contrary to actin, however, SEPT9_i3-mEos3.2 also displayed a significant freely diffusing population (Fig. 10, H and K; diffusive: 16.1 ± 1.3%, mean ± SEM). However, septin free-diffusion was very slow (Fig. 10 J and Fig. S5 G) with a diffusion constant D_{diff} = 0.087 ± 0.001 µm^2.s^{-1} (mean ± SEM) that is comparable to that of free diffusing transmembrane proteins (integrins: Rossier et al., 2012) or of a lipid-anchored protein bound to the plasma membrane by its PH domain (kindlin: Orre et al., 2021). Confined SEPT9_i3-mEos3.2 also diffused very slowly (Fig. S5 H) with a diffusion constant D_{conf} = 0.044 ± 0.001 µm^2.s^{-1}, comparable to that of mEos2-actin (0.057 ± 0.003 µm^2.s^{-1}; means ± SEM). Overall these results suggest that septins, when immobilized and confined, could indeed be anchoring actin SFs to the plasma membrane, while the free-diffusing

Downloaded from http://rupress.org/jcb/article-pdf/222/3/e202203016/1445844/jcb_202203016.pdf by guest on 20 October 2025

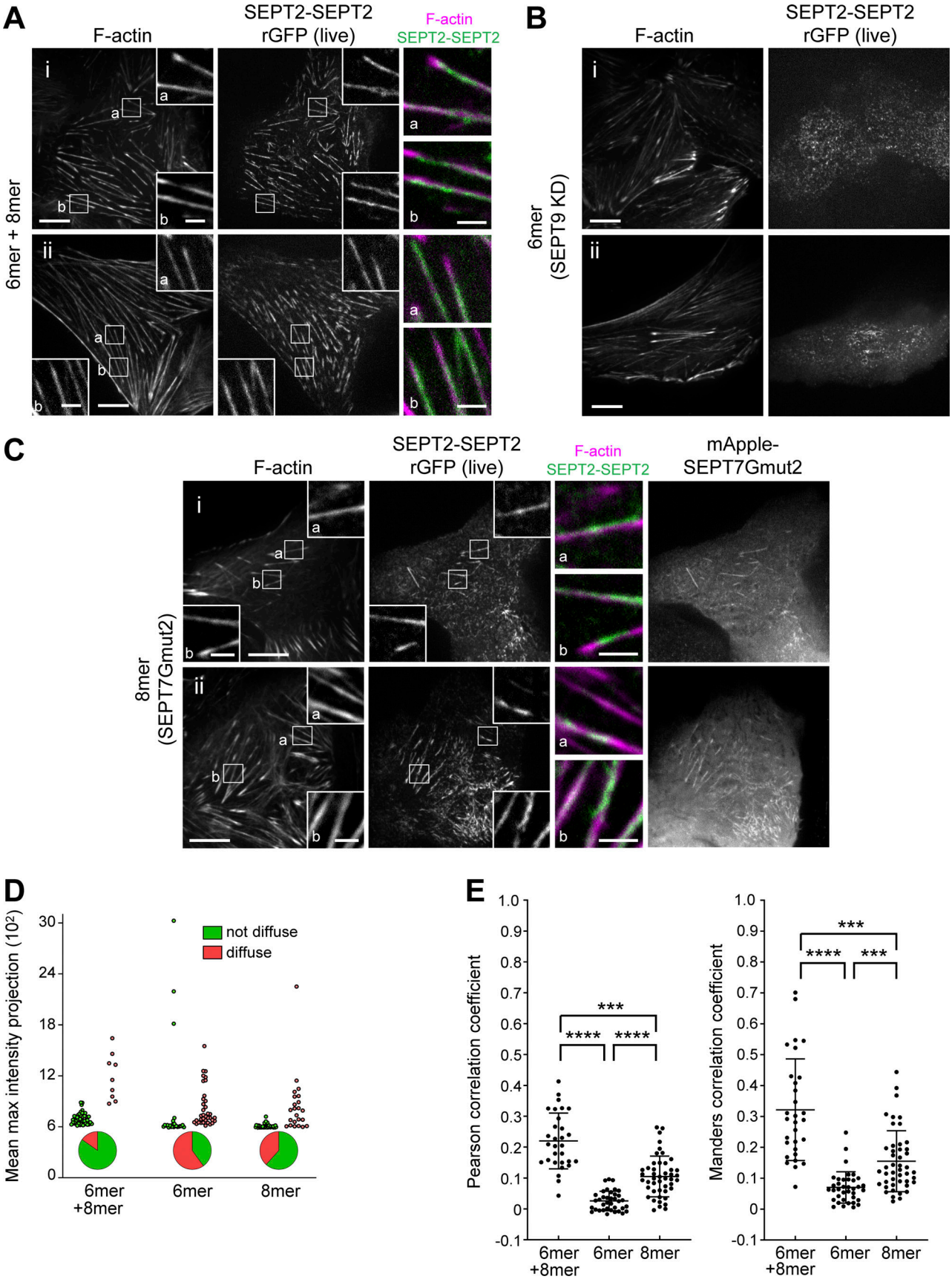

Figure 7. **Septin octamers are essential for the integrity of SF-associated septin filaments. (A–C)** Representative confocal micrographs of SEPT2-SEPT2 rGFP distribution in live cells co-labeled for F-actin (SiR-actin). Cells were treated with siRNA targeting SEPT2 (A), with siRNAs targeting both SEPT2 and SEPT9

Downloaded from http://rupress.org/jcb/article-pdf/222/3/e202203016/1445844/jcb_202203016.pdf by guest on 20 October 2025

(B), or with siRNA targeting both SEPT2 and SEPT7 and co-transfected with mApple-SEPT7Gmut2 (C). Examples in A and C show rGFP localizing to ventral SFs (a and b). Scale bars in large fields of views, 10 µm. Scale bars in insets, 2 µm. **(D)** Scatter dot plots depicting the distribution of diffuse cytosolic (red datapoints) vs. non-diffuse (green datapoints) phenotypes in cells under the same conditions as in A–C, also shown as pie graphs. Data points are from a total of 59 cells for wild-type and 60 cells for each perturbation condition, distributed among the two phenotypes. **(E)** Scatter dot plots (mean ± SD) depicting the distributions of calculated Pearson (left) and Manders (right) correlation coefficients for actin-septin colocalization in cells under the same conditions as in A–C. Data points for each plot, from left to right, are from a total of 30, 37, and 46 cells, respectively. Kruskal–Wallis test; *** P < 0.001, **** P < 0.0001.

septins display a diffusivity that is consistent with them being membrane-anchored.

Similarly to the MIET experiments, we used SEPT9_i3-mEos3.2-CAAX as a reference for septins targeted to the plasma membrane. SEPT9_i3-mEos3.2-CAAX did not localize specifically to SFs but decorated the whole plasma membrane (Fig. 10 I). In comparison with the behavior of SEPT9_i3-mEos3.2, SEPT9_i3-mEos3.2-CAAX displayed a smaller immobilized fraction (Fig. 10, I–K; immobile: 32.6 ± 0.5%) but increased free diffusion and confined diffusion fractions with an increased diffusion constant (D_{diff}: 0.328 ± 0.002 $\mu m^2.s^{-1}$; D_{conf}: 0.202 ± 0.002 $\mu m^2.s^{-1}$, mean ± SEM; Fig. S5, G and H). Interestingly, being stably anchored to the plasma membrane allowed SEPT9_i3-mEos3.2-CAAX to diffuse inside FAs (Fig. 10 I). The much lower diffusion coefficient of SEPT9_i3-mEos3.2 compared to that of SEPT9_i3-mEos3.2-CAAX is in line with freely diffusing SEPT9_i3 being fully incorporated into septin filaments and could reflect hop diffusion of septin filaments alternating between SFs and the plasma membrane.

Septins can associate with actin filaments in cells in a myosin-II independent manner

Although septins decorate myosin-II containing SFs in cells, reconstituted septin filaments can mediate membrane-actin anchoring in the absence of myosin-II. To address if myosin-II is required for binding septins to SFs, we examined the distribution of F-actin, septins, and the two most abundant non-muscle myosin heavy chain isoforms IIA (NMIIA) and IIB (NMIIB) in wild-type U2OS cells, in CRISPR-mediated NMIIA and NMIIB knock-out (KO) U2OS lines (Kage et al., 2022), as well as in NMIIA KO cells treated with NMIIB siRNA to remove both isoforms. Both NMIIA and NMIIB were present on septin-decorated SFs in wild-type cells (Fig. S5, I i and ii). In NMIIA KO cells, NMIIB still associated with septin-decorated SFs (Fig. S5, I iii), and NMIIA still associated with septin-decorated SFs in NMIIB KO cells (Fig. S5, I iv). Thus septin association with SFs does not depend specifically on NMIIA or on NMIIB. However, there is 78% identity among NMIIA and NMIIB, including within the coiled-coil region previously implicated in septin binding (Joo et al., 2007), raising the possibility that a shared septin-binding sequence could bind septins to SFs. To assess septin-SF binding in the absence of myosin-II, we turned to NMIIA KO cells treated with NMIIB siRNA (Fig. S5, J and K). NMIIA- and NMIIB-depleted cells showed a loss of SFs with dramatic cell shape changes, including "C" and dendritic shapes previously reported upon NMII inhibition or silencing (Cai et al., 2010). Interestingly, F-actin appeared as a dense mesh of loosely cross-linked filaments as well as arrays of asters, with septin filaments associating extensively with actin filaments in the meshes and asters (Fig. S5 K). Septins are thus able to associate with actin filaments in cells in a myosin-II independent manner.

Discussion

Employing a tripartite split-GFP complementation assay to probe SEPT2–SEPT2 interactions as a molecular readout for end-to-end septin polymerization, we showed that all septins on SFs organize as filaments. Mutants that disrupt specifically the SEPT7–SEPT7 interface allowed us to distinguish the contributions of hexamers vs. octamers. Our results showed that septin filaments on SFs contain exclusively octamers, which are essential for the integrity of septin filaments and the integrity of SFs. Septin fiber widths measured by SIM microscopy are compatible with their organization as paired septin filaments. Nanometer-resolved distance measurements and single-protein tracking showed that septin filaments are closely apposed to the plasma membrane and largely immobilized on SFs. Finally, reconstitution assays showed that septin filaments mediate actin-membrane anchoring. We propose that septin filaments anchor and stabilize actin fibers at the plasma membrane (working model in Fig. 10 L).

Whether septins organize as filaments in a specific cellular context can now be tested using the tools we have developed in this study, including in genetic animal model systems. Our mutants and split-GFP assays are easily adapted for other septins within the SEPT2 group when required by cell- and tissue-specific expression (Karlsson et al., 2021; Uhlen et al., 2015). Split-GFP assays can also be used as readouts for filament formation in the context of studies aiming to identify regulators or inhibitors of septin polymerization or septin mutants related to disease.

An unexpected result of our study is that human septin filament integrity in cells depends entirely on octamers, questioning the functional importance of hexamers. We speculate that it is the SEPT3 group septin, which is absent from hexamers, that dictates septin function. The observation that SEPT7 assembly is most sensitive to SEPT7 and SEPT9 expression levels, and the fact that SEPT7–SEPT7 interactions are stronger than SEPT7-SEPT9 ones (Rosa et al., 2020) suggest that SEPT9, and possibly the other SEPT3 group septins, may help prevent SEPT7 from forming ectopic bundles. It is intriguing that *Drosophila* does not have any SEPT3 group septins and thus contains only hexamers (Field et al., 1996). Interestingly, *Drosophila* septins occasionally form cytoplasmic bundles devoid of Anillin (Hickson and O'Farrell, 2008). Such bundles also form in the absence of Anillin's septin-binding domain that recruits septins to the plasma membrane (Kechad et al., 2012). We speculate that the formation of these bundles is analogous to the ectopic

Downloaded from http://rupress.org/jcb/article-pdf/222/3/e202203016/1445844/jcb_202203016.pdf by guest on 20 October 2025

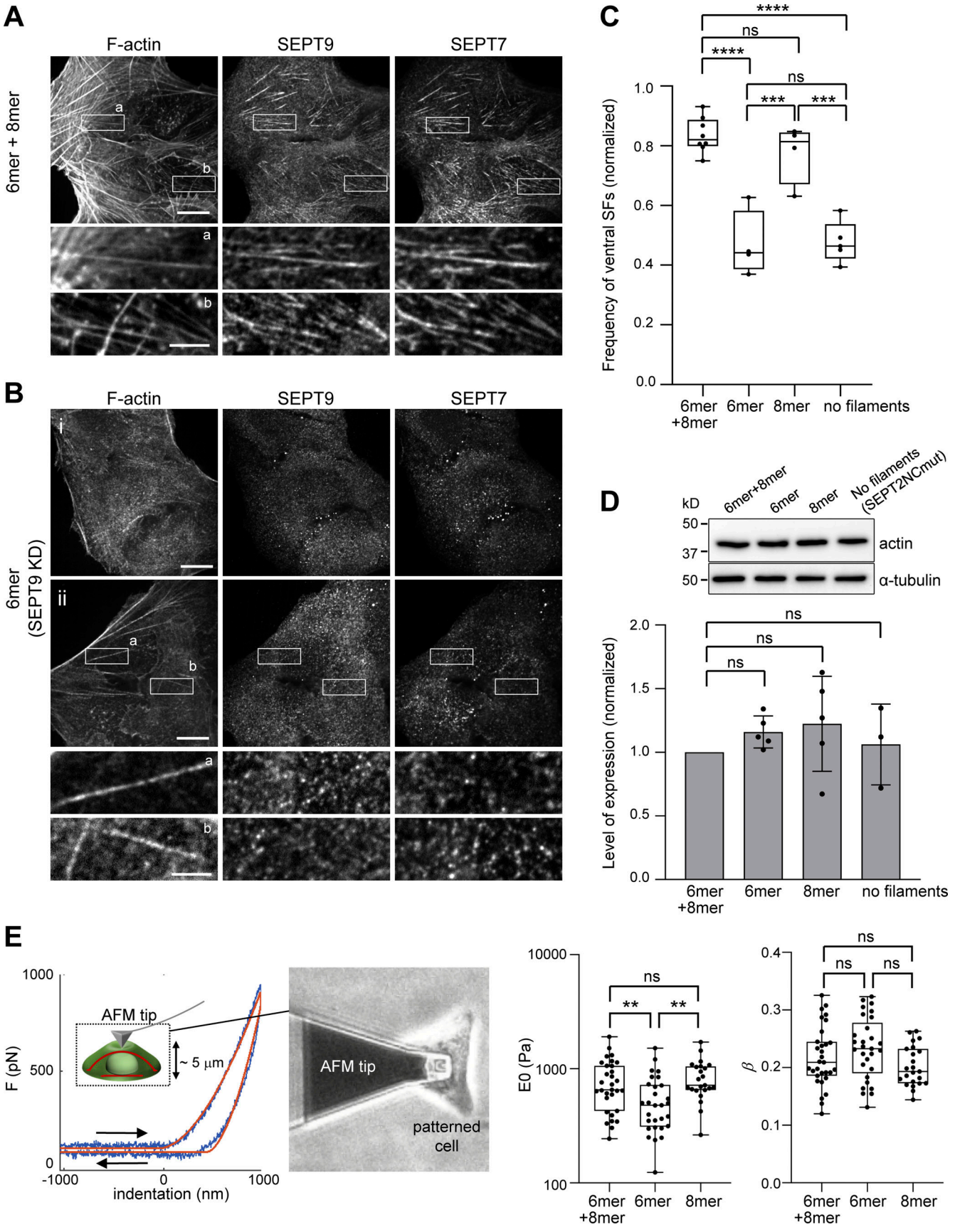

Figure 8. **Ventral SFs are significantly reduced in the absence of octamers or upon impairing septin polymerization. (A)** Representative confocal micrograph of cells co-stained for SEPT7, SEPT9, and F-actin (phalloidin). Examples show septins localizing to ventral SFs (a and b). **(B)** Representative confocal

Downloaded from http://rupress.org/jcb/article-pdf/222/3/e202203016/1445844/jcb_202203016.pdf by guest on 20 October 2025

micrographs of wild type U2OS cells treated with siRNA targeting SEPT9 and co-stained for SEPT7, SEPT9, and F-actin (phalloidin). Example (i) depicts cells with no ventral SFs, whereas example (ii) shows cells that have ventral SFs that are devoid of septins (a and b; see Materials and methods for classification). **(C)** Box plots showing the frequency of ventral SF presence in wild-type cells treated with siRNA targeting LacZ (6mer+8mer), siRNA targeting SEPT9 (6mer), siRNA targeting SEPT7 and co-transfected with msfGFP-SEPT7Gmut2 (8mer), and siRNA targeting SEPT2 and co-transfected with SEPT2NCmut-msfGFP (no filaments). The data points are plotted on top of the respective box plots; each data point corresponds to one round of experiments. On each box, the central mark indicates the median, and the bottom and top edges of the box indicate the 25th and 75th percentiles, respectively. The whiskers extend to the minimum and maximum values. The number of cells analyzed per experiment in each box plot, from left to right, is n = 46; 87; 104; 152; 18; 31; 26; 12 (6mer+8mer), n = 51; 83; 117; 165 (6mer), n = 66; 79; 84; 82 (8mer), and n = 99; 60; 67; 84; 51 (no filaments). The respective median frequencies are 82% (6mer+8mer), 44% (6mer), 81% (8mer), and 46% (no filaments). One-way ANOVA; ns = not significant; *** P < 0.001, **** P < 0.0001. **(D)** Top: Western blots of cell lysates probed with anti-actin and anti-α-tubulin antibodies under the same conditions as in C. Molecular weight markers are shown on the left. Bottom: Respective quantification of actin protein levels (mean + SD). Mean values (normalized to 1 for 6mer+8mer) are from three to five independent experiments. One-way ANOVA; ns = not significant. **(E)** Atomic force microscopy nanoindentation on cells under the conditions "6mer+8mer," "6mer," and "8mer" as described in C. Left: Example of an experimental force-indentation curve. Right and left arrows correspond to the approach and retraction curves, respectively. The solid red lines represent the fits to the viscolelastic model (see Materials and methods). The inset depicts the indentation of the cell, also showing ventral and dorsal SFs in red. The image on the right shows the cantilever tip indenting the dorsal membrane of a micropatterned wild-type cell. Right: Box plots showing the distributions of cell stiffness (E_0) and cell fluidity (β). E_0 values are plotted on a log scale. The data points are plotted on top of the respective box plots; each data point corresponds to one cell. On each box, the central mark indicates the median, and the bottom and top edges of the box indicate the 25th and 75th percentiles, respectively. The whiskers extend to the minimum and maximum values. The number of measurements in each box plot, from left to right, is n = 31, 29, 23. The respective median cell stiffness values are 656, 479, and 719 Pa, and the respective median cell fluidity values are 0.21, 0.23, and 0.19. One-way ANOVA for log(E_0) and for β; ns = not significant; ** P < 0.01. Source data are available for this figure: SourceData F8.

hexamer bundles we observed, forming at limiting amounts of a physiological partner.

Our findings suggest that actin-associated septin filaments in mammalian cells organize as paired septin filaments, with thicker septin fibers consisting of two to three double septin filaments. One single-molecule localization microscopy study of SF-associated septins has reported septin bundles with 25–150 filaments (Vissa et al., 2019), but this study assumed septin GTP-binding domains associating laterally without considering the presence of coiled-coils and the spacing occupied by coiled-coil pairing (Leonardo et al., 2021), so the number of filaments could be overestimated. We thus hypothesize that human septins in cells, like budding yeast septins, organize in a rather narrow range of assembly geometries. We speculate that the wide range of assembly geometries found for reconstituted septins in solution reflects their plasticity, but that the presence of a physiological partner leads to their native assembly into paired filaments (Bertin et al., 2010; Ong et al., 2014; Szuba et al., 2021).

Mammalian septins are distinct from other membrane-bound actin-binding and -crosslinking proteins in that they form filaments. Their capacity to polymerize, catalyzed by membrane binding (Szuba et al., 2021) and coupled with their ability to bind and cross-link actin filaments (Iv et al., 2021; Mavrakis et al., 2014), provides them with the unique potential to stabilize actin filament bundles and meshes at the plasma membrane over considerable distances. We propose that septins function by stabilizing ventral SFs, transverse arcs and perinuclear actin caps at the respective ventral and dorsal plasma membrane, participating in their generation or/and maintenance. It will be interesting to explore if cortical actin meshworks are also membrane attached through septins (Vadnjal et al., 2022). Septin enrichment adjacent to FAs lets us propose that they also contribute a stabilization function at the connection between FAs and SFs and thus impact FA maturation indirectly (Calvo et al., 2015; Dolat et al., 2014; Kang et al., 2021) by affecting the accumulation of mechanical tension on SFs.

The findings of this study lead to several remaining open questions. Whether septins in cells bind membranes and actin filaments directly or indirectly remains to be shown. Our data show that septins can associate with actin fibers in cells in the absence of myosin-II, supporting the possibility of direct septin-actin interactions in the context of SFs. The fact that septins are found only on contractile SFs suggests that myosin-II related signaling might be involved in their recruitment to SFs. Also what regulates septin polymerization in cells is still unknown. Cell-free reconstitution approaches and animal model systems promise to provide important further insights into the link between animal septin organization and function.

Materials and methods

Design of septin fusions for the tripartite split-GFP complementation assay

For the tripartite complementation assay to report SEPT-SEPT interactions with stringency, the amino acid linker length between SEPT and the β10- and β11-strands should not be too short in order to allow for the necessary proximity and flexibility for the β10- and β11-strands to orient in an antiparallel fashion for complementing GFP1-9, but it should be short enough to minimize reporting longer-range interactions. We used fluorescence imaging to test the dependence of split-GFP complementation on the linker length and on the position of the β10- and β11-tags by screening different homo- and hetero-septin combinations as shown in Fig. S2, A–C. All the combinations we tested resulted in fluorescence, reflecting the inherent flexibility of the N- and C-termini of SEPT2, 7 and 9. To allow for the most stringent complementation, we chose to use C-terminal fusions with 14-residue linkers for SEPT2-β10- and -β11 tags and for SEPT9-β10- and -β11 tags, and N-terminal fusions with 14-residue linkers for β10- and β11-SEPT7 tags. This short linker is comparable in length to the 10-residue-long β10- and β11-strands and thus long enough to allow the antiparallel arrangement of the latter. Protein structure models of human septin hexamers and octamers bearing full-length β10- and β11-tagged septins (see Materials and methods section "Modeling of human septin complexes") confirmed the efficiency of GFP complementation

Downloaded from http://rupress.org/jcb/article-pdf/222/3/e202203016/1445844/jcb_202203016.pdf by guest on 20 October 2025

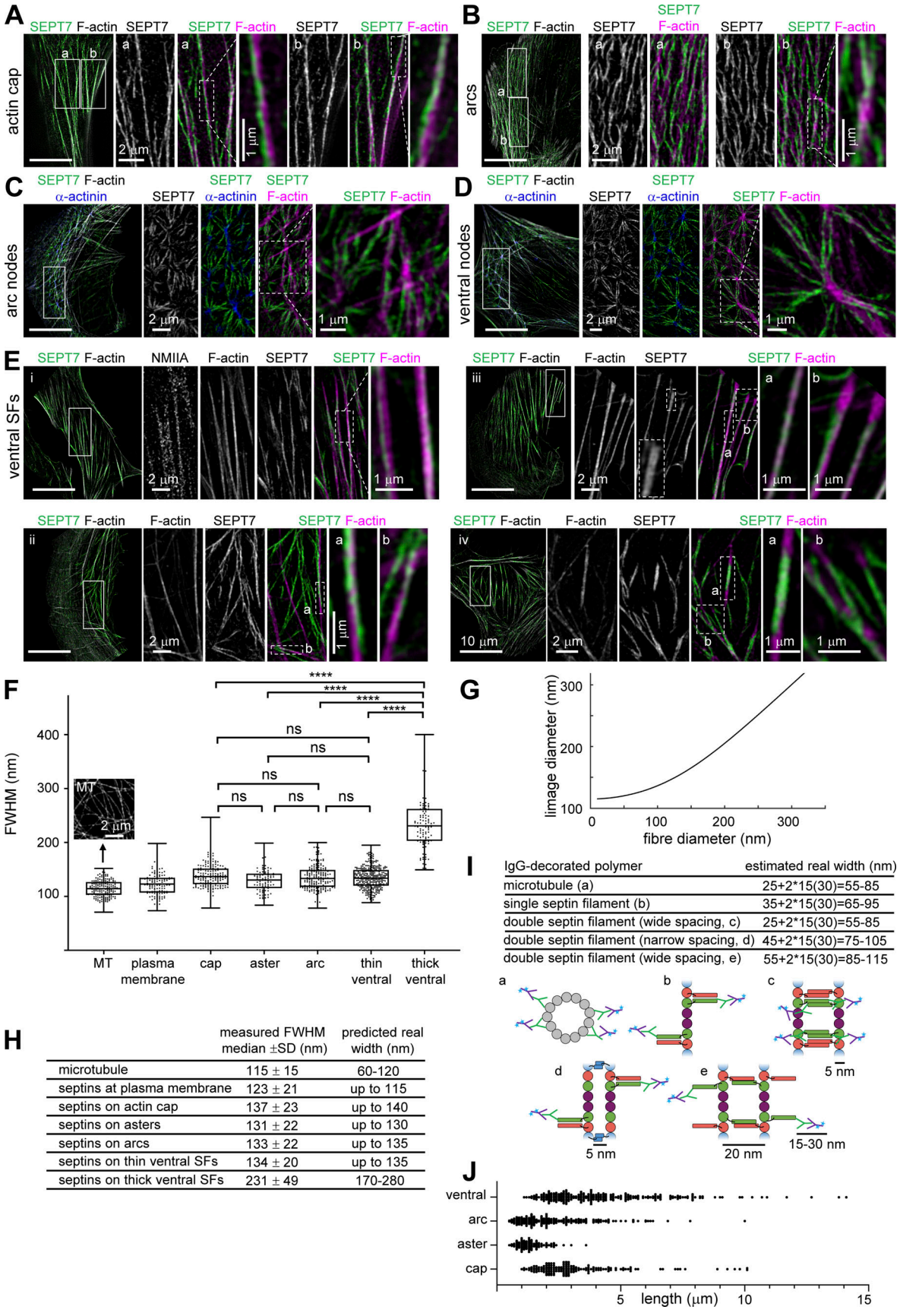

Figure 9. **Super-resolution structured illumination (SIM) microscopy of septin filaments on SFs. (A–E)** Representative SIM micrographs of SEPT7 immunostained cells co-stained for F-actin (phalloidin; A–E), and additionally for α-actinin (C and D) or non-muscle myosin heavy chain IIA (NMIIA; E). Examples

Downloaded from http://rupress.org/jcb/article-pdf/222/3/e202203016/1445844/jcb_202203016.pdf by guest on 20 October 2025

show septin filament localization to perinuclear actin caps (A), arcs (B) and arc nodes (C), ventral nodes (D), and ventral SFs (E, cells i–iv). The insets adjacent to the full field-of-views depict regions of interest (solid outlined boxes) shown at high magnification. Dashed outlined boxes and their respective insets show specific features at higher magnification. Scale bars in all large fields of views, 10 µm. Scale bars in insets, 1 or 2 µm as indicated. **(F–I)** Fiber width measurements and real size estimations from SIM images. Box plots in F depict the distributions of measured widths, as the full width at half maximum (FWHM), of microtubules (MT;inset shows an example SIM image of MTs) and septins associated with peripheral SFs ("plasma membrane"), perinuclear actin caps ("cap"), arc and ventral actin nodes ("aster"), arcs and ventral SFs; widths from thin and thick ventral septin fibers were plotted separately. The data points are plotted on top of the respective box plots; data points correspond to width measurements at multiple positions along MT and septin fibers and in multiple MT and septin fibers per cell in a total of 10 cells for MT and 10 cells for septin fiber measurements. On each box, the central mark indicates the median, and the bottom and top edges of the box indicate the 25th and 75th percentiles, respectively. The whiskers extend to the minimum and maximum values. The number of measurements in each box plot, from left to right, is n = 180, 123, 175, 88, 184, 330, 114. The respective median values are 115, 123, 137, 131, 133, 134, and 231 nm. Kruskal–Wallis test; ns = not significant; **** $P < 0.0001$. **(G)** Numerical simulations of the expected FWHM in SIM images ("image diameter") as a function of the real fiber diameter. The curve was generated from the convolution of a Gaussian point spread function (PSF) of 115 nm with an increasing fiber size. Fiber sizes above ∼200 nm scale linearly with the image sizes. These simulations were used together with FWHM measurements in SIM images (F) to estimate an upper width limit for septin fibers associated with the different types of SFs (H). These estimations were then compared to the real width ranges one expects from IgG antibody-decorated septins organizing as single or double filaments (I). Primary and fluorophore (cyan asterisk)-conjugated secondary antibodies are depicted in green and magenta, respectively. The primary SEPT7 antibody used in our immunostainings binds the very C-terminus of SEPT7. The narrow and wide spacings of paired filaments, the presence of homodimeric coiled coils for SEPT2, SEPT6 and SEPT7, and of heterodimeric coiled coils for SEPT6 and SEPT7 are based on experimental evidence from (de Almeida Marques et al., 2012; Leonardo et al., 2021; Low and Macara, 2006; Sala et al., 2016). **(J)** Scatter dot plots of length distributions for septin fibers on the indicated types of SFs. Bars depict median values. The number of measurements in each plot, from left to right, is n = 151, 97, 227, 249. The respective median values are 2.8, 1.3, 2.0, and 3.8 µm.

for the final chosen linker length and β10/β11-tag positioning (Fig. 2, A and B; Fig. 3, A and B; and Fig. 5, G and H).

Plasmids and cloning

Septin and msfGFP cDNAs were as described in (Iv et al., 2021). mApple and sfCherry2 cDNAs were PCR-amplified from Addgene plasmids #54862 and #83031, respectively. Three types of mammalian expression plasmids were used in this study. A pCMV backbone (Clontech) was used for the expression of full-length fluorescent protein (msfGFP/mApple) fusions. A pcDNA3.1 backbone (Thermo Fisher Scientific), also with a CMV promoter, was used for the expression of β10- or β11-tagged septins. Finally, a pTRIP TRE Bi vector, modified from pTRE-Tight-BI (Takara-Bio; Koraichi et al., 2018), bearing a bidirectional tetracycline response element (TRE) promoter and an IRES-TagBFP cassette downstream β10-tagged septins, was used for the doxycycline-inducible co-expression of β10- and β11-tagged septins (Fig. S2, D and E). pCMV and pTRIP TRE Bi plasmids were used for all results presented in the figures. The pcDNA3.1 plasmids were used only for the initial screening (Fig. S2, A–C).

All pCMV plasmids, SEPT2 constructs in pTRIP TRE Bi plasmids and all interface mutants in pTRIP TRE Bi plasmids were cloned using seamless cloning (In-Fusion HD Cloning Plus Kit from Takara Bio, 638910). All pcDNAs and all wild-type SEPT7 and SEPT9-containing constructs in pTRIP TRE Bi plasmids were generated with classical cloning. In this latter case, DNA fragments were amplified by PCR using the PCR Master Mix from Thermo Fisher Scientific (K0171), TaqFast DNA polymerase (G277; Applied Biological Materials) or Phusion High-Fidelity DNA Polymerase (M0530S; New England Biolabs) and ligated into double digested plasmids with the Rapid DNA Ligation Kit from Thermo Fisher Scientific (K1422). pCMV constructs were cloned into a NheI/BamHI linearized vector. pcDNA constructs were cloned into a NheI/XbaI linearized vector. pTRIP TRE Bi constructs were cloned in two steps: first the β10-tagged septins were cloned into a SacII/NheI digested vector, then the β11-tagged septins were cloned into a NdeI/XbaI digested vector carrying the β10-tagged septin. The starting methionine of septin sequences is included in the N-terminal β10- and β11-tagged versions.

Bacterial expression plasmids for generating wild-type SEPT2-msfGFP hexamers and octamers-9_i3 were described in Iv et al. (2021) and are available through Addgene (#174492, 174498, 174499, 174501). pnEA-vH plasmids for the bacterial expression of SEPT2NCmut-msfGFP and SEPT2-sfCherry2 were generated using seamless cloning following the same strategy described in Iv et al. (2021). All primers for seamless cloning were Cloning Oligo (<60 bp) or EXTREmer (>60 bp) synthesis and purification quality from Eurofins Genomics and are listed in Table S1. All restriction enzymes were FastDigest enzymes from Thermo Fisher Scientific or from New England Biolabs. All plasmids were verified by sequencing (Eurofins Genomics) after each cloning step. We have deposited all plasmids with the nonprofit repository Addgene. Note that the SEPT9_i1NCmut in this study is the same as the SEPT9_i1NCmut2 in Kuzmic et al. (2022). Plasmid mCherry-SEPT9_i1 was from Addgene (#71622).

Cell lines, cell culture, and transfection

U2OS osteosarcoma cells for the expression of full-length fluorescent protein septin fusions were from ATCC (HBT-96). For the inducible co-expression of β10- and β11-tagged septins in the context of the tripartite split-GFP complementation system, we generated an inducible U2OS-Tet-On-GFP1-9 cell line which expresses constitutively a GFP1-9 fragment and an anti-GFP VHH intrabody that enhances split-GFP fluorescence. To generate this cell line, U2OS cells were successively transduced with lentiviruses encoding rtTA, GFP1-9 (#130271; Addgene) and anti-GFP VHH G4 (#182236; Addgene) and tested for complementation efficiency using transient expression of a GFP10-zipper-GFP11 domain (Koraïchi et al., 2018). One additional round of transduction with GFP1-9 lentivirus led to an optimized U2OS-Tet-On-GFP1-9 cell line that showed 80% GFP positive cells upon expression of the GFP10-zipper-GFP11 domain. An IRES-TagBFP cassette downstream β10-tagged septins was used for monitoring septin expression. Cells were maintained in McCoy's medium

Downloaded from http://rupress.org/jcb/article-pdf/222/3/e202203016/1445844/jcb_202203016.pdf by guest on 20 October 2025

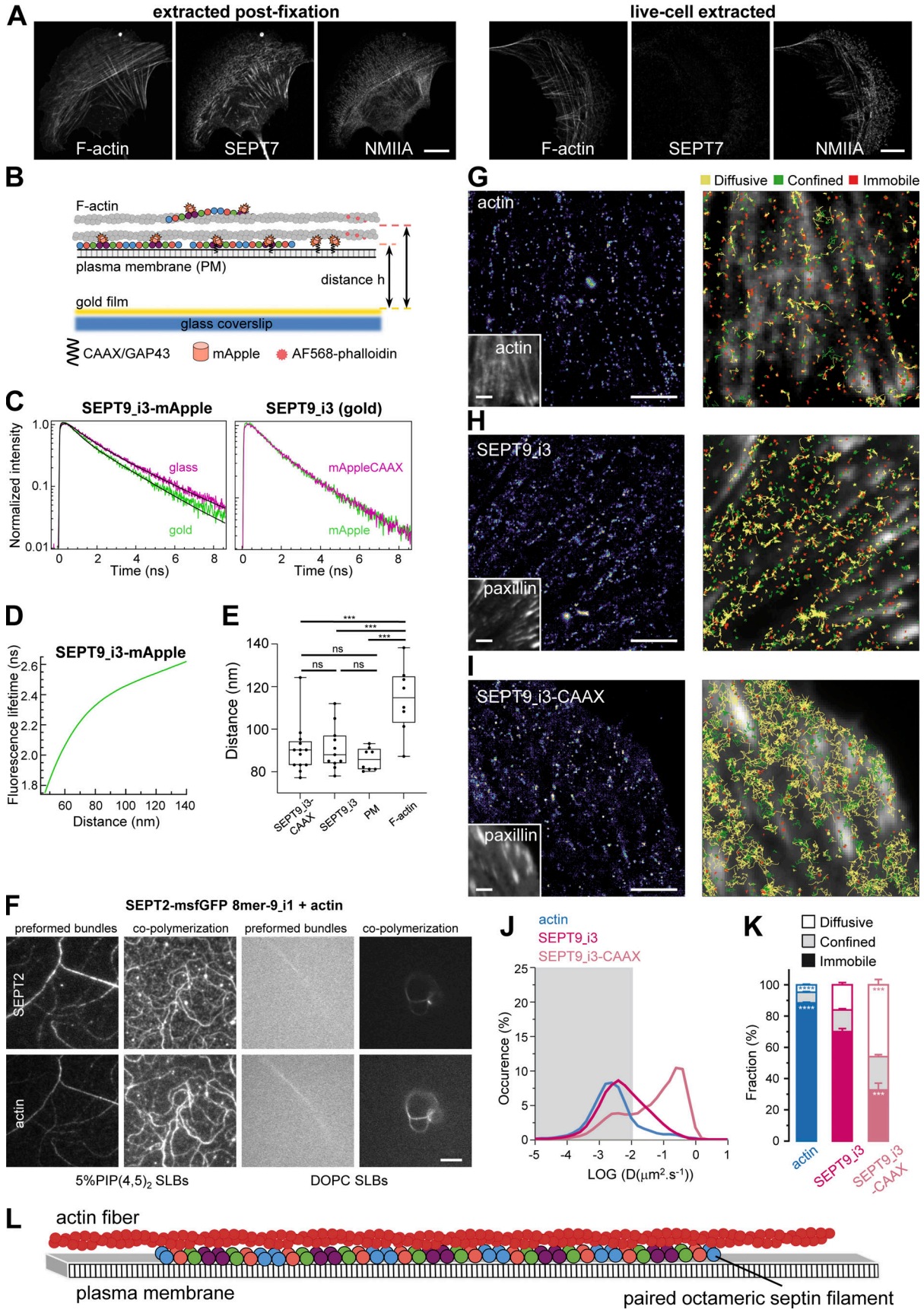

Figure 10. **Septin filaments are closely apposed to the plasma membrane, are largely immobilized on actin stress fibers, and can mediate actin-membrane anchoring. (A)** Representative confocal micrographs of SEPT7 immunostained cells co-stained for F-actin and non-muscle myosin heavy chain IIA

Downloaded from http://rupress.org/jcb/article-pdf/222/3/e202203016/1445844/jcb_202203016.pdf by guest on 20 October 2025

(NMIIA). Cells were either extracted after fixation (left panel) or were live-extracted right before fixation (right panel). Scale bars, 10 µm. **(B)** Schematic of the metal-induced energy transfer (MIET) assay in cells for probing fluorophore (mApple or AlexaFluor 568) distances from a gold-coated coverslip using fluorescence lifetime measurements. **(C–E)** C depicts representative examples of lifetime decay traces for SEPT9_i3-mApple on glass and in the presence of gold (left) and for SEPT9_i3-mApple and SEPT9_i3-mApple-CAAX in the presence of gold (right). The solid lines represent the numerical fits, showing the lifetime reduction due to the MIET process. The calculated lifetime-distance dependence for SEPT9_i3-mApple (D, see Materials and methods) was used to calculate the distance of SEPT9_i3-fused mApple, with or without the CAAX lipid anchor, from the coverslip (E). Lifetime decay traces and lifetime-distance dependence curves for GAP43-mApple (plasma membrane) and AF568-phalloidin (F-actin) are shown in Fig. S5, A and B. Box plots in E depict the distributions of calculated distances for SEPT9_i3-mApple-CAAX, SEPT9_i3, GAP43-mApple (plasma membrane, PM) and AF568-phalloidin (F-actin). The data points are plotted on top of the respective box plots; each data point corresponds to one cell. On each box, the central mark indicates the median, and the bottom and top edges of the box indicate the 25th and 75th percentiles, respectively. The whiskers extend to the minimum and maximum values. The number of measurements in each box plot, from left to right, is n = 13, 11, 8, 8. The respective median values are 90, 88, 86, and 115 nm. One-way ANOVA; ns = not significant; *** P < 0.001. **(F)** TIRF images of SEPT2-msfGFP 8mer-9_i1 (top row) and F-actin (bottom row), either co-polymerized on top of a supported lipid bilayer (SLB), or co-polymerized in solution to form preformed bundles that were then flushed onto the supported lipid bilayer. The supported lipid bilayer was composed either of 5% of $PI(4,5)P_2$, a septin-interacting lipid, and 95% DOPC (left panels), or 100% DOPC (right panels). Due to the shallow penetration depth (~100 nm) of TIRF together with the absence of crowding agents, only truly membrane-associated structures are visible. Scale bar, 5 µm. **(G–K)** Septins are primarily immobilized and confined on actin stress fibers but also undergo very slow lateral free diffusion in the vicinity of the plasma membrane. **(G–I)** Left: Super-resolution PALM intensity images of mEos2-Actin (G), SEPT9_i3-mEos3.2 (H) and SEPT9_i3-mEos3.2-CAAX (I) in mouse embryonic fibroblasts obtained from a sptPALM sequence (50 Hz, >80 s). Insets: low resolution images of GFP-actin (G) or EYFP-paxillin (H and I), which were co-expressed for FA labeling. Scale bars, 3 µm. Right: color-coded trajectories overlaid on FAs labeled by EYFP-paxillin or on FAs and SFs labeled by GFP-actin (grayscale) show the diffusion modes: free diffusion (yellow), confined diffusion (green) and immobilization (red). **(J)** Distributions of the diffusion coefficient D computed from the trajectories of mEos2-actin (blue), SEPT9_i3-mEos3.2 (magenta), and SEPT9_i3-CAAX-mEos3.2 (light magenta) obtained outside FAs, are shown in a logarithmic scale. The gray area including D values inferior to 0.011 $\mu m^2.s^{-1}$ corresponds to immobilized proteins. Values represent the average of the distributions obtained from different cells. **(K)** Fraction of mEos2-actin (blue), SEPT9_i3-mEos3.2 (magenta) and SEPT9_i3-mEos3.2-CAAX (light magenta) undergoing free diffusion, confined diffusion or immobilization outside FAs. Values represent the average of the fractions obtained from different cells (error bars: SEM). Results for SEPT9_i3-mEos3.2 (14 cells) correspond to pooled data from two independent experiments with n, the number of trajectories analyzed: SEPT9_i3-mEos3.2 n_{SEPT9_i3} = 72,720. Results for mEos2-actin (9 cells) and SEPT9_i3-mEos3.2-CAAX (5 cells) correspond each to data from one experiment with n, the number of trajectories analyzed: mEos2-actin n_{actin} = 34,715; SEPT9_i3-mEos3.2-CAAX $n_{SEPT9_i3\text{-}CAAX}$ = 37,339. Statistical significance in K was obtained using two-tailed, non-parametric Mann–Whitney rank sum test. The different conditions were compared to the SEPT9_i3-mEos3.2 condition. The resulting P values are indicated as follows: *** P < 0.001; **** P < 0.0001. **(L)** Working model supported by the results of this study. Septins in cells organize as paired, octamer-based filaments mediating actin-membrane anchoring.

(16600082; Gibco) supplemented with 10% fetal bovine serum (S181H; Dominique Dutscher), 100 U/ml penicillin and 100 µg/ml streptomycin antibiotics (P4333; Sigma-Aldrich) in a humidified atmosphere at 37°C containing 5% CO_2.

Transfections with pcDNAs, for the screening of β10- and β11-tag combinations (Fig. S2, A–C), were performed 16 h prior to immunostainings using jetPRIME (101000015; PolyPlus). To obtain single cells for imaging, 50 × 10^3 U2OS-Tet-On-GFP1-9 cells were typically grown on 18 mm coverslips (Knittel Glass MS0010), previously cleaned by sonication in 70% ethanol, and placed into a 12-well plate a day prior to the day of transfection, for allowing an optimal number of cells to attach and spread. A total of 0.4 µg of DNA and a 4:1 ratio of jetPRIME (µl) : DNA (µg) were used per reaction. To minimize septin overexpression artifacts, the total amount of DNA was composed by 30 ng of β10-septin, 30 ng of β11-septin and 340 ng of empty vector.

Transfections with either pCMV or pTRIP TRE Bi plasmids and siRNAs were performed through electroporation using the Neon Transfection System (MPK5000; Thermo Fisher Scientific). For pCMVs, a single 100-µl reaction using 1.8 × 10^6 U2OS cells, 300 pmol of each siRNA and 6 µg of each DNA was electroporated within the dedicated tip (MPK10096; Thermo Fisher Scientific). Electroporation parameters consisted in four pulses of 10 ms width and a voltage of 1,230 V. The electroporated cells were then inoculated in 5 ml of culture medium without antibiotics, and immediately divided for native-PAGE, SDS-PAGE/Western blots and immunostaining as follows: 3 ml in a 6-cm dish containing 2 ml of medium without antibiotics, 2 ml in a 6-cm dish containing 3 ml of medium without antibiotics, and 100 µl in the well of a 12-well plate containing a 18-mm coverslip in 900 µl of medium without antibiotics, respectively. A satisfactory septin knockdown efficiency was achieved within 48–96 h after electroporation. Typically, immunostaining and protein extraction were performed 72 h post electroporation.

For pTRIP TRE Bi plasmids, a single 100-µl reaction using 1.8 × 10^6 U2OS-Tet-On-GFP1-9 cells, 300 pmol of each siRNA and 6 µg of each DNA was electroporated within the dedicated tip using the same electroporation parameters described previously. The electroporated cells were then inoculated in 5.5 ml of culture medium without antibiotics and immediately divided for SDS-PAGE/Western blots, immunostaining and live cell imaging as follows: 5 ml in a 6-cm dish, 400 µl in the well of a 12-well plate containing a 18-mm coverslip in 600 µl of medium without antibiotics, and 200 µl in the well of a 24-well glass bottom plate (Cellvis, P24-1.5H-N) containing 800 µl of medium without antibiotics, respectively. After either 48 h, for samples intended for live cell imaging or immunostainings, or 72 h, for samples for biochemical analysis, protein expression was induced using 1 µg/ml of doxycycline (D9891; Sigma-Aldrich) for 16 h.

Septin mutant phenotype classification

The diffuse cytosolic vs. non-diffuse phenotype classification analysis for mutant characterization with pCMV plasmids (Fig. 2 H, Fig. 4 E, Fig. 6 C, and Fig. S4 A) was done from three independent experiments. Transfected cells were fixed and co-stained for actin and α-tubulin. Each round of experiments was composed of the 30 first fluorescent cells found randomly in the sample, with the exception of one round containing 11 cells for

Downloaded from http://rupress.org/jcb/article-pdf/222/3/e202203016/1445844/jcb_202203016.pdf by guest on 20 October 2025

msfGFP-SEPT7 and 8 cells for msfGFP-SEPT7Gmut1. Acquired images were classified as "diffuse cytosolic" in the presence of purely diffuse cytosolic signal or as "non-diffuse" in the presence of structure-like signal; no differentiation was applied for SF-, microtubule-, membrane-like or punctate signals in the latter case. The violin graphs representing the phenotype distributions show the mean intensity distribution calculated on the whole field of view from maximum intensity projections of all z-planes. The phenotype classification for reconstituted split-GFP fluorescence distribution (Fig. 2 F, Fig. 4, G and H; Fig. 6 D; and Fig. S4 B) was identical, in terms of the used criteria and graph display, but the data was generated from two independent experiments, with each experimental round composed of the 20 first fluorescent cells, in live cell imaging, with the exception of one round containing 13 cells for SEPT7Gmut1-SEPT7Gmut1 and 9 cells for SEPT7Gmut2-SEPT7Gmut2. For the septin-actin co-localization analysis, the diffuse cytosolic vs non-diffuse phenotype sorting is displayed both as scatter dot plots and as a pie graph to highlight the diffuse cytosolic vs. non-diffuse proportion from each condition. Bars in scatter dot plots depict means, and error bars represent SD. Violin plots, scatter dot plots, and pie graphs were prepared using GraphPad Prism. The number of cells used to assess the phenotypes for each condition is indicated in the respective legends.

RNA interference

Control synthetic small interfering RNA (siRNA) targeting the coding region of LacZ (5′-GCGGCUGCCGGAAUUUACC-3′) and siRNA targeting the 3′UTR region of all SEPT9 mRNA variants (5′-GGAUCUGAUUGAGGAUAAA-3′) were previously validated (Verdier-Pinard et al., 2017). The siRNA sequences targeting the 3′UTR regions of SEPT2 and SEPT7 were 5′-ACACUUUCCUGG AUAAAAA-3′ and 5′-GCAUUUAGCUGUAUUCAUA-3′, respectively. All siRNAs were designed to hybridize with 19-bp sequences in the 3′UTR regions of septin genes, thus knocking down endogenous septins while allowing the expression of the transfected plasmids. 21mer siRNAs, 20 nmol each, were synthesized with dTdT overhangs by Eurofins, and delivered as annealed and ready-to-use siRNA duplexes. siRNAs targeting the coding regions of non-muscle myosin heavy chain IIA (NMIIA; 5′-GCCACGCCCAGAAGAACGAGAAUGC-3′) and non-muscle myosin heavy chain IIB (NMIIB; 5′-UCAAUAAAGCUC UGGAUAGGACCAA-3′) were previously validated (Kage et al., 2022). 20 nmol of these 25mer siRNAs without overhangs were synthesized by Eurofins, and delivered as annealed and ready-to-use siRNA duplexes.

SDS-PAGE and Western blotting of cell lysates

The dish containing the cells was placed on ice and the cells were washed twice with PBS, without Ca^{2+} and Mg^{2+}, before being detached with 40 µl of ice-cold lysis buffer (10 mM Tris-HCl, pH 7.5, 148.5 mM NaCl, 0.5 mM EDTA, 0.5% NP-40, 1× PhosSTOP Roche, 5× cOmplete protease inhibitor cocktail Roche, 1 mM DTT) using a cell scraper (TPP 99003). The lysate was collected in a 1.5 ml tube and incubated on ice for 30 min. The lysates were then centrifuged at 20,000 *g* for 20 min at 4°C for removing cell debris. An aliquot of 6 µl was collected for protein quantification using the BCA Protein Assay (23227; Thermo Fisher Scientific) and the remaining clarified lysates were kept at −20°C until SDS-PAGE analysis.

The lysates were analyzed by 4–20% SDS-PAGE using Mini-PROTEAN TGX Precast Protein Gels (4561095; BioRad). Molecular mass markers were Precision Plus Protein All Blue Standards (1610373; BioRad) or Amersham ECL Rainbow Marker (RPN800E; Cytiva). For the Western blot, the gel, the PVDF Immobilon-P^{SQ} membrane (ISEQ85R; MERCK), filter pads, and filter papers were all incubated in transfer buffer (25 mM Tris, 192 mM glycine and 20% of methanol) for 15 min before assembly in the Mini Trans-Blot transfer cell (1703935; BioRad). The transfer was done at 4°C for 16 h at 110 mA constant current. The transfer efficiency was checked by Ponceau S staining (P7170; Sigma-Aldrich). The membrane was then blocked in a 3% wt/vol dry milk TBS-T solution (20 mM Tris-HCl pH7.5, 200 mM NaCl and 0.1% vol/vol Tween20) for 90 min under constant agitation. Primary and secondary antibodies were diluted in the same blocking solution and incubated over the membrane for 90 and 60 min, respectively. In between antibody incubations, membranes were washed three times for 10 min with TBS-T, and the very last wash right before ECL detection was done only with TBS.

The loaded amount of extracted protein in the gels was adapted depending on the expression promoter and the analyzed septin. For pCMV plasmids used to assess the knockdown efficiency (Fig. S2, F–H), a total of 4 µg of extracted protein was used for detecting endogenous SEPT2, 8 µg for endogenous SEPT7, and 4 µg for endogenous SEPT9. For pTRIP TRE Bi plasmids, a total of 8 µg of extracted protein was used for all analysis. To detect specific septins, we used rabbit anti-SEPT2 (1:2,500, HPA018481; Sigma-Aldrich), rabbit anti-SEPT7 (1:200, sc-20620; Santa Cruz Biotechnology) and rabbit anti-SEPT9 (1:4,000, 10769-1-AP; Proteintech). For detecting β10- and β11-tag expression, we used rabbit anti-β10 (1:5,000) and rabbit anti-β11 (1:5,000; Koraichi et al., 2018). For detecting tubulin as a loading control, we used mouse anti-α-tubulin (1:2,500, T9026; Sigma-Aldrich). For total actin level quantification (Fig. 8 D), we used mouse anti-actin (1:1,000, AC-40, ab11003; Abcam). Secondary HRP-conjugated antibodies were either anti-rabbit-IgG (1:10,000, GENA934; Cytiva) or anti-mouse-IgG (1:10,000, GENA931; Cytiva). Chemiluminescent detection was performed with an Amersham ImageQuant 800 imager (29399481; Cytiva) using Amersham ECL Select Western Blotting Detection Reagent (RPN2235; Cytiva) diluted five times in Milli-Q water. The membrane was incubated with the diluted reagent for 30 s, and washed for 10 s in TBS right before image acquisition. Images were collected in time series mode every 10 s, for a total of 50 images, and processed with ImageQuantTL software for quantification of the band intensities to measure expression levels. Expression quantification graphs for assessing septin knockdown efficiency were prepared using GraphPad Prism and are shown as mean values (normalized to 1 for siCtrl) with the error bar representing SD. Data are from at least three independent siRNA treatments. Data distribution for total actin level quantification (Fig. 8 D) was assumed to be normal, but this was not formally tested.

Downloaded from http://rupress.org/jcb/article-pdf/222/3/e202203016/1445844/jcb_202203016.pdf by guest on 20 October 2025

Native PAGE and Western blotting of cell lysates

The dish containing the cells was placed on ice and the cells were washed twice with PBS, without Ca^{2+} and Mg^{2+}, before being detached with 40 µl of ice-cold native lysis buffer (80 mM PIPES, pH 6.9, 2 mM $MgCl_2$, 4 mM EGTA, 0.2% saponin, 5× cOmplete protease inhibitor cocktail Roche). The lysate was collected in 1.5 ml tube and incubated on ice for 10 min. The lysates were then centrifuged at 14,000 *g* for 10 min at 4°C for removing cell debris. To prevent septin polymerization, clarified lysates were supplemented with NaCl, adding 10 µl of NaCl 5 M for each 100 µl of lysate. After 15 min of incubation on ice, the lysates were clarified in a second centrifugation step of 10 min, 14,000 *g* at 4°C. An aliquot of 12 µl was collected for protein quantification using the BCA Protein Assay (23227; Thermo Fisher Scientific), and the remaining clarified lysates were kept at −20°C until Native PAGE analysis.

The lysates were analyzed by 4–16% Native PAGE using precast Bis-Tris Mini Protein Protein Gels (BN1003BOX; Invitrogen) following the manufacturer's instructions. The molecular mass marker was NativeMark Unstained Protein Standard (LC0725; Invitrogen). For the Western blot, the gel, the PVDF Immobilon-P^{SQ} membrane, filter pads, and filter papers were all incubated in NuPAGE transfer buffer for 15 min before assembly. The transfer was done at 4°C for 16 h at 20 V constant voltage. The transfer efficiency was checked by destaining the membrane with an aqueous solution containing 25% of methanol and 10% of acetic acid. The protein marker was identified and the membrane completely destained with pure methanol for 3 min. The membrane was then blocked and stained with the respective antibodies as described for SDS-PAGE Western blots.

The loaded amount of extracted protein in the gels was again adapted depending on the analyzed septin. A total of 10 µg of extracted protein was used for detecting endogenous or exogenously expressed SEPT2 and SEPT7, and 10 or 4 µg for endogenous or exogenously expressed SEPT9, respectively. To detect specific septins, we used mouse anti-SEPT2 (1:7,500, 60075-1; Proteintech), rabbit anti-SEPT7 (1:200, sc-20620; Santa Cruz Biotechnology) and rabbit anti-SEPT9 (1:2,000, 10769-1-AP; Proteintech). Secondary HRP-conjugated antibodies were either anti-rabbit IgG (1:10,000, GENA934; Cytiva) or anti-mouse IgG (1:10,000, GENA931; Cytiva). Chemiluminescent detection was done with an Amersham ImageQuant 800 imager (29399481; Cytiva) using Amersham ECL Select Western Blotting Detection Reagent (RPN2235;Cytiva) as described previously for SDS-PAGE Western blot.

Immunofluorescence

Cells were fixed for 15 min with 4% paraformaldehyde (15714; Electron Microscopy Sciences) in 37°C-prewarmed cytoskeleton buffer (10 mM MES pH 6.1, 150 mM NaCl, 5 mM EGTA, 5 mM $MgCl_2$, 5 mM glucose), followed by 2 × 5 min wash steps in phosphate-buffered saline (PBS) solution, and a subsequent permeabilization and blocking step with PBS containing 0.1% saponin and 1% IgG-free/protease free bovine serum albumin (BSA; 001-000-161; Jackson ImmunoResearch) for 1 h at RT. Cells were incubated successively with primary antibodies for 16 h at 4°C in a humidified chamber, followed by secondary Alexa Fluor-conjugated IgG antibodies combined with 0.165 µM Alexa Fluor 647-phalloidin (A22287; Thermo Fisher Scientific) for 2 h at RT. Antibody solutions were prepared in PBS containing 0.1% saponin and 1% BSA, and 3 × 10 min wash steps in the same buffer were performed in between antibody incubations. Coverslips with stained cells were washed 2 × 5 min in PBS and then mounted with 15 µl Fluoromount (F4680; Sigma-Aldrich) for image acquisition. Primary antibodies were rabbit anti-SEPT2 (1:500, HPA018481; Sigma-Aldrich), rabbit anti-SEPT7 (1:500, 18991; IBL), rabbit anti-SEPT9 (1:200, 10769-1-AP; Proteintech), mouse anti-α-tubulin (1:10,000, T9026; Sigma-Aldrich), mouse anti-paxillin (1:500, 05–417; Merck Millipore). Secondary antibodies were donkey AlexaFluor488-conjugated anti-rabbit IgGs (1:500, A10037; Thermo Fisher Scientific) and donkey AlexaFluor568-conjugated anti-mouse IgGs (1:500, A21206; Thermo Fisher Scientific). For F-actin, SEPT9, and SEPT7 co-stainings, performed for the quantification of the number of ventral SFs in cells (see Materials and methods section "Quantification of the frequency of ventral SF presence upon septin perturbation"), rabbit anti-SEPT9 (1:200, 10769-1-AP; Proteintech) was combined with rat anti-SEPT7 (1:150, clone 10A7, described in Kuzmic et al. [2022]). Secondary antibodies in this case were donkey AlexaFluor488-conjugated anti-rabbit IgGs (1:500, A10037; Thermo Fisher Scientific) and goat AlexaFluor647-conjugated anti-rat IgGs (1:500, A21247; Thermo Fisher Scientific), and were incubated together with 0.165 µM Atto590-phalloidin (ATTO-TEC AD 590-81).

Immunostaining after live-cell extraction vs. after extraction post-fixation

To live-extract cells (Fig. 10 A), we incubated cells in 37°C-prewarmed cytoskeleton buffer containing 0.1% v/v Triton X-100 for 1 min, then replaced immediately with 37°C-prewarmed cytoskeleton buffer containing 4% paraformaldehyde (43368; Alfa Aesar) and fixed cells for 15 min. Cells were rinsed with PBS and incubated in a permeabilization/blocking solution of PBS containing 0.1% saponin and 5% goat serum (16210064; Thermo Fisher Scientific) overnight at 4°C. Cells were incubated successively with primary antibodies for 2 h at RT in a humidified chamber, followed by secondary Alexa Fluor-conjugated IgG antibodies combined with 0.165 µM Alexa Fluor 546-phalloidin (A22283; Thermo Fisher Scientific) for 1 h at RT. Antibody solutions were prepared in PBS containing 0.1% saponin and 5% goat serum, and 3 × 10 min wash steps in the same buffer were performed in between antibody incubations. Coverslips with stained cells were washed 2 × 5 min in PBS and then mounted with Fluoromount-G (0100-01; Southern Biotech) for image acquisition. Primary antibodies were rabbit anti-SEPT7 (1:400, 18991; IBL) and mouse anti-non-muscle myosin heavy chain IIA (NMIIA; 1:200, ab55456; Abcam). Secondary antibodies were goat AlexaFluor488-conjugated anti-mouse IgGs (1:400, A11001; Thermo Fisher Scientific) and goat AlexaFluor633-conjugated anti-rabbit IgGs (1:400, A21070; Thermo Fisher Scientific). The respective control experiment, i.e., extracting cells post-fixation (Fig. 10 A), involved fixing cells in 37°C-prewarmed cytoskeleton buffer containing 4% paraformaldehyde for 15 min, then extracting cells with PBS containing 0.5% Triton X-100 and 5%

Downloaded from http://rupress.org/jcb/article-pdf/222/3/e202203016/1445844/jcb_202203016.pdf by guest on 20 October 2025

goat serum for 10 min before overnight permeabilization/blocking and antibody incubations as described above. This last protocol was also used for the immunostainings shown in Fig. 9; and Fig. S1, C and D using the additional primary antibody mouse anti-α-actinin-1 (1:200, clone BM 75.2; Thermo Fisher Scientific). Cells shown in Fig. 9, Fig. 10 A; and Fig. S1, C and D were plated on fibronectin-coated coverslips and left to attach and spread for 6 h before immunostainings. Human plasma fibronectin was from Millipore (FC010) and was used at 20 µg/ml in 100 mM bicarbonate buffer, pH 8.5, for coating coverslips overnight at 4°C.

Split-GFP complementation in cells using recombinant purified GFP1-9

Recombinant GFP1-9 expression was achieved from a pET-28a (+) vector coding for GFP1–9 OPT (Cabantous et al., 2013) with an in-frame 6xHis coding sequence (#182240; Addgene). For protein expression, the plasmid was transformed into *Escherichia coli* BL21(DE3; C2527; New England Biolabs). A 3 ml overnight culture was inoculated into 50 ml of Luria-Bertani (LB) medium containing 35 µg/ml kanamycin and was grown at 37°C to A_{600nm} ~0.6. The temperature was reduced to 25°C prior to induction with 0.1 mM isopropyl β-D-thiogalactoside (IPTG) for 24 h. Bacterial cultures were collected by centrifugation at 4,200 *g* for 10 min. Cell pellets were resuspended in 20 ml lysis buffer (150 mM NaCl, 150 mM Tris-HCl, pH 7.2, 5% vol/vol glycerol, 0.2 mM TCEP, 10 mM imidazole) and lysed by sonication on ice with a 0.5-inch diameter probe with 30 s ON, 30 s OFF pulses for 4 min total. The lysate was centrifuged at 30,000 *g* for 20 min. The supernatant was loaded on a column with 1 ml of TALON Metal Affinity Resin (635503; Takara Bio) that was equilibrated with the lysis buffer. After two washes with 10 volumes of lysis buffer, recombinant GFP1–9 was eluted with the elution buffer (200 mM imidazole in the same buffer). Recombinant GFP1-9 fractions were pooled and dialyzed in TNG buffer (150 mM NaCl, 50 mM Tris-HCl, pH 7.2, 5% vol/vol glycerol). Protein concentration was determined with the Bio-Rad Protein Assay (5000002; Bio-Rad).

For split-GFP complementation in cells, wild-type U2OS cells were treated with SEPT2 siRNA and also co-transfected with SEPT2-β10- and SEPT2-β11-encoding pCMV plasmids, and plated on 18-mm coverslips as described above for immunostainings. 48 h post-electroporation, cells were fixed and permeabilized as described for immunofluorescence, and incubated with the recombinant purified GFP1-9 solution (0.2 mg/ml in TNG buffer) diluted twofold in the permeabilization buffer for 4 h at RT followed by overnight incubation at 4°C. After 2 × 10 min wash steps, cells were stained with 0.165 µM Alexa Fluor 647-phalloidin for 1 h at RT. Fluorescence images of SEPT2-SEPT2 reconstituted GFP in the phalloidin-stained cells were acquired as described in the confocal fluorescence microscopy methods section.

Myosin-II-dependence of septin recruitment to stress fibers

For septin costainings with non-muscle myosin heavy chain IIA (NMIIA) and non-muscle myosin heavy chain IIB (NMIIB), wild-type U2OS cells were treated with siLacZ siRNA and prepared for immunofluorescence as described in the respective sections. Primary antibodies were rabbit anti-NMIIA (1:400, 909801; BioLegend), rabbit anti-NMIIB (1:200, 3404; Cell Signaling), and rat anti-SEPT7 (1:150, clone 10A7, described in Kuzmic et al. [2022]), and were incubated for 4 h at RT. Secondary antibodies were donkey AlexaFluor488-conjugated anti-rabbit IgGs (1:400, A10037; Thermo Fisher Scientific) and goat AlexaFluor568-conjugated anti-rat IgGs (1:400, A11077; Thermo Fisher Scientific), and were incubated together with 0.165 µM Alexa Fluor 647-phalloidin (A22287; Thermo Fisher Scientific) for 1 h at RT.

To examine septins in the absence of a given NMII isoform, CRISPR-mediated NMIIA and NMIIB KO U2OS lines (Kage et al., 2022), a kind gift from Frieda Kage and Henry Higgs (Dartmouth College, Hanover, NH, USA), were treated with siLacZ siRNA and immunostained for SEPT7, F-actin and the myosin isoform that is not knocked-out, i.e., for NMIIB in the NMIIA KO line and for NMIIA in the NMIIB KO line, using the same antibodies described in this section. NMIIA KO and NMIIB KO U2OS lines were cultured as wild-type U2OS cells.

Given that NMIIA is by far the most abundant NMII in U2OS cells (Kage et al., 2022) and that the efficiency of knocking down NMIIB (~ 96–98%) was much higher than knocking down NMIIA in our hands (~ 60–76%), we chose to treat NMIIA KO cells with NMIIB siRNA to examine septins under conditions of minimal presence of NMII in U2OS cells. Treatment with NMIIB siRNA was performed as described in (Kage et al., 2022) but with electroporation. SDS-PAGE and Western blotting in the NMIIA KO and NMIIB KO cell lysates was performed as described in the respective Materials and methods section using the same rabbit NMII antibodies described in this section at 1:1,000 each, rabbit anti-SEPT7 (1:200, sc-20620; Santa Cruz Biotechnology), and mouse anti-α-tubulin (1:2,500, T9026; Sigma-Aldrich).

Quantification of the frequency of ventral SF presence upon septin perturbation

The frequency of ventral SF presence in wild-type U2OS cells treated with siLacZ siRNA (6mer+8mer), with SEPT9 siRNA (6mer), with SEPT7 siRNA and also transfected with msfGFP-SEPT7Gmut2 (8mer), and in U2OS cells treated with SEPT2 siRNA and also transfected with SEPT2NCmut-msfGFP (no filaments), was quantified from at least four independent experiments (Fig. 8 C). Electroporated cells were either incubated with SiR-actin for live cell imaging (two independent experiments for 6mer+8mer, 6mer and 8mer conditions) or fixed and co-stained for F-actin, SEPT9 and SEPT7 (from two to six independent experiments for 6mer+8mer, 6mer, 8mer and "no filaments" conditions). Each round of experiments was composed of at least 20 and 10 fields of view for live and fixed cell imaging, respectively. Only cells with most of their surface in the acquired field of view were considered for the quantification, and were classified regarding the presence, in the case of at least one detected ventral SF, or absence of ventral SFs based on the phalloidin or SiR-actin signal; no differentiation was applied for the density/number of ventral SFs, or the presence of other SF subtypes, as no clear effect could be detected in the latter. Each dot in the scatter plots represents the percentage of cells presenting

Downloaded from http://rupress.org/jcb/article-pdf/222/3/e202203016/1445844/jcb_202203016.pdf by guest on 20 October 2025

ventral SFs in a given round of experiments. Bars in scatter dot plots depict means, and error bars represent SD. Scatter dot plots were prepared using GraphPad Prism. The number of cells used to assess the phenotypes for each condition is indicated in the respective legends. Data distribution was assumed to be normal but this was not formally tested. For the quantification of the percentage of SEPT9 siRNA-treated cells containing SEPT7 vs. SEPT9-decorated SFs, two rounds of experiments using fixed cells were used. Only 2–3% of SEPT9 siRNA-treated cells showed SEPT7-decorated SFs, and these same SFs contained also SEPT9, corresponding to the small percentage of cells where SEPT9 was not knocked down.

Confocal fluorescence microscopy of cells and image processing

For live cell imaging, right before microscopy and due to the absence of CO_2 control on our microscope setup, the culture medium was exchanged by Leibovitz medium (21083027; Gibco) supplemented with 10% fetal bovine serum and antibiotics. Cells were kept at 37°C in a heating chamber (H301-T-UNIT-BL; OkoLab). Fluorescence images of live or fixed cells were acquired using a spinning disk unit (CSU-X1-M1 from Yokogawa) connected to the side-port of an inverted microscope (Eclipse Ti2-E from Nikon Instruments) using a Nikon Plan Apo ×100/1.45 NA oil immersion objective lens, 488- 561- and 641-nm laser lines (Coherent) and an iXon Ultra 888 EMCCD camera (1,024 × 1,024 pixels, 13 × 13 µm pixel size, Andor, Oxford Instruments) resulting in an image pixel size of 65 nm. Z-stacks were acquired with a Δz interval of 0.4 µm. Exposure times were in the range of 0.5–3.0 s depending on the exact condition. For the non-diffuse vs. diffuse cytosolic phenotype classification for septin mutant characterization, acquisition parameters were kept the same among imaging sessions. For actin or microtubule co-labeling in live cells, cells were incubated for 30 min with 0.5 µM of SiR-actin or 60 min with 0.5 µM of SiR-tubulin and 10 µM of verapamil in culture medium (SiR Cytoskeleton Kit, Spirochrome SC006).

Images were processed with the open-source image processing software ImageJ/Fiji. All shown images, except for the ones used for the septin-actin co-localization analysis that were acquired as single z-planes, are maximum intensity projections of two consecutive z-planes contrasted manually in order to optimize the image display. For septin-actin co-localization measurements, acquired channels of single z-planes, for septin and actin, were individually processed as follows: images were subjected to automatic contrast enhancement, allowing 0.1% of saturated pixels, then to a blurring with a Gaussian filter of radius 1.0 and a subsequent background subtraction using a rolling ball radius of seven pixels. A manual intensity threshold was used when calculating Pearson and Manders co-localization coefficients, using the JACoP plugin for ImageJ (Bolte and Cordelières, 2006).

Images shown in Fig. 10 A and Fig. S1, C and D were acquired on a Zeiss LSM 710 laser scanning confocal microscope using a PlanApochromat 100×/1.4 NA oil immersion objective lens, 488-543- and 633-nm laser lines for excitation, with all channels at 1AU for the pinholes. Z-stacks were acquired with a Δz interval of 0.48 µm. All shown images are single z-planes and were processed with ImageJ/Fiji.

Super-resolution structured illumination microscopy

Sample preparation and image acquisition

Cells for super-resolution structured illumination (SIM) microscopy were plated on high precision (170 ± 5 µm thick) 18 × 18 mm glass coverslips from Zeiss (474030-9000-000) and prepared for immunostainings as detailed in the section "Immunostaining after live-cell extraction vs. after extraction post-fixation"; all images shown in Fig. 9 and Fig. S4 K employ extraction post-fixation. For microtubule stainings used for microtubule width measurements in Fig. 9, F and H, cells were fixed with −20°C-prechilled methanol for 2 min at −20°C and rinsed with PBS before overnight permeabilization/blocking and antibody incubations as described in the above section. Primary antibodies were mouse tubulin (1:1,000, T9026; Sigma-Aldrich) and rabbit anti-SEPT7 (1:500, 18991; IBL). Secondary antibodies were goat AlexaFluor488-conjugated anti-mouse IgGs (1:400, A11001; Thermo Fisher Scientific) and goat AlexaFluor633-conjugated anti-rabbit IgGs (1:400, A21070; Thermo Fisher Scientific). Images in Fig. 9 were acquired on a Zeiss Elyra PS.1 super-resolution microscope using an alpha PlanApochromat 100×/1.46 NA DIC M27 Elyra oil immersion objective lens, 488-, 561-, and 642-nm laser lines for excitation and respective BP495-550, BP570-620 and LP655 emission filters. Z-stacks were acquired with a Δz interval of 0.101 µm. Images were processed and channel-aligned with the Zeiss ZEN Black software. Images in Fig. S4 K were acquired on a DeltaVision OMX SR (Leica Microsystems/Cytiva) super-resolution microscope using an Olympus PlanApo N 60×/1.42 NA oil immersion objective lens, 488- and 640-nm laser lines for excitation and respective 528/48 and 683/40 emission filters. Z-stacks were acquired with a Δz interval of 0.125 µm. Images were processed and channel-aligned with the DeltaVision softWoRx 7.0.0 software. All shown images are single z-planes and were prepared with ImageJ/Fiji.

Septin fiber diameter and length measurements

Full width at half maximum (FWHM) measurements for measuring the diameter of microtubules (MT) and septin fibers in SIM images (Fig. 9, F and H) were made with a custom-generated Matlab code (FilamentAnalysis.mlx), the source code of which is available at https://github.com/cchandre/Polarimetry. A line was drawn perpendicular to the axis of the MT or to the long axis of the septin fiber, and the FWHM was extracted from the intensity profile using the *findpeaks* Matlab function. We measured the width of MTs and septin fibers at multiple positions along their length and in multiple microtubules and multiple septin fibers for each SF type per cell. Box plots depicting the distribution of FWHM measurements (Fig. 9 F) were prepared using GraphPad Prism (one data point corresponds to one width measurement). The central mark indicates the median, and the bottom and top edges of the box indicate the 25th and 75th percentiles, respectively. The whiskers extend to the minimum and maximum values. The number of measurements per condition (MT or SF type) is indicated in the respective legend. A Kruskal–Wallis test followed

Downloaded from http://rupress.org/jcb/article-pdf/222/3/e202203016/1445844/jcb_202203016.pdf by guest on 20 October 2025

by a multiple comparison test was used for comparing the distributions.

Length measurements were implemented in the same custom-generated code. A line was drawn parallel to the long axis of the septin fiber and the length extracted with the *curveLength* Matlab function. We measured the length of multiple septin fibers for each SF type per cell. Scatter dot plots depicting the distribution of length measurements (Fig. 9 J) were prepared using GraphPad Prism (one data point corresponds to one length measurement). The number of measurements per SF type is indicated in the respective legend. Bars depict median values.

Numerical simulations for fiber size estimation

Numerical simulations of the expected FWHM in SIM images ("image diameter" in Fig. 9 G) as a function of the real fiber diameter ("fiber diameter" in Fig. 9 G) were made with a custom-generated Matlab code (Convolution_1D.m), the source code of which is available at https://github.com/cchandre/Polarimetry/tree/master/AdditionalFiles. A Gaussian point spread function (PSF) was used, and the curve was generated from the convolution of this PSF with an increasing fiber diameter size, using the conv Matlab function. Assuming a real antibody-decorated MT diameter size of ∼60 nm (Weber et al., 1978), the convolution curve permits to deduce the PSF size from the measured FWHM in isolated microtubule fibers (the median value is used). This PSF size being linearly dependent on the emission wavelength, it is then rescaled to account for the wavelength difference used in MT vs. septin imaging: MTs and septins were imaged at 488 and 642 nm, respectively, for SIM in Fig. 9, whereas MTs and septins for SIM in Fig. S4 K were imaged at 640 and 488 nm, respectively. To predict the real width of the respective septin fiber diameters (Fig. 9 H), the convolution curve was finally used for the estimated PSF, using as input the measured septin FWHM.

Production and purification of recombinant human septin complexes

Wild-type nonfluorescent and SEPT2-msfGFP hexamers and octamers-9_i3, SEPT2NCmut-msfGFP hexamers and octamers-9_i3, and SEPT2-sfCherry2 octamers-9_i3 were produced and purified as follows. Plasmids expressing SEPT2, SEPT2-msfGFP or SEPT2NCmut-msfGFP, and plasmids co-expressing SEPT2, SEPT2-msfGFP or SEPT2NCmut-msfGFP and SEPT6, were co-transformed with plasmids co-expressing SEPT6 and SEPT7 (#174499; Addgene), or SEPT7 and SEPT9_i3 (#174501; Addgene), for generating recombinant nonfluorescent, SEPT2-msfGFP, or SEPT2NCmut-msfGFP hexamers and octamers-9_i3 (Iv et al., 2021). Plasmids co-expressing SEPT2-sfCherry2 and SEPT6 were co-transformed with plasmids co-expressing SEPT7 and SEPT9_i3 (#174501; Addgene) to generate recombinant SEPT2-sfCherry2 octamers-9_i3. The N-terminus of SEPT2 is tagged with a His_6-tag, and the C-terminus of SEPT7 (for isolation of hexamers), or the C-terminus of SEPT9 (for isolation of octamers), is tagged with a Strep-tag. A purification scheme comprising a Strep-Tactin affinity column to capture Strep-tagged complexes, followed by a nickel affinity column to retain the Strep-tagged complexes that also bear His_6-tagged septins isolates hexamers and octamers (Iv et al., 2021).

Co-transformed *E. coli* BL21(DE3) were selected on LB agar plates with carbenicillin and spectinomycin each at 100 µg/ml. A single colony was selected to prepare an overnight LB medium preculture at 37°C with antibiotics at 100 µg/ml. Terrific Broth with antibiotics at 50 µg/ml, typically 3.5–5 L, was inoculated with the pre-culture and incubated at 37°C. Bacteria were left to grow to A_{600nm} ∼ 0.6–0.8 before inducing expression with 0.5 mM IPTG for overnight expression at 17°C. The culture was stopped by centrifuging at 3,400 *g* for 15 min and 4°C, and the supernatants were pooled and further centrifuged at 5,000 *g* for 10 min and 4°C. Bacteria pellets were stored at −20°C until protein purification. Bacteria expressing msfGFP- and sfCherry2-tagged septins yield yellow-greenish and pink-reddish pellets, respectively.

On the day of purification, the pellet was resuspended in ice-cold lysis buffer (50 mM Tris-HCl, pH 8, 300 mM KCl, 5 mM $MgCl_2$, 0.25 mg/ml lysozyme, 1 mM PMSF, cOmplete protease inhibitor cocktail [1 tablet per 50 ml], 10 mg/l DNase I, 20 mM $MgSO_4$) and lysed on ice using a tip sonicator with 5 cycles of 30 s "ON", 15 s "OFF". The lysate was clarified by centrifugation for 30 min at 20,000 *g* and 4°C, and the supernatant loaded on a StrepTrap HP column. Strep-tag-II-containing septin complexes were eluted with 50 mM Tris-HCl, pH 8, 300 mM KCl, 5 mM $MgCl_2$, and 2.5 mM desthiobiotin. The pooled fractions were then loaded to a HisTrap HP column, and His_6-tag-containing complexes eluted with 50 mM Tris-HCl at pH 8, 300 mM KCl, 5 mM $MgCl_2$, and 250 mM imidazole. Only the highest-concentration peak fractions were collected. Both affinity steps were performed on an ÄKTA pure protein purification system at 4°C (Cytiva). To remove imidazole, we either performed overnight dialysis or used a PD-10 column, also including DTT in this last step. The final elution buffer, in which septins are stored, was 50 mM Tris-HCl, pH 8, 300 mM KCl, 5 mM $MgCl_2$, and 1 mM DTT. Protein concentration was assessed with absorbance measurements at 280 nm from the calculated extinction coefficients using ExPASy, and protein aliquots were flash-frozen in liquid nitrogen and stored at −80°C until further use.

Chemicals used for recombinant septin complex production and purification are as follows. *E. coli* BL21(DE3) from Agilent (200131). Carbenicillin (C3416), spectinomycin (S4014), LB broth medium (L3022), LB agar (L2897), SOC medium (S1797) from Sigma-Aldrich. Terrific Broth from MP Biomedicals (091012017). IPTG (EU0008-C) and lysozyme (5933) from Euromedex. Imidazole from Thermo Fisher Scientific (Fisher Chemical I/0010/53). PMSF (78830), cOmplete Protease Inhibitor Cocktail Tablets (11836145001; Roche), DNase I (10104159001; Roche), *d*-Desthiobiotin (D1411), and DTT (D0632) from Sigma-Aldrich. HisTrap HP 1 ml columns (17524701) and StrepTrap HP 1 ml columns from Cytiva (28907546). 20 K MWCO Slide-A-Lyzer cassettes from Thermo Fisher Scientific (87735). PD-10 desalting columns from Cytiva (17085101).

Sample preparation for fluorescence microscopy of in vitro reconstituted actin and septins

To prepare flow cells, glass slides and coverslips were cleaned for 15 min in base-piranha solution (Milli-Q water, 30% ammonium hydroxide, 35% hydrogen peroxide at a 5:1:1 volume

Downloaded from http://rupress.org/jcb/article-pdf/222/3/e202203016/1445844/jcb_202203016.pdf by guest on 20 October 2025

ratio), rinsed with Milli-Q water and stored in 0.1 M KOH up to 1 mo. Right before assembling flow cells, slides and coverslips were rinsed with Milli-Q water and dried with synthetic air. Flow cells with ∼10 µl channels were assembled by sandwiching ∼2-mm-wide and ∼2.5-cm-long strips of Parafilm between a cleaned glass slide and coverslip and melting on a hot plate at 120°C. The resulting chambers were passivated by incubating for 45 min with 1 M KOH, rinsing with actin polymerization buffer (5 mM Tris-HCl, pH 8, 50 mM KCl, 1 mM $MgCl_2$, 0.2 mM Na_2ATP, 1 mM DTT), incubating for another 45 min with 0.2 mg/ml PLL-PEG, and rinsing with actin polymerization buffer. Flow cells were placed in a Petri-dish along with tissue paper soaked in water to prevent flow channels from drying during the incubation steps and until use.

Lyophilized rabbit skeletal muscle G-actin was resuspended to 5 mg/ml (119 µM) in G-buffer (5 mM Tris-HCl pH 8, 0.2 mM Na_2ATP, 0.1 mM $CaCl_2$, 1 mM DTT), aliquots snap-frozen in liquid nitrogen and stored at −80°C. Frozen aliquots were thawed and centrifuged for 30 min at 120,000 *g* in a benchtop Beckman air-driven ultracentrifuge (Beckman Coulter Airfuge, 340401) to clear the solution from aggregates. Clarified G-actin was kept at 4°C and used within 3–4 wk.

For actin-septin reconstitution experiments, thawed septin aliquots were cleared for 15 min at 120,000 g in a Beckman airfuge right before use. To polymerize G-actin in the presence of septins, we mixed G-actin, previously diluted with G-buffer to 5 µM, with septins, either nonfluorescent ones or msfGFP-labeled septins (at 20% msfGFP molar ratio for wild-type septins, and 100% GFP for SEPT2NC septins) to a final actin concentration of 1 µM and a final septin concentration of 0.3 µM, right before polymerization in actin polymerization buffer, additionally containing 1 mM Trolox, 2 mM protocatechuic acid (PCA), 0.1 µM protocatechuate 3,4-dioxygenase (PCD) and 0.1% wt/vol methylcellulose. To fluorescently label actin filaments, we polymerized G-actin in the presence of 1 µM Alexa Fluor 568-conjugated phalloidin.

Actin-septin samples were prepared with a final volume of 10 µl, were loaded immediately into passivated flow channels upon mixing of the components to start polymerization, and flow channels were sealed with VALAP (1:1:1 vasoline:lanoline: paraffin). The contributions of KCl and $MgCl_2$ from the septin elution buffer were taken into account to yield the same final composition of actin polymerization buffer. Actin-septin samples were incubated overnight at RT in the dark before observation. To polymerize septins in the absence of actin, we followed the same procedure as above, but replaced the G-actin solution with G-buffer. Septins were used at 20% msfGFP and 20% sfCherry2 molar ratio for wild-type septins and at 100% GFP for SEPT2NC septins.

The sources and identifiers for proteins, materials and chemicals are as follows. Glass slides (26 × 76 mm; AA00000102E01FST20) and glass coverslips (24 × 60 mm; BB02400600A113FST0) from Thermo Scientific. Ammonium hydroxide solution (221228) and hydrogen peroxide solution (95299) from SIGMA. PLL-PEG from SuSoS AG (PLL(20)-g[3.5]-PEG(2)). Rabbit skeletal muscle G-actin from Cytoskeleton, Inc. (AKL99). Alexa Fluor 568-phalloidin from Thermo Fisher Scientific (A12380). Methylcellulose (M0512), Trolox (238813), protocatechuic acid (03930590), protocatechuate 3,4-dioxygenase (P8279) from Sigma-Aldrich.

Confocal fluorescence microscopy of reconstituted actin-septins and image processing

Reconstituted actin-septin assemblies were imaged on the same spinning disk microscope setup described for imaging cells using the same objective lens and camera. Images were acquired with an exposure time of 0.1 s. Actin-septin bundles were imaged close to the surface. Septin filament bundles were also found at the surface, but the clusters of interconnected filament bundles were observed floating in the bulk of the flow channels. To capture such clusters, z-stacks were acquired over 10–50 µm using a Δz interval of 0.5 µm. Images were processed with ImageJ/Fiji. Images of actin-septin bundles are from single planes. Images of septin filament bundles are from maximum-intensity z projections. The contrast of all images shown was adjusted post-acquisition so that both dim and bright structures are visible without saturation. All images use an inverted grayscale, with bright signals appearing black in a white background.

Metal-induced energy transfer assays

U2OS cells were transfected with SEPT9_i3-mApple, SEPT9_i3-mApple-CAAX, or GAP43-mApple with FuGeneHD (E2311; Promega). 16 h post-transfection, cells were plated on glass coverslips (for obtaining reference lifetime measurements, see below) and on gold-coated glass coverslips, previously cleaned with 70% ethanol. Cells were left to attach and spread for 24 h, then fixed for 15 min using 4% paraformaldehyde (15714; Electron Microscopy Sciences) in cytoskeleton buffer (10 mM MES – pH 6.1 with NaOH, 150 mM NaCl, 5 mM EGTA, 5 mM glucose, 5 mM $MgCl_2$). The excess of cytosolic protein content was washed out with a permeabilization/blocking step (0.1% saponin, 1% BSA in PBS) for 1 h at room temperature. Labeling of F-actin in U2OS cells was achieved with AlexaFluor568-phalloidin (A12380; Invitrogen) at 165 nM in permeabilization/blocking solution for 1 h. The samples were maintained in PBS until and throughout the measurements.

Metal-induced energy transfer (MIET) was performed following the concept introduced by Enderlein and coworkers (Chizhik et al., 2014). Briefly, we measured the fluorescence lifetime of emitters in the vicinity of a 18 nm-thick gold film. From the calibration of the fluorescence lifetime dependence with the distance to the gold film (Chizhik et al., 2014), the distance between the fluorophore and the metal is recovered. The MIET calibration curve was computed using the MIET-GUI Matlab code developed by the Enderlein group (https://www.uni-goettingen.de/de/software/532664.html). For mApple, we used a peak emission wavelength at 610 nm and a quantum yield of 49%. For Alexa Fluor 568, the emission peak was 603 nm and the quantum yield 69%. Our calculation used the fluorescence lifetime of the dyes measured on a glass coverslip, in the absence of the metal layer, to account for the slight 0.1 ns lifetime change induced by the functionalization of the dye to septin, GAP43 or phalloidin. An isotropic orientation of the fluorophores is assumed (Chizhik et al., 2014).

Downloaded from http://rupress.org/jcb/article-pdf/222/3/e202203016/1445844/jcb_202203016.pdf by guest on 20 October 2025

We used a gold film of 18 nm thickness deposited by electron-beam assisted evaporation of gold on a borosilicate glass coverslip (Bühler Syrus Pro 710). A 2 nm-thick chromium layer is used to promote the adhesion of gold on the glass coverslip. For the MIET calibration, the refractive indexes of the gold and chromium layers were taken from Rosenblatt et al. (2020) and Johnson and Christy (1974), respectively, while the refractive index of 1.52 for the borosilicate glass coverslip was provided by the supplier (D 263 M glass by Schott AG).

The fluorescence lifetime measurements were performed with a home built confocal microscope with a 557 nm iChrome-TVIS laser (Toptica GmbH, pulse duration 3 ps, 40 MHz repetition rate) and a Zeiss C-Apochromat 63×, 1.2 NA water immersion objective. The excitation power remained below 2 µW on the sample to avoid photobleaching during the measurement. The fluorescence light was collected by the same microscope objective and filtered using a dichroic mirror (ZT 405/488/561/640rpc; Chroma), long-pass filter (ET570LP; Chroma) and bandpass filter (ET595/50 m; Chroma). The confocal pinhole diameter was 50 µm. The photon counting detection used an avalanche photodiode (MPD-5CTC; Picoquant) connected to a time correlated counting module (HydraHarp400; PicoQuant). The temporal resolution (full width at half maximum of the instrument response function) was measured to be 38 ps. The fluorescence lifetime histograms were fitted using SymPhoTime 64 software (PicoQuant GmbH) with a reconvolution taking into account the measured instrument response function. All the histograms were fitted using a biexponential function which provided a better fit to the intensity decay than a single exponential decay. About 20% of the total detected intensity corresponded to the short lifetime component (below 0.5 ns), which was not considered further for the analysis. The MIET distance measurements were taken on the long lifetime component which represented more than 80% of the total detected photons. The distribution of calculated distances from lifetime measurements for each condition is represented in box plots using GraphPad Prism (one data point per cell for each condition). The central mark indicates the median, and the bottom and top edges of the box indicate the 25th and 75th percentiles, respectively. The whiskers extend to the minimum and maximum values. The number of cells per condition is indicated in the respective legend. One-way ANOVA followed by a multiple comparison test was used for comparing the distributions. Data distribution was assumed to be normal, but this was not formally tested.

Supported lipid bilayer assays

Small unilamellar vesicle formation

We used three types of lipids, 1,2-dioleoyl-sn-glycero-3-phospho-(1′-myo-inositol-4′,5′-bisphosphate; ammonium salt; PI(4,5)P_2; 850155P; Sigma-Aldrich), 1,2-dioleoyl-sn-glycero-3-phosphocholine (DOPC; 850375C; Sigma-Aldrich), and 1,2-dioleoyl-sn-glycero-3-phosphoethanolamine-N-(Cyanine 5; DOPE-Cy5; 810335C; Sigma-Aldrich), all from Avanti Polar Lipids. The lipids were mixed in chloroform, or, in case PI(4,5)P_2 was present, in a 20:9:1 chloroform/methanol/water mixture in a glass vial. The organic solvent was then evaporated completely using a stream of N_2 followed by overnight incubation in a dessicator. The dried lipid film was resuspended in buffer to give a total lipid concentration of 0.25 mM. We used a sodium citrate buffer of pH 4.8 (50 mM citrate, made of equal molarity trisodium citrate and citric acid mixed in a 2:3 volume ratio, 50 mM KCl, 0.1 mM ethylenediaminetetraacetic acid) in case PI(4,5)P_2 was present, and otherwise F-buffer of pH 7.4 (20 mM Tris-HCl, 2 mM $MgCl_2$, 50 mM KCl, 1 mM DTT). The lipids were dissolved by four cycles of 1 min vortexing and 5 min incubation. Finally, small unilamellar vesicles (SUVs) were obtained by sonicating the lipid solution using an Ultrasonic homogeniser series HD 2000.2 sonicator equipped with a BR30 cup resonator (Bandelin) at 10% amplitude for 30 min with pulses of 5 s on and 5 s off to avoid excessive heating.

Protein preparation

Unlabeled septin octamers and SEPT2-msfGFP octamers were purified in house as previously reported (Iv et al., 2021). The protein was stored in aliquots in septin storage buffer (20 mM Tris HCl, pH 7.4, 2 mM $MgCl_2$, 300 mM KCl, 1 mM DTT), at −80°C. Before each experiment, unlabeled and labeled septin octamers were mixed in a 9:1 molar ratio in septin storage buffer at a total concentration of 1,800 nM. Lyophilized monomeric actin (G-actin) from rabbit skeletal muscle (8101-03; Hypermol) was resuspended following the manufacturer's instructions and dialyzed against G-buffer (5 mM Tris-HCl, pH 7.8, 0.1 mM $CaCl_2$, 0.2 mM ATP, and 1 mM DTT) to remove residual disaccharides from the freeze-drying process. Protein aggregates were removed by centrifugation at 148,000 × *g* for 1 h and the supernatant was snap-frozen and stored in aliquots at −80°C. Fluorescently tagged G-actin was prepared by covalent modification with Alexa Fluor 594 Carboxylic Acid (15461054; Thermo Fisher Scientific; Alvarado and Koenderink, 2015). Before experiments, G-actin aliquots were thawed, and any aggregates were removed by leaving the protein on ice for at least 2 h and subsequently centrifuging at 148,000 × *g* for 20 min. Unlabeled and fluorescent actin were mixed in a 9:1 molar ratio in G-buffer at a total G-actin concentration of 5 µM.

Sample preparation

Supported lipid bilayers (SLB) were formed in custom-made flow channels made of nr. 1 Menzel coverslips (11961988; Thermo Fisher Scientific) and glass slides (11879022; Thermo Fisher Scientific). The coverslips and glass slides were first cleaned in base piranha solution (5% hydrogen peroxide, 5% ammonium hydroxide) at 70°C for 10 min, extensively washed with Milli-Q water, and stored in Milli-Q water for a maximum of 5 d. Just before use, a coverslip and a slide were dried with a stream of N_2 gas. Flow channels were prepared by sandwiching 2 × 20 mm parafilm strips separated by ∼3 mm between the glass slide and the coverslip. The parafilm was then melted by placing the chambers on a hot plate at 120°C and gently pressing on top with clean tweezers. After cooling down, an SUV solution (7–12 µl, depending on the distance between the parafilm strips) was pipetted into the channels and incubated in a humid chamber for at least 20 min to promote SUV rupture and SLB formation. Residual SUVs were removed by washing with four

Downloaded from http://rupress.org/jcb/article-pdf/222/3/e202203016/1445844/jcb_202203016.pdf by guest on 20 October 2025

channel volumes of F-buffer for DOPC SLBs or with two channel volumes of sodium citrate buffer followed by 2 channel volumes of F-buffer for 5% PI(4,5)P_2 SLBs. DOPC SLBs contained 99.7% DOPC and 0.3% DOPE-Cy5; 5%PIP2 SLBs also contained 94.7% DOPC and 0.3% DOPE-Cy5.

Septin octamers and actin were co-polymerized at room temperature in polymerization buffer (20 mM Tris-HCl, pH 7.4, 2 mM $MgCl_2$, 50 mM KCl, 1 mM DTT, 0.5 mM ATP, 1 mM GTP) supplemented with 1 mM Trolox to suppress blinking, and an oxygen scavenging system composed of 1 mM protocatechuic acid and 0.05 µM of procatechuate 3,4-dioxygenase to minimize photobleaching. We first prepared a 5× master buffer (100 mM Tris HCl, pH 7.4, 10 mM $MgCl_2$, 5 mM DTT, 2.5 mM ATP, 5 mM GTP, 5 mM Trolox and 5 mM protocatechuic acid). To prepare the sample, we mixed the master buffer (fivefold dilution), 0.05 µM of procatechuate 3,4-dioxygenase, the G-actin mix (fivefold dilution to give a final concentration of 1 µM), and the septin mix (sixfold dilution, to give a final concentration of 300 nM), in that order. The mixture was either immediately added to the flow channels containing the SLBs and incubated for 1 h in a humid environment, or first incubated in the tube for 1 h to promote septin-actin bundle formation and then added to the flow channels using a cut pipette tip to minimize bundle disruption. For the sequential addition of septin octamers and actin, first septin octamers were diluted into the polymerization buffer, immediately added to the flow channels, and incubated for ∼30 min in a humid environment. Afterwards, the channels were washed with 1× channel volumes of F-buffer to remove unbound septin octamers; only 1× channel volume is used in this case to minimize disruption of the membrane-bound septin filament mesh. Finally, either pre-polymerized F-actin in polymerization buffer, or G-actin freshly added to polymerization buffer, was flushed into the flow channels with a cut tip to minimize actin filament disruption and incubated for 1 h. The channels were then sealed with Dow Corning high-vacuum silicone grease (Z273554; Sigma-Aldrich) to avoid drying while imaging.

Image acquisition

The samples were immediately imaged using a Nikon Ti2-E microscope complemented with a Gataca iLAS2 azimuthal TIRF illumination system. The sample was illuminated with 488- and 561-nm lasers (Gataca laser combiner iLAS2) to visualize the septin and the actin signals, respectively. The fluorescence signal was split with a Cairn Research Optosplit II ByPass containing a Chroma ZT 543 rdc dichroic mirror and filtered with either a 525/50 or a 600/50 chroma bandpass filter. The images were collected with a Nikon Apo TIRF 100× oil, NA 1.49 objective and recorded with an Andor iXon Ultra 897 EM-CCD camera using an exposure time of 50 ms. To check that the SLBs were uniform and free of defects, we examined DOPE-Cy5 distribution by illuminating with a 642-nm laser filtered with a 708/75 chroma bandpass filter and recorded using an exposure time of 20 ms. We checked SLB fluidity by fluorescence recovery after photobleaching of DOPE-Cy5.

Atomic force microscopy

Sample preparation

Measurements were made on cells plated on Y shape-micropatterned substrates to minimize variability due to size and shape differences among cells (Rigato et al., 2015). 12-mm glass coverslips were coated with 0.1 mg/ml PLL-PEG (PLL[20]-g[3.5]-PEG[2], Susos) before being illuminated with a deep-UV lamp through a quartz-chrome photomask bearing the micropattern features (Front Range Photomask) designed using AutoCAD (Autodesk). We used Y-shaped micropatterns with a spread area of ∼1,500 mm^2. Micropatterned coverslips were then incubated with 25 µg/ml fibronectin and 5 µg/ml fibrinogen-GFP, the latter for visualizing micropatterns. Wild type U2OS cells treated with siLacZ siRNA (6mer + 8mer), with SEPT9 siRNA (6mer), and U2OS cells treated with SEPT7 siRNA and also transfected with msfGFP-SEPT7Gmut2 (8mer) were seeded on fibronectin-coated micropatterns 48 h post-electroporation. Cells were incubated for 5–7 h to attach and spread adopting a triangular shape. The expression of msfGFP-SEPT7Gmut2 for the 8mer condition was confirmed through the detection of fluorescence in each measured cell.

Force spectroscopy experiments and data analysis

Atomic force microscopy-force spectroscopy (AFM-FS) was performed on the dorsal perinuclear region of individual cells at room temperature. We used a MLCT-Bio-DC (D) cantilever featuring a four-sided regular pyramid with a semi-open angle of 35°. The spring constant of the cantilevers was determined in air using the Sader method (Sader et al., 2012) and the optical lever sensitivity from the thermal spectrum in liquid (Sumbul et al., 2020). Force-distance curves were acquired applying a maximum force of 0.8 nN with a ramp range of 5 µm, at the same approach and retract velocity of 5 µm/s on a Nanowizard 4 AFM microscope (JPK-Bruker). The indentation depth was on the order of 1 µm. 31 cells, 29 cells, and 23 cells were probed for the 6mer + 8mer, 6mer, and 8mer condition, respectively. For each cell, about 15–30 force curves were acquired across three different contact points, resulting in a total of 576, 630, and 501 force curves for the 6mer + 8mer, 6mer, and 8mer condition, respectively. To extract the cell viscoelastic properties, we fitted the Ting numerical viscoelastic model for a four-sided regular pyramidal tip of semi-open angle (theta) to the experimental force-distance curves (Bilodeau, 1992; Efremov et al., 2017):

$$F(t,\delta(t)) = \begin{cases} \frac{3\tan\theta}{4(1-\nu^2)}\int_0^t E(t-\tau)\frac{\partial\delta^2}{\partial\tau}d\tau, 0 \le t \le t_m \\ \frac{3\tan\theta}{4(1-\nu^2)}\int_0^{t_1} E(t-\tau)\frac{\partial\delta^2}{\partial\tau}d\tau, t_m \le t \le t_{ind} \end{cases}$$

where F is the applied force; δ is the indentation; t is the time since initial contact, t_m is the duration of approach trace, t_{ind} is the duration of complete indentation cycle, and t_1 determined by solving the equation

$$\int_{t_1(t)}^{t} E(t-\tau)\frac{\partial\delta(t)}{\partial\tau}d\tau = 0$$

We assumed that the time-dependent Young's modulus followed a power law relationship:

$$E(t) = E_0\left(\frac{t}{t_0}\right)^{-\beta}$$

Downloaded from http://rupress.org/jcb/article-pdf/222/3/e202203016/1445844/jcb_202203016.pdf by guest on 20 October 2025

where E_0 is the elastic modulus at time t_0, β is the fluidity of the cell and t_0 is the reference time, arbitrarily assumed 1 s. A viscous drag force (F_d) proportional to the trace velocity (v) was also added to the force traces using a precalibrated value of the viscous drag coefficient (b = 5 pN s/µm), $F_d = b \cdot v$.

The values of $\log_{10}(E_0)$ and β extracted from each force measurement were pooled by cell and then averaged. The data was reproduced in three independent experiments and their distribution represented in box plots using GraphPad Prism (one data point per cell for each condition). The central mark indicates the median, and the bottom and top edges of the box indicate the 25th and 75th percentiles, respectively. The whiskers extend to the minimum and maximum values. The number of cells per condition is indicated in the respective legend. E_0 values (in Pa) were plotted on a log scale. One-way ANOVA followed by a multiple comparison test was used for comparing the distributions of E_0 values using the $\log_{10}(E_0)$ values, given the log-normal distribution of E_0.

Single particle tracking Photo-activated localization microscopy (sptPALM)

Cell culture

Mouse embryonic fibroblasts were cultured in DMEM (10313-021; Gibco) with 10% fetal calf serum (FCS, CVFSVF00-01; Eurobio scientific). Transient transfections of plasmids were performed 2 d before experiments using the Amaxa nucleofector (VPD-1004; Lonza). The cells were detached with trypsin/EDTA, the trypsin was inactivated using DMEM with 10% FCS, and the cells were washed and suspended in serum-free Ringer solution (150 mM NaCl, 5 mM KCl, 2 mM $CaCl_2$, 2 mM $MgCl_2$, 10 mM HEPES-Na pH 7.4, 2 g/liter glucose), then incubated for 30 min in Ringer solution before plating on fibronectin-coated glass coverslips (human plasma fibronectin at 10 µg/ml, 10838039001; Roche).

Plasmids

SEPT9_i3-mEos3.2 and SEPT9_i3-mEos3.2-CAAX were cloned in a pCMV plasmid backbone with seamless cloning into a NheI/BamHI linearized vector (primers in Table S1). EGFP-human β-actin was provided by A. Matus (Friedrich Miescher Institute for Biomedical Research, Switzerland). The mEos2-actin construct was generated from EGFP-actin as described in Rossier et al. (2012). EYFP-human paxillin (isoform alpha) was used as described in Rossier et al. (2012).

Optical setup and image acquisition

sptPALM acquisitions were steered by MetaMorph software (Molecular Devices) with an inverted motorized microscope (Nikon Ti) equipped with a temperature control system (The Cube, The Box, Life Imaging Services), a Nikon CFI Apo TIRF 100× oil, NA 1.49 objective and a Perfect Focus System, allowing long acquisition in TIRF illumination mode.

Imaging was performed at least 3 h after seeding the cells on fibronectin-coated coverslips mounted in a Ludin chamber (Life Imaging Services). For photoactivation localization microscopy, cells expressing mEos2 and mEos3.2 tagged constructs were photoactivated using a 405 nm laser (Omicron) and the resulting photoconverted single molecule fluorescence was excited with a 561 nm laser (Cobolt Jive). Both lasers illuminated the sample simultaneously. Their respective power was adjusted to keep the number of the stochastically activated molecules constant and well separated during the acquisition. Fluorescence was collected by the combination of a dichroic and emission filters (D101-R561 and F39-617 respectively, Chroma) and a sensitive EMCCD (electron-multiplying charge-coupled device, Evolve, Photometric). The acquisition was performed in streaming mode at 50 Hz. Either EYFP-paxillin or GFP-actin were imaged using a conventional GFP filter cube (ET470/40, T495LPXR, ET525/50; Chroma). Using this filter cube does not allow spectral separation of the unconverted pool of mEos from the GFP fluorescent signal. However, with all of the constructs used, whether the mEos signal was highly or poorly enriched in FAs, we were still able to detect FAs.

Single molecule segmentation and tracking

A typical sptPALM experiment leads to a set of at least 4,000 images per cell, analyzed in order to extract molecule localization and dynamics. Single molecule fluorescent spots were localized and tracked over time using a combination of wavelet segmentation and simulated annealing algorithms (Izeddin et al., 2012; Racine et al., 2006; Racine et al., 2007). Under the experimental conditions described above, the resolution of the system was quantified to 59 nm (Full Width at Half Maximum, FWHM). This spatial resolution depends on the image signal to noise ratio and the segmentation algorithm (Cheezum et al., 2001) and was determined using fixed mEos2 samples. We analyzed 130 2D distributions of single molecule positions belonging to long trajectories (>50 frames) by bi-dimensional Gaussian fitting, the resolution being determined as 2.3 s_{xy}, where s_{xy} is the pointing accuracy.

For the trajectory analysis, FAs ROIs were identified manually from EYFP-paxillin or GFP-actin images. The corresponding binary mask was used to sort single-molecule data analyses to specific regions. We analyzed trajectories lasting at least 260 ms (≥13 points) with a custom Matlab routine analyzing the mean squared displacement (MSD), which describes the diffusion properties of a molecule, computed as (Eq. 1):

$$MSD(t = n\Delta t) = \frac{\sum_{i=1}^{N-n}(x_{i+n} - x_i)^2 + (y_{i+n} - y_i)^2}{N - n} \quad (1)$$

where x_i and y_i are the coordinates of the label position at time $I \times \Delta t$. We defined the measured diffusion coefficient D as the slope of the affine regression line fitted to the n = 1–4 values of the MSD($n \times \Delta t$). The MSD was computed then fitted on a duration equal to 80% (minimum of 10 points, 200 ms) of the whole stretch by (Eq. 2):

$$MSD(t) = \frac{4r_{conf}^2}{3}(1 - e^{-t/\tau}) \quad (2)$$

where r_{conf} is the measured confinement radius and τ the time constant $\tau = (r_{conf}^2/3D_{conf})$. To reduce the inaccuracy of the MSD fit due to downsampling for larger time intervals, we used a weighted fit. Trajectories were sorted in three groups: immobile, confined diffusion, and free diffusion. Immobile trajectories

Downloaded from http://rupress.org/jcb/article-pdf/222/3/e202203016/1445844/jcb_202203016.pdf by guest on 20 October 2025

were defined as trajectories with $D < 0.011\ \mu m^2.s^{-1}$, corresponding to molecules which explored an area inferior to the one defined by the image spatial resolution $\sim(0.05\ \mu m)^2$ during the time used to fit the initial slope of the MSD (Rossier et al., 2012; four points, 80 ms): $D_{threshold}=(0.059\ \mu m)^2/(4 \times 4 \times 0.02\ s)\sim 0.011\ \mu m^2.s^{-1}$. To separate trajectories displaying free diffusion from confined diffusion, we used the time constant calculated τ for each trajectory. Confined and free diffusion events were defined as trajectories with a time constant respectively inferior and superior to half the time interval used to compute the MSD (100 ms). Statistical significance tests were prepared using GraphPad Prism.

Modeling of human septin complexes

Models of full-length human septin complexes were built for analyzing and interpreting split-GFP experiments. The septin GTP-binding domains (GBDs) used as templates for the SEPT2, 6 and 7 models using SWISS-MODEL homology modeling software (Waterhouse et al., 2018) were from PDB accession no. 7M6J (Leonardo et al., 2021), the most complete human septin hexamer structure to date, which includes α0 helices for SEPT6 and 7. As solved in its integrity, the SEPT6 GBD remained unchanged and was used as is. The SEPT7 GBD structure was completed using SWISS-MODEL. As the use of the SEPT2 GBD from 7 M6J for modeling SEPT2 led to clashes in the modeled SEPT2-SEPT2 NC interface, the SEPT2 GBD subunit was modeled using the SEPT7 GBD structure from 7 M6J as a template. The lack of structural information for the short N-terminal extensions of SEPT2, 6, and 7 prompted us to model them as disordered segments using Phyre2 (Kelley et al., 2015). The C-terminal domains of SEPT2, 6, and 7 were modeled with CCFold (Guzenko and Strelkov, 2018) for the coiled–coil (CC) parts and Phyre2 for the flexible parts, as detailed in Iv et al. (2021). The homodimeric parallel SEPT2CC was used unaltered with respect to Iv et al. (2021). The previously modeled SEPT6 and 7 helices in the SEPT6-SEPT7 parallel coiled–coil in Iv et al. (2021) were repositioned slightly after comparison with the only parallel septin CC structure to date (PDB accession no. 6WCU; Leonardo et al., 2021). GBDs, N- and C-terminal extensions were then combined with PyMOL open-source software. When necessary, the disordered segments were manually modified to avoid steric clashes and to adjust distances. The SEPT9_i3 model used was the one built for (Iv et al., 2021) and included already N- and C-terminal extensions. Hexameric SEPT2-SEPT6-SEPT7-SEPT7-SEPT6-SEPT2 and octameric SEPT2-SEPT6-SEPT7-SEPT9-SEPT9-SEPT7-SEPT6-SEPT2 complexes were built by fitting the modeled structures to the hexamer from the PDB accession no. 7M6J.

To analyze and interpret the split-GFP experiments, the entire constructs used in the assays, including β10- and β11-tagged septins and the reconstituted GFP, were modeled. To this aim, the split GFP structure (PDB accession no. 4KF5) was added to the modeled septin complexes. The flexible linkers linking the reconstituted GFP to the septin of interest were built manually using PyMOL; their straight-ish appearance in the models is due to the polypeptide chains being built as linear structures. To mimic paired septin filaments with narrow spacing (Leonardo et al., 2021), mediated by homodimeric SEPT2 antiparallel CCs (Fig. 5 H), septin complexes were duplicated and placed parallel to each other with a gap of ∼5 nm. The bent conformation of the septin was built by rotating the CC domain manually by 90° relative to the GBD. The helices within the homodimeric SEPT2 antiparallel CC were positioned using the antiparallel SEPT4CC structure from PDB accession no. 6WB3 as a reference (Leonardo et al., 2021). All manual interventions were realized using PyMOL.

Statistics and reproducibility

The distributions of measurements, or of phenotypes in the case of septin mutant characterization, are represented with GraphPad Prism using box plots, violin plots, and scatter dot plots as indicated in the respective methods sections and legends. Bars, error bars (SD or SEM), and box plot features are as indicated in the respective figure legends. The number of measurements in each plot and the numbers of experiments are indicated in the respective figure legend or methods. Statistical significance tests were performed with GraphPad Prism. The tests applied and the obtained P values are mentioned in the respective figure legend. Experiments were repeated at least three times independently to ensure reproducibility. Experiments from Fig. 1 F, Fig. 2, C and D; Fig. 10, C–F, Fig. 10 H; Fig. S3, B and C; and Fig. S5, I–K were performed twice. Experiments from Fig. 10, G and I were performed once. No data were excluded from the analyses.

Online supplemental material

Fig. S1 shows examples of SEPT2, SEPT7, and SEPT9 distribution in cells from immunostainings and live imaging of GFP fusions. Fig. S2 contains details on the design of the tripartite split-GFP complementation assay for probing septin organization. Fig. S3 depicts the mutants used in this study, as well as examples of cell-free reconstitution of actin-septin assembly. Fig. S4 contains data that support that all septins on microtubules organize as octamer-based filaments. Fig. S5 contains data that support that septin filaments can mediate actin-membrane anchoring in the absence of myosin-II. Table S1 shows oligonucleotide primer sequences used for the generation of the plasmids used in this study.

Data availability

All data supporting the findings of this study are available within the article and its supporting information files. The source datasets generated and analyzed during the current study are available from the corresponding author on reasonable request. The source codes for the custom-generated Matlab codes for measurements of fiber diameter (FWHM) and length, and for numerical simulations of expected fiber diameter (FWHM) from SIM images has been deposited to Github. The respective links are mentioned in the relevant Materials and methods sections.

Acknowledgments

We thank Josette Perrier and Cendrine Nicoletti (iSm2) for hosting protein purification. The authors thank Artemis Kosta, Hugo Le Guenno and the Microscopy Core Facility of IMM for

Downloaded from http://rupress.org/jcb/article-pdf/222/3/e202203016/1445844/jcb_202203016.pdf by guest on 20 October 2025

SIM microscopy. We thank R. Sterling for technical assistance and the IINS Cell culture facility, especially E. Verdier and N. Retailleau for technical help (IINS Cell Biology Facility, grant no. ANR-10-LABX-43). We also thank J.B. Sibarita (IINS) for support with sptPALM analysis.

This research received funding from the Agence Nationale de la Recherche (ANR grants ANR-17-CE13-0014 SEPTIMORF to M. Mavrakis; ANR-17-CE09-0026-01 AntennaFRET to J. Wenger; ANR-20-CE42-0003 3DPolariSR to V. Milanović and O. Rossier), the Fondation ARC pour la recherche sur le cancer (grant ARCDOC42020010001242 to C.S. Martins), and from the Cancéropôle PACA, Institut National du Cancer and Conseil Régional PACA (Bourse mobilité to M. Mavrakis). We further acknowledge financial support from the French Ministry of Research, CNRS and the Conseil Régional Nouvelle-Aquitaine (grant MechanoStem to O. Rossier and V. Milanović). We acknowledged the France-BioImaging infrastructure supported by the French National Research Agency (ANR-10-INBS-04). This project has received funding from the European Research Council (ERC) under the European Union's Horizon 2020 research and innovation program (grant agreements No. 723241 to J. Wenger and No. 772257 to F. Rico). This project has received funding from the European Union's Horizon 2020 research and Innovation program under the H2020-MSCA-ITN-2018 Grant Agreement n. 812772. This work was supported in part by the National Institutes of Health (R01GM122375 to S. Kumar). Confocal microscopy with the Zeiss LSM710 microscope and SIM with the Zeiss Elyra PS.1 microscope was performed at the UC Berkeley Biological Imaging Facility, which was supported in part by the National Institutes of Health S10 program under award numbers 1S10RR026866-01 and 1S10OD018136-01. G. Castro-Linares and G.H. Koenderink gratefully acknowledge financial support by the Netherlands Organization for Scientific Research (NWO/OCW) through the "BaSyC—Building a Synthetic Cell" Gravitation grant (024.003.019).

Author contributions: C.S. Martins: investigation, conceptualization, methodology, funding acquisition, writing—original draft, writing—review & editing; C. Taveneau, G. Castro-Linares: investigation, writing—original draft, writing—review & editing; M. Baibakov, N. Buzhinsky, M. Eroles, V. Milanović, S. Omi, J.-D. Pedelacq, F. Iv, L. Bouillard, A. Llewellyn, M. Gomes, M. Belhabib, M. Kuzmić, S. Lee: investigation; P. Verdier-Pinard, A. Badache: investigation, writing—review & editing; S. Kumar: supervision, funding acquisition, resources; C. Chandre: software; S. Brasselet: software, writing—original draft; F. Rico: supervision, funding acquisition, writing—original draft, writing—review & editing; O. Rossier, J. Wenger: investigation, supervision, funding acquisition, writing—original draft; G.H. Koenderink: supervision, funding acquisition, writing—review & editing; S. Cabantous, M. Mavrakis: investigation, conceptualization, methodology, funding acquisition, project administration, supervision, writing—original draft, writing—review & editing.

Disclosures: The authors declare no competing interests exist.

Submitted: 4 March 2022
Revised: 20 October 2022
Accepted: 1 December 2022

References

Adam, J.C., J.R. Pringle, and M. Peifer. 2000. Evidence for functional differentiation among Drosophila septins in cytokinesis and cellularization. *Mol. Biol. Cell.* 11:3123–3135. https://doi.org/10.1091/mbc.11.9.3123

Alvarado, J., and G.H. Koenderink. 2015. Reconstituting cytoskeletal contraction events with biomimetic actin-myosin active gels. *Methods Cell Biol.* 128:83–103. https://doi.org/10.1016/bs.mcb.2015.02.001

Bertin, A., M.A. McMurray, P. Grob, S.S. Park, G. Garcia III, I. Patanwala, H.L. Ng, T. Alber, J. Thorner, and E. Nogales. 2008. Saccharomyces cerevisiae septins: Supramolecular organization of heterooligomers and the mechanism of filament assembly. *Proc. Natl. Acad. Sci. USA.* 105: 8274–8279. https://doi.org/10.1073/pnas.0803330105

Bertin, A., M.A. McMurray, J. Pierson, L. Thai, K.L. McDonald, E.A. Zehr, G. García III, P. Peters, J. Thorner, and E. Nogales. 2012. Three-dimensional ultrastructure of the septin filament network in Saccharomyces cerevisiae. *Mol. Biol. Cell.* 23:423–432. https://doi.org/10.1091/mbc.e11-10-0850

Bertin, A., M.A. McMurray, L. Thai, G. Garcia III, V. Votin, P. Grob, T. Allyn, J. Thorner, and E. Nogales. 2010. Phosphatidylinositol-4,5-bisphosphate promotes budding yeast septin filament assembly and organization. *J. Mol. Biol.* 404:711–731. https://doi.org/10.1016/j.jmb.2010.10.002

Bilodeau, G.G. 1992. Regular pyramid punch problem. *J. Appl. Mech.* 59: 519–523. https://doi.org/10.1115/1.2893754

Bolte, S., and F.P. Cordelières. 2006. A guided tour into subcellular colocalization analysis in light microscopy. *J Microsc.* 224:213–232. https://doi.org/10.1111/j.1365-2818.2006.01706.x

Bridges, A.A., M.S. Jentzsch, P.W. Oakes, P. Occhipinti, and A.S. Gladfelter. 2016. Micron-scale plasma membrane curvature is recognized by the septin cytoskeleton. *J. Cell Biol.* 213:23–32. https://doi.org/10.1083/jcb.201512029

Brognara, G., H.D. Pereira, J. Brandão-Neto, A.P.U. Araujo, and R.C. Garratt. 2019. Revisiting SEPT7 and the slippage of β-strands in the septin family. *J. Struct. Biol.* 207:67–73. https://doi.org/10.1016/j.jsb.2019.04.015

Byers, B., and L. Goetsch. 1976. A highly ordered ring of membrane-associated filaments in budding yeast. *J. Cell Biol.* 69:717–721. https://doi.org/10.1083/jcb.69.3.717

Cabantous, S., H.B. Nguyen, J.D. Pedelacq, F. Koraïchi, A. Chaudhary, K. Ganguly, M.A. Lockard, G. Favre, T.C. Terwilliger, and G.S. Waldo. 2013. A new protein-protein interaction sensor based on tripartite split-GFP association. *Sci. Rep.* 3:2854. https://doi.org/10.1038/srep02854

Cai, Y., O. Rossier, N.C. Gauthier, N. Biais, M.A. Fardin, X. Zhang, L.W. Miller, B. Ladoux, V.W. Cornish, and M.P. Sheetz. 2010. Cytoskeletal coherence requires myosin-IIA contractility. *J. Cell Sci.* 123:413–423. https://doi.org/10.1242/jcs.058297

Calvo, F., R. Ranftl, S. Hooper, A.J. Farrugia, E. Moeendarbary, A. Bruckbauer, F. Batista, G. Charras, and E. Sahai. 2015. Cdc42EP3/BORG2 and septin network enables mechano-transduction and the emergence of cancer-associated fibroblasts. *Cell Rep.* 13:2699–2714. https://doi.org/10.1016/j.celrep.2015.11.052

Cao, L., X. Ding, W. Yu, X. Yang, S. Shen, and L. Yu. 2007. Phylogenetic and evolutionary analysis of the septin protein family in metazoan. *FEBS Lett.* 581:5526–5532. https://doi.org/10.1016/j.febslet.2007.10.032

Cavini, I.A., D.A. Leonardo, H.V.D. Rosa, D.K.S.V. Castro, H. D'Muniz Pereira, N.F. Valadares, A.P.U. Araujo, and R.C. Garratt. 2021. The structural Biology of septins and their filaments: An update. *Front. Cell Dev. Biol.* 9: 765085. https://doi.org/10.3389/fcell.2021.765085

Cheezum, M.K., W.F. Walker, and W.H. Guilford. 2001. Quantitative comparison of algorithms for tracking single fluorescent particles. *Biophys. J.* 81:2378–2388. https://doi.org/10.1016/S0006-3495(01)75884-5

Chizhik, A.I., J. Rother, I. Gregor, A. Janshoff, and J. Enderlein. 2014. Metal-induced energy transfer for live cell nanoscopy. *Nat. Photonics.* 8: 124–127. https://doi.org/10.1038/nphoton.2013.345

Chowdhury, F., B. Huang, and N. Wang. 2021. Cytoskeletal prestress: The cellular hallmark in mechanobiology and mechanomedicine. *Cytoskeleton.* 78:249–276. https://doi.org/10.1002/cm.21658

Connolly, D., Z. Yang, M. Castaldi, N. Simmons, M.H. Oktay, S. Coniglio, M.J. Fazzari, P. Verdier-Pinard, and C. Montagna. 2011. Septin 9 isoform expression, localization and epigenetic changes during human and mouse breast cancer progression. *Breast Cancer Res.* 13:R76. https://doi.org/10.1186/bcr2924

de Almeida Marques, I., N.F. Valadares, W. Garcia, J.C. Damalio, J.N. Macedo, A.P. de Araújo, C.A. Botello, J.M. Andreu, and R.C. Garratt. 2012. Septin C-terminal domain interactions: Implications for filament stability and assembly. *Cell Biochem. Biophys.* 62:317–328. https://doi.org/10.1007/s12013-011-9307-0

Downloaded from http://rupress.org/jcb/article-pdf/222/3/e202203016/1445844/jcb_202203016.pdf by guest on 20 October 2025

DeRose, B.T., R.S. Kelley, R. Ravi, B. Kokona, J. Beld, E.T. Spiliotis, and S.B. Padrick. 2020. Production and analysis of a mammalian septin hetero-octamer complex. *Cytoskeleton*. 77:485–499. https://doi.org/10.1002/cm.21643

Dolat, L., J.L. Hunyara, J.R. Bowen, E.P. Karasmanis, M. Elgawly, V.E. Galkin, and E.T. Spiliotis. 2014. Septins promote stress fiber-mediated maturation of focal adhesions and renal epithelial motility. *J. Cell Biol.* 207: 225–235. https://doi.org/10.1083/jcb.201405050

Dolat, L., and E.T. Spiliotis. 2016. Septins promote macropinosome maturation and traffic to the lysosome by facilitating membrane fusion. *J. Cell Biol.* 214:517–527. https://doi.org/10.1083/jcb.201603030

Echard, A., G.R. Hickson, E. Foley, and P.H. O'Farrell. 2004. Terminal cytokinesis events uncovered after an RNAi screen. *Curr. Biol.* 14:1685–1693. https://doi.org/10.1016/j.cub.2004.08.063

Efremov, Y.M., W.H. Wang, S.D. Hardy, R.L. Geahlen, and A. Raman. 2017. Measuring nanoscale viscoelastic parameters of cells directly from AFM force-displacement curves. *Sci. Rep.* 7:1541. https://doi.org/10.1038/s41598-017-01784-3

Estey, M.P., C. Di Ciano-Oliveira, C.D. Froese, M.T. Bejide, and W.S. Trimble. 2010. Distinct roles of septins in cytokinesis: SEPT9 mediates midbody abscission. *J. Cell Biol.* 191:741–749. https://doi.org/10.1083/jcb.201006031

Fares, H., M. Peifer, and J.R. Pringle. 1995. Localization and possible functions of Drosophila septins. *Mol. Biol. Cell*. 6:1843–1859. https://doi.org/10.1091/mbc.6.12.1843

Farkasovsky, M., P. Herter, B. Voss, and A. Wittinghofer. 2005. Nucleotide binding and filament assembly of recombinant yeast septin complexes. *Biol. Chem.* 386:643–656. https://doi.org/10.1515/BC.2005.075

Farrugia, A.J., J. Rodríguez, J.L. Orgaz, M. Lucas, V. Sanz-Moreno, and F. Calvo. 2020. CDC42EP5/BORG3 modulates SEPT9 to promote actomyosin function, migration, and invasion. *J. Cell Biol.* 219:e201912159. https://doi.org/10.1083/jcb.201912159

Field, C.M., O. al-Awar, J. Rosenblatt, M.L. Wong, B. Alberts, and T.J. Mitchison. 1996. A purified Drosophila septin complex forms filaments and exhibits GTPase activity. *J. Cell Biol.* 133:605–616. https://doi.org/10.1083/jcb.133.3.605

Finger, F.P., K.R. Kopish, and J.G. White. 2003. A role for septins in cellular and axonal migration in C. elegans. *Dev. Biol.* 261:220–234. https://doi.org/10.1016/S0012-1606(03)00296-3

Founounou, N., N. Loyer, and R. Le Borgne. 2013. Septins regulate the contractility of the actomyosin ring to enable adherens junction remodeling during cytokinesis of epithelial cells. *Dev. Cell*. 24:242–255. https://doi.org/10.1016/j.devcel.2013.01.008

Frazier, J.A., M.L. Wong, M.S. Longtine, J.R. Pringle, M. Mann, T.J. Mitchison, and C. Field. 1998. Polymerization of purified yeast septins: Evidence that organized filament arrays may not be required for septin function. *J. Cell Biol.* 143:737–749. https://doi.org/10.1083/jcb.143.3.737

Füchtbauer, A., L.B. Lassen, A.B. Jensen, J. Howard, A.S. Quiroga, S. Warming, A.B. Sørensen, F.S. Pedersen, and E.M. Füchtbauer. 2011. Septin9 is involved in septin filament formation and cellular stability. *Biol. Chem.* 392:769–777. https://doi.org/10.1515/BC.2011.088

Garcia, G., III, A. Bertin, Z. Li, Y. Song, M.A. McMurray, J. Thorner, and E. Nogales. 2011. Subunit-dependent modulation of septin assembly: Budding yeast septin Shs1 promotes ring and gauze formation. *J. Cell Biol.* 195:993–1004. https://doi.org/10.1083/jcb.201107123

Gilden, J.K., S. Peck, Y.C. Chen, and M.F. Krummel. 2012. The septin cytoskeleton facilitates membrane retraction during motility and blebbing. *J. Cell Biol.* 196:103–114. https://doi.org/10.1083/jcb.201105127

Guzenko, D., and S.V. Strelkov. 2018. CCFold: Rapid and accurate prediction of coiled-coil structures and application to modelling intermediate filaments. *Bioinformatics*. 34:215–222. https://doi.org/10.1093/bioinformatics/btx551

Hagiwara, A., Y. Tanaka, R. Hikawa, N. Morone, A. Kusumi, H. Kimura, and M. Kinoshita. 2011. Submembranous septins as relatively stable components of actin-based membrane skeleton. *Cytoskeleton*. 68:512–525. https://doi.org/10.1002/cm.20528

Hamel, V., P. Guichard, M. Fournier, R. Guiet, I. Flückiger, A. Seitz, and P. Gönczy. 2014. Correlative multicolor 3D SIM and STORM microscopy. *Biomed. Opt. Express*. 5:3326–3336. https://doi.org/10.1364/BOE.5.003326

Hartwell, L.H. 1971. Genetic control of the cell division cycle in yeast. IV. Genes controlling bud emergence and cytokinesis. *Exp. Cell Res.* 69: 265–276. https://doi.org/10.1016/0014-4827(71)90223-0

Hartwell, L.H., J. Culotti, and B. Reid. 1970. Genetic control of the cell-division cycle in yeast. I. Detection of mutants. *Proc. Natl. Acad. Sci. USA*. 66: 352–359. https://doi.org/10.1073/pnas.66.2.352

Hickson, G.R., and P.H. O'Farrell. 2008. Rho-dependent control of anillin behavior during cytokinesis. *J. Cell Biol.* 180:285–294. https://doi.org/10.1083/jcb.200709005

Hsu, S.C., C.D. Hazuka, R. Roth, D.L. Foletti, J. Heuser, and R.H. Scheller. 1998. Subunit composition, protein interactions, and structures of the mammalian brain sec6/8 complex and septin filaments. *Neuron*. 20:1111–1122. https://doi.org/10.1016/S0896-6273(00)80493-6

Huijbregts, R.P., A. Svitin, M.W. Stinnett, M.B. Renfrow, and I. Chesnokov. 2009. Drosophila Orc6 facilitates GTPase activity and filament formation of the septin complex. *Mol. Biol. Cell*. 20:270–281. https://doi.org/10.1091/mbc.e08-07-0754

Ihara, M., A. Kinoshita, S. Yamada, H. Tanaka, A. Tanigaki, A. Kitano, M. Goto, K. Okubo, H. Nishiyama, O. Ogawa, et al. 2005. Cortical organization by the septin cytoskeleton is essential for structural and mechanical integrity of mammalian spermatozoa. *Dev. Cell*. 8:343–352. https://doi.org/10.1016/j.devcel.2004.12.005

Iv, F., C.S. Martins, G. Castro-Linares, C. Taveneau, P. Barbier, P. Verdier-Pinard, L. Camoin, S. Audebert, F.C. Tsai, L. Ramond, et al. 2021. Insights into animal septins using recombinant human septin octamers with distinct SEPT9 isoforms. *J. Cell Sci.* 134:jcs258484. https://doi.org/10.1242/jcs.258484

Izeddin, I., J. Boulanger, V. Racine, C.G. Specht, A. Kechkar, D. Nair, A. Triller, D. Choquet, M. Dahan, and J.B. Sibarita. 2012. Wavelet analysis for single molecule localization microscopy. *Opt. Express*. 20:2081–2095. https://doi.org/10.1364/OE.20.002081

Joberty, G., R.R. Perlungher, P.J. Sheffield, M. Kinoshita, M. Noda, T. Haystead, and I.G. Macara. 2001. Borg proteins control septin organization and are negatively regulated by Cdc42. *Nat. Cell Biol.* 3:861–866. https://doi.org/10.1038/ncb1001-861

John, C.M., R.K. Hite, C.S. Weirich, D.J. Fitzgerald, H. Jawhari, M. Faty, D. Schläpfer, R. Kroschewski, F.K. Winkler, T. Walz, et al. 2007. The Caenorhabditis elegans septin complex is nonpolar. *EMBO J.* 26: 3296–3307. https://doi.org/10.1038/sj.emboj.7601775

Johnson, P.B., and R.W. Christy. 1974. Optical constants of transition metals: Ti, V, Cr, Mn, Fe, Co, Ni, and Pd. *Phys. Rev. B Solid State*. 9:5056–5070. https://doi.org/10.1103/PhysRevB.9.5056

Joo, E., M.C. Surka, and W.S. Trimble. 2007. Mammalian SEPT2 is required for scaffolding nonmuscle myosin II and its kinases. *Dev. Cell*. 13: 677–690. https://doi.org/10.1016/j.devcel.2007.09.001

Kage, F., M. Vicente-Manzanares, B.C. McEwan, A.N. Kettenbach, and H.N. Higgs. 2022. Myosin II proteins are required for organization of calcium-induced actin networks upstream of mitochondrial division. *Mol. Biol. Cell*. 33:ar63. https://doi.org/10.1091/mbc.E22-01-0005

Kang, N., T.S. Matsui, S. Liu, and S. Deguchi. 2021. ARHGAP4-SEPT2-SEPT9 complex enables both up- and down-modulation of integrin-mediated focal adhesions, cell migration, and invasion. *Mol. Biol. Cell*. 32:ar28. https://doi.org/10.1091/mbc.E21-01-0010

Karlsson, M., C. Zhang, L. Méar, W. Zhong, A. Digre, B. Katona, E. Sjöstedt, L. Butler, J. Odeberg, P. Dusart, et al. 2021. A single-cell type transcriptomics map of human tissues. *Sci. Adv.* 7:eabh2169. https://doi.org/10.1126/sciadv.abh2169

Kechad, A., S. Jananji, Y. Ruella, and G.R. Hickson. 2012. Anillin acts as a bifunctional linker coordinating midbody ring biogenesis during cytokinesis. *Curr. Biol.* 22:197–203. https://doi.org/10.1016/j.cub.2011.11.062

Kelley, L.A., S. Mezulis, C.M. Yates, M.N. Wass, and M.J. Sternberg. 2015. The Phyre2 web portal for protein modeling, prediction and analysis. *Nat. Protoc.* 10:845–858. https://doi.org/10.1038/nprot.2015.053

Kim, M.S., C.D. Froese, M.P. Estey, and W.S. Trimble. 2011. SEPT9 occupies the terminal positions in septin octamers and mediates polymerization-dependent functions in abscission. *J. Cell Biol.* 195:815–826. https://doi.org/10.1083/jcb.201106131

Kim, M.S., C.D. Froese, H. Xie, and W.S. Trimble. 2012. Uncovering principles that control septin-septin interactions. *J. Biol. Chem.* 287:30406–30413. https://doi.org/10.1074/jbc.M112.387464

Kim, S.K., A. Shindo, T.J. Park, E.C. Oh, S. Ghosh, R.S. Gray, R.A. Lewis, C.A. Johnson, T. Attie-Bittach, N. Katsanis, and J.B. Wallingford. 2010. Planar cell polarity acts through septins to control collective cell movement and ciliogenesis. *Science*. 329:1337–1340. https://doi.org/10.1126/science.1191184

Kinoshita, M. 2003. Assembly of mammalian septins. *J. Biochem.* 134:491–496. https://doi.org/10.1093/jb/mvg182

Kinoshita, M., C.M. Field, M.L. Coughlin, A.F. Straight, and T.J. Mitchison. 2002. Self- and actin-templated assembly of Mammalian septins. *Dev. Cell*. 3:791–802. https://doi.org/10.1016/S1534-5807(02)00366-0

Kinoshita, M., S. Kumar, A. Mizoguchi, C. Ide, A. Kinoshita, T. Haraguchi, Y. Hiraoka, and M. Noda. 1997. Nedd5, a mammalian septin, is a novel

Downloaded from http://rupress.org/jcb/article-pdf/222/3/e202203016/1445844/jcb_202203016.pdf by guest on 20 October 2025

cytoskeletal component interacting with actin-based structures. *Genes Dev.* 11:1535–1547. https://doi.org/10.1101/gad.11.12.1535

Kissel, H., M.M. Georgescu, S. Larisch, K. Manova, G.R. Hunnicutt, and H. Steller. 2005. The Sept4 septin locus is required for sperm terminal differentiation in mice. *Dev. Cell.* 8:353–364. https://doi.org/10.1016/j.devcel.2005.01.021

Koraïchi, F., R. Gence, C. Bouchenot, S. Grosjean, I. Lajoie-Mazenc, G. Favre, and S. Cabantous. 2018. High-content tripartite split-GFP cell-based assays to screen for modulators of small GTPase activation. *J. Cell Sci.* 131:jcs210419. https://doi.org/10.1242/jcs.210419

Kumagai, P.S., C.S. Martins, E.M. Sales, H.V.D. Rosa, D.C. Mendonça, J.C.P. Damalio, F. Spinozzi, R. Itri, and A.P.U. Araujo. 2019. Correct partner makes the difference: Septin G-interface plays a critical role in amyloid formation. *Int. J. Biol. Macromol.* 133:428–435. https://doi.org/10.1016/j.ijbiomac.2019.04.105

Kuo, Y.C., Y.H. Lin, H.I. Chen, Y.Y. Wang, Y.W. Chiou, H.H. Lin, H.A. Pan, C.M. Wu, S.M. Su, C.C. Hsu, and P.L. Kuo. 2012. SEPT12 mutations cause male infertility with defective sperm annulus. *Hum. Mutat.* 33:710–719. https://doi.org/10.1002/humu.22028

Kuzmić, M., G. Castro Linares, J. Leischner Fialová, F. Iv, D. Salaün, A. Llewellyn, M. Gomes, M. Belhabib, Y. Liu, K. Asano, et al. 2022. Septin-microtubule association via a motif unique to isoform 1 of septin 9 tunes stress fibers. *J. Cell Sci.* 135:jcs258850. https://doi.org/10.1242/jcs.258850

Leonardo, D.A., I.A. Cavini, F.A. Sala, D.C. Mendonça, H.V.D. Rosa, P.S. Kumagai, E. Crusca Jr, N.F. Valadares, I.A. Marques, J. Brandão-Neto, et al. 2021. Orientational ambiguity in septin coiled coils and its structural basis. *J. Mol. Biol.* 433:166889. https://doi.org/10.1016/j.jmb.2021.166889

Liu, Z., Q.P. Vong, C. Liu, and Y. Zheng. 2014. Borg5 is required for angiogenesis by regulating persistent directional migration of the cardiac microvascular endothelial cells. *Mol. Biol. Cell.* 25:841–851. https://doi.org/10.1091/mbc.e13-09-0543

Low, C., and I.G. Macara. 2006. Structural analysis of septin 2, 6, and 7 complexes. *J. Biol. Chem.* 281:30697–30706. https://doi.org/10.1074/jbc.M605179200

Manley, S., J.M. Gillette, G.H. Patterson, H. Shroff, H.F. Hess, E. Betzig, and J. Lippincott-Schwartz. 2008. High-density mapping of single-molecule trajectories with photoactivated localization microscopy. *Nat. Methods.* 5:155–157. https://doi.org/10.1038/nmeth.1176

Mavrakis, M., Y. Azou-Gros, F.C. Tsai, J. Alvarado, A. Bertin, F. Iv, A. Kress, S. Brasselet, G.H. Koenderink, and T. Lecuit. 2014. Septins promote F-actin ring formation by crosslinking actin filaments into curved bundles. *Nat. Cell Biol.* 16:322–334. https://doi.org/10.1038/ncb2921

McMurray, M.A., A. Bertin, G. Garcia III, L. Lam, E. Nogales, and J. Thorner. 2011. Septin filament formation is essential in budding yeast. *Dev. Cell.* 20:540–549. https://doi.org/10.1016/j.devcel.2011.02.004

Mendonça, D.C., J.N. Macedo, S.L. Guimarães, F.L. Barroso da Silva, A. Cassago, R.C. Garratt, R.V. Portugal, and A.P.U. Araujo. 2019. A revised order of subunits in mammalian septin complexes. *Cytoskeleton.* 76:457–466. https://doi.org/10.1002/cm.21569

Menon, M.B., A. Sawada, A. Chaturvedi, P. Mishra, K. Schuster-Gossler, M. Galla, A. Schambach, A. Gossler, R. Förster, M. Heuser, et al. 2014. Genetic deletion of SEPT7 reveals a cell type-specific role of septins in microtubule destabilization for the completion of cytokinesis. *PLoS Genet.* 10:e1004558. https://doi.org/10.1371/journal.pgen.1004558

Momany, M., F. Pan, and R.L. Malmberg. 2008. Evolution and conserved domains of the septins. In The Septins. P.A. Hall, S.E.H. Russell, and J.R. Pringle, editors. John Wiley & Sons, Ltd. 35–45. https://doi.org/10.1002/9780470779705.ch2

Mostowy, S., M. Bonazzi, M.A. Hamon, T.N. Tham, A. Mallet, M. Lelek, E. Gouin, C. Demangel, R. Brosch, C. Zimmer, et al. 2010. Entrapment of intracytosolic bacteria by septin cage-like structures. *Cell Host Microbe.* 8:433–444. https://doi.org/10.1016/j.chom.2010.10.009

Mostowy, S., S. Janel, C. Forestier, C. Roduit, S. Kasas, J. Pizarro-Cerdá, P. Cossart, and F. Lafont. 2011. A role for septins in the interaction between the Listeria monocytogenes INVASION PROTEIN InlB and the Met receptor. *Biophys. J.* 100:1949–1959. https://doi.org/10.1016/j.bpj.2011.02.040

Neufeld, T.P., and G.M. Rubin. 1994. The Drosophila peanut gene is required for cytokinesis and encodes a protein similar to yeast putative bud neck filament proteins. *Cell.* 77:371–379. https://doi.org/10.1016/0092-8674(94)90152-X

Nguyen, T.Q., H. Sawa, H. Okano, and J.G. White. 2000. The C. elegans septin genes, unc-59 and unc-61, are required for normal postembryonic cytokineses and morphogenesis but have no essential function in embryogenesis. *J. Cell Sci.* 113:3825–3837. https://doi.org/10.1242/jcs.113.21.3825

Nishihama, R., M. Onishi, and J.R. Pringle. 2011. New insights into the phylogenetic distribution and evolutionary origins of the septins. *Biol. Chem.* 392:681–687. https://doi.org/10.1515/BC.2011.086

Ong, K., C. Wloka, S. Okada, T. Svitkina, and E. Bi. 2014. Architecture and dynamic remodelling of the septin cytoskeleton during the cell cycle. *Nat. Commun.* 5:5698. https://doi.org/10.1038/ncomms6698

Orré, T., A. Joly, Z. Karatas, B. Kastberger, C. Cabriel, R.T. Böttcher, S. Lévêque-Fort, J.B. Sibarita, R. Fässler, B. Wehrle-Haller, et al. 2021. Molecular motion and tridimensional nanoscale localization of kindlin control integrin activation in focal adhesions. *Nat. Commun.* 12:3104. https://doi.org/10.1038/s41467-021-23372-w

Pan, F., R.L. Malmberg, and M. Momany. 2007. Analysis of septins across kingdoms reveals orthology and new motifs. *BMC Evol. Biol.* 7:103. https://doi.org/10.1186/1471-2148-7-103

Racine, V., A. Hertzog, J. Jouanneau, J. Salamero, C. Kervrann, and J.B. Sibarita. 2006. Multiple-target tracking of 3D fluorescent objects based on simulated annealing. *I S Biomed. Imaging.* 1020–1023. https://doi.org/10.1109/ISBI.2006.1625094

Racine, V., M. Sachse, J. Salamero, V. Fraisier, A. Trubuil, and J.B. Sibarita. 2007. Visualization and quantification of vesicle trafficking on a three-dimensional cytoskeleton network in living cells. *J. Microsc.* 225:214–228. https://doi.org/10.1111/j.1365-2818.2007.01723.x

Rigato, A., F. Rico, F. Eghiaian, M. Piel, and S. Scheuring. 2015. Atomic force microscopy mechanical mapping of micropatterned cells shows adhesion geometry-dependent mechanical response on local and global scales. *ACS Nano.* 9:5846–5856. https://doi.org/10.1021/acsnano.5b00430

Rodal, A.A., L. Kozubowski, B.L. Goode, D.G. Drubin, and J.H. Hartwig. 2005. Actin and septin ultrastructures at the budding yeast cell cortex. *Mol. Biol. Cell.* 16:372–384. https://doi.org/10.1091/mbc.e04-08-0734

Rosa, H.V.D., D.A. Leonardo, G. Brognara, J. Brandão-Neto, H. D'Muniz Pereira, A.P.U. Araújo, and R.C. Garratt. 2020. Molecular recognition at septin interfaces: The switches hold the key. *J. Mol. Biol.* 432:5784–5801. https://doi.org/10.1016/j.jmb.2020.09.001

Röseler, S., K. Sandrock, I. Bartsch, A. Busse, H. Omran, N.T. Loges, and B. Zieger. 2011. Lethal phenotype of mice carrying a Sept11 null mutation. *Biol. Chem.* 392:779–781. https://doi.org/10.1515/BC.2011.093

Rosenblatt, G., B. Simkhovich, G. Bartal, and M. Orenstein. 2020. Nonmodal plasmonics: Controlling the forced optical response of nanostructures. *Phys. Rev. X.* 10:011071. https://doi.org/10.1103/PhysRevX.10.011071

Rossier, O., V. Octeau, J.B. Sibarita, C. Leduc, B. Tessier, D. Nair, V. Gatterdam, O. Destaing, C. Albigès-Rizo, R. Tampé, et al. 2012. Integrins β1 and β3 exhibit distinct dynamic nanoscale organizations inside focal adhesions. *Nat. Cell Biol.* 14:1057–1067. https://doi.org/10.1038/ncb2588

Sader, J.E., J.A. Sanelli, B.D. Adamson, J.P. Monty, X. Wei, S.A. Crawford, J.R. Friend, I. Marusic, P. Mulvaney, and E.J. Bieske. 2012. Spring constant calibration of atomic force microscope cantilevers of arbitrary shape. *Rev. Sci. Instrum.* 83:103705. https://doi.org/10.1063/1.4757398

Sala, F.A., N.F. Valadares, J.N. Macedo, J.C. Borges, and R.C. Garratt. 2016. Heterotypic coiled-coil formation is essential for the correct assembly of the septin heterofilament. *Biophys. J.* 111:2608–2619. https://doi.org/10.1016/j.bpj.2016.10.032

Salameh, J., I. Cantaloube, B. Benoit, C. Poüs, and A. Baillet. 2021. Cdc42 and its BORG2 and BORG3 effectors control the subcellular localization of septins between actin stress fibers and microtubules. *Curr. Biol.* 31:4088–4103.e5. https://doi.org/10.1016/j.cub.2021.07.004

Schmidt, K., and B.J. Nichols. 2004. Functional interdependence between septin and actin cytoskeleton. *BMC Cell Biol.* 5:43. https://doi.org/10.1186/1471-2121-5-43

Sellin, M.E., L. Sandblad, S. Stenmark, and M. Gullberg. 2011. Deciphering the rules governing assembly order of mammalian septin complexes. *Mol. Biol. Cell.* 22:3152–3164. https://doi.org/10.1091/mbc.e11-03-0253

Sellin, M.E., S. Stenmark, and M. Gullberg. 2014. Cell type-specific expression of SEPT3-homology subgroup members controls the subunit number of heteromeric septin complexes. *Mol. Biol. Cell.* 25:1594–1607. https://doi.org/10.1091/mbc.e13-09-0553

Shindo, A., and J.B. Wallingford. 2014. PCP and septins compartmentalize cortical actomyosin to direct collective cell movement. *Science.* 343:649–652. https://doi.org/10.1126/science.1243126

Sirajuddin, M., M. Farkasovsky, F. Hauer, D. Kühlmann, I.G. Macara, M. Weyand, H. Stark, and A. Wittinghofer. 2007. Structural insight into filament formation by mammalian septins. *Nature.* 449:311–315. https://doi.org/10.1038/nature06052

Downloaded from http://rupress.org/jcb/article-pdf/222/3/e202203016/1445844/jcb_202203016.pdf by guest on 20 October 2025

Soroor, F., M.S. Kim, O. Palander, Y. Balachandran, R.F. Collins, S. Benlekbir, J.L. Rubinstein, and W.S. Trimble. 2021. Revised subunit order of mammalian septin complexes explains their in vitro polymerization properties. *Mol. Biol. Cell*. 32:289–300. https://doi.org/10.1091/mbc.E20-06-0398

Steels, J.D., M.P. Estey, C.D. Froese, D. Reynaud, C. Pace-Asciak, and W.S. Trimble. 2007. Sept12 is a component of the mammalian sperm tail annulus. *Cell Motil. Cytoskeleton*. 64:794–807. https://doi.org/10.1002/cm.20224

Sumbul, F., N. Hassanpour, J. Rodriguez-Ramos, and F. Rico. 2020. One-step calibration of AFM in liquid. *Front. Phys.* 8:301. https://doi.org/10.3389/fphy.2020.00301

Surka, M.C., C.W. Tsang, and W.S. Trimble. 2002. The mammalian septin MSF localizes with microtubules and is required for completion of cytokinesis. *Mol. Biol. Cell*. 13:3532–3545. https://doi.org/10.1091/mbc.e02-01-0042

Szuba, A., F. Bano, G. Castro-Linares, F. Iv, M. Mavrakis, R.P. Richter, A. Bertin, and G.H. Koenderink. 2021. Membrane binding controls ordered self-assembly of animal septins. *Elife*. 10:e63349. https://doi.org/10.7554/eLife.63349

Tada, T., A. Simonetta, M. Batterton, M. Kinoshita, D. Edbauer, and M. Sheng. 2007. Role of Septin cytoskeleton in spine morphogenesis and dendrite development in neurons. *Curr. Biol.* 17:1752–1758. https://doi.org/10.1016/j.cub.2007.09.039

Tanaka-Takiguchi, Y., M. Kinoshita, and K. Takiguchi. 2009. Septin-mediated uniform bracing of phospholipid membranes. *Curr. Biol.* 19:140–145. https://doi.org/10.1016/j.cub.2008.12.030

Targa, B., L. Klipfel, I. Cantaloube, J. Salameh, B. Benoit, C. Poüs, and A. Baillet. 2019. Septin filament coalignment with microtubules depends on SEPT9_i1 and tubulin polyglutamylation, and is an early feature of acquired cell resistance to paclitaxel. *Cell Death Dis.* 10:54. https://doi.org/10.1038/s41419-019-1318-6

Tojkander, S., G. Gateva, and P. Lappalainen. 2012. Actin stress fibers: Assembly, dynamics and biological roles. *J. Cell Sci.* 125:1855–1864. https://doi.org/10.1242/jcs.098087

Tooley, A.J., J. Gilden, J. Jacobelli, P. Beemiller, W.S. Trimble, M. Kinoshita, and M.F. Krummel. 2009. Amoeboid T lymphocytes require the septin cytoskeleton for cortical integrity and persistent motility. *Nat. Cell Biol.* 11:17–26. https://doi.org/10.1038/ncb1808

Uhlén, M., L. Fagerberg, B.M. Hallström, C. Lindskog, P. Oksvold, A. Mardinoglu, Å. Sivertsson, C. Kampf, E. Sjöstedt, A. Asplund, et al. 2015. Proteomics. Tissue-based map of the human proteome. *Science*. 347:1260419. https://doi.org/10.1126/science.1260419

Vadnjal, N., S. Nourreddine, G. Lavoie, M. Serres, P.P. Roux, and E.K. Paluch. 2022. Proteomic analysis of the actin cortex in interphase and mitosis. *J. Cell Sci.* 135:jcs259993. https://doi.org/10.1242/jcs.259993

Verdier-Pinard, P., D. Salaun, H. Bouguenina, S. Shimada, M. Pophillat, S. Audebert, E. Agavnian, S. Coslet, E. Charafe-Jauffret, T. Tachibana, and A. Badache. 2017. Septin 9_i2 is downregulated in tumors, impairs cancer cell migration and alters subnuclear actin filaments. *Sci. Rep.* 7:44976. https://doi.org/10.1038/srep44976

Versele, M., and J. Thorner. 2004. Septin collar formation in budding yeast requires GTP binding and direct phosphorylation by the PAK, Cla4. *J. Cell Biol.* 164:701–715. https://doi.org/10.1083/jcb.200312070

Vissa, A., M. Giuliani, C.D. Froese, M.S. Kim, F. Soroor, P.K. Kim, W.S. Trimble, and C.M. Yip. 2019. Single-molecule localization microscopy of septin bundles in mammalian cells. *Cytoskeleton*. 76:63–72. https://doi.org/10.1002/cm.21481

Wang, N., I.M. Tolić-Nørrelykke, J. Chen, S.M. Mijailovich, J.P. Butler, J.J. Fredberg, and D. Stamenović. 2002. Cell prestress. I. Stiffness and prestress are closely associated in adherent contractile cells. *Am. J. Physiol. Cell Physiol.* 282:C606–C616. https://doi.org/10.1152/ajpcell.00269.2001

Waterhouse, A., M. Bertoni, S. Bienert, G. Studer, G. Tauriello, R. Gumienny, F.T. Heer, T.A.P. de Beer, C. Rempfer, L. Bordoli, et al. 2018. SWISS-MODEL: Homology modelling of protein structures and complexes. *Nucleic Acids Res.* 46:W296–W303. https://doi.org/10.1093/nar/gky427

Weber, K., P.C. Rathke, and M. Osborn. 1978. Cytoplasmic microtubular images in glutaraldehyde-fixed tissue culture cells by electron microscopy and by immunofluorescence microscopy. *Proc. Natl. Acad. Sci. USA*. 75:1820–1824. https://doi.org/10.1073/pnas.75.4.1820

Wegel, E., A. Göhler, B.C. Lagerholm, A. Wainman, S. Uphoff, R. Kaufmann, and I.M. Dobbie. 2016. Imaging cellular structures in super-resolution with SIM, STED and localisation microscopy: A practical comparison. *Sci. Rep.* 6:27290. https://doi.org/10.1038/srep27290

Xie, H., M. Surka, J. Howard, and W.S. Trimble. 1999. Characterization of the mammalian septin H5: Distinct patterns of cytoskeletal and membrane association from other septin proteins. *Cell Motil. Cytoskeleton*. 43:52–62. https://doi.org/10.1002/(SICI)1097-0169(1999)43:1<52::AID-CM6>3.0.CO;2-5

Xie, Y., J.P. Vessey, A. Konecna, R. Dahm, P. Macchi, and M.A. Kiebler. 2007. The GTP-binding protein Septin 7 is critical for dendrite branching and dendritic-spine morphology. *Curr. Biol.* 17:1746–1751. https://doi.org/10.1016/j.cub.2007.08.042

Yamada, S., T. Isogai, R. Tero, Y. Tanaka-Takiguchi, T. Ujihara, M. Kinoshita, and K. Takiguchi. 2016. Septin interferes with the temperature-dependent domain formation and disappearance of lipid bilayer membranes. *Langmuir*. 32:12823–12832. https://doi.org/10.1021/acs.langmuir.6b03452

Zent, E., I. Vetter, and A. Wittinghofer. 2011. Structural and biochemical properties of Sept7, a unique septin required for filament formation. *Biol. Chem.* 392:791–797. https://doi.org/10.1515/BC.2011.082

Zhang, J., C. Kong, H. Xie, P.S. McPherson, S. Grinstein, and W.S. Trimble. 1999. Phosphatidylinositol polyphosphate binding to the mammalian septin H5 is modulated by GTP. *Curr. Biol.* 9:1458–1467. https://doi.org/10.1016/S0960-9822(00)80115-3

Downloaded from http://rupress.org/jcb/article-pdf/222/3/e202203016/1445844/jcb_202203016.pdf by guest on 20 October 2025

JCB

Supplemental material

Downloaded from http://rupress.org/jcb/article-pdf/222/3/e202203016/1445844/jcb_202203016.pdf by guest on 20 October 2025

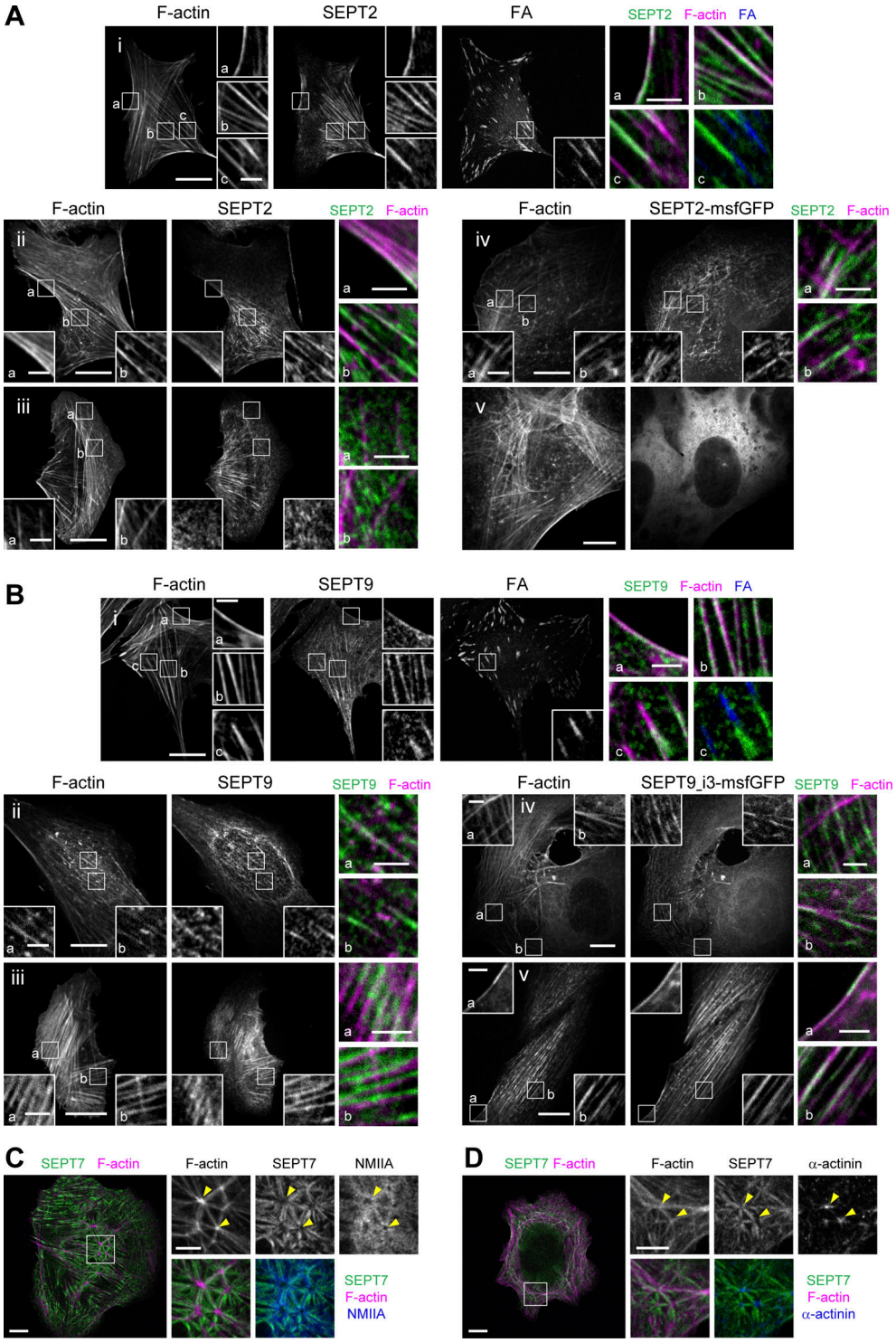

Figure S1. **SEPT2, SEPT7 and SEPT9 distribution on different types of stress fibers in U2OS cells. (A)** Representative confocal micrographs of SEPT2 immunostained cells (i–iii) and cells expressing SEPT2-msfGFP (iv and v). SEPT2 immunostained cells are co-stained for F-actin (phalloidin) and the FA protein paxillin. Examples show SEPT2 localizing (i) to peripheral (a) and ventral (b and c) SFs and excluded from focal adhesions (FAc) , (ii) to peripheral (a) and perinuclear actin caps (b), (iii) to transverse arcs (b) and excluded from dorsal SFs (a and b), (iv) to transverse arcs (a and b) and excluded from dorsal SFs (a), and (v) showing a diffuse cytosolic phenotype. **(B)** Representative confocal micrographs of SEPT9 immunostained cells (i–iii) and cells expressing SEPT9_i3-msfGFP (iv and v). SEPT9 immunostained cells are co-stained for F-actin (phalloidin) and the FA protein paxillin. Examples show SEPT9 localizing (i) to peripheral (a) and ventral (b and c) SFs and excluded from focal adhesions (FA; c), (ii) to perinuclear actin caps (a and b), (iii) to transverse arcs (a) and ventral SFs (b), (iv) to transverse arcs (a) and excluded from dorsal SFs (a) and to ventral SFs (b), and (v) to peripheral (a) and perinuclear actin caps (b). **(C and D)** Representative confocal micrographs of SEPT7 immunostainings showing SEPT7 localizing to ventral actin nodes. Cells are co-stained for F-actin (phalloidin) and non-muscle myosin heavy chain IIA (NMIIA; C) or α-actinin (D). Yellow arrowheads point to two actin nodes in each example. Scale bars in large fields of views, 10 µm. Scale bars in insets, 2 µm (A and B) and 5 µm (C and D). Related to Fig. 1 B.

Downloaded from http://rupress.org/jcb/article-pdf/222/3/e202203016/1445844/jcb_202203016.pdf by guest on 20 October 2025

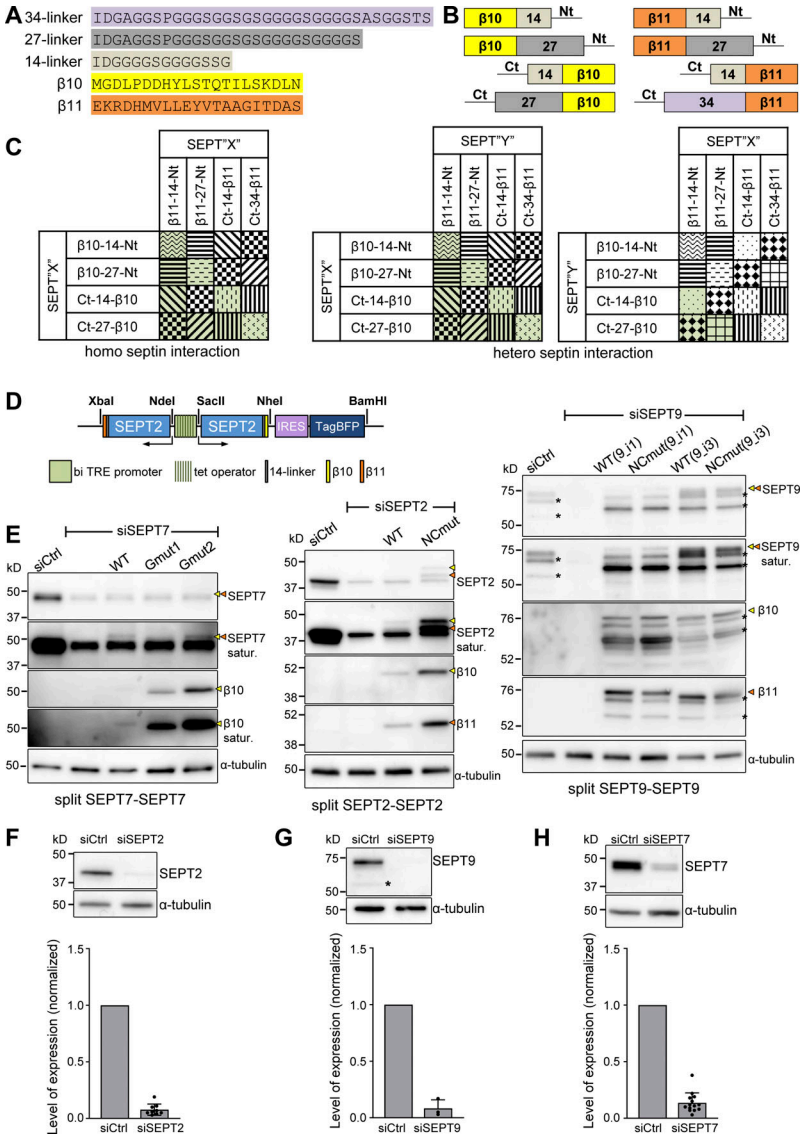

Figure S2. **Design of the tripartite split-GFP complementation assay for probing septin organization. (A)** Sequences of the β10- and β11-tags used for all split assays and of the linker sequences tested in screening experiments (B and C); 14-residue linkers were used throughout this study. **(B)** Schematic of N- and C-terminal β10- and β11-tag septin fusions tested in screening experiments (C) using short or long linkers (A). **(C)** Schematic of β10- and β11-septin fusion combinations for screening tripartite split GFP complementation. Combinations with the same pattern were considered to be equivalent (for example, SEPT2-14-β10/β11-14-SEPT2 and SEPT2-14-β11/β10-14-SEPT2). The combinations in green are the ones tested experimentally. **(D)** Schematic of the pTRIP TRE Bi vector bearing a bidirectional tetracycline response element (TRE) promoter for the doxycycline-inducible co-expression of β10- and β11-tagged septins. An IRES-TagBFP cassette was used for monitoring septin expression. Restriction sites used for subcloning are indicated (see methods for details). **(E)** Left: Western blots of U2OS-Tet-On-GFP1-9 cell line lysates probed with anti-SEPT7, anti-β10 and anti-α-tubulin antibodies upon treatment with siRNAs targeting LacZ (siCtrl), SEPT7 (siSEPT7), and targeting SEPT7 while co-expressing wild-type β10- and β11-SEPT7 (WT), β10- and β11-SEPT7Gmut1 (Gmut1), and β10- and β11-SEPT7Gmut2 (Gmut2). Yellow and orange arrowheads point to bands correspond to β10- and β11-fusions. The SEPT7 and β10 blots are also shown saturated on purpose for displaying weaker bands. Molecular weight markers are shown on the left. Middle: Western blots of U2OS-Tet-On-GFP1-9 cell line lysates probed with anti-SEPT2, anti-β10, anti-β11, and anti-α-tubulin antibodies upon treatment with siRNAs targeting LacZ (siCtrl), SEPT2 (siSEPT2), and targeting SEPT2 while co-expressing wild-type SEPT2-β10 and -β11 (WT) or SEPT2NCmut-β10 and -β11 (NCmut). Yellow and orange arrowheads point to bands correspond to β10- and β11-fusions. The SEPT2 blot is also shown saturated on purpose for displaying weaker bands. Right: Western blots of U2OS-Tet-On-GFP1-9 cell line lysates probed with anti-SEPT9, anti-β10, anti-β11, and anti-α-tubulin antibodies upon treatment with siRNAs targeting LacZ (siCtrl), SEPT9 (siSEPT9), and targeting SEPT9 while co-expressing wild-type SEPT9-β10 and -β11 (WT) or SEPT9NCmut-β10 and -β11 (NCmut) for both SEPT9_i1 and SEPT9_i3. Yellow and orange arrowheads point to bands correspond to β10- and β11-fusions. The SEPT9 blot is also shown saturated on purpose for displaying weaker bands. Asterisks point to SEPT9 degradation products. **(F)** Western blot of U2OS cell lysates probed with anti-SEPT2 and anti-α-tubulin antibodies upon treatment with siRNAs targeting LacZ (siCtrl) or SEPT2 (siSEPT2). Molecular weight markers are shown on the left. Bottom, respective quantification of SEPT2 protein levels (mean + SD). Mean values (normalized to 1 for siCtrl) are from three independent siCtrl and nine independent siSEPT2 treatments. SEPT2 was knocked down on average by 92%. **(G)** Same as F for SEPT9. The asterisk points to a SEPT9 degradation product. Mean values (normalized to 1 for siCtrl) are from three independent siCtrl and three independent siSEPT9 treatments. SEPT9 was knocked down on average by 92%. **(H)** Same as F for SEPT7. Mean values (normalized to 1 for siCtrl) are from 3 independent siCtrl and 12 independent siSEPT7 treatments. SEPT7 was knocked down on average by 86%. Source data are available for this figure: SourceData FS2.

Downloaded from http://rupress.org/jcb/article-pdf/222/3/e202203016/1445844/jcb_202203016.pdf by guest on 20 October 2025

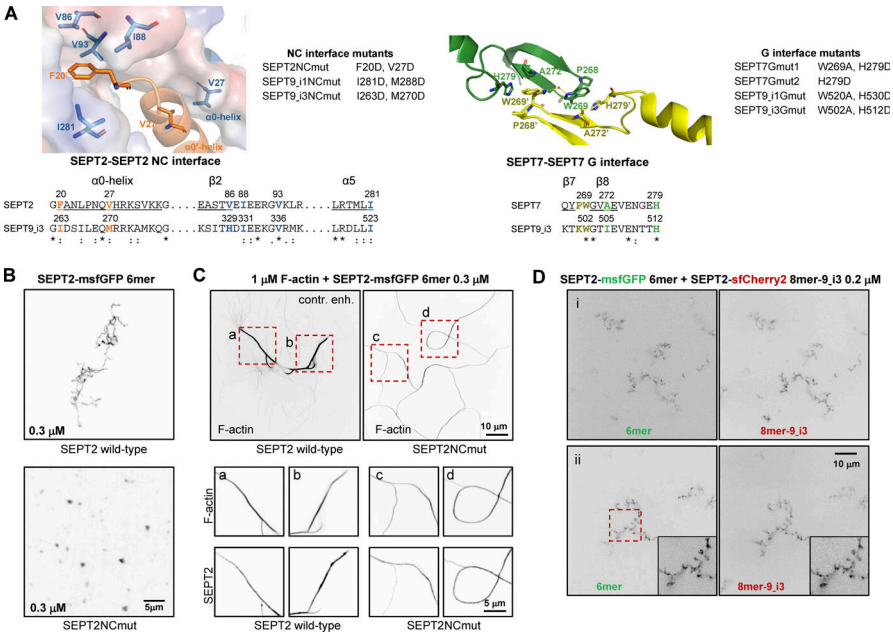

Figure S3. **Septin interface mutants used in this study and cell-free reconstitution of septin assembly. (A)** Left, top: Conserved residues in the SEPT2-SEPT2 NC interface are shown in the crystal structure of human SEPT2 homodimers (PDB accession no. 2QA5; Sirajuddin et al., 2007). The backbone structure is displayed as a cartoon representation in PyMOL, with critical residues represented as sticks (deep blue and red for nitrogen and oxygen atoms, respectively). Residues F20 from the hook-loop of one SEPT2 subunit (orange) interact with the hydrophobic cleft formed by V86, I88, V93, and I281 of the adjacent SEPT2 subunit (blue). The importance of this phenylalanine in anchoring the α0 helix at the NC interface was emphasized only recently (Cavini et al., 2021). The blue subunit's surface representation highlights the complementary of shape between the two SEPT2 subunits in this interface. The interaction between the α0 helices of each subunit is also stabilized through a hydrophobic interaction between their respective V27. Left, bottom: Sequence alignment of the regions including the residues shown in the NC interface structure for SEPT2 and SEPT9_i3. The structural elements (α0, β2, α5) related to these residues are underlined and shown above the sequences. The consensus symbols are from ClustalW alignments of all human septins (*, fully conserved residue; colon, conservation between residues with strongly similar physicochemical properties; period, conservation between residues with weakly similar physicochemical properties). We note that the residues described above are strictly or physicochemically conserved (except for V86), highlighting their importance in stabilizing the SEPT2-SEPT2 NC interface. The NC interface mutants used in this study are listed on the right of the crystal structure. A mutation of F20D/I263D is expected to destabilize the hydrophobic pocket depicted above, whereas a V27D/M270D is expected to destabilize the α0 helices interface. Importantly, a strictly conserved aspartate (SEPT2 E90, corresponding to SEPT6 E90 and SEPT7 E102 which are well defined in the cryo-EM structure of the SEPT6-SEPT7 NC interface [Mendonca et al., 2019]) in the loop connecting β2 and β3 is pointing to the hydrophobic cleft where the phenylalanine resides. The F20D mutation is thus expected to result in a repulsion between the aspartate and glutamate and contribute further to the destabilization of the NC interface. Right, top: Conserved residues in the SEPT7-SEPT7 G interface are shown in the crystal structure of human SEPT7 homodimers (PDB accession no. 6N0B; Brognara et al., 2019). The backbone structure is displayed as a cartoon representation in PyMOL, with critical residues represented as sticks (deep blue and red for nitrogen and oxygen atoms, respectively). Residues W269 of one SEPT7 subunit (yellow) interact with residues W269, A272 and H279 in the adjacent SEPT7 subunit (green; Sirajuddin et al., 2007; Zent et al., 2011). W269 from adjacent subunits interact through a water molecule bridge through hydrogen bonds. In addition, each W269 is engaged in π-π interactions with H279 and CH-π interactions with A272 of the opposite subunit. Right, bottom: Sequence alignment of the regions including the residues shown in the G interface structure for SEPT7 and SEPT9_i3. The structural elements (β7, β8) related to these residues are underlined and shown above the sequences. The consensus symbols are from ClustalW alignments of all human septins (*, fully conserved residue; colon, conservation between residues with strongly similar physicochemical properties). Notice that W269 and H279 are both strictly conserved, showing their importance in stabilizing this interface. The G interface mutants that were used in this study are listed on the right of the crystal structure. The presence of both mutations W269A and H279D in SEPT7 and SEPT9 is expected to destabilize the SEPT7-SEPT7 and SEPT7-SEPT9 G-interfaces. The loss of the aromatic cycle properties in the mutant W269A does not allow the abovementioned critical interactions mediated by the wild-type Trp. W269A is expected to destabilize H279 and potentially change its orientation. In addition, the much smaller size of the alanine will poorly mimic the hydrophobic interaction between W269 and H279, weakening the G-interface. Note that W269 is in the vicinity of Y267 of the same subunit. This tyrosine interacts with the nucleotide buried within the G-interface. Consequently, any mutations destabilizing W269 could dramatically destabilize the overall G-interface because of a domino effect. Similarly, H279D is expected to preclude hydrophobic interactions with W269 and thus destabilize the latter. The single mutation H279D in SEPT7 is expected to destabilize the SEPT7-SEPT7 G-interface when present in both SEPT7 subunits, but not the SEPT7-SEPT9 interface with wild-type SEPT9. **(B)** Representative spinning disk fluorescence images of septin filament assembly upon polymerization of hexamers in solution at the indicated final protomer concentration. Protomers contained either wild-type SEPT2 (top panel) or SEPT2NCmut (bottom panel). Images use an inverted grayscale. Related to Fig. 2 C. **(C)** Representative spinning disk fluorescence images of reconstituted actin filaments, polymerizing in the presence of septin hexamers in solution. Protomers contained either wild-type SEPT2 or SEPT2NCmut. Actin filaments are visualized with AlexaFluor568-conjugated phalloidin, and septins with SEPT2-msfGFP. One example of large fields of view are shown for each condition, depicting cross-linking of actin filaments; only actin labeling is shown. The image for actin in the presence of wild-type hexamers is contrast-enhanced on purpose in order to saturate the actin bundles so that weaker-intensity single actin filaments are also visible. Insets on the bottom show higher magnifications of selected regions of interest on the top (dashed squares in red). Two regions of interest (a and b for wild-type SEPT2 and c and d for SEPT2NCmut) are shown in each case, depicting both the actin and septin signals. Scale bars in all large fields of views, 10 μm. Scale bars in all insets, 5 μm. **(D)** Representative spinning disk fluorescence images of septin filament assembly upon co-polymerization of hexamers containing SEPT2-msfGFP and octamers-9_i3 containing SEPT2-sfCherry2 at the indicated final protomer concentration. Images use an inverted grayscale. Scale bars in all large fields of views, 10 μm.

Downloaded from http://rupress.org/jcb/article-pdf/222/3/e202203016/1445844/jcb_202203016.pdf by guest on 20 October 2025

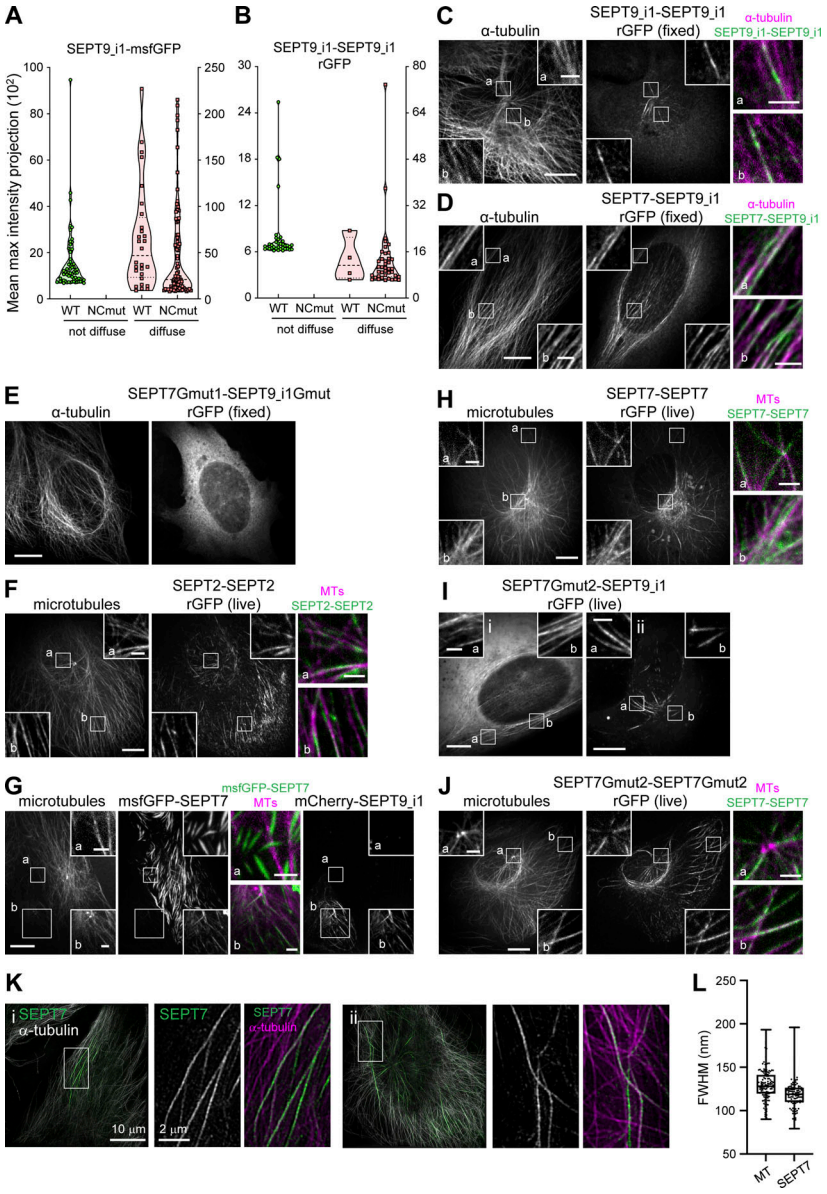

Figure S4. **All septins on microtubules organize as octamer-based filaments. (A)** Violin plots depicting the distribution of diffuse cytosolic (red datapoints) vs. non-diffuse (green datapoints) phenotypes as a function of the intensity of the msfGFP signal in cells expressing wild-type SEPT9_i1-msfGFP or SEPT9_i1NCmut-msfGFP. Data points are from a total of 90 cells each for wild-type and mutant SEPT9 distributed among the two phenotypes. **(B)** Violin plots depicting the distribution of diffuse cytosolic (red datapoints) vs. non-diffuse (green datapoints) phenotypes as a function of the intensity of the rGFP signal in GFP1-9 cells co-expressing wild-type SEPT9_i1-β10 and -β11 or SEPT9_i1NCmut-β10 and -β11. Data points are from a total of 40 cells each for wild-type and mutant SEPT9 distributed among the two phenotypes. **(C)** Representative confocal micrograph of SEPT9_i1-SEPT9_i1 rGFP distribution in fixed cells co-stained for microtubules (α-tubulin). **(D)** Representative example of a GFP1-9 cell co-expressing β11-SEPT7 and SEPT9_i1-β10 and co-stained for α-tubulin, with rGFP localizing to microtubules. **(E)** Representative example of GFP1-9 cell co-expressing β11-SEPT7Gmut1 and SEPT9_i1Gmut-β10 co-stained for α-tubulin showing a diffuse cytosolic phenotype. **(F)** Representative confocal micrograph of SEPT2-SEPT2 rGFP distribution in a live cell co-expressing mCherry-SEPT9_i1 (not shown) and labeled for microtubules (SiR-tubulin). **(G)** Representative example of a cell (bottom left) co-expressing msfGFP-SEPT7 and mCherry-SEPT9_i1 and labeled for microtubules (SiR-tubulin) showing msfGFP-SEPT7 localizing to microtubules (b). A cell expressing only msfGFP-SEPT7 (top right) shows msfGFP-SEPT7 localizing to ectopic bundles not co-localizing with microtubules (a). Scale bars in large fields of views, 10 µm. Scale bars in insets, 2 µm. Related to Fig. 5 E. **(H)** Representative confocal micrograph of SEPT7-SEPT7 rGFP distribution in a live cell co-expressing mCherry-SEPT9_i1 (not shown) and labeled for microtubules (SiR-tubulin). **(I)** Representative examples of GFP1-9 cells co-expressing β11-SEPT7Gmut2 and SEPT9_i1-β10 with rGFP localizing to microtubules. **(J)** Representative example of a GFP1-9 cell co-expressing β10- and β11-SEPT7Gmut2 co-expressing mCherry-SEPT9_i1 (not shown) and labeled for microtubules (SiR-tubulin). **(C–J)** Scale bars in large fields of views, 10 µm. Scale bars in insets, 2 µm. **(K)** Representative SIM micrographs of cells (i, ii) expressing mCherry-SEPT9_i1 (not shown) co-stained for SEPT7 and α-tubulin. Scale bars in large fields of views, 10 µm. Scale bars in insets, 2 µm. **(L)** Box plots depict the distributions of measured widths, as the full width at half maximum (FWHM), of microtubules (MT) and MT-associated septins (SEPT7). The data points are plotted on top of the respective box plots; data points correspond to width measurements at multiple positions along MT and septin fibers and in multiple MT and septin fibers per cell in a total of 8 cells. On each box, the central mark indicates the median, and the bottom and top edges of the box indicate the 25th and 75th percentiles, respectively. The whiskers extend to the minimum and maximum values. The number of measurements is *n* = 128 and 112 for MTs and septins, respectively. The respective median values are 128 and 119 nm for MTs and septins, respectively.

Downloaded from http://rupress.org/jcb/article-pdf/222/3/e202203016/1445844/jcb_202203016.pdf by guest on 20 October 2025

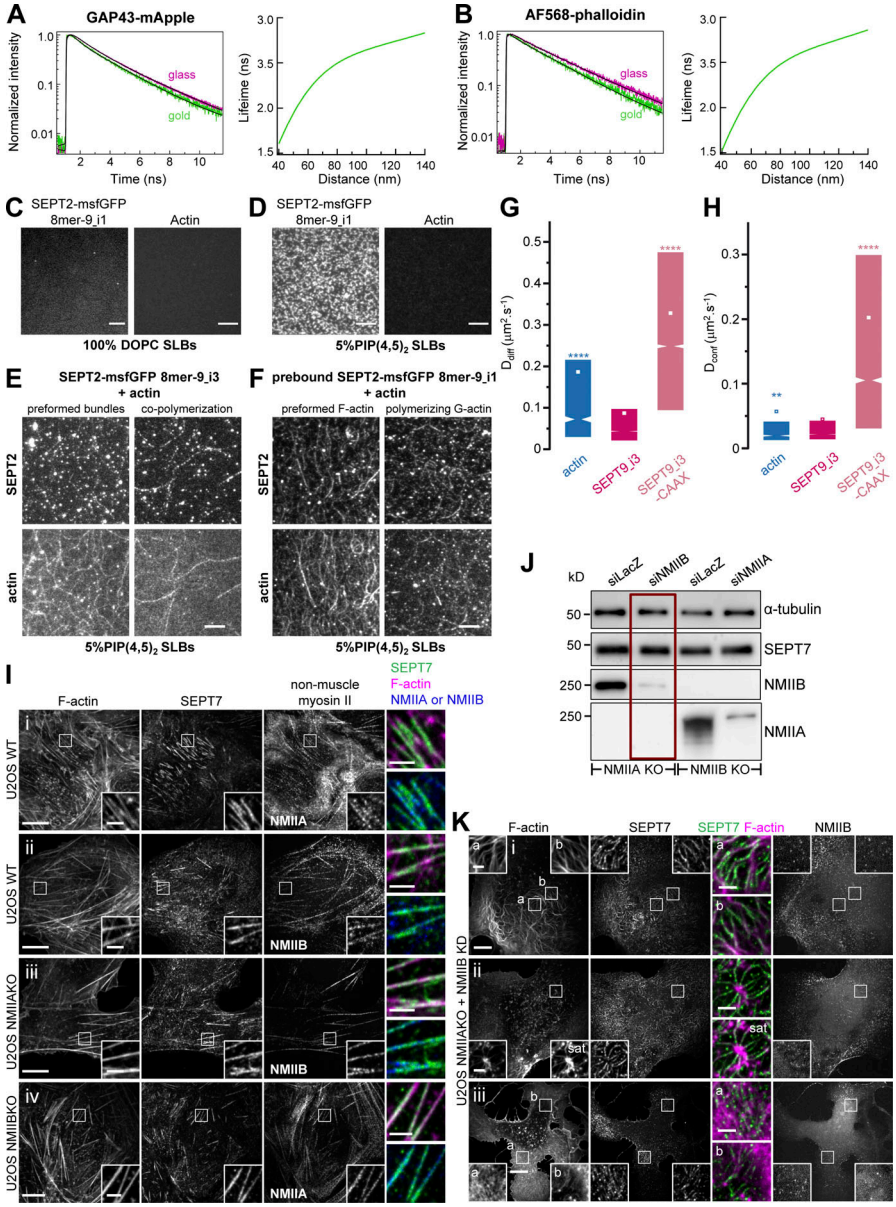

Figure S5. **Septin filaments are closely apposed to the plasma membrane, are immobilized on actin stress fibers, and can mediate actin-membrane anchoring in the absence of myosin-II. (A and B)** depict representative examples of lifetime decay traces for GAP43-mApple (A, left) and AF568-phalloidin (F-actin; B, left) on glass and in the presence of gold. The solid lines represent the numerical fits, showing the lifetime reduction due to the MIET process. The respective calculated lifetime-distance dependences, used to calculate the distances of the fluorophores from the coverslip (Fig. 10 E) are shown in the respective right panels. Related to Fig. 10, B–E. **(C and D)** TIRF images of SEPT2-msfGFP 8mer-9_i1 alone (left) or F-actin alone (right) on top of a supported lipid bilayer (SLB) composed of 100% DOPC (C) or 5% PI(4,5)P_2 and 95% DOPC (D). Scale bar, 5 µm. Related to Fig. 10 F. **(E)** TIRF images of SEPT2-msfGFP 8mer-9_i3 and F-actin, either co-polymerized on top of an SLB, or co-polymerized in solution to form preformed bundles that were then flushed onto the supported lipid bilayer. The supported lipid bilayer was composed of 5% of PI(4,5)P_2, a septin-interacting lipid, and 95% DOPC. Scale bar, 5 µm. Related to Fig. 10 F. **(F)** TIRF images of SEPT2-msfGFP 8mer-9_i1 prepolymerized on top of a supported lipid bilayer (SLB), with actin added in a second step to the membrane-bound septin filaments, either as prepolymerized actin filaments or as G-actin. The supported lipid bilayer was composed of 5% PI(4,5)P_2 and 95% DOPC. Scale bar, 5 µm. Related to Fig. 10 F. **(G and H)** Box plots displaying the median (notch) and mean (square) ± percentile (25–75%) of diffusion coefficients corresponding to the free diffusion (D_{diff}) (G) and confined diffusion (D_{conf}) (H) trajectories outside FAs from sptPALM. Related to Fig. 10, G–K. Statistical significance was obtained using two-tailed, non-parametric Mann–Whitney rank sum test. The different conditions were compared to the SEPT9_i3-mEos3.2 condition. The resulting P values are indicated as follows: ** P < 0.01; **** P < 0.0001. **(I)** Representative confocal micrographs of U2OS cells co-stained for F-actin (phalloidin), SEPT7 and non-muscle myosin heavy chain isoforms IIA (NMIIA) or IIB (NMIIB). Wild-type U2OS cells were co-stained for either NMIIA (i) or NMIIB (ii). NMIIA KO U2OS cells were co-stained for NMIIB (iii). NMIIB KO U2OS cells were co-stained for NMIIA (iv). **(J)** Western blot of NMIIA KO and NMIIB KO U2OS cell lysates probed with anti-α-tubulin, anti-SEPT7, anti-NMIIA and anti-NMIIB antibodies. NMIIA KO cells were treated either with LacZ or NMIIB siRNA. NMIIB KO cells were treated either with LacZ or NMIIA siRNA. Molecular weight markers are shown on the left. The condition shown with the red rectangle corresponds to the images shown in K. **(K)** Representative confocal micrographs of NMIIA KO U2OS cells (i–iii) treated with NMIIB siRNA and co-stained for F-actin (phalloidin), SEPT7 and NMIIB. Scale bars in large fields of views, 10 µm. Scale bars in insets, 2 µm. Source data are available for this figure: SourceData FS5.

Downloaded from http://rupress.org/jcb/article-pdf/222/3/e202203016/1445844/jcb_202203016.pdf by guest on 20 October 2025

Provided online is Table S1. Table S1 shows oligonucleotide primer sequences used for the generation of the plasmids used in this study.

Downloaded from http://rupress.org/jcb/article-pdf/222/3/e202203016/1445844/jcb_202203016.pdf by guest on 20 October 2025